SAPIENZA
UNIVERSITÀ DI ROMA

Semi-analytical Approaches to Gravitational Radiation from Astrophysical Sources

IRAP PhD

Dottorato di Ricerca in Fisica – XXX Ciclo

Candidate

José Fernando Rodríguez Ruiz
ID number Passport AO154849

Thesis Advisor

Prof. Jorge Armando
Rueda Hernandez

A thesis submitted in partial fulfillment of the requirements
for the degree of Doctor of Philosophy in Physics

July 2019

Thesis defended on 19 July 2019
in front of a Board of Examiners composed by:

Prof. Fulvio Ricci, Sapienza – Università di Roma, Rome, Italy (chairman)

Prof. Stefano Vitale, University of Trento, Trento, Italy

Prof. Wen-Biao, Han Chinese Academy of Sciences, CAS; Shanghai Astronomical Observatory, Shanghai, China

---

Semi-analytical Approaches to Gravitational Radiation from Astrophysical Sources

Ph.D. thesis. Sapienza – University of Rome

ISBN: 000000000-0

This thesis has been typeset by LaTeX and the Sapthesis class.

Version: September 24, 2019

Author’s email: joferoru@gmail.com

Dedicated to
Margarita and my parents Luz Marina and Carlos Julio

Abstract

Electromagnetic (EM) astronomical observations have improved the understanding of many astrophysical phenomena, e.g. X-ray binaries, gamma-ray bursts (GRBs) among others. These EM signals are in general incoherent and some information is lost during the propagation. In contrast, gravitational waves (GW) are mostly emitted by the coherent motion of large amounts of matter and can give the additional missing information. However, GWs are rather weak and their detection requires great technological efforts. Since it is expected that the GW signal is smaller than the noise in the detector, the matched-filter technique is usually used for claiming detection and for determining the parameters of the source. This requires knowledge of the physical signal and of the noise, the latter is usually not perfectly known. Numerical-relativity (NR) can provide accurate templates for binary black hole mergers and partially accurate template for binary neutron stars or binary white dwarfs, but currently, simulations are computationally demanding. Semi-analytical approaches to GW can provide solution to this issue. Besides, since they are constructed following basic principles, they provide clear physical interpretations and consistency tests to observational results. This thesis was devoted to the development and study of semi-analytical models of GW radiation from different astrophysical sources.

From the basic physics of black holes (BHs), this work introduced the "helicoidal drift sequence" (HDS), which describes the dynamics of an inspiraling test particle driven by GW emission on the *Kerr spacetime*. It was found that the final plunge, after the passage of the innermost stable circular orbit (ISCO), is nearly geodesic and emits less GWs than the amount implied by other semi-analytical approaches e.g. Ori & Thorne (2000).

Next, the HDS augmented with the Newtonian center-of-mass point of view, was used here to construct "test particle" waveforms in order to model binary black hole (BBH) mergers with comparable mass components. Since this work uses a Kerr "background", even in the case of BBHs with spin-less components, the model effectively incorporates frame dragging due to the orbital angular momentum of the system. Test particle waveforms, up to the frequency of the ISCO, were found to be in excellent agreement with the ones of NR simulations. The contribution of the orbital angular momentum of the system to frame dragging was not taken into a account by previous semi-analytical models.

This work also studied consistency between EM and GW observations. The recent GW event GW170817, consistent with a binary neutron star (BNS) merger, was associated with the EM counterpart GRB170817-AT 2017gfo. From the GW data, an independent calculation of the localization of the source was made in this work. It was found that the latter localization is consistent with the one inferred from the EM data. On the other hand, the EM counterpart is not consistent when it is compared with the prototype of known GRBs. An alternative scenario, namely the merger of a binary white dwarf, is introduced to explain the EM emission.

The recent classification of GRBs and the inferred observed rates given by Ruffini et al. (2018b), were used in this work to compute the detection rate of GWs from BNS, BH-NS and NS-WD systems, by earth-based interferometers. Namely, the inferred detection rate of GWs from BNSs, for design sensitivity (2022+) of LIGO-Virgo detectors is $\sim 0.1 - 0.2$ yr^{-1}, consistent with lower limits of rates found in the literature.

In addition, two overlooked astrophysical GW sources were studied: deformed, rotating white dwarf-like objects, called in this work chirping ellipsoids (CELs), and extreme mass-ratio inspirals (EMRIs) composed of a planet-like object and an intermediate-mass BH. It was found that CELs are quasi-monochromactic GW sources and individually detectable by planned space-based missions such as *LISA, TianQin and Taiji*. Equally important, this work shows that the CEL waveform is practically indistinguishable from the one the aforementioned EMRIs and from the one of non-interacting double white dwarfs (DWDs). In view of this degeneracy, the rates of these sources were estimated and it was found that all the systems have similar rates. The kind of EMRIs studied here do not accumulate the sufficient signal-to-noise ratio to be individually detected by future space-based interferometers, but owing to the fact that they exhibit a rate comparable to DWDs, they are plausible stochastic GW sources. As a consequence of the similarity of the rates of CELs and DWDs, it is expected significant source confusion between them. On the other hand, this work found that the detection degeneracy is not present along the whole lifetime of the systems. Namely, their phase-time evolution become different from some frequency, which in the case of EMRIs is given by the GW frequency when the less massive component is tidally disrupted, and in the case of a DWD by the frequency when Roche-Lobe overflow occurs. Hence, it is possible to break the detection degeneracy.

Finally, the question of the post-merger object of BNSs is addressed by means of the laws of energy, angular momentum and baryonic mass conservation. When there is not prompt formation of a BH, it was found that if the total mass of the binary is lower than some discriminant mass, the post-merger compact star does not exhibit bound matter in the form of a disk. This post-merger object can give rise to a new kind of GRB (not yet observed): ultra-short gamma ray flash. If a joint GW and electromagnetic observation of this kind of event takes place, the approach presented here can be used to set a more stringent lower limit on the critical mass of non-rotating neutron stars.

Contents

Notation

The universal gravitation constant is G y and c is the speed of light in vacuum.

Greek indices can be any of the numbers $\{0, 1, 2, 3\}$ and latin indices any of $\{1, 2, 3\}$.

The partial derivative $\partial_\mu A^\nu$ will be denoted by $A^\nu{}_{,\mu}$ and the covariant derivative $\nabla_\mu A^\nu$ by $A^\nu{}_{;\mu}$.

The flat spacetime metric is denoted by $\eta_{\mu\nu} = \mathrm{diag}(-1, 1, 1, 1)$.

The spacetime signture of the spacetime $g_{\mu\nu}$ is $(-, +, +, +)$.

The Christoffel symbols are:

$$\Gamma^\rho_{\mu\nu} = \frac{1}{2} g^{\rho\sigma} \left[g_{\mu\sigma,\nu} + g_{\nu\sigma,\mu} - g_{\mu\nu,\sigma} \right].$$

The components of the Riemann and Ricci tensors are given by

$$\begin{aligned} R^\rho{}_{\mu\lambda\nu} &= \Gamma^\rho_{\mu\nu,\lambda} - \Gamma^\rho_{\mu\lambda,\nu} + \Gamma^\rho_{\lambda\sigma}\Gamma^\sigma_{\mu\nu} - \Gamma^\rho_{\nu\sigma}\Gamma^\sigma_{\mu\lambda}, \\ R_{\mu\nu} &= R^\rho{}_{\mu\rho\nu}. \end{aligned}$$

Chapter 1

Introduction

1.1 Historical Context of Electromagnetic and Gravitational Wave Astronomy

The field of astrophysics has a vast development thanks to radio, microwave, infrared, optical, X-ray and γ-ray astronomy. When the universe is seen in wavelengths different to visible light, new phenomena appear which are "invisible to the eye". From the birth of radio astronomy with the discovery of radio waves from the Milky way by Jansky (1933), to the discovery of pulsars by Hewish et al. (1968), new processes, confirmations and questions were brought to the field of astrophysics and gravitation. The discovery of the binary pulsar PSR 1913+16 (Hulse & Taylor, 1975) and in special its long time observation (see e.g. Weisberg & Taylor, 2005) constituted the first experimental evidence of the existence of gravitational waves (GWs). On the other hand, the discovery of cosmic microwave background radiation (Penzias & Wilson, 1965) pushed forward the development of physical cosmology. Cosmic X-ray sources (Giacconi et al., 1962; Byram et al., 1966) provided the first hints on the existence of black holes (BHs). Cygnus-X1 is widely recognized as the first discovered BH. In addition, γ-ray bursts (GRBs) introduced the question on the origin of one of the most luminous events in the sky (Klebesadel et al., 1973) (see also (Ruffini et al., 2018a) for a historical review).

Subsequent electromagnetic observations gave important information on the progenitors of GRBs. First, with the observations carried by the detector BATSE, it was introduced the classification of GRBs according to their prompt emission duration: short GRBs with $T_{90} < 2$ s and long GRBs with $T_{90} > 2$ s, where T_{90} is the time when 90% of the GRBs counts occur in the detector (Kouveliotou et al., 1993). This implies at least two different progenitors, however, further observations hinted towards the existence of more than two possible progenitors (see chapter 6). GRBs are followed by an afterglow in the X-ray, optical, microwave and radio band. When this afterglow is observed, it is possible to determine the corresponding host galaxy and its redshift, which can give crucial information on the environment where the GRB was produced. In addition, a supernova (SN) is observed, when it is instrumentally possible, temporally and spatially coincident with the long GRB[1]. Some inner engines models, are the *collapsar* model (MacFadyen & Woosley, 1999; Woosley & MacFadyen, 1999) or the *magnetar* model (Usov, 1992, 1994), in which the engine is a single object, and the induced gravitational collapse paradigm (IGC) (Rueda & Ruffini, 2012; Fryer et al., 2014; Becerra et al., 2015), in which the engine is a binary system. Regarding short GRBs, there is strong observational and theoretical evidence that are originated in NS-NS or NS-BH mergers (see e.g. Eichler et al., 1989a; Paczynski, 1991; Mészáros & Rees, 1997; Rosswog et al., 2003a; Lee et al., 2004a; Berger, 2014). A long path followed in the understanding of GRBs progenitors. For example, from the theoretical analysis of electromagnetic observations, the recent classification of GRBs into 9 subfamilies of progenitors, all of them binary systems, was presented in (Ruffini et al., 2016b). This gives only a small picture (many important observational and theoretical advances were not mentioned) of the great progress made in astrophysics. This new era of broadband electromagnetic (EM) astronomy brought a revolution in physics, possibly comparable with the birth of modern optical astronomy, when Galilei (1610) observed for the first time the three moons of Jupiter.

On the other hand, electromagnetic emission from astrophysical sources is in general incoherent and is easily absorbed and re-emitted during its path from the source to the observer. In contrast, GWs which were theoretically predicted nearly 100 years ago by Einstein (1916, 1918), provide information on the coherent motion of the source and propagate nearly unperturbed to the observer (see e.g. Maggiore, 2008). Join electromagnetic and gravitational observations could give additional information about astrophysical events. Moreover, models of electromagnetic emission can be constrained with GW data, and vice versa. Gravitational wave astronomy could bring a new astrophysical revolution. However, GWs are very dim and hard to be directly detected. These are the “two sides” of GW astronomy: it can give important information that EM astronomy can not, but it requires great technological efforts[2].

The first device to directly detect GWs was proposed by Weber (1960), which is a resonant bar with narrow sensitivity bandwidth. Weber latter claimed its experimental discovery (Weber, 1969), but was later discarded given its no reproducibility with other similar detectors (see e.g. Amaldi & Pizzella, 1979). On the other hand, theoretical consequences of Weber’s discovery showed inconsistency with known results. For example, assuming isotropic radiation, this discovery implied a very short lifetime of the universe. The search of a plausible source for this radiation (with not such a high emission) lead to the proposal in ref. (Misner, 1972) of beamed radiation coming from a BH at the center of the galaxy. Nevertheless, GWs from a star orbiting a supermassive BH do not exhibit beamed radiation (Davis et al., 1971, 1972b; Detweiler, 1978; Detweiler & Szedenits, 1979), ruling out this explanation. The search of plausible sources and theoretical consistency aided in clarifying (discarding) this claim. Despite Weber’s discovery was neither consistent with other observational data, nor with its theoretical implications, this incident motivated the astrophysical

---

[1] For example, the first coincident GRB with a SN was GRB 980425/SN 1998bw (Galama et al., 1999), see also (Woosley & Bloom, 2006; Della Valle, 2011; Cano et al., 2017) for a review on coincident observations of GRB-SN.

[2] Even the theoretical existence of GWs was not taken as certain due to the symmetry of the theory under gauge transformations (see sec. 2.1.1). The hard task to properly define the energy transported by GWs induced doubtful thoughts in the scientific community (Eddington, 1922). Feynman (see e.g. foreword of Feynman (1995)) and Bondi (1960) solved this issue with the “sticky bead” thought experiment. Doubts even raised by Einstein & Rosen (1937) were finally cleared up in ref. (Weber & Wheeler, 1957).

community to put effort in identifying plausible sources of GWs for the construction of future detectors (see e.g. Thorne, 1980a, for a review).

Fortunately, GWs were later “vindicated”, with the aid of EM data, when the binary pulsar PSR1913 + 16 was discovered in 1974 and its time evolution was observed. The emission of GWs from a binary system, such as PSR1913 + 16, will inevitably induce energy and angular momentum losses, and therefore the orbital period will change with time (Landau & Lifshitz, 1951; Peters & Mathews, 1963). This orbital decay has been observed for a long time and coincides almost perfectly with General Relativity prediction (see e.g. Taylor & Weisberg, 1982; Weisberg & Taylor, 2005). Although this provides an indirect measure of GWs, it is a *direct* consequence of the non-instantaneous propagation of the gravitational interaction (see e.g. Damour, 2015, for a discussion on this matter).

1.2 Current Gravitational Wave Astronomy

A new era came with the propose of interferometers to detect GWs (Gertsenshteĭn & Pustovoĭt, 1963; Weiss, 1972; Drever, 1977; Forward, 1978). This new class of detectors are operated by large scientific collaborations, e.g. the LIGO (Barish & Weiss, 1999) or Virgo collaborations (Accadia et al., 2012). Currently, (earth-based) interferometers are almost two-three orders of magnitude more sensitive than resonant bars, and have wider bandwidths (10 Hz– kHz). Forthcoming space-based detectors such *LISA* (Amaro-Seoane et al., 2017) or *TianQin* (Luo et al., 2016) will provide information on low-frequency sources. Despite the great sensitivity of these new detectors, the gravitational wave signal may deep inside the noise. In principle, this is not an obstacle to detect the signal. That the noise is greater than the signal is a common problem physics, like in radio-signal processing. The solution consists in filtering the data properly, which requires some knowledge of the physical signal and on the noise. In fact the optimal-filter, i.e. the one which gives the higher signal-to-noise ratio is the signal itself (Wiener, 1949) (see chapter 5). Hence, currently within the matched-filter technique[3], accurate GW templates and a complete bank are needed to claim detection.

The Einstein’s field equations are second order, non-linear partial differential equations, few exact radiative solutions are known and they do not correspond to any physically real system (see e.g. Einstein & Rosen, 1937; Bondi et al., 1959; also secs. 35.9-35.12 of Misner et al., 2017 and sec. 109 of Landau & Lifshitz, 1975). The solution of Einstein’s field equations constituted a new field called Numerical-Relativity (NR), as far as the author knows, it began with the work of Smarr (1975) and has continued its important development until now. For the sake of concreteness, one source of GWs is a binary system composed of two black holes (BBH). The evolution of the last orbits, together with the merger and ringdown of a BBH was not achieved until the work of Pretorius (2005). Currently, these simulations are computational expensive (Lehner & Pretorius, 2014; Shibata, 2016) and are not suitable for constructing complete template banks. However, they can be used to construct phenomenological templates (Ajith et al., 2007, 2011; Husa et al., 2016) and constitute the “point of reference” for approximate methods. Faster semi-analytic models

---

[3] LIGO-Virgo Collaboration also uses pipelines which do not rely on templates to claim detection (Klimenko et al., 2008).

are needed to construct a complete bank. Binary post-Newtonian waveforms (Blanchet, 2006) provide a solution to this issue, moreover they can be used to describe binaries with other components such as a binary neutron stars (BNS) or a neutron star-black hole binary (NS-BH), but are limited to the weak-field, low-velocity regime. Therefore, these templates are suitable for describing the inspiral regime of *LISA-TianQin-Taiji* binaries (large total mass, less compact binary components e.g. binary white dwarf, or very early inspiral), or of LIGO/Virgo binaries (low total mass $\sim 3\ M_{\odot}$). The effective one-body formalism (see e.g. Buonanno & Damour, 1999, 2000; Damour & Nagar, 2009) combines the Post-Newtonian approach with strong-field effects of perturbation theory, and is later calibrated with NR. In this thesis, an alternative approach for BBHs will be presented, putting special attention on the underlying physical principles (see below).

In addition, NR simulations of a BNS, NS-BH, binary white dwarf (WD) or WD-NS binary have been performed over the years (see e.g. Shibata & Taniguchi, 2011; Faber & Rasio, 2012; Lorén-Aguilar et al., 2009; Paschalidis et al., 2011), and semi-analytic approximations have been also introduced (Damour & Nagar, 2010; Bernuzzi et al., 2015b). Core collapse, another source of GWs has been simulated (see Fryer & New, 2011, for a review), but it is a challenge to current computers to include all the physical processes involved in the event (Sathyaprakash & Schutz, 2009, see also for a review on other sources of GWs). Quoting Richard P. Feynman: “But the real glory of science is that we can find a way of thinking such that the law is evident”, these semi-analytical methods might not only provide a solution to the computational costs of NR but also give physical insight on the physical processes. It is very important to focus on the physics behind approximate methods.

Recently, on September 14, 2015 a GW event consistent with the merger of a BBH was reported by the LIGO-Virgo Collaboration (Abbott et al., 2016a). Great enthusiasm was held in the scientific community for the first direct detection of GWs. This event was followed by other 10 events, 9 consistent with the merger of a BBH (Abbott et al., 2016c, 2017b,c,d, 2018b). This can open a new window to study astrophysical black holes. For example, a new family of BH masses was found and poses questions on the formation channels. More exactly, the inferred effective spin parameter of the BBH, for the majority of the events[4], is rather small and consistent with zero, whereas from binary evolution of main-sequence stars, BHs are expected to be rapidly rotating. This points to Wolf-Rayet stars as the possible progenitors of low spin BBH (Hotokezaka & Piran, 2017b), but other issues remain (see Hotokezaka & Piran, 2017a, for a detailed discussion). The other event GW170817, which is not consistent with a BBH merger, but with the merger of a BNS, was announced by the LIGO/Virgo Collaboration (Abbott et al., 2017a). An EM counterpart, the GRB 170817A (see e.g. Abbott & et al., 2017; Goldstein et al., 2017; Verrecchia et al., 2017) and the optical transient AT 2017gfo (see e.g. Abbott et al., 2017e; Arcavi et al., 2017; Haggard et al., 2017; Smartt et al., 2017; Troja et al., 2017) was associated with this GW event. It is important to mention that the first GCN reported in the timeline of events related to GRB 170817 or GW 170817, was given by the Fermi-GBM telescope, GCN524666471 (Fermi GBM, 2017). A discussion on the consistency of GRB 170817 with other known GRBs will be presented in chapter 5.

---

[4] The 90% credible interval does not include zero for only GW151226 and GW17028 (Abbott et al., 2018b).

1.3 Outline of the Thesis

Semi-analytical approaches to GW emission are more than mere academic exercises. They are important, as already stated, in view of their cheap computational costs. Besides, since they are constructed following basic principles, they can provide clear physical interpretations and consistency tests to observational results. Currently, semi-analytical methods to GW radiation (GWR) do not fully incorporate, in the opinion of the author, crucial aspects, such as frame dragging due to the orbital angular momentum of a BBH. On the other hand, analytical models of detectable but overlooked sources, have not been yet fully developed. Moreover, the aftermath of the merger of a binary neutron star is not currently known both theoretically and observationally. Therefore, it is needed to reexamine current models, and to construct new ones. This thesis was devoted to develop and study models of GWR from different astrophysical sources. Consistency of the GRB emission model of ref. (Ruffini et al., 2016b) with GWs detection is also addressed.

Chapter 2 reviews the basic principles of GWs from Einstein's theory of General Relativity. Chapter 3 introduces a physical framework, based on BH physics, for computing the GWR of a test particle inspiraling into a *Schwarzschild or a Kerr BH*. First, it reviews the general aspects of a test particle plunging into a BH and compares it with the case of circular orbits. After computing the GW fluxes to infinite, the dynamical evolution of the inspiraling test particle (GW driven) is addressed. Qualitatively speaking, the test particle evolves adiabatically in quasi-circular orbits up to zone near inner-most stable circular orbit (ISCO). This work emphasizes the nearly geodesic transition to the plunge into the BH. The form of the effective potential implies that the transition phase must be nearly conservative, i.e. appreciable GWR is not expected after the passage of the ISCO (see sec. 3.2 for more details). This fact was also stated *qualitatively* on (Ori & Thorne, 2000), and was quantitatively implemented via a Taylor expansion around the ISCO. However, it was extrapolated beyond its region of validity. An alternative implementation of the nearly geodesic hypothesis is performed here via the Hamiltonian formalism of a test particle on the *Kerr spacetime*, without any series expansion (Rodríguez et al., 2018; Rodriguez et al., 2018). The plunge of different theoretical treatments, (Ori & Thorne, 2000) or NR (SXS Catalog, 2018), is compared with the approach presented here. The amount of radiated energy in the transition to the plunge was computed and was found to be less than the one given by the other approaches. This higher amount of radiated energy is not physically justified from the point of view taken here. More exactly, it was found that this discrepancy in the GWR induces different estimations of the final mass of the BH.

In chapter 4 is presented an extrapolation of the previous work to the case of BBH with comparable-mass components. As a working hypothesis, the mass of the test particle is replaced by the reduced mass of the BBH, and the mass of the BH by the total mass, i.e. the Newtonian center-of-mass point of view. The dynamics up to the ISCO, and its corresponding waveform were computed on a Kerr "background" augmented with the latter assumption. In order to compare and contrast the waveforms in a gauge-invariant manner, the intrinsic time-domain phase evolution, Q_ω, was calculated for both waveforms. The fitting-factor was also computed (Apostolatos, 1995). BBH simulations from SXS Catalog (2018) with equal masses and equal aligned spins, and with different mass ratios, $q = m_1/m_2 \neq 1$, but spinless, were compared and contrasted with "test-particle waveforms". It was found a remarkable, and at first unexpected agreement between the current approach and NR simulations, up to the ISCO frequency. It is more important perhaps that the Schwarzschild background augmented with Newtonian center-of-mass hypothesis does not "reproduce" the NR waveform. In contrast, it was found that each of the studied NR waveforms, can be reproduced by computing the augmented[5] "test particle" waveform on a Kerr background with the proper spin parameter, called the "effective" spin parameter $a_{\rm eff}$. It was found that $a_{\rm eff} \neq 0$, even in the case of spinless merging components. This clearly shows the contribution of the orbital angular momentum to the BBH dynamics. This effect was not previously taken into account by other semi-analytical models (Rodríguez et al., 2018).

Chapter 5 first reviews some general aspects of the matched-filter technique used in GW data analysis. Afterwards, it makes a phenomenological test-particle analysis of GW150914 that provides physical insight of the merger. The BBH derived parameters (Rodriguez et al., 2016), are in agreement with the values given by LIGO/Virgo Collaboration. As stated before, GW170817 provides an excellent scenario to test consistency of EM emission models and GWs. First, and independent calculation of the position from GW data is presented here. The position was found to be consistent with the one given by the EM counterpart (Haggard et al., 2017, e.g). However, GRB 170817A is not consistent with previously known GRBs. More exactly, its light curve is not consistent when it is compared with the prototype of known GRBs (Rueda et al., 2018b). This issue was also mentioned on (Abbott & et al., 2017) and some possible scenarios were proposed to explain it. An alternative scenario proposed by Rueda et al. (2018b), namely a WD-WD merger, will be presented in this chapter. This kind of merger produces a kilonova emission, like the one in a BNS merger but its GW signal is not detectable by current earth-based detectors.

Chapter 6 presents the inferred GW detection rates according to the GRB classification introduced in (Ruffini et al., 2016b). The latter classification states that *all* GRB subfamilies have a binary progenitor, composed by different combinations of carbon-oxygen cores ($\rm CO_{core}$), NSs, BHs and WDs. The traditional model of long bursts assumes a single BH and consequently it is not expected to emit GWs (as a binary system). In contrast, here long bursts are assumed to be originated in binary systems and have been sub-classified as X-ray flashes (XRFs), binary-driven hypernovae (BdHNe), and BH-supernovae (BH-SNe). Short bursts, are assumed to be originated in NS-NS mergers, and are sub-classified as short gamma-ray flashes (S-GRFs) and short GRBs (S-GRBs), the latter when a BH is formed. Two additional families are also present: ultra-short GRBs (U-GRBs) and gamma-ray flashes (GRFs), originated in NS-BH and NS-WD mergers, respectively. The estimated occurrence GRB rate from observations and their corresponding GW emission is presented here in order to assess their detectability by Advanced LIGO, Advanced Virgo, eLISA, and resonant bars (Ruffini et al., 2018b). The derived detection rate of BNS, for design sensitivity (2022+) is $\sim 0.1 - 0.2$ yr^{-1}, consistent with lower limits of rates found in the literature.

Chapter 7 studies a semi-analytical model of GWR from deformed stars whose matter is described by a polytropic EOS, namely compressible Riemann S-type ellipsoids Lai et al. (1993). Here, it was found that the star has an early chirping-like behaviour, hereafter this object will be called a chirping ellipsoid (CEL). The potential detection of these type of

---

[5] In the sense of the Newtonian center-of-mass.

sources by future space-based GW observatories such as *LISA*, *TianQin, Taiji*, can reveal previously undetected astrophysical processes in system of compact objects (eg. white dwarf binary mergers). This work found that CELs are quasi-monochromatic sources and can be detected during one year of observation. Moreover, it was found that the GW phase and amplitude evolution of CELs (mass $\sim$ 1 $\mathrm{M}_{\odot}$, radius $\sim$ 10^3 km, polytropic equation of state with index $n \approx 3$) is almost indistinguishable from some binary systems: extreme mass-ratio inspirals (EMRIs) composed of an intermediate-mass (e.g. 10^3 $M_{\odot}$) black hole and a planet-like (e.g. 10^{-4} $M_{\odot}$) companion, and double-detached white dwarfs Rodriguez et al. (2018). The kind of EMRIs studied here can not be individually resolved during one year of observation, breaking the degeneracy between CELs and EMRIs. From reasonable astrophysical assumptions, the rate in the local Universe of CELs, EMRIs in the mass range considered here, and DWDs are very similar. Therefore, i) EMRIs are plausible stochastic GW sources, ii) it is expected significant source confusion between CEL-DWD. However, the chirp epoch of each of the aforementioned systems, ends at a different frequency, and in general it is satisfied that $f_{\rm EMRI}^{\rm end} < f_{\rm DWD}^{\rm end} < f_{\rm CEL}^{\rm end}$, in other words, for $f > f_{\rm DWD}^{\rm end}$ the only possible source of these kind of quasi-monochromatic GWs is a CEL. Hence, a partial solution to the degeneracy CEL-DWD was found here. The frequency at the end of the chirp is given by the value when the less-massive component is tidally disrupted, for the case of an EMRI, and by the frequency at the onset of Roche-lobe overflow, for the case of a DWD. It is one of the aims of this work to call attention on these type of sources in order to break completely the detection degeneracy.

Finally, chapter 8 introduces a scheme to assess some properties of the remnant of BNS mergers. This work is focused on BNS mergers whose remnant is a stable supramassive NS supported by uniform rotation. The (quasi) universal relations of baryonic and gravitational mass for rotating NSs, derived on (Cipolletta et al., 2015), together with the conservation of baryonic mass and specific angular momentum were used to assess the mass of the remnant NS, assumed to be in the mass-shedding sequence. In order to form a disk is necessary that the maximum specific angular momentum at the moment of the merger, $l_{\rm mrg}^{\rm max}$, be larger than the one of the ISCO around the newly born NS, $l_{c,\rm ISCO}$. This latter was obtained from EOS-independent formula for the angular momentum of a test particle at the ISCO of a uniformly rotating NS (Cipolletta et al., 2017). When the ISCO is "outside" the star, it is possible to form a *detached* disk. In the opposite case, there can be stable orbits up to surface of the star, thus the remnant configuration will be unstable and more similar to a hypermassive NS (differentially rotating supported NS), which is outside the scope of this work. The equations obtained by applying the above conservation laws to the BNS merger, were solved here and it was found that the necessary condition for the formation of a *detached* disk implies a *discriminant* total mass for the BNS, above which it is not possible to form a disk. BNS mergers above this latter mass would lead to a new class of S-GRF, an ultrashort GRF (U-GRF). In addition to the gamma-ray prompt emission, U-GRFs should have an associated kilonova with only dynamical component from matter expelled by tides, but not with disk-wind component from post-merger accretion outflows. The discriminant BNS mass for selected EOS will be presented in this chapter, and supposing the (future) observation of an U-SGF, a new method for constraining the NS EOS will be also presented. The GW emission of this remnant will be estimated with the semi-analytical method of chapter 7, together with its detectability by current GW interferometers.

1.4 List of Publications

Articles published

- R. Ruffini, **J. Rodriguez**, M. Muccino, J. A. Rueda, Y. Aimuratov, U. Barres de Almeida, L. Becerra, C. L. Bianco, C, Cherunini, S. Filippi, D. Gizzi, M. Kovacevic, R. Moradi, F. G. Oliveira, B. Pisani, Y. Wang. On the rate and on the gravitational wave emission of short and long GRBs. ApJ, 859, 30 (2018). Chapter 6.
- **J. F. Rodriguez**, J. A. Rueda & R. Ruffini, Comparison and contrast of test-particle and numerical-relativity waveform templates. Journal of Cosmology and Astro-Particle Physics, 2018, 030. Chapter 4
- **J. F. Rodriguez**, J. A. Rueda & R. Ruffini, On the Final Gravitational Wave Burst from Binary Black Holes Mergers. ARep, 62, 940 (2018). Chapter 3
- J. A. Rueda, R. Ruffini, Y. Wang, , U. Barres de Almeida C. L. Bianco, Y. Chen, R. V. Lobato, C. Maia, D. Primorac, R. Moradi, **J. F. Rodriguez**. GRB 170817A-GW170817-AT 2017gfo and the observations of NS-NS, NS-WD and WD-WD mergers. Journal of Cosmology and Astro-Particle Physics, 2018, 006. Chapter 5

Articles submitted or in preparation

- **J. F. Rodriguez**, J. A. Rueda, R. Ruffini, J. I. Zuluaga, J. M. Blanco-Iglesias, P. Loren-Aguilar. Gravitational radiation and detection degeneracy with binary systems: A conceptual pathfinder for space-based gravitational-wave observatories. Submitted to Phys. Rev. D (2019). Chapter 7
- **J. F. Rodriguez**, J. A. Rueda, R. Ruffini. On disk formation around the central remnant neutron star produced in a neutron star binary merger. In preparation. Chapter 8

Proceedings

- **J. F. Rodriguez**, J. A. Rueda, R. Ruffini. Strong-field gravitational-wave emission in Schwarzschild and Kerr geometries: some general considerations. EPJWC, 02006, EPJWC.168 (2018). Chapter 3.
- J. A. Rueda, R. Ruffini, ; **J. F. Rodriguez**, M. Muccino, Y. Aimuratov, U. Barres de Almeida, L. Becerra, C. L Bianco, C. Cherubini, S. Filippi, M. Kovacevic, R. Moradi, G. B.; Pisani, Y. Wang, The binary progenitors of short and long GRBs and their gravitational-wave emission. EPJWC, 01006, EPJWC.168 (2018). Chapter 6.
- J. A. Rueda, R. Ruffini, Y. Wang, , U. Barres de Almeida C. L. Bianco, Y. Chen, R. V. Lobato, C. Maia, D. Primorac, R. Moradi, **J. F. Rodriguez**. GRB 170817A-GW170817-AT 2017gfo and the observations of NS-NS, NS-WD and WD-WD mergers. The Fifteenth Marcel Grossmann Meeting - MG15, E15, (2018). Chapter 5.

Chapter 2

Fundamentals of Gravitational Waves

This chapter shows the classical results and discusses the basic ideas of the propagation and generation of GWs. The physical consequences of the passing of GWs will be reviewed. The quadrupole formula for binary systems and rotating stars will be presented.

2.1 General Relativity and Gravitational Waves

The theory of General Relativity (Einstein, 1915) constitutes one of the most elegant theories in physics. It is the standard theory describing the gravitational interaction. This theory reconciles the idea of non-instantaneous interaction with the gravitational force. Therefore, it is not surprising (but not trivial), that "waves of gravity" propagating with finite speed appear within this theory. Nevertheless, due to the non-linear nature of the Einstein field equations (EFE), the generation of gravitational waves is rather complicated. In the weak-field limit, the EFE are linear and it turns out that in a special gauge, they correspond to a wave equation. The existence of GWs can be also be elucidated in the asymptotic behaviour at null infinity. The pioneer work of Bondi et al. (1962, sec. 2) states that hyperbolic equations, such EFE, allow solutions that suddenly change ("time bomb") and these solutions are propagated along null-congruences. The EFE are given by

$$R_{\mu\nu} - \frac{1}{2} g_{\mu\nu} R = \frac{8\pi G}{c^4} T_{\mu\nu}. \tag{2.1}$$

In the weak-field limit the spacetime metric $g_{\mu\nu}$ is nearly flat, more exactly, it is supposed that there exist a coordinate system where the metric has the simple form:

$$g_{\mu\nu} = \eta_{\mu\nu} + h_{\mu\nu}, \tag{2.2}$$

where $|h_{\mu\nu}| \ll 1$. This kind of coordinate system or reference frame is called *nearly Lorentz reference frame* (NLF) (Thorne, 1989). It is physically possible to construct such a reference frame provided that gravitational fields are weak in the universe, except in the vicinity of black holes and neutron stars, or at the beginning of the universe. When this last expression is substituted in the EFE, and expanded to linear order in $h_{\mu\nu}$, the following equation is obtained (see appendix A for details[1]):

$$\bar{h}_{\mu\nu,\lambda}{}^{,\lambda} + \eta_{\mu\nu}\bar{h}_{\alpha\beta}{}^{,\alpha\beta} - 2\bar{h}_{\lambda(\mu,\nu)}{}^{,\lambda} = -\frac{16\pi G}{c^4}T_{\mu\nu}\,, \tag{2.3}$$

where $\bar{h}_{\mu\nu} = h_{\mu\nu} - \eta_{\mu\nu}h/2$ and $h \equiv h_{\mu}{}^{\mu}$. The weak-field approximation can be regarded as a classical field theory of $h_{\mu\nu}$ on a flat background. To linear order in $h_{\mu\nu}$, the indices are raised and lowered with the flat metric $\eta_{\mu\nu}$. The source can be self-gravitating but the gravitational field inside must be weak (see e.g. (Landau & Lifshitz, 1951) or the appendix C for details).

2.1.1 Gauge Transformations

The form of the metric (2.2) is invariant, i.e. $g_{\mu\nu} \mapsto \eta_{\mu\nu} + h'_{\mu\nu}$ with $|h'_{\mu\nu}| \ll 1$, under the coordinate transformation,

$$x'^{\mu} = x^{\mu} + \xi^{\mu}(x), \tag{2.4}$$

where ξ^{μ} are functions of the original coordinates that satisfy $\xi^{\mu}{}_{,\nu} \ll 1$. These coordinate transformations are called, *gauge transformations*. The metric perturbation $\bar{h}_{\mu\nu}$ is transformed as follows:

$$\bar{h}_{\mu\nu} \mapsto \bar{h}'_{\mu\nu} = \bar{h}_{\mu\nu} - 2\xi_{(\mu,\nu)} + \eta_{\mu\nu}\xi^{\alpha}{}_{,\alpha}\,. \tag{2.5}$$

The existence of these transformations can lead to the claim that GWs are entirely coordinate generated. Nevertheless, this assumption is not correct and as it will be shown, there are two degrees of freedom that cannot be “gauged away”. The situation is similar to the case of electromagnetic waves, where there are transformations of the four-potential that leave the electric and magnetic fields invariant. The electric and magnetic field analog in gravitation is given by the Riemann tensor, which is invariant under (2.4). The ξ^{μ} functions can be chosen to satisfy,

$$\bar{h}_{\mu\nu}{}^{,\nu} = 0. \tag{2.6}$$

This gauge, called the Lorentz gauge, imposes 4 constrains on the components of the symmetric tensor $\bar{h}_{\mu\nu}$, leaving 6 independent ones. The EFE in this gauge are given by,

$$\Box\bar{h}_{\mu\nu} \equiv \bar{h}_{\mu\nu,\alpha}{}^{\alpha} = -\frac{16G\pi}{c^4}T_{\mu\nu}\,. \tag{2.7}$$

Moreover, the condition (2.6) implies $T^{\mu\nu}{}_{,\nu} = 0$, meaning that the energy and momentum of the source must follow the conservation laws of flat spacetime. Therefore, the system must be closed and the back-reaction of $h_{\mu\nu}$ on the motion of the source is neglected. In vacuum, eq. (2.7) is a *wave propagation* equation and has harmonic plane wave solutions,

$$\bar{h}_{\mu\nu} = \Re[A_{\mu\nu}\exp(ik_{\mu}x^{\mu})],$$

where k^{μ} is a constant null four-vector, $k_{\mu}k^{\mu} = 0$ and the polarization tensor satisfy $A_{\mu\nu}k^{\nu} = 0$. The perturbation field can now be regarded as a wave propagating at the speed of light.

---

[1] Some of the appendices in this book contain simple calculations or a long expressions necessary to arrive at the results presented. Although they are not necessary to understand the underlying physics, the author believes that they are important if any reader wants to reproduce the results. Some appendices only constitute a reference for the author.

Traceless-Transverse Gauge or Frame

A new gauge transformation can be done to reduce the degrees of freedom without compromising the Lorentz gauge condition. It can be seen from the eq. (2.5) that if the functions associated with the new gauge satisfy $\Box\xi_\mu = 0$, the transformed field is still in the Lorentz gauge. Therefore, some components of $\bar{h}_{\mu\nu}$ can be set to *zero* provided that ξ_μ satisfies the same equation. Note that this cannot be done inside the source where $T_{\mu\nu} \neq 0$. A (global) four-velocity u^α is chosen and as coordinate condition, $\bar{h}_{\mu\nu}u^\nu = 0$ is imposed, i.e. the perturbation field is *transverse* in the new coordinates. In a Lorentz frame where $u^\alpha = \delta^\alpha_0$, the perturbation is purely spatial. These conditions constitute only 3 constraints, as a consequence of the Lorentz gauge, thus in addition $\bar{h}_\mu{}^\mu = 0$ is required. In this gauge, which is called *traceless-transverse* (TT), $\bar{h}_{\mu\nu} = h_{\mu\nu}$. The TT gauge conditions can be summarized as,

$$h_{0\mu} = 0, \quad h_\mu{}^\mu = 0, \quad h_{ij}{}^{,j} = 0, \tag{2.8}$$

where the last equality is a consequence of the Lorentz gauge. There are 8 conditions on the components of $h_{\mu\nu}$, thus there are only 2 degrees of freedom. The components of the perturbation field in this particular gauge are denoted by $h^{\mathrm{TT}}_{\mu\nu}$.

For a plane wave solution the TT conditions read $A_{0\mu} = 0$, $A_\mu{}^\mu = 0$, $A_{\mu\nu}k^\nu = 0$, and if the wave is propagating along the z axis, its components are given by,

$$h^{\mathrm{TT}}_{ij} = \begin{pmatrix} A_+ & A_\times & 0 \\ A_\times & -A_+ & 0 \\ 0 & 0 & 0 \end{pmatrix} \cos[\omega(t - z/c)]. \tag{2.9}$$

Since the GW in the TT gauge is two dimensional, it can be expressed in terms of 2 basis tensors,

$$\mathbf{h} = h_+\mathbf{e}_+ h_\times \mathbf{e}_\times, \tag{2.10}$$

where $\mathbf{e}_+, \mathbf{e}_\times$ are called the “unit” linear polarizations tensors and are given by,

$$\mathbf{e}_+ \equiv \mathbf{e}_x \otimes \mathbf{e}_x - \mathbf{e}_y \otimes \mathbf{e}_y, \tag{2.11}$$

$$\mathbf{e}_\times \equiv \mathbf{e}_x \otimes \mathbf{e}_y + \mathbf{e}_y \otimes \mathbf{e}_x. \tag{2.12}$$

Once in the Lorentz gauge, the TT components of a plane wave solution, propagating in the $\hat{\mathbf{n}} = \mathbf{k}/|\mathbf{k}|$ direction, can be obtained by using the projection operator P_{ij},

$$\begin{aligned} P_{ij} &= \delta_{ij} - n_i n_j, \\ h^{\mathrm{TT}}_{ij} &= P_{il}P_{jm}h_{lm} - \frac{1}{2}P_{ij}P_{lm}h_{lm} = \Lambda_{ij,lm}\bar{h}_{lm}. \end{aligned} \tag{2.13}$$

The fact that these are the true degrees of freedom of the GWs can be understood by splitting $\bar{h}_{\mu\nu}$ in gauge-invariant parts. The gauge transformations introduced some ambiguity in the physical reality of the perturbation $\bar{h}_{\mu\nu}$. In order to eliminated this ambiguity the theory must involve only gauge-invariant quantities. The transverse part $P_{il}P_{jm}h_{lm}$ is invariant under (2.4), consequently h^{TT}_{ij} and $h^{\mathrm{T}}_{ij} = (1/2)(P_{lm}h_{lm})P_{ij}$ are invariant. There is another gauge invariant quantity (Misner et al., 2017),

$$\tilde{h}_{0k} = \bar{h}_{0k} - \nabla^{-2}\big(\bar{h}_0{}^\mu{}_{,\mu k} + \bar{h}_{kl,l0}\big). \tag{2.14}$$

However, it turns out that the linearized EFE imply that both $\widetilde{h}_{0k}$ and h^{T}_{ij} vanish in empty space. The Lorentz gauge condition, implies $\bar{h}_{0k} = 0$ due to the previous result and, $\bar{h}_{00} = 0$ given that the field is dynamical. In conclusion, h^{TT}_{ij} is the only the gauge invariant part and contains the true degrees of freedom of GWs.

The physical meaning of TT gauge can be understood by studying the geodesic equation. If a set of test masses is at rest before the arriving of a GW, $dx^i/d\tau = 0$, the law of motion is given by,

$$\frac{d^2x^i}{d\tau^2} = -\Gamma^i_{00}\left(\frac{dx^0}{d\tau}\right)^2. \tag{2.15}$$

In this frame $h_{0\mu} = 0$, which implies that $\Gamma^i_{00} = 0$. Therefore, the test masses will remain at rest even though the GW is passing, i.e. the *spatial coordinates are co-moving.* However, this does not mean that the GW do not affect the test particles. Indeed, the proper distance between the test particles do change by the passing of the GW. If two test masses are on a plane perpendicular to the propagation direction, the distance to linear order in the GW amplitude is,

$$L' = \int \sqrt{1 + h^{\mathrm{TT}}_{ij} n^i n^j}\, d\lambda \approx L\left(1 + \frac{1}{2} h^{\mathrm{TT}}_{ij} n^i n^j\right), \tag{2.16}$$

where L is the (initial) distance in flat spacetime, and n^i is the unit vector between the two masses, $n_i k^i = 0$. The fractional strain $(L' - L)/L = \delta L/L$ is proportional to the amplitude. If the masses are on a plane parallel to the propagation, $h^{\mathrm{TT}}_{ij} n^i n^j = 0$ and there will be no displacement. A simple example is the action of a linearly polarized ($A_\times = 0$) plane wave propagating in the z direction, on a set of test masses on the xy plane. To linear order in the amplitude, the spatial metric can be transformed to the "cartesian" form $ds^2 = dX^2 + dY^2$, with the change of coordinates (Hartle, 2003),

$$X = \left(1 + \frac{a}{2}\sin\omega t\right)x, \quad Y = \left(1 - \frac{a}{2}\sin\omega t\right)y.$$

The distance from the origin to the test masses is given by the usual expression in cartesian coordinates, i.e. X and Y are physical distances. Therefore, for a circle of test masses, $x^2 + y^2 = 1$, the GW deforms the pattern into an ellipse,

$$\frac{X^2}{A^2} + \frac{Y^2}{B^2} = 1$$

where $A = 1 + (a/2)\sin\omega t$ and $B = 1 - (a/2)\sin\omega t$ are the semi axes. The pattern changes periodically with the GW. If the GW is polarized in the other direction, $A_+ = 0$, the ellipse is rotated $\pi/4$.

It is very important to study the behaviour of the GW polarizations under rotations around the propagation direction, and under Lorentz boosts. After rotating the matrix (2.9) an angle ψ around the z axis, the new polarizations are,

$$h'_+ = h_+\cos 2\psi - h_\times \sin 2\psi, \tag{2.17}$$

$$h'_\times = h_+\sin 2\psi + h_\times \cos 2\psi, \tag{2.18}$$

This result can be written more compactly as $n = h_+ \mp i h_\times \mapsto n' = (h_+ \mp i h_\times)e^{\mp i 2\psi}$. In other words, the quantity $h_+ \mp i h_\times$ has a spin-weight of ∓ 2 under rotations around the propagation direction (see appendix B). On the other hand, the GW polarizations are *invariant* under Lorentz boosts, i.e. the degrees of freedom of GW are the same in any nearly Lorentz frame (Thorne, 1989).

Proper Reference Frame

In the TT frame the gravitational field has the simple form already presented, but this frame is not the usually used by the experimentalist in the laboratory. The usual frame used is called the proper reference frame (PRF). In this frame all the laboratory apparatus is at rest, and the spatial coordinate grid is not marked by free test masses, as in TT frame. At the origin of the frame there is a set of cartesian axes and an ideal clock. As far as the spacetime curvature allows, a cartesian grid is constructed to give the spatial coordinates $x^{\hat{i}}$, and synchronized clocks are placed within this grid to mark the time coordinate $x^{\hat{0}}$. The spacetime line element is given by,

$$ds^2 = -(1 + 2a_{\hat{i}}x^{\hat{i}} + R_{\hat{i}\hat{0}\hat{j}\hat{0}}x^{i}x^{j})(dx^{\hat{0}})^2 - 2(\varepsilon_{\hat{i}\hat{j}\hat{k}}x^{\hat{j}}\Omega^{\hat{k}} + 2R_{0\hat{i}\hat{j}k}x^{\hat{j}}x^{\hat{k}}/3)dx^{\hat{0}}dx^{\hat{i}} \\ + (\delta_{\hat{i}\hat{j}} + R_{\hat{l}\hat{k}\hat{i}\hat{j}}x^{\hat{l}}x^{\hat{k}})dx^{\hat{i}}dx^{\hat{j}}. \tag{2.19}$$

If the laboratory is free-falling and not rotating, $a^{\hat{i}} = 0$ and $\Omega^{\hat{i}} = 0$, the frame is a local inertial reference frame (LIF). For simplicity, the subsequent analysis will suppose that the laboratory is a LIF whose origin is at a test mass A. The behaviour of another test mass B, as seen from the test mass A, is governed by the geodesic deviation equation,

$$\frac{D^2 x_B^{\hat{i}}}{d\tau^2} = -R_{\hat{i}\hat{0}\hat{j}\hat{0}}x_B^{\hat{j}}, \tag{2.20}$$

where $x_B^{\hat{i}}$ are the spatial coordinates of B, which on the LIF correspond to the components of the separation vector between the two geodesics. Because the analysis is done in a LIF, $D/d\tau$ can be replaced by $d/d\tau$. It was shown previously that the spatial coordinates of the TT frame follows the motion of free test masses, therefore there is a TT frame that moves with the particle A. Provided that the Riemann tensor is gauge-invariant, its expression in the proper frame, evaluated at the origin is the same as in TT frame that moves with the particle A. Hence, the equation of motion for the test mass B is,

$$\frac{d^2 x_B^{\hat{i}}}{dt^2} = \frac{1}{2}\frac{\partial^2 h_{ij}^{\mathrm{TT}}}{\partial t^2}x_B^{\hat{j}}, \tag{2.21}$$

where t is the time coordinate of the TT frame[2]. The right hand side of this last equation can be interpreted as a force acting on the test mass B due to the GW. When the reference frame is not free-falling and is rotating, eq. (2.21) is modified by adding the terms $-a^{\hat{i}}$ (minus the local acceleration of gravity), $-2\varepsilon_{\hat{i}\hat{j}\hat{k}}\Omega_{\hat{j}}dx^{\hat{k}}/dt$ (coriolis acceleration). On the other hand, in eq. (2.20) the Riemann tensor can have the contributions from inhomogeneities in the gravitational field other than from GWs, e.g. Newtonian noises. Finally, it can be seen that the PRF metric is an expansion in powers of $x^{\hat{i}}$ around flat spacetime, and in order to this expansion be valid the condition $|x^{\hat{i}}|/\lambda\!\!\!^{-} \ll 1$ must be satisfied.

---

[2] In the TT frame, $d\tau = dt[1 - (\delta_{ij} + h_{ij}^{\mathrm{TT}})(dx^i/dt)(dx^j/dt)]^{1/2}$. For the test mass A, $dx^i/dt = 0$, therefore $d\tau = dt$.

2.2 Gravitational Waves on Curved Spacetime

After the discussion of linear perturbations, it arises the question of whether this procedure can be extended to higher orders. In order to answer this question, this section will review the short-wave approximation (see e.g. Brill & Hartle, 1964; Maggiore, 2008; Misner et al., 2017). The notion of GWs was clear in the previous section provided that the background was flat and there was a distinction between background and perturbation. It was showed that the EFE imply that the perturbation field in the Lorentz gauge satisfies a wave equation. When the background is curved the notion of a perturbation becomes ambiguous.

The generation and propagation of GWs in the general case (curved background and higher orders in $h_{\mu\nu}$) can be understood more easily when the space is divided into regions determined by the reduced wavelength $\lambdabar \equiv \lambda/2\pi$, the background length scale $\mathscr{R}$ and the distance to the source r (Thorne, 1980b), as shown in fig. 2.1. This procedure is similar to the case of electromagnetic radiation (see e.g. Jackson, 1998). As usual, the near-zone, $\lambdabar > r$, is the region where the retardation effects are negligible and the field can be assumed as instantaneous. The GW *generation zone* comprises the inner zone of the sphere of radius r_i, whose value will be determined later. The wave-zone (radiation-zone) is characterized by $\lambdabar \ll r$. This latter is divided in two zones, the first one is between the radius r_i and radius r_o, called the *local wave zone*. In this zone the background (due to the source or due to other masses) does not affect propagation of the GWs. Therefore, within this zone there is not red shift, nor backscatter produced by the source, and the curvature due to nearby masses is negligible $r \ll \mathscr{R}$. This is equivalent to a GW propagating in a flat background and the formalism of the previous section can be applied. Therefore, r_i is given by the greatest value of r for which one of the following phenomena occurs: (a) the field becomes near-zone field, (b) there is redshift or (c) backscatter by the curvature of the source, (d) the outer limit of the source is reached. The outer radius $r > r_o$ is determined by the point where any of the following occurs: there is redshift and/or refraction produced by the background (not due to the source) $r \gg \mathscr{R}$, or the phase shift $(GM/\pi c^2)\ln(r/r_i)$ is of the order of $\lambdabar$[3]. This split of the space allows to separate the generation and propagation of GWs.

The formalism to split the spacetime into background and perturbations was originally introduced by Wheeler (1955). A priori, there is no standard criteria to separate the background and the perturbation. The short-wave formalism proposes to separate the spacetime metric according to the frequency (or wavelength). The short-wavelength (high frequency) component is considered to be the perturbation, whereas the background is considered to posses a large scale length denoted by $\mathscr{R}$, or a low frequency, $f^{(\mathrm{B})}$. The order of magnitude of the perturbation (amplitude) is denoted by $\mathscr{A}$, and by *ansatz* is small. In other words, $h_{\mu\nu}$ is a small ripple propagating in a large scale background $g^{(\mathrm{B})}_{\mu\nu}$,

$$g_{\mu\nu} = g^{(\mathrm{B})}_{\mu\nu} + h_{\mu\nu}. \tag{2.22}$$

First, the EFE are rewritten in the form,

$$R_{\mu\nu} = \frac{8\pi G}{c^4}\left(T_{\mu\nu} - \frac{1}{2}g_{\mu\nu}T\right), \tag{2.23}$$

---

[3] This phase shift turns out to be a coordinate effect of the harmonic coordinates (Blanchet, 2006).

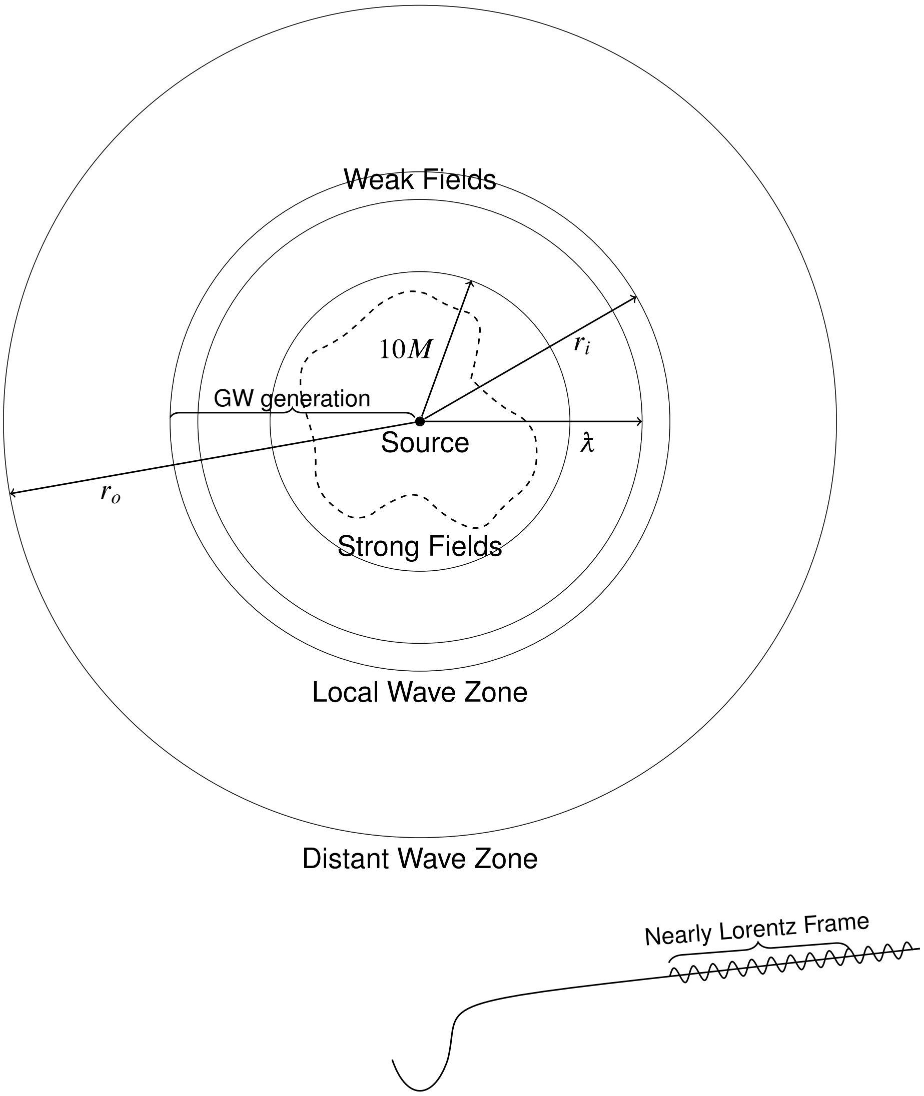

Figure 2.1 Scheme (not to scale) of the important zones in the gravitational wave generation and propagation. The figure is based on the fig. 1 presented on (Thorne, 1977).

and expanded to second order in $h_{\mu\nu}$ (see appendix A for the corresponding expressions):

$$R^{(\mathrm{B})}_{\mu\nu} + R^{(1)}_{\mu\nu}(h) + R^{(2)}_{\mu\nu}(h) = \frac{8\pi G}{c^4}\left(T_{\mu\nu} - \frac{1}{2}g_{\mu\nu}T\right) + \mathcal{O}(h^3). \tag{2.24}$$

Now, this last equation is split according to the two length (time) scales $\lambdabar$ and $\mathcal{R}$. In order to achieve this task, the auxiliary length scale $\bar{l}$, which satisfies $\lambdabar < \bar{l} < \mathcal{R}$, is introduced. None of the physical quantities varies with $\bar{l}$. The operation $\langle F\rangle$ indicates the average of F over a volume $\bar{l}^3$ and it is used to "smooth" quantities. The rapidly varying $h_{\mu\nu}$ is canceled out by this average, $\langle g_{\mu\nu}\rangle = g^{(\mathrm{B})}_{\mu\nu}$. The part $R^{(1)}_{\mu\nu}$ is linear in $h_{\mu\nu}$ so it varies with the scale $\lambdabar$, and its average is zero. On the other hand, since $R^{(2)}_{\mu\nu}$ is quadratic, $h_{\mu\nu}$ can be combined to give a large-scale quantity (Maggiore, 2008). The slowly varying part (length scale $\mathcal{R}$)

of eq. (2.24) is given by

$$R^{(B)}_{\mu\nu} + \langle R^{(2)}_{\mu\nu}(h)\rangle = \frac{8\pi G}{c^4}\left\langle T_{\mu\nu} - \frac{1}{2}g_{\mu\nu}T\right\rangle. \tag{2.25}$$

This last expression shows that the background curvature is due to the non-linear effect of the perturbation and to the energy-momentum content of matter or other type of fields. When these last are negligible, the curvature is due only to the perturbation and the scales must satisfy $\lambda\!\!\bar{}\,/\mathcal{R} \sim \mathcal{A}$. When the curvature is produced by matter or other fields, $\lambda\!\!\bar{}\,/\mathcal{R} \gg \mathcal{A}$ must be satisfied. It is very important to note that once the analysis is promoted to second order, it is inevitable that the background is curved. The linear approximation neither exhibit self-interaction nor generation of background curvature. When the analysis on a flat background is extended to second order, the EFE imply that $\mathcal{A} = 0$. Therefore, second order perturbation theory on a flat background has no physical sense. The long-scale equation can be used to define the "energy-momentum" tensor of GWs.

$$T^{(\mathrm{GW})}_{\mu\nu} = -\frac{c^4}{8\pi G}\left\langle R^{(2)}_{\mu\nu}(h) - \frac{1}{2}g^{(B)}_{\mu\nu}R^{(2)}(h)\right\rangle. \tag{2.26}$$

The energy-momentum tensor of GWs can also be obtained from the Landau-Lifshitz pseudotensor (Landau & Lifshitz, 1951) (see appendix C). Far away from the source, the background spacetime is expected to be nearly flat, i.e. there exist a NLF which covers this far region. In the Lorentz gauge the energy-momentum tensor is reduced to,

$$T^{(\mathrm{GW})}_{\mu\nu} = \frac{c^4}{32\pi G}\langle \partial_\mu h_{\alpha\beta}\partial_\nu h^{\alpha\beta}\rangle, \tag{2.27}$$

and it turns out to be gauge invariant, therefore it is convenient to use the most simple frame, namely the TT. Hence the energy density of the GWs is given by,

$$\rho^{\mathrm{GW}} = T^{(\mathrm{GW})00} = \frac{c^2}{32\pi G}\langle \dot{h}^{\mathrm{TT}}_{ij}\dot{h}^{\mathrm{TT}}_{ij}\rangle = \frac{c^2}{16\pi G}\langle \dot{h}^2_+ + \dot{h}^2_\times\rangle, \tag{2.28}$$

where the over dot indicates time differentiation ∂_t (not $\partial_0 = c^{-1}\partial_t$), and the energy flux S^i is,

$$S^i = T^{(\mathrm{GW})0i} = \frac{c^4}{32\pi G}\langle \partial^0 h^{\mathrm{TT}}_{mn}\partial^i h^{\mathrm{TT}}_{mn}\rangle. \tag{2.29}$$

For a GW propagating in the $n^i = x^i/r$ direction[4], the radial energy flux is $S^r = n_i S^i = cT^{(\mathrm{GW})00}$. Thus, the GW luminosity, i.e. the total energy per unit time crossing the surface of a sphere of radius r, is obtained by integrating (2.29).

$$L_{\mathrm{GW}} = \int dA\, n_i T^{(\mathrm{GW})0i} = \frac{c^3 r^2}{16\pi G}\int d\Omega\langle \dot{h}^2_+ + \dot{h}^2_\times\rangle, \tag{2.30}$$

where $d\Omega$ is the solid angle differential element. The spectrum of the GWs can be found by applying Parseval's theorem to the last expression,

$$\frac{dE}{df d\Omega} = \frac{\pi c^3}{2G}f^2 r^2\left(|\tilde{h}_+(f)|^2 + |\tilde{h}_\times(f)|^2\right). \tag{2.31}$$

---

[4] $\partial_0 h^{\mathrm{TT}}_{mn} = -n^i\partial_i h^{\mathrm{TT}}_{mn} = \partial_r h^{\mathrm{TT}}_{mn}$, to leading order in r

The momentum flux can be obtained from $\Pi^{ij} = T^{(\mathrm{GW})ij}$. Again, for a GW propagating radially the k component of the momentum flux in the radial direction is $n_i \Pi^{ij} = T^{(\mathrm{GW})0j}$, and the total momentum per unit time carried away is,

$$\frac{dP^i}{dt} = \frac{c^3 r^2}{32\pi G} \int d\Omega \langle \dot{h}^{\mathrm{TT}}_{mn} \partial^i \dot{h}^{\mathrm{TT}}_{mn} \rangle, \tag{2.32}$$

On the other hand, the short-scale or "wave" part of any quantity can be obtained by subtracting the long-scale part, e.g. $F^{\text{short}} = F - \langle F \rangle$. Thus, the short-scale part of the EFE is given by,

$$R^{(1)}_{\mu\nu}(h) + R^{(2)}_{\mu\nu}(h) - \langle R^{(2)}_{\mu\nu}(h) \rangle = \frac{8\pi G}{c^4} \left[T_{\mu\nu} - \frac{1}{2} g_{\mu\nu} T \right]^{\text{short}}, \tag{2.33}$$

which implies that $h_{\mu\nu}$ must receive corrections of second order in $\mathcal{A}$. i.e to second order in $h_{\mu\nu}$, GWs not only generate background curvature but also GWs (self-interaction). The next section will discuss this equation in vacuum.

2.2.1 Wave Propagation

This section will study eq. (2.33) in vacuum and will show that indeed it corresponds to a wave propagation equation in curved spacetime. First, some formal results of the propagation in the near zone will be presented. The local the wave-zone is characterized by the absence of background effects, thus the propagation equation in the Lorentz gauge is given by the wave equation,

$$\Box \bar{h}_{\mu\nu} = 0. \tag{2.34}$$

Recall that in the TT frame $\bar{h}_{\mu\nu}$ is purely spatial. "Fourier basis solutions" of the spatial components of eq. (2.34) are given by (Thorne, 1980b),

$$\psi^{\epsilon\omega l'lm}_{ij} = \sqrt{\frac{|\omega|}{2\pi}} e^{-i\omega t} h^{\epsilon l}(\omega r/c) T^{l'lm}_{ij}(\theta, \phi),, \tag{2.35}$$

where $\epsilon = 1, -1$ indicates ingoing or outgoing solutions respectively,

$$h^{+l} = j^l + i y^l, \quad h^{-l} = j^l - i y^l, \tag{2.36}$$

j^l and y^l are the spherical Bessel functions (Arfken & Webber, 2005), and T^{lm}_{ij} are the tensor spherical harmonics that will be discussed in appendix B. This basis solutions provide a tensor Green's function (Thorne, 1980b),

$$\Box_x G^{\epsilon}(x, x')_{ij \cdot lm} = -\frac{1}{2}(\delta_{il}\delta_{jm} + \delta_{im}\delta_{jl})\delta^4(x - x') \tag{2.37}$$

$$G^{\epsilon}(x, x')_{ij \cdot lm} = i\epsilon \sum_{l'lm} \int d\omega \ \mathrm{sgn}(\omega) \psi^{\epsilon\omega l'lm}_{ij}(x) [\Phi^{\omega l'lm}_{ij}(x')]^* \qquad \text{if } r > r', \tag{2.38}$$

$$= i\epsilon \sum_{l'lm} \int d\omega \ \mathrm{sgn}(\omega) \Phi^{\omega l'lm}_{ij}(x) [\psi^{(-\epsilon)\omega l'lm}_{ij}(x')]^* \qquad \text{if } r > r', \tag{2.39}$$

where $\Phi_{ij}^{\omega l' lm} = (\psi_{ij}^{\epsilon\omega l' lm} + \psi_{ij}^{(-\epsilon)\omega l' lm})/2$ are "standing wave" solutions. Tensor Green's function can be used to solve the wave equation with source as a expansion in tensor spherical harmonics (see Thorne, 1980b, eqs. (5.7) and (5.8)). On the other hand, a more simple, in the author's opinion, general solution of (2.34) can be expressed in terms of purely spatial symmetric trace free (STF) tensors,

$$\bar{h}^{\mu\nu} = \sum_{l=0}^{\infty} \partial_L \left[\frac{1}{r} H_L^{\mu\nu}(u) \right], \tag{2.40}$$

where $u = t - r/c$, and the multi-index notation $F_L \equiv F_{i_1 i_2 i_3 \ldots i_l}$ is used. The tensor $H_L^{\mu\nu}$ is STF in the indices L. This solution will be discussed in more detail in appendix B. As a result, (only) at linearized level, physical principles of light propagation which do not involve polarization, such as Fermat's principle, Huygens' principle, interference or scalar diffraction, also apply to the propagation of GWs. For example, when the analysis is promoted to higher orders (or in the full non-linear analysis) GWs do not satisfy Huygens' principle (see e.g Bondi et al., 1962).

Regarding the distant wave-zone, the propagation equation to linear order in $h_{\mu\nu}$ (linear order in $\mathcal{A}$) is,

$$-2R_{\mu\nu}^{(1)} = \bar{h}_{\mu\nu|\alpha}{}^{|\alpha} + g_{\mu\nu}^{(B)} \bar{h}_{\alpha\beta}{}^{|\alpha\beta} - 2\bar{h}_{\alpha(\mu|}{}^{\alpha}{}_{\nu)} + 2R_{\alpha\mu\beta\nu}^{(B)} \bar{h}^{\alpha\beta} - 2R_{\alpha\mu}^{(B)} \bar{h}_{\nu}{}^{\alpha} = 0, \tag{2.41}$$

where $\bar{h}_{\mu\nu} \equiv h_{\mu\nu} - (1/2) g_{\mu\nu}^{(B)} h$, and the subindex $|$ indicates covariant differentiation with respect to the background metric (see app. A). As in the flat background case, here there are gauge transformations,

$$h'_{\mu\nu} = h_{\mu\nu} - 2\xi_{(\mu|\nu)}, \tag{2.42}$$

and it can be imposed a generalized Lorentz gauge, $\bar{h}_{\alpha\beta}{}^{|\beta} = 0$. Equation (2.25) in vacuum implies that $R_{\mu\nu}^{(B)} \sim \mathcal{A}^2/\lambdabar^2$, so the last term in (2.41) is $\sim \mathcal{A}^3/\lambdabar^2$ and it can be neglected relative to the others. Finally, in the Lorentz gauge the propagation equation is,

$$\bar{h}_{\mu\nu|\alpha}{}^{\alpha} + 2R_{\alpha\mu\beta\nu}^{(B)} \bar{h}^{\alpha\beta} = 0, \tag{2.43}$$

which is the generalization of eq. (2.34) to curved spacetime, and is independent of value of $\lambdabar/\mathcal{R}$. When the latter is $\ll 1$ (short wavelengths) the propagation equation corresponds to a wave equation in curved spacetime, $\bar{h}_{\mu\nu|\alpha}{}^{\alpha} = 0$, and the concept of GW is clear. The background curvature affects the propagation via the covariant derivatives and/or via the explicit curvature coupling through the Riemann tensor.

The propagation of GWs can be studied within the approximation of *geometrical optics* (see e.g. Landau & Lifshitz, 1951; Misner et al., 2017). Locally, the GWs are regarded as plane waves, i.e, in a region $|\bar{x}^i| \gg \lambdabar$ and in a time interval $\tau \gg T_{\mathrm{GW}}$, the wave vector is nearly constant, $k_{,i} \approx 0$, and the GW is nearly monochromatic $f_{\mathrm{GW},0} = (T_{\mathrm{GW}}^{-1})_{,0} \approx 0$; the amplitude is also nearly constant $H_{\mu\nu,\alpha} \approx 0$. The typical length over which these last quantities vary is $\underline{\mathcal{L}} \gg \lambdabar$. Basically, the geometrical optics approximation is the limit $\lambda \to 0$. The field $\bar{h}_{\mu\nu}$ is conveniently expressed as,

$$\bar{h}_{\mu\nu} = \Re\big[H_{\mu\nu} e^{i\psi(x^\mu)/\epsilon}\big] = \Re\big[(A_{\mu\nu} + \epsilon B_{\mu\nu} + \epsilon^2 C_{\mu\nu} + \ldots) e^{i\psi(x^\mu)/\epsilon}\big], \tag{2.44}$$

where ψ, called the *eikonal*, is a large quantity proportional to $1/\bar{\lambda}$, i.e. the eikonal is a rapidly varying quantity whereas the amplitude is nearly constant and receives corrections in powers of $\epsilon \propto \bar{\lambda}$. In addition, the background curvature is $\mathscr{R} \gg \lambda$. The dummy parameter ϵ is introduced to make easier the analysis when the limit $\bar{\lambda} \to 0$ is applied. By substituting (2.44) in eq. (2.43) and grouping terms according to the order of ϵ the following expressions are obtained,

$$\psi_{,\mu}\psi^{,\mu} = k_\mu k^\mu = 0 \quad \text{(Leading order)}, \tag{2.45}$$

$$2A_{\mu\nu|\alpha}k^\alpha + A_{\mu\nu}{k_{\alpha|}}^{\alpha} = 0 \quad \text{(Next-to-leading order)}. \tag{2.46}$$

Now, by taking the covariant derivate of (2.45) and from the fact that partial and covariant differentiation commute for a scalar, e.g. ψ, the wave-vector satisfies the geodesic equation,

$$k^\mu k_{\nu|\mu} = 0. \tag{2.47}$$

The rays of the GWs (curves parallel to k^μ) are geodesics of massless particles (gravitons). The spatial wavefronts (space-like surfaces perpendicular to k^i) change their shape according to the background curvature (refraction). The GW frequency, $\omega_{\rm GW} = d\psi/d\tau = k_\mu u^\mu$ measured by a static observer with four-velocity $u^\mu = \delta^\mu_0 u^0$, also presents redshift due to the background curvature. According to (2.46), the GW amplitude defined as $\mathcal{A} \equiv (A^*_{\mu\nu}A^{\mu\nu})^{1/2}/2$, satisfies the equation,

$$\mathcal{A}_{|\mu}k^\mu + \frac{1}{2}\mathcal{A}{k_{\mu|}}^{\mu} = 0, \tag{2.48}$$

which is equivalent to $(\mathcal{A}^2 k^\mu)_{|\mu} = 0$ and corresponds to the conservation of the number of rays. The polarization tensor $e_{\mu\nu} \equiv A_{\mu\nu}/\mathcal{A}$ is parallel transported along the ray,

$$e_{\mu\nu|\alpha}k^\alpha = 0. \tag{2.49}$$

The Lorentz gauge condition implies that the polarization tensor is orthogonal to k_μ. In summary, GW propagation effects due to the background include refraction (change in the direction of the propagation) and redshift (change of wavelength). When the curvature background is $\mathscr{R} \sim \bar{\lambda}$ the waves are backscattered and a patron of tails appears, like the ringing tail when a black hole is perturbed (see e.g. Press (1971) or chapter 3).

The geometrical optics approximation is not valid near *caustics*, i.e. the loci of the center of curvatures of the wavefronts. In order to analyze the GW propagation near caustics, a NLF is constructed in the near zone of the caustics so the formalism of flat spacetime can be used, e.g. diffraction formalism. After the problem is solved in the zone around the caustic, the solution is propagated with the geometrical optics formalism (Thorne, 1989). The caustic region must be much smaller than the background curvature. A physical caustic of GWs can occur in the near region of the focal point of a gravitational lens.

2.3 Weak-field and Low-velocity Approximation to Gravitational Radiation

Having discussed the propagation of GWs, this section is dedicated to compute GWR within the weak-field limit. In the classical theory of electromagnetism there is no radiation from the electric monopole moment of the source. In GWR the monopole also does not contribute. In electromagnetism, the first contribution comes from the electric and the magnetic dipole moment. However, the gravitational dipole mass moment contribution to GWR is null because of the conservation of linear momentum. Consequently, the first contribution is expected to come from the quadrupole moment. The fundamental equation to solve is (2.7). The Green's function $G(x, x')$ of the scalar version of this equation, for no-ingoing radiation at null infinity is given by (Jackson, 1998),

$$\Box_x G(x, x') = \delta^4(x - x'), \tag{2.50}$$

$$G(x, x') = -\frac{\delta[c(t - t_{\text{ret}})]}{4\pi|\mathbf{x} - \mathbf{x}'|}, \tag{2.51}$$

where t_{ret} is the "retarded time" $t_{\text{ret}} = t - |\mathbf{x} - \mathbf{x}'|/c$. Therefore, the solution of (2.7) is

$$\bar{h}_{\mu\nu} = \frac{4G}{c^4} \int \frac{T_{\mu\nu}(t_{\text{ret}}, \mathbf{x}')}{|\mathbf{x} - \mathbf{x}'|} d^3x'. \tag{2.52}$$

All that remains is to solve this integral to a given precision. The system of reference is chosen so that the spatial origin is inside the source. In the radiation zone, $r \gg |\mathbf{x}'|_{\max} = r'$, where r' is the largest dimension of the source, the leading term of $|\mathbf{x} - \mathbf{x}'|^{-1}$ is $1/r$, and the argument $|\mathbf{x} - \mathbf{x}'|/c$ of $T_{\mu\nu}$ can be expanded in powers of r'/r,

$$|\mathbf{x} - \mathbf{x}'| = r\left[1 - \frac{\mathbf{x}' \cdot \hat{\mathbf{n}}}{r} + \mathcal{O}\left(\frac{r'^2}{r^2}\right)\right], \tag{2.53}$$

where $\hat{\mathbf{n}} = \mathbf{x}/r$. It is important to note that the cut-off in the series depends on the time behaviour of the source. For instance, whether the time delay $\mathbf{x} \cdot \hat{\mathbf{n}}/c$ is negligible or not, does not depend on its value relative to r/c, but on the time scale of the function $T_{\mu\nu}$. The radiation zone or wave zone is defined as the region where (i) $r \gg r'$, (ii) $r \gg c/\omega = \lambda\!\!\!^{-}$ and (iii) $r \gg \omega r'^2$ (Weinberg, 1972). Actually, these conditions are not approximations since it is always possible to find the region where they are satisfied. Since the radiation zone conditions are given in terms of the wavelength, it is convenient to expand the field into its Fourier components,

$$h_{ij}^{\text{TT}} = \frac{4G}{c^4 r} \Lambda_{ij,lm} \int \frac{d\omega}{2\pi} \tilde{T}_{lm}(\omega, \mathbf{x}') e^{-i\omega(t - r/c + \mathbf{x}' \cdot \hat{\mathbf{n}}/\mathbf{c})} d^3x'. \tag{2.54}$$

The retardation r/c is much larger that the period $2\pi\omega^{-1}$ and cannot be neglected in the exponent; the terms of order r'^2/r or higher, can be neglected by virtue of the last wave zone condition. So far the only approximation that has been made is $|h_{\mu\nu}| \ll 1$, namely the field $h_{\mu\nu}$ is *weak*[5].

On the other hand, most of the astrophysical sources have the property that their velocity is much less than the speed of light. For a self-gravitating system the square of the velocity is $v^2 \sim 2GM/r'$, where M is the total mass of the system. That is, the velocity is of order of the speed of light when the typical length is of the order of the Schwarzschild radius $2GM/c^2$. From eq. (2.54), the frequency of the source is of the order of GW frequency,

---

[5] For self-gravitating systems, the weak-field approximation is equivalent to low-velocity approximation (see below). When other forces are present, but the gravitational field is weak, this approximation is valid for all velocities of the system.

and the velocity is of the order of $v \sim \omega r' = (c/\lambdabar)r'$. Consequently, if the velocity is much less than the speed of light, $r'/\lambdabar \ll 1$, and viceversa. This approximation is called the *low-velocity* approximation and allows to expand the exponent inside the integral in powers of $(i\omega\mathbf{x}' \cdot \hat{\mathbf{n}}/c)$,

$$\exp(-i\omega\mathbf{x}' \cdot \hat{\mathbf{n}}/c) \approx 1 - \frac{i\omega\mathbf{x}' \cdot \hat{\mathbf{n}}}{c} - \frac{\omega^2(\mathbf{x}' \cdot \hat{\mathbf{n}})^2}{2c^2} + \ldots \tag{2.55}$$

Since the expansion was made in the frequency domain, it is equivalent to an expansion in the time domain, around $u = t - r/c$,

$$T_{ij}(t_{\text{ret}}, \mathbf{x}') \approx T_{ij}(u, \mathbf{x}') + \frac{\mathbf{x}' \cdot \hat{\mathbf{n}}}{c} \frac{\partial T_{ij}}{\partial t}\bigg|_u + \frac{(\mathbf{x}' \cdot \hat{\mathbf{n}})^2}{2c^2} \frac{\partial^2 T_{ij}}{\partial t^2}\bigg|_u + \ldots \tag{2.56}$$

The leading term of GWR in the *weak-field and low-velocity* approximation is given (in the TT frame) by the term $T_{ij}(t', \mathbf{x}')$ inside the integral of eq. (2.52). The local conservation of energy-momentum allows to re-express this result in terms of the mass-moments as follows. From $T^{\mu\nu}$, $\nu = 0$, it can be deduced that,

$$(T^{00} x_i x_j)_{,00} = T^{lm}{}_{,lm}\, x_i x_j, \tag{2.57}$$

and by integrating by parts,

$$\frac{1}{c^2} \frac{d^2}{dt^2} \int T^{00} x_i x_j d^3x = 2 \int T_{ij} d^3x. \tag{2.58}$$

For a non-relativistic source, the T^{00} is given by the rest energy density, ρc^2, so the GWR can be expressed in terms of the second mass moment of the source I_{ij},

$$I_{ij} = \int \rho(x) x_i x_i d^3x \tag{2.59}$$

This last symmetric tensor can be split into a trace-free tensor plus a diagonal tensor constructed from its trace. When the second mass moment tensor is projected by means of $\Lambda_{ij,lm}$ the diagonal tensor is canceled out, thus the only part which contributes is the trace-free part,

$$\not{I}_{ij} = \int \rho(x_i x_j - \frac{1}{3}\delta_{ij} r^2) d^3x, \tag{2.60}$$

which is called the *reduced quadrupole moment*. Finally, the leading term of GWR is given by,

$$h_{ij}^{\text{TT}}(t - r/c, x^i)\Big|_{\text{quad}} = \frac{2G}{c^4 r} \Lambda_{ij,lm} \ddot{\not{I}}_{lm}(t - r/c), \tag{2.61}$$

and is called the Newtonian-quadrupole approximation (Einstein, 1918; Landau & Lifshitz, 1951).

2.3.1 Binary System

The low-velocity approximation has shown that in order to compute the GWR to leading order (quadrupole) all that is needed is the quadrupole moment $\not{I}_{ij}$ of the source. The

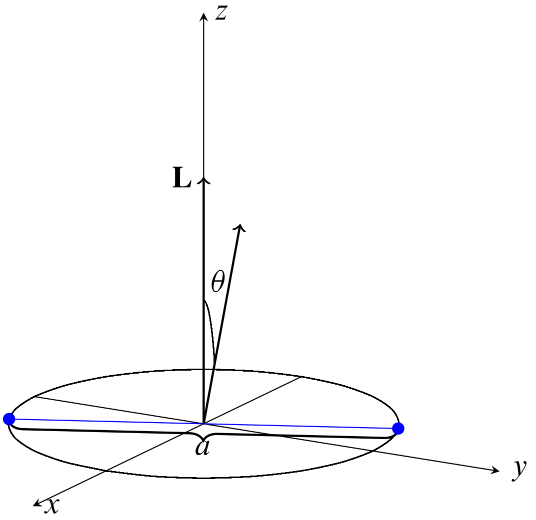

Figure 2.2 Binary system which during the adiabatic inspiral phase can be regarded as composed of two point-like masses. The coordinate system is chosen so that the binary plane lies on the xy plane. The distance between the masses is denoted by a. The total orbital angular momentum is $\mathbf{L}$ is in the z directions and makes an angle θ with respect the line of sight.

first astrophysical source of interest is a self-gravitating system composed of two bodies. In reality the system can be composed of stars or black holes (or even exoplanets). The dynamics of the system is given by Newton's laws. The origin of the system of reference is chosen at the center of mass. The two body problem can be converted into an equivalent one body problem of a particle of mass $\mu = m_1 m_2/(m_1 + m_2)$, called the reduced mass, in a external field gravitational field, $Gm_1 m_2/|\mathbf{r}|$, where $\mathbf{a} = \mathbf{r_1} - \mathbf{r_2}$ is separation radius vector between the two bodies. The system is confined to a plane and the total angular momentum is conserved when GWR reaction is not taken into account (see fig. 2.2). As a first approximation, it is supposed that the system describes a circular orbit. The angular velocity ω_{orb} is given by the Kepler's law,

$$\omega_{\text{orb}}^2 = \frac{GM}{a^3}, \tag{2.62}$$

where $M = m_1 + m_2$ is the total mass, and the total energy is given by,

$$E = -\frac{1}{2}\mu\dot{\mathbf{a}}^2 = -\frac{Gm_1 m_2}{2a}. \tag{2.63}$$

The coordinates are chosen so that the system moves in the xy plane and the total angular momentum is on the z direction. The reduced quadrupole moment of this equivalent system is given by,

$$Ɨ_{xx} = \mu a^2\left(\frac{1-\cos 2\omega_{\text{orb}}t}{2} - \frac{1}{3}\right), \tag{2.64}$$

$$Ɨ_{yy} = \mu a^2\left(\frac{1+\cos 2\omega_{\text{orb}}t}{2} - \frac{1}{3}\right), \tag{2.65}$$

$$Ɨ_{zz} = -\frac{\mu r^2}{3}, \tag{2.66}$$

$$Ɨ_{xy} = -\mu a^2\frac{\sin 2\omega_{\text{orb}}t}{2}. \tag{2.67}$$

The GW polarizations as a function of the distance to the source r and the propagation direction (θ, ϕ) are,

$$h_+ = \frac{4GM}{c^2 r}\nu\left(\frac{GM\omega_{\text{orb}}}{c^3}\right)^{2/3}\cos\omega u\left(\frac{1+\cos^2\theta}{2}\right), \tag{2.68}$$

$$h_\times = \frac{4GM}{c^2 r}\nu\left(\frac{GM\omega_{\text{orb}}}{c^3}\right)^{2/3}\sin\omega u\cos\theta, \tag{2.69}$$

where $\nu \equiv \mu/M$ is the *symmetric mass ratio*, $u = t - r/c$ is the retarded time, θ is the angle between the total angular momentum and the line of sight, and the GW angular frequency is twice the orbital, $\omega = 2\omega_{\text{orb}}$. The angular distribution of the luminosity is,

$$\frac{dL_{\text{GW}}}{d\Omega} = \frac{2\nu^2 c^5}{\pi G}\left(\frac{GM\omega_{\text{orb}}}{c^3}\right)^{10/3}\left[\frac{(1+\cos^2\theta)^2}{4} + \cos^2\theta\right], \tag{2.70}$$

and the total luminosity is given by,

$$L_{\text{GW}} = \frac{32}{5}\frac{c^5}{G}\nu^2\left(\frac{GM\omega_{\text{orb}}}{c^3}\right)^{10/3} = \frac{32}{5}\frac{c^5}{G}\nu^2\left(\frac{v^2}{c^2}\right)^5. \tag{2.71}$$

The binary system is emitting waves that carry away energy, therefore its total energy must decrease according to the law,

$$-\frac{dE}{dt} = L_{\text{GW}}, \tag{2.72}$$

and from the eq. (2.63) it can be seen that when the system losses energy its radius decreases or equivalently the angular velocity increases. For the sake of consistency the radial velocity must be small in order to the luminosity formula, which was calculated for strict circular orbits, be valid. In other words the orbital period must be much smaller than the typical time of radial falling. In this way, the evolution of the system consists of a series of quasi-static circular orbits. The above conditions are fulfilled when $\dot{\omega}_{\text{orb}} \ll \omega_{\text{orb}}^2$, i.e. when the system evolves adiabatically (see e.g. Landau & Lifshitz, 1969, for a definition of adiabatic motion). The evolution law for the GW angular frequency can be deduced from (2.72),

$$\dot{\omega} = \left(\frac{3}{5}\right)2^{7/3}\nu\left(\frac{GM}{c^3}\right)^{5/3}\omega^{11/3} = \left(\frac{3}{5}\right)2^{7/3}\left(\frac{GM_c}{c^3}\right)^{5/3}\omega^{11/3}, \tag{2.73}$$

where $M_c = \nu^{3/5}M = \mu^{3/5}M^{2/5}$ is the *chirp mass*, which provides a characteristic time scale for the evolution of binary system. The *intrinsic time-domain phase evolution*,

$Q_\omega \equiv \omega^2/\dot{\omega}$ introduced by Damour et al. (2013), is a normalized quantity to compare the phase of different waveforms, which for the binary system is given by,

$$Q_\omega^{\text{bin}} = \frac{1}{\nu}\left(\frac{5}{3}\right)2^{-7/3}\left(\frac{GM}{c^3}\omega\right)^{-5/3} = \left(\frac{5}{3}\right)2^{-7/3}\left(\frac{GM_c\omega}{c^3}\right)^{-5/3}. \tag{2.74}$$

The number of GW cycles N in the frequency interval $[\omega_0, \omega_1]$ is,

$$N = (2\pi)^{-1}\int_{\omega_0}^{\omega_1} Q_\omega d\ln\omega. \tag{2.75}$$

The time evolution of the frequency, phase and the separation radius is found by integrating eq. (2.73),

$$\dot{\Phi}(t) = \omega(t) = \frac{1}{4}\left(\frac{c^3}{GM_c}\right)^{5/8}\left(\frac{5}{t_{\text{coal}} - t}\right)^{3/8} \tag{2.76}$$

$$\Phi(t) = -2\left[\frac{c^3(t_{\text{coal}} - t)}{5GM_c}\right]^{5/8} + \Phi_0 = -\frac{3}{5}Q_\omega^{\text{bin}} + \Phi_0 \tag{2.77}$$

$$a(t) = a_0\left(\frac{t_{\text{coal}} - t}{t_{\text{coal}} - t_0}\right)^{1/4} \tag{2.78}$$

where a_0 is the (initial) separation radius at time t_0, and at the coalescence time $a(t_{\text{coal}}) = 0$. When the orbital period of a binary is known, eq. (2.76) can be used to estimated the time to coalescence, $t_{\text{coal}} - t$,

$$t_{\text{coal}} - t = \frac{5}{\nu}\left(\frac{T_{\text{orb}}}{16\pi}\right)^{8/3}\left(\frac{GM}{c^3}\right)^{-5/3}. \tag{2.79}$$

Formally, the frequency has a divergence at a finite time, t_{coal}. Nevertheless, this time is never achieved because the two body will contact each other before this happens, or if the components are compact enough, the system will reach before a point where the gravitational field is so strong that they begin to plunge. This last point can be estimated by the inner-most stable circular (ISCO) of the system, e.g. the ISCO of a Schwarszschild black hole $a_{\text{ISCO}} = 6GM/c^2$. As a good approximation the above formulas are valid up to the ISCO.

Provided that the frequency changes with time, the GW polarizations for a binary evolving under the action of GWR have increasing amplitudes and the phase is changed, according to eq. (2.77), $\omega u \mapsto \Phi(u)$, i.e the GW have chirping-like behaviour. The matched-filter technique uses the Fourier transform of the waveform to detect GWs in interferometers (see chapter 5). The Fourier transform of the evolving GW polarizations is found by the stationary phase method,

$$\tilde{h}_+(f) = A(f)e^{i\Psi_+(f)}(1 + \cos^2\theta)/2, \tag{2.80}$$

$$\tilde{h}_\times(f) = A(f)e^{i\Psi_\times(f)}\cos\theta, \tag{2.81}$$

where the fourier phase is,

$$\Psi_+(f) = 2\pi f t_{\text{coal}} + \frac{9}{40}Q_\omega^{\text{bin}} - \Phi_0 - \frac{\pi}{4} = \Psi_\times - \frac{\pi}{2}, \tag{2.82}$$

and the amplitude,

$$A(f) = 2\nu \frac{GM}{c^2 r}\left(\frac{GM}{c^3}\pi f\right)^{2/3} \frac{Q_\omega^{1/2}}{f\sqrt{2\pi}}. \tag{2.83}$$

The GW spectrum is found by substituting the above Fourier transforms in eq. (2.31),

$$\frac{dE}{df} = \frac{16}{5}\pi\nu^2 \frac{GM^2}{c}\left(\frac{GM}{c^3}\pi f\right)^{4/3} Q_\omega = \frac{\pi^{2/3}\nu}{3}\left(\frac{GMf}{c^3}\right)^{-1/3}\frac{GM^2}{c}. \tag{2.84}$$

The spectrum during this phase depends linearly on the symmetric mass ratio and has a power law in the frequency. The total energy radiated in the frequency interval $[f_0, f_1]$ is,

$$\Delta E_{\rm insp} = \frac{\pi^{2/3}}{2G}\nu(GM)^{5/3}(f_1^{2/3} - f_0^{2/3}). \tag{2.85}$$

However, a better estimate for the radiated energy up to the ISCO is given by the binding energy of that orbit in the Schwarszchild metric,

$$E_{\rm insp} \lesssim (1 - \sqrt{8/9})\nu M c^2. \tag{2.86}$$

An indirect observation of GWs can be made by measuring the change in the orbital period $P_{\rm orb}$, which is given by eq. (2.73),

$$\dot{P}_{\rm orb} = -\frac{192\pi}{5}\left(\frac{GM_c 2\pi}{c^3 P_{\rm orb}}\right)^{5/3}. \tag{2.87}$$

However, this formula corresponds to the circular orbits case, when the orbits are ellipses the above expression receives corrections in terms of the orbit eccentricity e (Maggiore, 2008),

$$\dot{P}_{\rm orb}\big|_{\rm ellip} = \dot{P}_{\rm orb}\big|_{\rm circ}\left(1 + \frac{73}{24}e^2 + \frac{37}{96}e^4\right). \tag{2.88}$$

The continuous observation of the binary pulsar PSR B1913+16 (Hulse & Taylor, 1975) gives a ratio between the data and the predicted value of General Relativity of (Weisberg & Taylor, 2005),

$$\frac{\dot{P}_{\rm exp}}{\dot{P}_{\rm teo}} = 1.0013 \pm 0.0021. \tag{2.89}$$

This theoretical prediction of the secular decrease of the orbital period is a direct consequence of General Relativity's prediction of GWs.

Propagation on the Friedmann-Lemaître-Robertson-Walker Background

The propagation of GWs from binary systems to cosmological distances is analyzed with the formalism of geometrical optics. The universe is described by the Friedmann-Lemaître-Robertson-Walker (FLRW) metric (Weinberg, 2008) whose line element is (for euclidean space),

$$ds^2 = a^2(\eta)[d\eta^2 + dr^2 + r^2 d\Omega^2] = a^2\eta_{\mu\nu}dx^\mu d^\nu, \tag{2.90}$$

where η is the conformal time. The geometrical optics limits corresponds to the case when $da/d\eta \ll \omega_0 a$, where ω_0 is the GW angular frequency measured in the local wave zone.

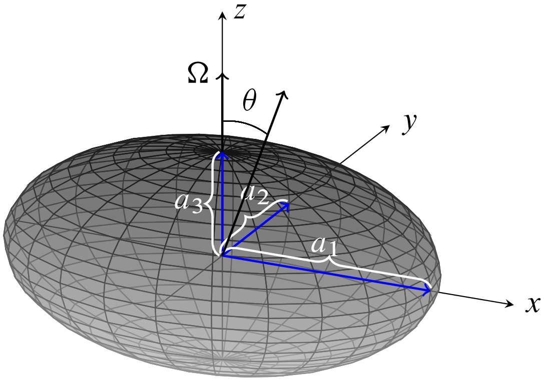

Figure 2.3 Illustration of a deformed star rotating around the z axis. The angle between the axis of rotation and the line of sight is denoted by θ

Note that the metric is conformal to Minkowski, therefore null geodesics are the *same* curve in both spacetimes (Wald, 2010). The rays of GWs propagating radially outward on the Minkowski spacetime are given by $t - r/c = \text{const}$, thus radial rays on the (FLRW) metric are, $\eta - r/c = \text{const}$. The affine parameters of the two geodesics are related, $d\lambda'/d\lambda = \kappa^{-1}a(\eta)^2$, where κ is a constant. Consequently, the wave-vector of GWs in the FLRW metric is, $k^\mu = (\kappa/a^2)(\omega_0/c, k_0, 0, 0)$. The GW frequency measured by a static observer is $\omega_{\text{GW}} = \omega_0/a(\eta)$, so there is a redshift when the frequency is measured along the same ray at two different positions,

$$\frac{\omega_{\text{GW}}^{\text{em}}}{\omega_{\text{GW}}^{\text{obs}}} = \frac{a(\eta_{\text{obs}})}{a(\eta_{\text{em}})} \equiv 1 + z, \tag{2.91}$$

where z is the cosmological redshift. Since the number of cycles is a physical invariant quantity, the times of arrival are also redshifted $t_{\text{obs}}/t_{\text{em}} = (1+z)$. When this two relations are substituted in eq. (2.76), the frequency as a function of time has the same form but with the substitution $M_c \mapsto \mathcal{M}_c = (1 + z)M_c$. This can be seen as the redshift of the characteristic unit of time. Regarding the amplitude, eq. (2.46) implies that $[(ar)A_{\mu\nu}]_{|\alpha}k^\alpha = 0$. Hence the amplitude decreases $\propto (ar)^{-1}$.

2.3.2 Rotating Star

Another astrophysical source of GWs is a rotating star. Compact stars rotating very fast have been observed since the discovery of pulsars by Hewish et al. (1968), e.g. the GW emission by the pulsar NP 0530 in the Crab Nebula (Lovelace et al., 1968; Cocke et al., 1969), was first estimated in (Ferrari & Ruffini, 1969). This section will analyze the case of an incompressible star whose shape is an ellipsoid. The more general case of a compressible star will be analyzed in the chapter 7. The star is rotating with angular velocity Ω, around one of its principal axes, a_3, which is aligned with the axis z, and the other axes a_1, a_2 are aligned with the axes x and y of a rotating frame with the same angular velocity of the star. The inertia tensor of a rigid body is (Landau & Lifshitz, 1969),

$$Q_{ij} = \int (r^2\delta_{ij} - x_i x_j) d^3x, \tag{2.92}$$

and it is related to the reduced quadrupole moment by, $\not{I}_{ij} = Q\delta_{ij}/3 - Q_{ij}$. In the frame rotating the star appears static and the inertia tensor is diagonal $Q_{ij} = \mathrm{diag}(Q_1, Q_2, Q_3)$,

$$Q_1 = \frac{M}{5}(a_2^2 + a_3^2) \tag{2.93}$$

$$Q_2 = \frac{M}{5}(a_1^2 + a_3^2), \tag{2.94}$$

$$Q_3 = \frac{M}{5}(a_1^2 + a_2^2), \tag{2.95}$$

where M is the mass of the star. The inertial (rest) frame in which the star rotates is related to the latter frame by a rotation $\alpha = \Omega t$ around the z axis. After performing the change of coordinates, the components of the inertia tensor in the rest frame are,

$$Q_{11} = \frac{Q_1 + Q_2}{2} + \frac{Q_1 - Q_2}{2}\cos 2\Omega t, \tag{2.96}$$

$$Q_{22} = \frac{Q_1 + Q_2}{2} - \frac{Q_2 - Q_1}{2}\cos 2\Omega t, \tag{2.97}$$

$$Q_{33} = Q_3, \tag{2.98}$$

$$Q_{12} = \frac{Q_1 - Q_2}{2}\sin 2\Omega t. \tag{2.99}$$

It can be seen that the trace of Q_{ij} is a time-independent number, therefore the second time derivative of the reduced quadrupole moment is $\ddot{\not{I}}_{ij} = -\ddot{Q}_{ij}$. The GW polarizations are given by,

$$h_+ = \frac{4G}{c^4 r}\frac{M}{5}(a_1^2 - a_2^2)\Omega^2 \cos 2\Omega u \frac{(1 + \cos^2\theta)}{2}, \tag{2.100}$$

$$h_\times = \frac{4G}{c^4 r}\frac{M}{5}(a_1^2 - a_2^2)\Omega^2 \sin 2\Omega u \cos\theta, \tag{2.101}$$

where u as usual, is the retarded time, and θ is the angle between the line of sight and the axis of rotation (see fig. 2.3). If the semiaxes a_1 and a_2 are equal, there is no GR, i.e. axis-symmetric rotation do not emit GWs. The GW luminosity is,

$$L_{\mathrm{GW}} = \frac{32}{5}\frac{G}{c^5}(I_{11} - I_{22})^2\Omega^6. \tag{2.102}$$

The emission of GWs will induce that the star moment of inertia (shape) and angular rotation change over time. The existence of these deformed stars and its evolution will be discussed in chapter 7.

Chapter 3

Test Particle Approach to Gravitational Radiation

The last chapter reviewed the general principles of GWR and discussed one approximation, namely the weak-field and low-velocity approximation. The last stages in the coalescence of compact objects binaries are characterized by strong gravitational fields and high velocities. Hence, the problem must be analyzed using other formalisms such as BH perturbation theory or the numerical solution of the full EFE. This last approach constituted a challenging task which was not solved successfully until the work of (Pretorius, 2005). On the other hand, numerical relativity simulations are computational expensive and sometimes the physics is hard to extract. Perturbation methods have been developing since the work of Regge & Wheeler (1957) and provide physical insight in the strong-field and comparable masses regime (see e.g sec.). Moreover perturbation theory constitute a semi-analytic and computational cheap method to compute GWs. The transition zone between the ISCO and the merger will be studied here by means of an approach different to that presented in the literature. The energy radiated in this regime can be used to infer the final mass of the BH formed in the merger. A comparison between the approaches will be also presented in this chapter. It will be argued that the merger has no burst nature. Strictly speaking, the approach presented here is only valid in the test particle limit, but as it will be shown in the next chapter, there is good agreement with numerical-relativity (comparable masses regime). It points to the existence of a quasi-Newtonian center-of-mass theorem[1] in some General Relativity scenarios. This motivates the comparison between the current approach prediction of the final BH mass and the numerical relativity reported value. This chapter is based on the publication (Rodriguez et al., 2018).

3.1 Radiation from a Test Particle Plunging into a Black Hole

This chapter will use geometrized units $G = c = 1$. The mathematical formalism to analyze perturbations in the gravitational field of a Schwarzschild BH was developed by Regge & Wheeler (1957), where they defined some tensor spherical harmonics $\mathbf{\Psi}^{lm}$, $\mathbf{\Phi}^{lm}$,

---

[1] This means is the reduction of the two body problem to one body problem.

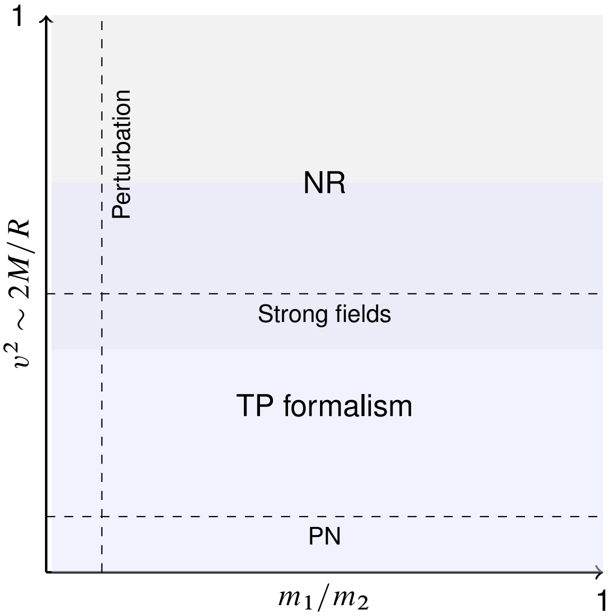

Figure 3.1 Regimes of validity of the different approaches to GR. The post-Newtonian formalism (PN) is valid when the velocities of the system are small compared to the speed of light. Numerical Relativity (NR), in principle is valid in all regimes, but due to computational reasons, far orbits, i.e. slow velocities regime are not covered by the simulations.

χ^{lm} and showed that the Schwarzschild's BH was stable. These spherical harmonics can be used separate the EFE, as done by Zerilli (1970) who studied a test particle of mass μ, radially falling into a BH of mass M. The amount of radiated energy was estimated to be $\Delta E \sim 0.0016(\mu/M)\mu$. A brief review of the exact calculation done by Davis et al. (1971, 1972a) will be presented below. The perturbation field $h_{\mu\nu}$ on a Schwarzschild background is decomposed into the Regge-Wheeler spherical harmonics (Regge & Wheeler, 1957). After replacing this in $G^{(1)}_{\mu\nu}(h) = \delta T_{\mu\nu}$ (see (A.13)), where $\delta T_{\mu\nu}$ is the energy-momentum tensor of the test particle, it can be shown that the radial part of the perturbation is governed by the following equation, whose Fourier transform is (Zerilli, 1970),

$$\frac{d^2 R_l}{dr_*^2} + [\omega^2 + V_l(r)]R_l(r,\omega) = S_l(r,\omega), \tag{3.1}$$

with $r_* = r + 2M\ln(r/2M - 1)$, the "tortoise" coordinate, $dr/dr_* = (1 - 2M/r)$. The potential V_l is,

$$V_l = \left(1 - \frac{2M}{r}\right)\left[\frac{2\lambda^2(\lambda+1)(r/M)^3 + 6\lambda^2(r/M)^2 + 18(r/M)\lambda + 18}{(r/M)^3(\lambda r + 3M)^2}\right], \tag{3.2}$$

with $\lambda = (l-1)(l+2)/2$, and the source is given by,

$$S_l(r,\omega) = -\frac{4\mu}{\lambda(r/M)+3}\sqrt{l+1/2}\left(1 - \frac{2M}{r}\right)\left[\sqrt{\frac{r}{2M}} - \frac{2i\lambda}{\omega(\lambda(r/M)+3)}\right]e^{i\omega T(r)}, \tag{3.3}$$

where $T(r)$ is the time coordinate of the particle (see e.g. (Hartle, 2003) for the explicit expression). In this case, the harmonics with $m \neq 0$ vanish and the perturbation in the radiation gauge (GW) is $h_{\mu\nu} \propto \psi(t,r)\Psi^{0m}_{\mu\nu}$, where,

$$\psi_l(t,r) = \frac{1}{\sqrt{2\pi}} \int R_l(r,\omega) e^{-i\omega t} d\omega. \tag{3.4}$$

The key point is to impose the correct boundary conditions to solve eq. (3.1),

$$\lim_{r_* \to -\infty} R_{l\omega}(r_*) = A^{\rm in}_{l\omega} e^{-i\omega r_*}, \quad \text{ingoing radiation at the horizon,} \tag{3.5}$$

$$\lim_{r_* \to \infty} R_{l\omega}(r_*) = A^{\rm out}_{l\omega} e^{i\omega r_*}, \quad \text{outgoing radiation at infinity} \tag{3.6}$$

Then, use Green's function method to solve boundary valued problems (Arfken & Webber, 2005). The two independent solutions of the homogeneous equation that satisfy the boundary conditions of ingoing and outgoing radiation are $R^H_{l\omega}(r_*)$ and $R^\infty_{l\omega}(r_*)$, respectively. The solution of the inhomogeneous equation is given by,

$$R_{l\omega}(r_*) = Z^\infty_{l\omega}(r_*) R^H_{l\omega}(r_*) + Z^H_{l\omega}(r_*) R^\infty_{l\omega}(r_*), \tag{3.7}$$

where

$$Z^H_{l\omega}(r_*) = \frac{1}{W} \int_{-\infty}^{r_*} S_{l\omega}(r'_*) R^H_{l\omega}(r'_*) dr'_*, \tag{3.8}$$

$$Z^\infty_{l\omega}(r_*) = \frac{1}{W} \int_{r_*}^{\infty} S_{l\omega}(r'_*) R^\infty_{l\omega}(r'_*) dr'_*, \tag{3.9}$$

and W is the Wronskian of $R^H_{l\omega}$ and $R^\infty_{l\omega}$. In the limit $r_* \to \infty$, where the GWs are detected,the solutions become $R^H_{l\omega} = \alpha_\omega e^{i\omega r_*} + \beta_\omega e^{-i\omega r_*}$, because of the vanishing of potential V_l, and $R^\infty_{l\omega} = e^{i\omega r_*}$ due to the boundary condition. In addition, $Z^\infty_{l\omega} = 0$ and the Wronskian is $i\omega\beta_\omega$. Therefore, the coefficient $A^{\rm out}_{l\omega}$ is given by,

$$A^{\rm out}_{l\omega} = \frac{1}{i2\omega\beta_\omega} \int_{-\infty}^{\infty} S_{l\omega}(r'_*) R^H_{l\omega}(r'_*) dr'_*, \tag{3.10}$$

and the energy spectrum is (see fig. 3.2),

$$\frac{dE_l}{d\omega} = \frac{1}{32\pi} \frac{(l+2)!}{(l-2)!} \omega^2 |A_{l\omega}|^2. \tag{3.11}$$

The GW is quadrupole dominant and the total energy radiated to infinity is $\approx 0.0104\mu^2/M$, nearly 7 times greater than the Zerilli's estimation. The spectrum has a peak at $\omega M = 0.32$, after there is an exponential cut off (Davis et al., 1971). The general features of the pulse were analyzed in (Davis et al., 1972a). The waveform is composed by a precursor which is slowly growing and by a sharp burst of emission where most of the energy is radiated. Some of the GW energy is store "in the resonant cavity" of the background spacetime, which is radiated at the end as a ringing-tail whose characteristic frequency is $\omega M \sim l/\sqrt{27}$ (Press, 1971)[2].

---

[2] Background GWs back-scattering.

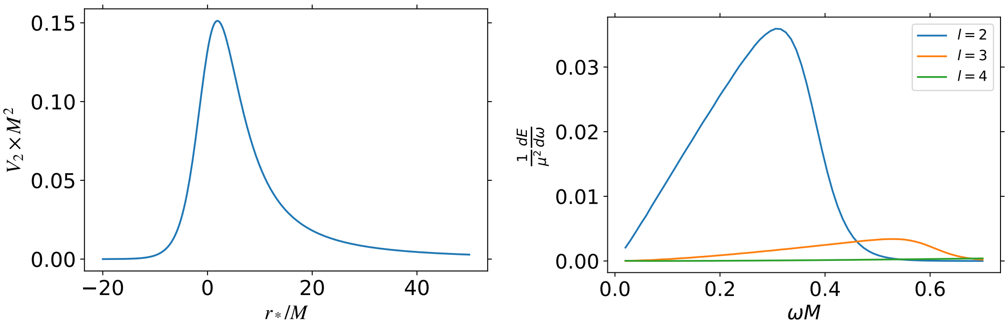

Figure 3.2 Left: Zerilli Potential for $l = 2$, it can be seen the asymptotic decay. Right: spectrum of the GWR emitted by a test particle radially falling into a Schwarzschild BH. The results were obtained with the Green's function technique (for details see e.g. Mitsou, 2011). Quadrupole emission is dominant in this high relativistic case.

The above calculation was generalized to the case of nonvanishing initial angular momentum J (Detweiler & Szedenits, 1979). The spectrum has a peak near $\omega M \sim 0.36$ for all the J studied. However, the spectrum has a vertical scale change which depends on the angular momentum, thus the total energy scales with J. The following empirical law was found $\Delta E \approx \Delta E_{J=0}[1 + 0.11 \exp(1.53 J/(\mu M))]$ (Rodriguez et al., 2016). On the other hand, when the test particle has an initial speed there is a difference in the low-frequency spectrum and a larger emission of energy (Ruffini, 1973a), but the general features of the waveform are maintained. The next generalization was the extension to the case of a Kerr BH. Perturbation theory on a Kerr background is done by means of the Newman-Penrose formalism (Newman & Penrose, 1962) (see appendix D). The energy radiated from a test particle radially falling along the BH spin axis is $\Delta E_{a\neq 0} \approx 0.0170 M(\mu/M)$ almost 1.65 times larger than the spinless case. Finally, the energy radiated by test particle plunging into a Kerr BH with nonvanishing angular momentum was analyzed on (Kojima & Nakamura, 1984). The waveform in this case also presents the same nature: a precursor, a burst and the ringdown.

3.2 Gravitational Radiation from Circular Orbits

The GWR emitted by a test particle in a circular orbit is of great interest for astrophysical sources. The relativistic case on Schwarzschild background was analyzed in (Davis et al., 1972b), which was motivated by the search of a source of gravitational synchrotron radiation. This radiation was calculated within the Regee-Wheeler-Zerilli formalism previously presented and it was found that the energy spectrum is quadrupole dominant, as shown in the fig. 3.3, and therefore has no beaming.

The next development came with computation on the Kerr spacetime. As already mentioned, it is convenient to analyze the problem with the Newman-Penrose formalism. This approach, used by Teukolsky, involves curvature perturbations instead of metric perturbations. It was found that scalar, vector and tensor perturbations are governed by a single master equation, whose solution can be separated in Fourier and spheroidal harmonic modes

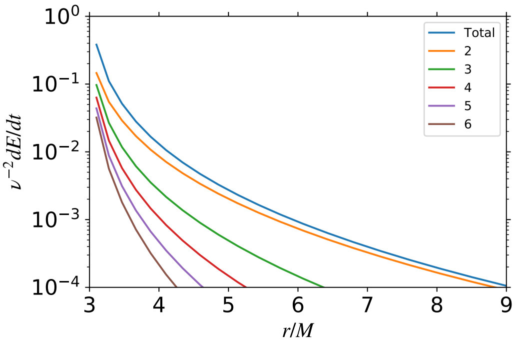

Figure 3.3 Power of the gravitational waves emitted by test particle in a circular orbit in the Schwarzschild spacetime. Selected values of the multipole are shown. The high multipoles are subdominant are therefore the is no beaming in the emission.

(Teukolsky, 1972, 1973; Teukolsky & Press, 1974). Unfortunately, the Teukolsky radial equation has a long-range potential and its numerical integration with boundary conditions is difficult. A change of variable was found by Sasaki & Nakamura (1982b,a), which introduces a short-range and well-behaved potential $U(r)$. The Sasaki-Nakamura (radial) equation is given by,

$$X''_{lm\omega} - F(r)X'_{lm\omega} - U(r)X_{lm\omega} = \mathcal{S}_{lm\omega}. \tag{3.12}$$

Details on the functions F, U and $S_{lm\omega}$ and their numerical solution can be found in (Sasaki & Nakamura, 1982a) or in the appendix D (see, also (Hughes, 2000; Nakano et al., 2016)). The task is accomplished by first solving numerically the eq. (3.12) with the suitable boundary conditions, and then inverting the transformation to find the original radial function. The solution of the Eq. (3.12) is obtained by using the Green's function technique for boundary value problems. The two solutions of the homogeneous Sasaki-Nakamura equation are $X^H_{lm\omega}$, which satisfies the boundary condition of in-going radiation at the outer horizon, and $X^\infty_{lm\omega}$ which satisfies the boundary condition of out-going radiation at ∞. In the case of corotating circular orbits, the energy and angular momentum fluxes carried by the gravitational waves to infinity are,

$$\begin{aligned} \frac{dE}{dt} &= \sum_{l\geq 2}^{\infty}\sum_{m=-l}^{l}\frac{|Z^H_{lm\omega}|^2}{4\pi\omega_m^2}, \\ \frac{dJ}{dt} &= \sum_{l\geq 2}^{\infty}\sum_{m=-l}^{l}\frac{m|Z^H_{lm\omega}|^2}{4\pi\omega_m^3}, \end{aligned} \tag{3.13}$$

where $\omega_m = m\Omega$, and $Z^H_{lm\omega}$ is a complex number which depends on the orbital frequency Ω. Fig. 3.4 shows the total energy flux dE/dt for selected values of the black-hole dimensionless spin. The contribution of the gravitational-wave modes $l \geq 2$ to the total energy flux at infinity is shown in Fig. 3.4. The enhancement of higher multipoles does not occur either in the case of the Kerr metric, where also the quadrupole contribution is largely predominant. No synchrotron gravitational radiation can occur either in the Schwarzschild or

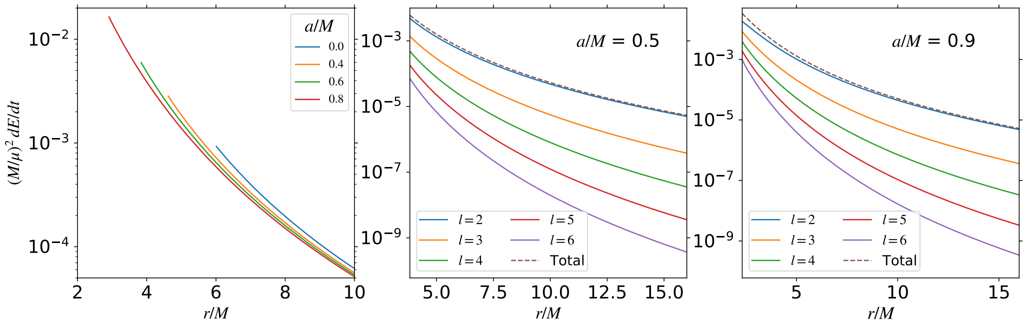

Figure 3.4 Left: comparison of the total gravitational-wave energy flux at infinity, $\dot{E} \equiv dE/dt$, emitted by the test particle in circular orbits around the BH for selected values of the black-hole dimensionless spin, as a function of the dimensionless radial position, r/M. Center and Right: contribution of the gravitational-wave modes $l \geq 2$ to the total gravitational-wave energy flux at infinity in the case of a test particle in circular orbits of radius r around a Kerr BH with $a/M = 0.5$ (center panel) and with $a/M = 0.5$ (right panel). It can be seen that the quadrupole dominates the gravitational-wave emission.

the Kerr case. The contribution of higher multipoles becomes relevant only for near-horizon orbits around nearly extremal BHs (Gralla et al., 2016).

The behaviour of the test particle under the action of GWR reaction can be understood *a la* Landau & Lifshitz by claiming energy and angular momentum conservation. The losses by GWR induce the particle to slowly go from one circular orbit to another. This behaviour can be visualized in terms of the effective potential given by (see fig. 3.5),

$$V_{\rm eff} = 1 - \frac{2M}{r} + \frac{l^2 - a^2(\epsilon^2 - 1)}{r^2} - \frac{2M(l - a\epsilon)^2}{r^3}, \tag{3.14}$$

which leads to a radial equation of motion

$$\epsilon^2 = \left(\frac{dr}{d\tau}\right)^2 + V_{\rm eff}, \tag{3.15}$$

where $\epsilon \equiv E/\mu$ and $l \equiv L/\mu$ are the particle's energy and angular momentum per unit mass, and τ is the proper time. Corotating circular orbits (obtained from the conditions $dr/d\tau = 0$ and $\partial V_{\rm eff}/\partial r = 0$) have energy and orbital angular momentum given by (Ruffini & Wheeler, 1969; Rees et al., 1974),

$$\epsilon = \frac{E}{\mu} = \frac{r^2 - 2Mr + aM^{1/2}r^{1/2}}{r(r^2 - 3Mr + 2aM^{1/2}r^{1/2})^{1/2}}, \tag{3.16}$$

$$\frac{l}{M} = \frac{L}{\mu M} = \frac{r^2 - 2aM^{1/2}r^{1/2} + a^2}{r^{3/4}(r^{3/2} - 3Mr^{1/2} + 2aM^{1/2})^{1/2}}. \tag{3.17}$$

The ISCO is given by the inflection point of the effective potential, i.e. the radius for which $\partial^2 V_{\rm eff}/\partial r^2 = 0$. In the case of $a/M = 0$ (Schwarzschild metric), it is located at $r_{\rm ISCO} = 6M$ and $E_{\rm ISCO}/\mu = 2\sqrt{2}/3$ and $L_{\rm ISCO}/(\mu M) = 2\sqrt{3}$. In the case of an extreme Kerr BH, $a/M = 1$, the ISCO is located very close (but not coincident) to the black-hole horizon,

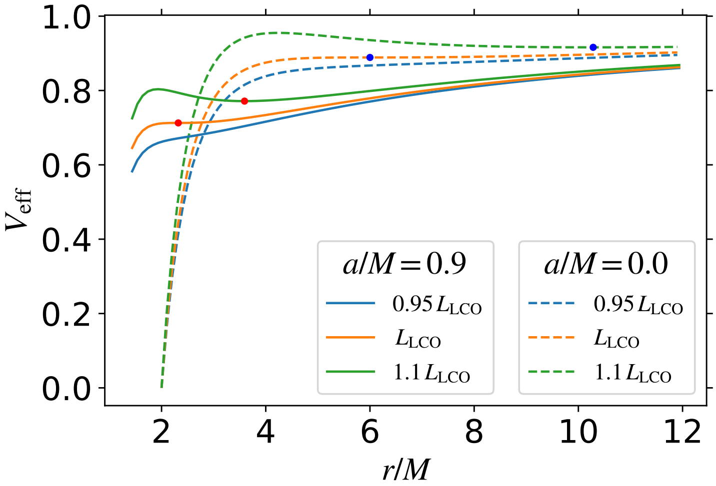

Figure 3.5 $V_{\rm eff}$ for different values of the particle angular momentum in the case of a Schwarzschild BH (dashed curves) and a Kerr BH with $a/M = 0.9$ (solid curves). The blue and red dots indicate the test particle on the minimum of the potential in the Schwarzschild and Kerr cases, respectively.

i.e. $r_{\rm ISCO} \to r_+$ where $r_+ = M$, and $E_{\rm ISCO}/\mu = \sqrt{3}/3$ and $L_{\rm ISCO}/(\mu M) = 2\sqrt{3}/3$. Namely, for an extreme BH there exist circular orbits up to very close to the black-hole horizon (see e.g. ref. (Bardeen et al., 1972) for additional details). From the fig. 3.5 it can be seen that in principle a large amount of energy can be radiated in the Schwarzschild case. In contrast, the Kerr spacetime the flatness effective potential implies lower energy radiation .

3.3 Helicoidal Drifting Sequence

The Hamiltonian formalism was used to analyze the dynamics of a test particle in the field of a Kerr BH, and the trajectory that was found is called helicoidal drifting sequence (HDS). The Hamiltonian of a test particle of mass μ in the field of a Kerr BH of mass M is given by (see e.g. ref. (Jantzen et al., 1992), and references therein)

$$H = -p_t = -N^i p_i + N\sqrt{\mu^2 + \gamma^{ij} p_i p_j}, \tag{3.18}$$

where $N = 1/\sqrt{-g^{00}}$, $N^i = -g^{ti}/g^{tt}$ and $\gamma^{ij} = g^{ij} + N^i N^j/N^2 = g^{ij} - g^{ti} g^{tj}/g^{tt}$, and $g^{\mu\nu}$ are the standard contravariant components of the Kerr spacetime metric in the Boyer-Lindquist coordinates. The latin indexes stand for the spatial Boyer-Lindquist coordinates (r, θ, ϕ). The momenta p_r and p_ϕ are the radial and the angular momentum of the particle, respectively. The Hamilton's canonical equations for a test particle on the equatorial plane $\theta = \pi/2$ under the action of radial and azimuthal dissipative effects are,

$$\frac{dr}{dt} = \frac{\partial H}{\partial p_r}, \quad \frac{d\phi}{dt} \equiv \Omega = \frac{\partial H}{\partial p_\phi}, \quad \frac{dp_r}{dt} = -\frac{\partial H}{\partial r} + \mathcal{F}_r^{\rm nc}, \quad \frac{dp_\phi}{dt} = \mathcal{F}_\phi^{\rm nc}, \tag{3.19}$$

This work only considers the *gravitational-radiation-reaction* part of the non-conservative force (see e.g. ref. (Poisson et al., 2011) for a review on the subject), so the radial and azimuthal are given by the following non-conservative forces, $\mathcal{F}_r^{\rm nc} = 0$, $\mathcal{F}_\phi^{\rm nc} = -dJ/dt$, where J is the angular momentum carried out to infinity by the GW (3.13). This assumption is supported from previous results that show that the linear momentum carried out by the waves to infinity satisfies $dp_r^{\rm GW}/dt \ll |\partial H/\partial r|$ (Fitchett & Detweiler, 1984). In the case of purely quadrupolar waves in strict circular orbits the following equality is satisfied:

$$\frac{dJ}{dt} = \frac{1}{\Omega}\frac{dE}{dt}. \tag{3.20}$$

However, since there is radial drift and a small contribution of higher order multipoles, the above equality must not be strictly satisfied (see eq. 3.13). The numerical computations showed that $|1 - \Omega(dJ/dt)/(dE/dt)| \sim 10^{-6}$ during the evolution. The smallness of this value imply that the motion is indeed quasi-circular, but it is sufficiently large (with respect to the numerical precision of our calculations) to conclude that the equality (3.20) is not verified in the HDS evolution, as expected.

It has been traditional to treat the evolution using the so-called adiabatic approximation that assumes a particle moving from a circular orbit to the next (see, e.g., ref. (Finn & Thorne, 2000; Hughes, 2001)), due to the energy and angular momentum radiation. For example, since the energy can be expressed in terms of r, a change in the energy induces a change in r. Thus, a dynamical equation for r can be found by differentiating (3.16) and equating it to the gravitational energy flux. The evolution is found by integrating this last equation instead of solving the equations of motion (3.19). This approximation, although sufficient to estimate some general properties of the evolution, lacks of the appropriate inclusion of the non-zero radial motion of the particle in the equations of motion. This radial drift becomes essential to trigger the final plunge to the BH. When the radial momentum is properly included, the ISCO location does not represent any longer a point where the equations of motion break down. Indeed, the conditions of "adiabaticity" are kept up to such distances (see figure 3.7 and related discussion in Sec. 3.4). In contrast, within the adiabatic approach it is needed the introduction of a separate treatment of the transition to the plunge phase (see ref. (Finn & Thorne, 2000; Hughes, 2001) and Sec. 3.4 for details).

It is appropriate to mention other treatments in the literature on the problem of a binary system under the action gravitational radiation. The effective-one-body (EOB) approach was proposed in (Buonanno & Damour, 1999) to overcome the known problem of the non-convergence of the higher-order post-Newtonian successive approximations. The EOB treatment "maps" the post-Newtonian binary into a "Schwarzschild deformed metric" which depends on the mass-ratio. In the extreme mass-ratio limit $\mu/M \to 0$, the metric becomes the Schwarzschild one.However, the treatment of the waveform and/or the gravitational-wave fluxes is constructed on a post-Newtonian basis. The Kerr metric, within EOB, has been used to treat *spinning merging components* (Damour, 2001). However, also that EOB treatment is based on a post-Newtonian treatment for the waveforms and/or fluxes. Thus, although they are calibrated to fit strong-field results, the EOB approach remains conditioned by the non-convergence of the post-Newtonian formalism.

The set of equations of motion (3.19) was first used in (Han & Cao, 2011), also using the radiation-reaction term obtained from the numerical solution of the Teukolsky equation. However, they analyze the case of intermediate mass-ratios with the conservative dynamics given by the EOB treatment. There has been also introduced a different method to compute the evolution of the circular orbits that is based on linking one to the next by describing

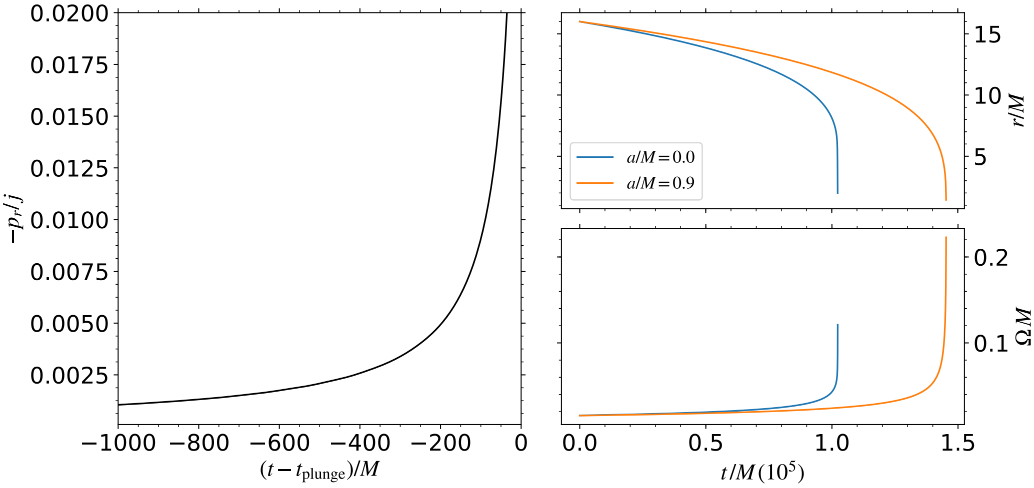

Figure 3.6 On the left, the ratio p_r/j of the radial momentum to the angular momentum per unit mass, of a test particle around a Kerr BH with $a/M = 0.9$, and mass-ratio $\mu/M = 1/100$. The plot shows the ratio from $r \approx 4.53M$ up to the location of the ISCO at $r \approx 2.32M$. The upper and lower panels on the right show the dimensionless radial position, r/M, and dimensionless orbital angular velocity, ΩM, respectively. The initial position at time $t/M = 0$ is $r/M = 15.9$. The case of a Schwarzschild BH is shown in blue while the case of a Kerr BH with $a/M = 0.9$ is shown in orange.

changes in the "constants" of motion (Pound & Poisson, 2008), and finding the envelope. Such reference circular orbits, called "osculating orbits", with a planar force have been applied to the inspiral of a particle in the Schwarzschild (Pound & Poisson, 2008) and in the Kerr spacetime (Gair et al., 2011). Since here is not include the radial velocity in the calculation of the gravitational-wave, namely we use exact circular orbits for the flux, our scheme and the osculating orbits become equivalent under these assumptions. However, we use the fully relativistic gravitational-wave flux instead of post-Newtonian approximations as in (Pound & Poisson, 2008). More recently, a test particle inspiraling into a Kerr BH was treated in the ref. (Taracchini et al., 2014), similarly as done here, but with the drawback of incorporating the GW flux after the ISCO up to the light ring (unstable circular orbits), even though it is given by the Teukolsky equation.

On the other hand, full numerical-relativity simulations are available only for relatively large mass-ratios $\gtrsim 1/10$. Therefore, it is not currently possible to perform a one-to-one comparison between numerical-relativity simulations and the test-particle treatment. However, a comparison of the SXS waveforms with the ones obtained, in the comparable-mass regime (Rodríguez et al., 2018) is presented in next chapter.

3.4 Numerical Results

Equations (3.19) are numerically solved with the suitable initial conditions for quasi-circular orbits on the equatorial plane. At the initial time $t_0 = 0$ the initial distance is r_0, and the initial phase is $\phi(t_0, r_0) = 0$. The angular momentum is $p_\phi(t_0, r_0) = L_0$, where $L_0 \equiv L(r_0)$ is given by eq. (3.17). The initial condition for the radial momentum can be obtained from

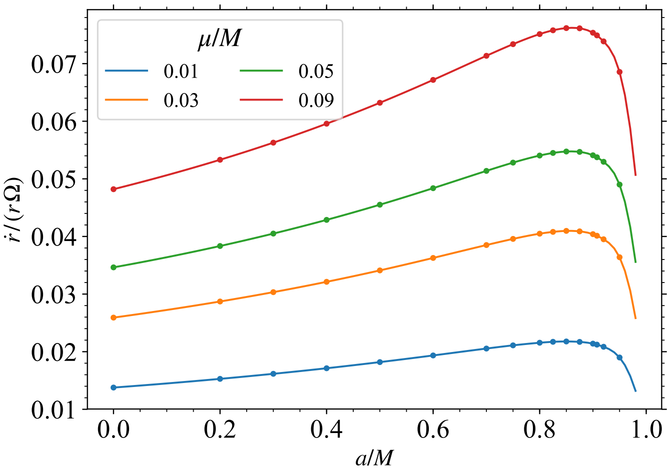

Figure 3.7 Ratio of the orbital to radiation-reaction timescale $T_{\rm orb}/T_{\rm rad} = |\dot{r}|/(r\Omega)$ evaluated at the location of the ISCO, for selected mass-ratios and selected values of the black-hole spin parameter.

the equations of motion as follows. The radiative force induces the radial velocity:

$$\left(\frac{dp_\phi}{dt}\right)\bigg|_{t_0,r_0} = \left(\frac{dp_\phi}{dr}\right)\left(\frac{dr}{dt}\right)\bigg|_{t_0,r_0} = \mathcal{F}^{\rm nc}_\phi\Big|_{r_0}. \tag{3.21}$$

The non-zero radial velocity is related to p_r via eqs. (3.19), and by introducing it into the above expression a non-linear algebraic equation for $p_r|_{r_0}$ is obtained. This equation can be solved numerically given the above conditions and, at leading order, can be solved analytically:

$$p_r\big|_{r_0} = \sqrt{\left(\mu^2 + \frac{r_0^2 L_0^2}{\Lambda_0}\right)\frac{r_0^2\Delta_0}{\Lambda_0}}\,\frac{\Lambda_0\mathcal{F}^{\rm nc}_\phi\big|_{r_0}}{dL/dr_0(r_0^2+a^2)^2}, \tag{3.22}$$

where $\Delta_0 = r_0^2 - 2Mr_0 + a^2$ and $\Lambda_0 = (r_0^2+a^2)^2 - a^2\Delta_0$. This equation gives the initial condition for p_r with very high accuracy and can be safely used provided that the initial radius is sufficiently far from the ISCO. For instance, the initial position $r_0 = 15.9M$, for Kerr BH with spin parameter $a/M = 0.9$ and a mass-ratio $\mu/M = 1/100$, gives an initial p_r accurate within nine digits. This initial radial velocity, if given at a large enough radius r_0, reduces to the "adiabatic" approximation. This can be seen from eqs. (3.21) and (3.13), which imply $dr/dt = -(dJ/dt)/(dp_\phi/dr)$. The property of a strict circular orbit, namely eq. (3.20), is satisfied in the system by one part in a million, therefore the condition $dr/dt = -(1/\Omega)(dE/dt)/(dp_\phi/dr)$ is approximately satisfied with the same accuracy. Now, by replacing Ω via eqs. (3.19), it is obtained $dr/dt = (dE/dt)/(dE/dr)$, which is the flux-balance condition of the adiabatic approximation, adopted e.g. in (Ori & Thorne, 2000).

Figure 3.6 shows the ratio of the radial momentum, p_r, to the angular momentum per unit mass, $j \equiv p_\phi/\mu$, during the HDS obtained for the aforementioned initial conditions. It can be seen how the contribution of the radial momentum increases as the particle approaches the location of the ISCO. In this example, p_r becomes $\sim 4\%$ of the angular momentum per unit mass. It is also shown the sharp decrease (increase) of r (Ω) near the location

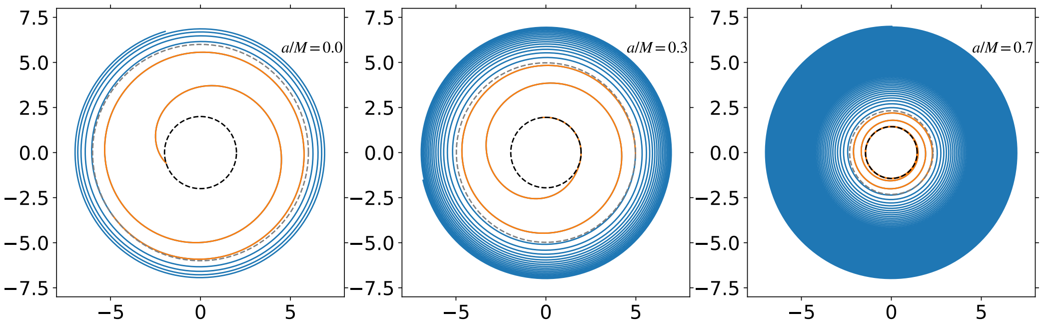

Figure 3.8 Trajectory of a test particle in the HDS around a Schwarzschild BH, $a/M = 0$ (left panel) and around a Kerr BH with $a/M = 0.5$ (center panel) and with $a/M = 0.9$ (right panel). The blue part of the trajectory goes from $r = 7M$ up to the location of the corresponding ISCO (marked with a gray-dashed circle), while the orange color indicates the plunge regime. The black-hole horizon is indicated with a black-dashed circle. The mass-ratio is $\mu/M = 1/100$.

of the ISCO, which suggests that the "adiabaticity" of the system may be loose at such distance. The system can be considered to evolve adiabatically if the ratio of orbital to radiation-reaction timescale is much smaller than unity. Following (Cutler et al., 1994), $T_{\rm orb}/T_{\rm rad}$ is defined in terms of the tangential and radial velocity, $T_{\rm orb}/T_{\rm rad} \equiv |\dot{r}|/(r\Omega)$. Since this ratio increases for decreasing values of r, it reaches its largest value during the HDS at the location of the ISCO. Figure 3.7 shows the above ratio evaluated at the location of the ISCO, for selected values of μ/M and black-hole spin parameters. It can be seen that for the current example with $a/M = 0.9$, the timescales ratio $T_{\rm orb}/T_{\rm rad} \sim 0.02$ at $r_{\rm ISCO}/M = 2.32$. Finally, figure 3.8 shows the trajectory of the test particle in the HDS around a Schwarzschild BH, $a/M = 0$ (left panel) and around a Kerr BH with $a/M = 0.5$ (center panel) and with $a/M = 0.9$ (right panel). It can be seen the effect of the black-hole spin in the particle trajectory. The bigger a/M the more the particle rotates before reaching the ISCO.

3.5 Plunge into the Black Hole

A physical insight of the plunge into the BH can be obtained from the radial effective potential (3.14). Figure 3.5 compares $V_{\rm eff}$ with $a/M = 0$ (Schwarzschild) and with $a/M = 0.9$, for three selected values of the orbital angular momentum of the particle, L: one larger, one equal, and one smaller than the value at the ISCO, $L_{\rm ISCO}$. For $L > L_{\rm ISCO}$, a small decrease in L due to the gravitational radiation makes the particle to go from one minimum to the next one, namely it goes from one circular orbit to another with smaller radius. At $L = L_{\rm ISCO}$ the particle reaches the ISCO and, for $L < L_{\rm ISCO}$, the effective potential has no minima, i.e. no circular orbits exist and the particle fall into the BH.

In the realistic situation, the full numerical integration of the equations of motion shows that, indeed, when the particle passes the location of the ISCO, it possesses a large radial momentum (see figure 3.6) and angular momentum $L < L_{\rm ISCO}$, so it continues falling towards the BH, smoothly, without any further radiation loss. Figure 3.5 shows that the

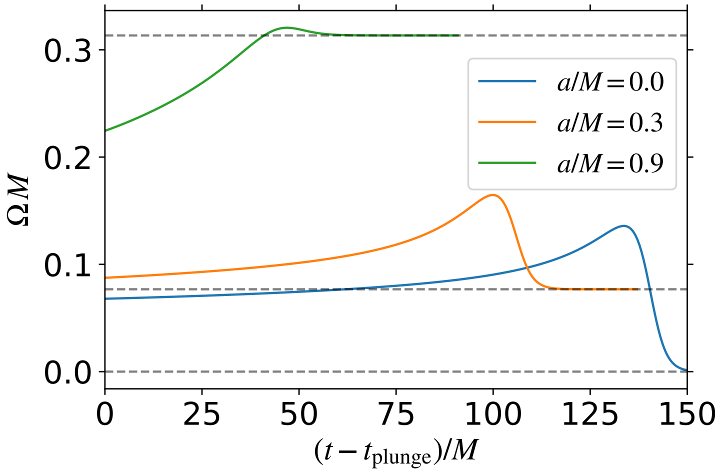

Figure 3.9 Angular velocity of the particle, $\Omega = d\phi/dt$ after the crossing of the ISCO, in the case of Kerr with $a/M = 0.9$ (green), $a/M = 0.3$ (orange) and in the case of Schwarzschild (blue). The mass-ratio is $\mu/M = 1/100$. The gray-dashed horizontal lines show the corresponding values of the angular velocity of the black-hole horizon.

plunge to the BH is markedly different in the Schwarzschild and Kerr cases. While the effective potential for $L = L_{\rm ISCO}$ is zero at the horizon in Schwarzschild, it reaches a finite non-zero value for Kerr. The flatness of the effective potential from the ISCO to the horizon, in the Kerr case, implies a very little amount of energy and angular momentum radiated out to infinity during the final plunge. This can be also understood from the fact that, due to frame-dragging effect, the particle is forced to approach the Kerr black-hole horizon tidally locked, hence it approaches the BH with non-zero angular momentum. These features were confirmed by the numerical integration done here (see figure 3.9).

Since the plunge is (nearly) geodesic we integrate the equations of motion during this part of the evolution without energy and momentum losses. It is worthwhile to emphasize that there is an uncertainty in the definition of the end of the inspiral phase. It was defined as the time when the particle, following the HDS, reaches the ISCO, but it could have been defined, for instance, as the time when the particle angular velocity reaches the corresponding value of the ISCO (see e.g. (Buonanno & Damour, 2000)). Despite the fact that these two times do not generally coincide, in both cases a region around the adiabatic time of the ISCO is created (see figure 3.11). Within this region, extending out and in the adiabatic time of the ISCO, the particle radiates following the radiation law of circular orbits (3.13). This region connects the inspiral (quasi-circular orbits) regime to the plunge (geodesic) regime where the gravitational radiation is negligible. It is also important to mention that in order to approach the horizon, the momentum p_{r^*}, conjugate to the tortoise radial coordinate r^* defined by $dr^*/dr = (r^2 + a^2)/(r^2 - 2Mr + a^2)$, was used in the numerical integration. Figure 3.5 shows the full evolution of the test particle until it reaches the black-hole horizon, for three selected cases: $a/M = 0, 0.5, 0.9$. The fact that the particle corotates and approaches tidally locked to the BH is shown in the figure 3.9. The angular velocity of the black-hole horizon is given by $\Omega_+ = a/(r_+^2 + a^2)$ (Ruffini, 1973b), where $r_+ = M + \sqrt{M^2 - a^2}$ is the BH outer horizon radius. The evolution of the energy, the radial and angular momentum of the particle during this phase is shown in figure 3.10. It can be seen that both the energy and the angular momentum are conserved, and that the difference in the effective potential between the ISCO and outer the horizon (see figure 3.5) is fully converted into the particle's in-falling kinetic energy. It can see that for non-zero BH rotation, in agreement with the effective potential shown in figure 3.9, the difference is smaller. Consequently, the particle approaches the horizon with lower radial velocity than in the Schwarzschild case where it tends to the speed of light.

The above results are now contrasted with the different treatments in the literature, in particular with the approach found in (Ori & Thorne, 2000), which will be referred as Ori-Thorne (OT). In this last treatment, approximate equations of motion and their corresponding semi-analytic solutions for "the transition to plunge" regime were derived. The approximation basically consists in a Taylor expansion of the energy and the angular momentum around the ISCO values, which is equivalent to the use of an approximate effective potential. Both the angular velocity and the energy radiated in GW, are assumed to be equal to their values around the ISCO. The boundary conditions are set by imposing that the solution matches the adiabatic motion before the ISCO, and after a fully geodesic (i.e. non-radiative) plunge. From these results, semi-analytic formulas were obtained for the particle's energy and angular-momentum in the "transition" regime, E_f and L_f, which are expressed as "deficits" with respect to the ISCO values,

$$\Delta E \equiv E_f - E_{\text{ISCO}}, \qquad \Delta L \equiv L_f - L_{\text{ISCO}}. \tag{3.23}$$

Although this work agrees with general qualitative picture of OT, it can be checked from the eq. (3.26) and table I found in the mentioned work, that the "deficits" are much larger than the ones obtained here by the full numerical integration.

A first contrast of the two approaches, for the case of a BH with spin parameter $a/M = 0.9$, is shown in figure 3.11, where it is compared the particle's radial trajectory near the location of the ISCO. It can be seen that the two solutions converge at a large distance from the BH. This indicates, as mentioned in section 3.4, that these two solutions satisfy the same initial condition set by the adiabatic approximation. In addition, figure 3.12 shows the comparison, for the same case, of the energy and the angular momentum "deficits", ΔE and ΔL, obtained from the present approach, i.e. by adopting $E_f \equiv H(t_{\text{plunge}})$ and $L_f = p_\phi(t_{\text{plunge}})$, with OT. The above result implies a larger amount of gravitational radiation in the last approach. The main reason for this additional emission is the OT assumption of keeping the particle radiating at the rate of the ISCO (which is the highest one of all circular orbits; see figure 3.4), before and long after crossing it ($T > 1$ in figure 3.11). This work found that the extrapolation of such an approximation much beyond the ISCO is the cause of the larger discrepancy in the results. It is clear that this extra radiation is needed under the assumption of strict circular orbits. This is due to the fact that in the absence of such a radiation, there is no reason for the particle to plunge into the BH given that the ISCO is stable. When the radial drift is considered, as in the HDS, there is an increasing contribution of the radial momentum (see figures 3.6 and 3.10) that modifies the effective potential. In this context the ISCO does not play any special role and only assists the passing of the particle in virtue of the previously acquired radial momentum. As a consequence, it is expected that in the HDS the test particle smoothly falls into the Kerr BH with negligible GW emission. The only radiation comes from the non-circular plunge trajectory followed by the particle (e.g. the orange-color trajectories in figure 3.8) which must be much smaller than the gravitational radiation per orbit at the ISCO. This explains

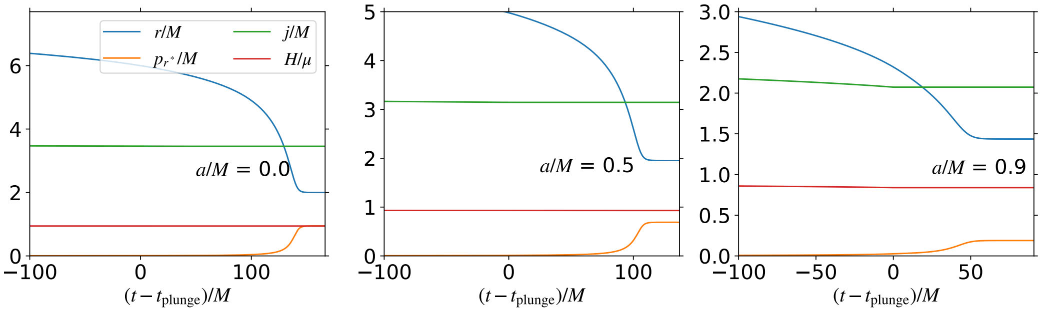

Figure 3.10 Physical properties of a test particle in the final plunging into a Schwarzschild BH, $a/M = 0$ (left panel), into a Kerr BH with $a/M = 0.5$ (center panel) and with $a/M = 0.9$ (right panel). The mass-ratio is $\mu/M = 1/100$. We show the particle radial position, r/M (blue), dimensionless angular momentum, j/M (green), dimensionless radial momentum, p_{r*} (orange), and the dimensionless energy, H/μ (red).

the additional GW radiation obtained in OT with respect results found here.

This discrepancy causes differences in the estimation of the mass of the final BH. The latter can be expressed as $M_f = M + \Delta E_{\text{rad}}$, where $\Delta E_{\text{rad}} \equiv E_f - \mu < 0$, M is the total mass of the black-hole binary and E_f is the final energy of the test particle. Thus, one can write the energy radiated as,

$$\Delta E_{\text{rad}} = \Delta E_{\text{ad}} + \Delta E, \tag{3.24}$$

where $\Delta E_{\text{ad}} \equiv E_{\text{ISCO}} - \mu$ is the energy radiated up to the location of the ISCO within the adiabatic strict circular motion approximation, and ΔE is the energy "deficit" with respect to the approximation defined in Eq. (3.23). It can be checked that, for the case of an equal-mass binary, the contribution of ΔE to M_f (in the $a/M = 0.9$ case) is about 10%, while in the HDS case it is only about 1% (see figure 3.12). This additional amount of gravitational radiation in OT will lead to a more energetic gravitational waveform in the final merging phase. It is interesting that a similarly energetic plunge leading to a burst of radiation, is present in the numerical-relativity waveforms of the SXS Catalog. Such a feature is also found in the binary mergers modeled via the EOB formalism which adopts a treatment similar to the one of OT (see ref. (Buonanno & Damour, 2000) for details).

Now, the dependence of the radiated energy and angular momentum on the mass-ratio, μ/M is studied. For a given a black-hole spin, the semi-analytic treatment of OT predicts that the above-defined energy and angular momentum "deficits" scale with the mass-ratio as $|\Delta E|_{\text{OT}}/\mu \propto (\mu/M)^{4/5}$ and $|\Delta L|_{\text{OT}}/(\mu M) \propto (\mu/M)^{4/5}$. The following empirical laws were found from the present results, $\Delta E_{\text{HDS}}/\mu \propto (\mu/M)^{0.72}$ and $\Delta L_{\text{HDS}}/(\mu M) \propto (\mu/M)^{0.81}$. The different scaling with the mass-ratio of the radiated energy and angular momentum, within the HDS treatment, implies that the ratio $\Delta E/\Delta L$ depends on the mass-ratio. This is consistent with the fact that the particle in the HDS case does not follow strict circular orbits, as in the case of OT. For strict circular orbits, the energy to angular momentum ratio gives, at any radius, the value of the particle's angular velocity which depends only on the black-hole spin. Figure 3.12 shows explicitly these differences. It is also interesting to compare the energy radiated predicted by the above models with the one found in numerical-relativity simulations. The working hypothesis that the test parti-

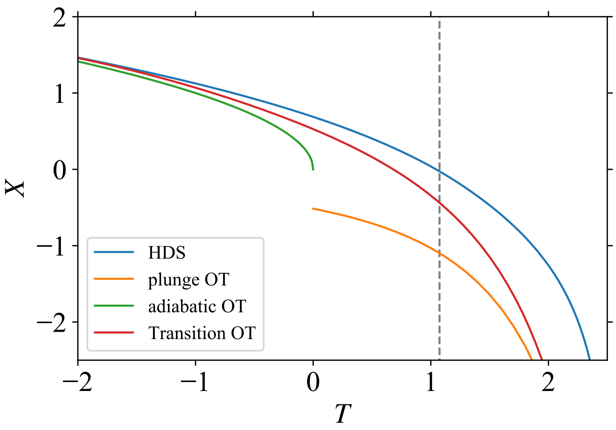

Figure 3.11 Comparison for the case $a/M = 0.9$, during the transition regime of our treatment and the one of ref. (Ori & Thorne, 2000). The variable X is the normalized difference between the particle's radial position and the ISCO. The variable T is the normalized proper time with $T = 0$ at $r = r_{\rm ISCO}$ in the strict adiabatic sequence. The details on the normalization can be found in (Ori & Thorne, 2000). It can be seen that near the ISCO, i.e. around $X = 0$ and for $T < 0$, the two trajectories are similar, but for $T > 0$ they become separated. This is consistent with the expansion of the effective potential around the ISCO which is expected to be valid only near $X = T = 0$. The vertical dashed line corresponds to $t_{\rm plunge}$ in our present HDS approach, $T \approx 1$.

cle treatment might be a good approximation of the real two-body system of comparable masses is applied here, in view of the agreement in the waveforms that will be presented in the next chapter. First, from the data available in the SXS Catalog, the corresponding energy "deficit" $\Delta E/\mu$, for different mass-ratios μ/M is calculated. The procedure is done following eq. (3.24), i.e. the value of $\Delta E_{\rm ad}$, which depends only on the BH spin, is subtracted from the difference between the mass of the final Kerr BH and the initial total mass, $M - M_f$. Figure 3.12 shows the results for $\mu/M = 0.08$–0.25. It can be seen that the value of $\Delta E/\mu$ obtained from the numerical-relativity data scales linearly with μ/M. In other words, simulations follow exactly the same scaling of the energy radiated in the case of a purely radial plunge of a test particle into a Schwarzschild BH, i.e. $\Delta E/\mu \propto \mu/M$ (Davis et al., 1971), and not the one expected from the particle plunge derived either in (Ori & Thorne, 2000) or in the present work.

3.6 Conclusions

Two different cases of gravitational radiation, in the strong-field limit, from test particles falling into an already formed BH have been considered. The first is a test particle plunging from infinity either initially at rest or with finite kinetic energy. It leads to a gravitational waves emission composed of three different parts: "*a precursor, a main burst and a ringing tail*". The amplitude of the burst depends on the angular momentum of the particle and of the BH. The comparison between a Schwarzschild and a Kerr BH shows quantitative but not qualitative differences. The structure of the multipoles can be in used principle to determine

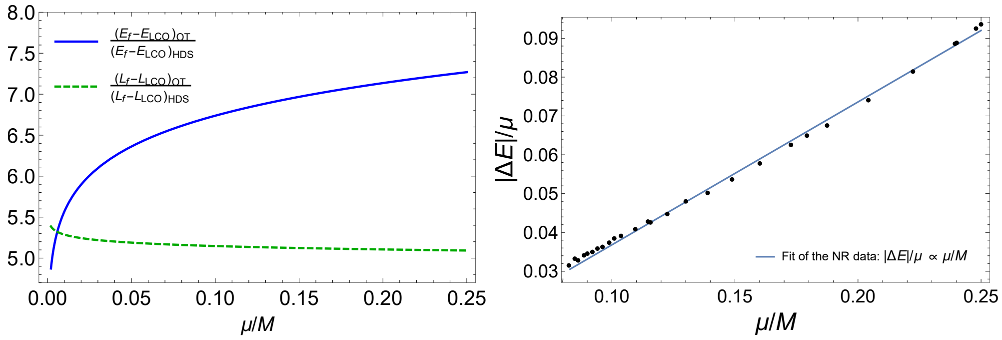

Figure 3.12 Left: comparison for the case $a/M = 0.9$, of the quantities $E_f - E_{\rm ISCO}$ and $L_f - L_{\rm ISCO}$ obtained from our HDS, and the semi-analytic formulas of ref. (Ori & Thorne, 2000). Right: energy "deficit" $\Delta E/\mu$ estimated from the numerical-relativity simulations of the SXS Catalog. It is surprising that it scales in the same way as the energy radiated in a purely radial plunge into a Schwarzschild BH (Davis et al., 1971).

the angular momentum of both the particle and the BH. The second case, a particle starting from a finite radius in a circular orbit, leads to the HDS, smoothly merging into the BH. The difference between the Schwarzschild and the Kerr metric is specially manifest at and after the ISCO. When the radiation reaction is taken into account (see figure 3.8) there is an increasing contribution of the radial momentum in the HDS as the particle approaches the horizon (see Figs. 3.6 and 3.10). This phenomenon is further enhanced by the different effective potential of the Schwarzschild and Kerr cases. The final phase is the one of a test particle smoothly merging in the Kerr BH without any burst. The results were compared and contrasted with the approach of ref. (Ori & Thorne, 2000) and it was found that in the latter a larger amount of gravitational radiation is emitted in the transition to the plunge. The consequences of such a difference in the estimation of the mass of the final BH formed in the merger were calculated.

It was shown how the energy and the angular momentum radiated scale with the mass-ratio, μ/M, and it was shown the difference of the scaling with the results of ref. (Ori & Thorne, 2000). Stimulated by the agreement of the HDS and numerical-relativity waveforms in the comparable mass regime (see next chapter), a comparison of the energy radiated and its scaling with the mass-ratio between the two formalism was done. It was found that $\Delta E/\mu$ scales linearly with μ/M in the numerical-relativity simulations, following exactly the scaling of a purely radial plunge of a test particle into a Schwarzschild BH (Davis et al., 1971), but not the scaling predicted in (Ori & Thorne, 2000) nor the one of the HDS treatment presented here. On the other hand the work of Anninos et al. (1995) showed great agreement between test particle scaling law with μ/M, for head-on BH collisions, if the mass of the particle is replaced by the reduced mass (Newtonian-center-of-mass view). It seems that the final plunge in the coalescence of BHs needs further investigation of the underlying physics. Finally, ref. (Liu et al., 2018) showed a feature in the final burst of the event GW150914 Abbott et al. (2016b) and points to the existence of an even more energetic burst which is absent in the templates used for parameter estimation of the source.

Chapter 4

Test Particle Waveforms

This chapter is based on the publication (Rodríguez et al., 2018). The determination of the trajectory of a test particle around a Kerr BH allows the explicit construction of the corresponding waveform. This chapter attempts to understand the underlying physics of the templates publicly available from numerical-relativity simulations (see SXS Catalog for details). The following three assumptions are adopted only as working hypothesis[1], which are not necessarily considered as valid:

1. The trajectory of a test particle is calculated following the work presented in the previous chapter.
2. In order to step from a test particle of mass m to a binary BH of comparable masses m_1 and m_2, the Newtonian center of mass description is adopted by assuming $m = \mu$, where $\mu = m_1 m_2/M$ is the reduced mass of the binary and $M = m_1 + m_2$ is the total mass.
3. The waveform of the HDS all the way up to the passage over the last circular orbit. As shown in previous chapter, it is not expect any significant gravitational-wave emission during the final smooth merging of the particle into the Kerr BH. This final part of the waveform needs further development and analysis.

4.1 General Considerations of the Reduced Mass

It is clear from the Newtonian center of mass approach that the dimensionless spin parameter, a/M, where $a = J/M = \mu\sqrt{r/M}$ is the orbital angular momentum per unit mass and r is the separation radius, is typically much larger than unity in any self-gravitating binary system of comparable masses. For equal masses, it converges from above, namely from $a/M > 1$, to $a/M = 1$ only when $r = 16M$. This implies that only massive neutron stars or BHs can reach BH formation in their final merger process. Most important, the condition of $a/M = 1$ under these conditions can only by reach from above, i.e. from

---

[1] This can be also motivated by the agreement between BH head-on collisions and the radially in-fall of a test particle (Anninos et al., 1995)

$a/M > 1$, and not by accretion. This gives a tangible way to see implemented, by emission of gravitational waves, the no-hair theorem (see e.g. Ruffini & Wheeler, 1971, fig. 1).

By hypothesis, the GW emission is computed by changing in the equations of motion the mass of the test particle by the reduced mass, and the BH mass by the total mass. The GW radiation-reaction, after performing the same change, is included in the equations of motion. The dynamical evolution of the system is calculated obtaining the HDS of orbits all the way up to the final smooth merger. The background turned out to be always the Kerr metric. This result, following similar attempts in the literature, is regarded as an *effective* one body scheme to describe the merger of two BHs of comparable mass.

4.2 Waveform

During the initial phases of the HDS of the particle, the motion is quasi-circular, i.e. the radial velocity is relatively small with respect to the tangential velocity. Thus, the gravitational waveform can be, in first approximation, constructed from circular-orbit waves. The GW can be obtained from the scalar ψ_4 (see e.g. Detweiler (1978) or appendix D),

$$\frac{1}{2}(h_+ - ih_\times) = -\frac{1}{R}\sum_{l,m}\frac{Z^H_{lm}}{\omega_m^2}{}_{-2}S_{lm}(\Theta)e^{im\Phi}e^{-i\omega_m(t-R^*)}, \tag{4.1}$$

where R is the distance from the Kerr BH to the observer, Θ is the angle between the axis of rotation and the observer, Φ is the azimuthal coordinate of the orbiting body at $t = 0$; R^* is the Kerr "tortoise" coordinate, and ${}_{-2}S_{lm}$ are the spheroidal harmonics of spin -2 Teukolsky (1973). The complex numbers $Z^H_{lm\omega}$ that depend on $\omega_m = m\omega$, where ω is the orbital angular velocity, where computed in Rodriguez et al. (2017) to estimate the gravitational-wave radiation flux, dE/dt, for a particle moving in a circular orbit on the Kerr metric. This radiation has been computed in the Teukolsky formalism of curvature perturbations (Teukolsky, 1973; Teukolsky & Press, 1974) with the aid of the Sasaki-Nakamura radial equation (Sasaki & Nakamura, 1982b,a).

As the HDS of orbits progresses, the wave frequency changes with time and we evaluate the acquisition of radial momentum. This implies that the complex number $Z_{lm\omega}$ evolves with time, inducing a variable wave amplitude and phase shift. We also replace $\omega_m(t - R^*)$ in the exponential by $m\phi(t - R^*)$ (see, e.g., Hughes (2001)), where ϕ is the azimuthal (Boyer-Linquist) coordinate of the test particle along the trajectory. As usual the waveform is decomposed into the spin-weighted spherical harmonics ${}_sY_{lm}(\theta, \phi)$ as follows (Newman & Penrose, 1966):

$$R(h_+ - ih_\times) = \sum_{l,m} h_{lm}(t - R^*){}_{-2}Y_{lm}(\Theta, \Phi), \tag{4.2}$$

where

$$h_{lm} = -2\frac{Q_{lm}}{\omega_m^2}e^{-im\phi(t-R^*)}, \quad Q_{lm} = \int d(\cos\Theta)\sum_{l',m'} Z^H_{l'm\omega}{}_{-2}S_{l'm'\omega}(\Theta){}_{-2}Y_{lm}(\Theta, 0). \tag{4.3}$$

Near the last circular orbit the radial momentum significantly grows (see fig. 3.6). The radial motion effects are only included implicitly through the orbital phase ϕ obtained from the numerical integration of eqs. (3.19) which include the effects of both radial drift and radiation-reaction.

4.3 Comparison of the Waveforms

In order to do the comparison of the treatments, the HDS was started at some large distance r_0 at time $t = 0$ the evolution was computed up to the passage over the last circular orbit, at time $t = t_{\text{plunge}}$. The waveform was found by using the method described in the above section. Since the values of the initial time and phase of the two simulations are arbitrary, a constant change of time and phase is performed which minimizes the overall differences between the two waveforms. Furthermore, given that the comparison is done at infinity, the two waveforms are expressed as a function of the same time coordinate.

The fitting-factor F was found to quantify the difference between the waveforms,

$$F \equiv (h_1|h_2)/\sqrt{(h_1|h_1)(h_2|h_2)}, \quad (h_1|h_2) \equiv 4\mathfrak{Re}\left[\int_0^\infty h_1(f)\tilde{h}_2(f)/S_n(f)df\right], \tag{4.4}$$

where f is the GW frequency in the detector's frame, $\tilde{h}_i(f)$ is the Fourier transform of the waveform $h_i(t)$ and $S_n(f)$ is the power-spectrum density of the detector's noise. The latter is the Advanced LIGO noise (see, e.g., Abbott et al. (2016b)). The mismatch, $\mathcal{M} \equiv 1 - F$, was obtained from the fitting-factor. Since the function $S_n(f)$ is given in physical units (Hertz) then a value for the total mass of the system has to be specified to calculate the fitting factor. For all the examples shown below the $M = 70\ M_\odot$ was used.

Another way to quantify the difference between two waveforms is by the *intrinsic* time-domain phase evolution $Q_\omega = \omega^2/\dot{\omega}$, where $\omega = d\phi/dt$ and ϕ is the gravitational-wave phase. *The small correction in the phase* from the term Q_{lm} in Eq. (4.3) was not taken into account in order to avoid the noise arising from the interpolation of the radiation flux. The calculation of Q_ω was done as stated in ref. (Damour et al., 2013), although some difficulties were reported there due to the inherent oscillations present in the numerical-relativity data. However, here is not performed any fit of the numerical-relativity Q_ω function.

4.3.1 Merging Black Holes of Equal Mass and Equal Aligned Spins

The comparison was done first in the equal mass and aligned spins regime. The first numerical-relativity simulation was `BBH:0230` (SXS Catalog, 2018; Chu et al., 2016): the coalescence of two BHs with $m_1 = m_2 = M/2$ and dimensionless spin parameters $a_1/m_1 = a_2/m_2 = 0.8$, forming a Kerr BH with dimensionless spin parameter $a_f/M_f = 0.907516$. This system is particularly interesting since it is characterized by equal-mass and high-spin components, properties which are in principle different from the non-spinning, test particle domain adopted here. No agreement between the two treatments should be a priori expected.

Fig. 4.1 shows the comparison between the two waveforms. A "test particle" of mass $m =$

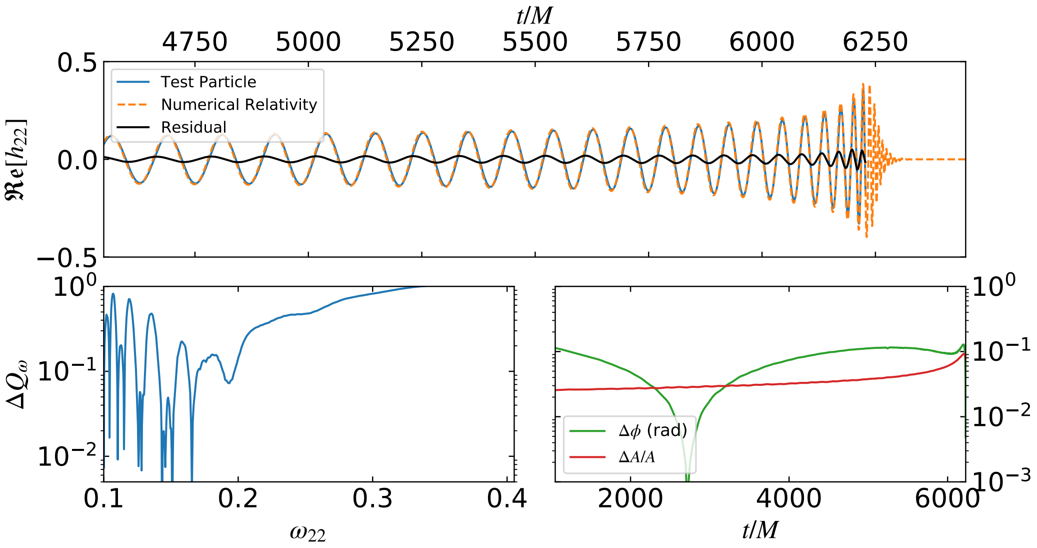

Figure 4.1 First comparison of the HDS and the numerical-relativity waveforms. Top panel: the dashed orange curve is the numerical-relativity waveform `BBH:0230` of the coalescence of a binary BH with $m_1 = m_2$ and $a_1/m_1 = a_2/m_2 = 0.8$, forming a Kerr BH with spin parameter $a_f/M_f = 0.907516$. The continuous blue curve is the test-particle waveform during the HDS adopting $m = M/4$ and a dimensionless spin of the Kerr BH nearly equal to the one of the newly-formed Kerr BH of the merger simulation, 0.9075. The time is normalized to the total binary mass, M, and the comparison is made up to the instant of passage of the test particle at the location of the last stable circular orbit. Left lower panel: intrinsic time-domain phase difference evolution ΔQ_ω as a function of the frequency of the $l = m = 2$ gravitational-wave mode, ω_{22} Right lower panel: phase difference $\Delta\phi$ (in radians; green curve) and relative difference of the amplitudes of the two waveforms shown in the top panel during the entire time of the comparison.

$\mu = m_1 m_2/M = M/4$ was used, and a Kerr BH of mass M with spin parameter nearly equal to the BH formed in the merger, i.e. $a/M = 0.9075$, was chosen. For completeness of the comparison is shown, for this time interval, the difference between the GW phases, $\Delta\phi$ (green curve), and the relative difference between the waveform amplitudes, $\Delta A/A$ (red curve). A value $F \approx 0.993$ was obtained, so there is a mismatch $\mathcal{M} = 0.007$, during the entire time interval of the comparison, i.e. $t/M \approx 1702.03$–6182.19, corresponding to an interval of separation distances $r/M = 14.95$–2.27, where the latter is the location of the last circular orbit. It can be seen that, regardless of the Q_ω oscillations for the numerical-relativity data, $\Delta Q_\omega = |Q_\omega^{\rm TP} - Q_\omega^{\rm NR}| \lessapprox 1$. This specific simulation constitutes the best agreement between the numerical-relativity simulations and the HDS treatment among the cases we have studied.

Next, in Fig. 4.2 is shown the comparison with the numerical-relativity simulation `BBH:0228` of the merger of two BHs with aligned spins $a_1/m_1 = a_2/m_2 = 0.6$ that forms a BH with spin $a_f/M_f = 0.857813$ (SXS Catalog, 2018; Chu et al., 2016). It was found here a new feature with respect to the previous comparison: the best matching waveform did not correspond to the one generated by the HDS in a Kerr BH with (nearly) the same spin of the newly-formed BH. Instead, the agreement was obtained for the HDS in a Kerr BH with an

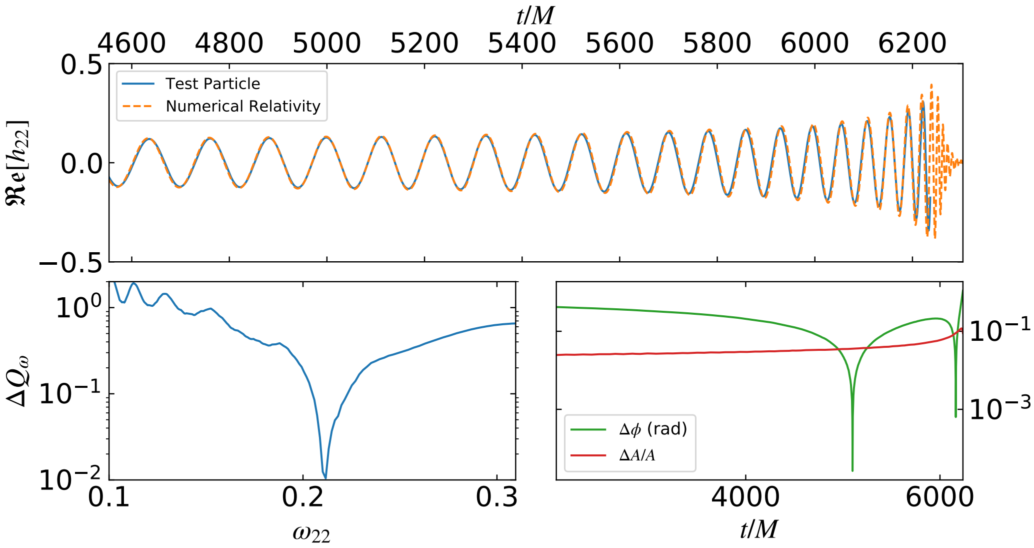

Figure 4.2 Comparison of the HDS and the numerical-relativity waveforms. Top panel: The dashed orange curve is the numerical-relativity waveform `BBH:0228` SXS Catalog (2018); Chu et al. (2016) of the coalescence of a binary black-hole with $m_1 = m_2$ and $a_1/m_1 = a_2/m_2 = 0.6$, forming a Kerr BH with spin parameter $a_f/M_f = 0.857813$. The continuous blue curve is the test-particle waveform during the HDS adopting $m = M/4$ and a dimensionless spin of the Kerr BH $a_{\rm eff}/M = 0.8$. We use for the HDS the same mass-ratio of the numerical-relativity simulation. Left lower panel: intrinsic time-domain phase difference evolution $\Delta Q_\omega = |Q_\omega^{\rm TP} - Q_\omega^{\rm NR}|$ as a function of the frequency of the $l = m = 2$ gravitational-wave mode, ω_{22}. Right lower panel: phase difference $\Delta\phi$ (in radians; green curve) and relative difference of the amplitudes of the two waveforms.

"effective" spin parameter $a_{\rm eff}/M = 0.8$. The fitting factor for this case is $F = 0.972$, which is between the final spin and the initial spins parameters.

The above result hinted to the existence of an effective spin parameter which produces good matching with the numerical-relativity. Thus, more comparisons were performed with other waveforms of the SXS catalog to confirm this conjecture. The results are presented in Fig. 4.3 and Table 4.1. As a conclusion, when the HDS treatment has the same mass ratio as the one of the numerical-relativity simulation, it can always be found an effective spin of the Kerr BH of the HDS which produces excellent agreement between the waveforms. It can be also seen from ΔQ_ω that, regardless of the oscillations inherent in the numerical-relativity simulations, the two phase evolutions agree each other. Nevertheless, the agreement between the two waveforms decreases in some part of the evolution, suggesting that the effective spin $a_{\rm eff}$ might change with time.

4.3.2 Merging Black Holes with Unequal Mass and Spinless

Coalescence of spinless BHs were analyzed with different mass ratios, $q = m_2/m_1 = 1, 1/2, 1/3, 1/4, m_1 \geq m_2$ (see Fig. 4.4). The effective spin varies proportionally with the binary mass ratio. This also shows that, although the BHs do not spin, there is some spin on

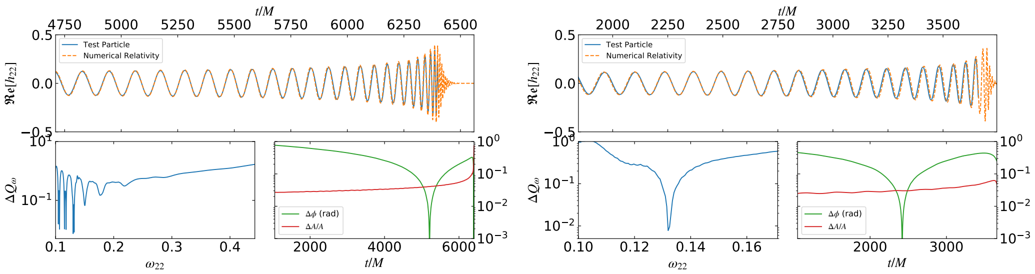

Figure 4.3 Comparison of numerical-relativity waveform and HDS waveforms. Left panel: `BBH:0157`, coalescence of a binary black-hole with $m_1 = m_2$ and $a_1/m_1 = a_2/m_2 = 0.949586$, forming a Kerr BH with spin parameter $a_f/M_f = 0.940851$ SXS Catalog (2018); Hemberger et al. (2013). For the HDS treatment we find an effective spin parameter $a_{\rm eff}/M_f = 0.99$. Right panel: `BBH:0001`, coalescence of a binary black-hole with $m_1 = m_2$ and $a_1/m_1 = a_2/m_2 = 1.2 \times 10^{-7}$ (i.e. spinless case), forming a Kerr BH with spin parameter $a_f/M_f = 0.686461$ SXS Catalog (2018); Mroue et al. (2013). For the HDS treatment we find an effective spin parameter $a_{\rm eff}/M = 0.36$. Again, we found that the effective spin parameter of the Kerr BH in the HDS treatment is neither the one of the newly-formed BH nor the one of the merging BHs of the numerical-relativity simulation.

Table 4.1 Column 1: Code of the numerical-relativity simulation of the SXS Catalog (2018). Column 2: Spin parameter of the merging BHs, a_i/m_i. Column 3: Spin parameter of the newly-formed BH, a_f/m_f. Column 4: Effective spin $a_{\rm eff}/M_f$ of the Kerr BH in the HDS treatment that gives good agreement with the numerical-relativity simulation. Column 5: Fitting factor between the numerical-relativity and HDS waveforms. All the simulations are for equal-mass binaries.

Simulation	a_i/m_i	a_f/M_f	$a_{\rm eff}/M_f$	F
`BBH:0001`	1.209309×10^{-7}	0.686461	0.36	0.96
`BBH:0157`	0.949586	0.940851	0.99	0.93
`BBH:0228`	0.600000	0.857813	0.80	0.972
`BBH:0230`	0.800000	0.907516	0.9075	0.993

the background spacetime even before the formation of the final spinning BH. The effective spin turned out to be always less than the spin of the newly formed BH.

The formation of the Kerr BH from binaries of BHs of comparable masses occurs from above, namely from $a/M > 1$ at larger distances to $a/M \lesssim 1$ as the objects approach each other. Only in the case of binaries with extreme mass-ratios $\mu/M \ll 1$, the merger leads to a slowly-rotating BH, and, only when $\mu/M \to 0$, the formation of a Schwarzschild BH can be approached. This is consistent with our results above of an effective spin of the BH proportional to the mass ratio, so that we expect a vanishing spin, i.e. a Schwarzschild BH, only in the limiting case of a vanishing mass ratio.

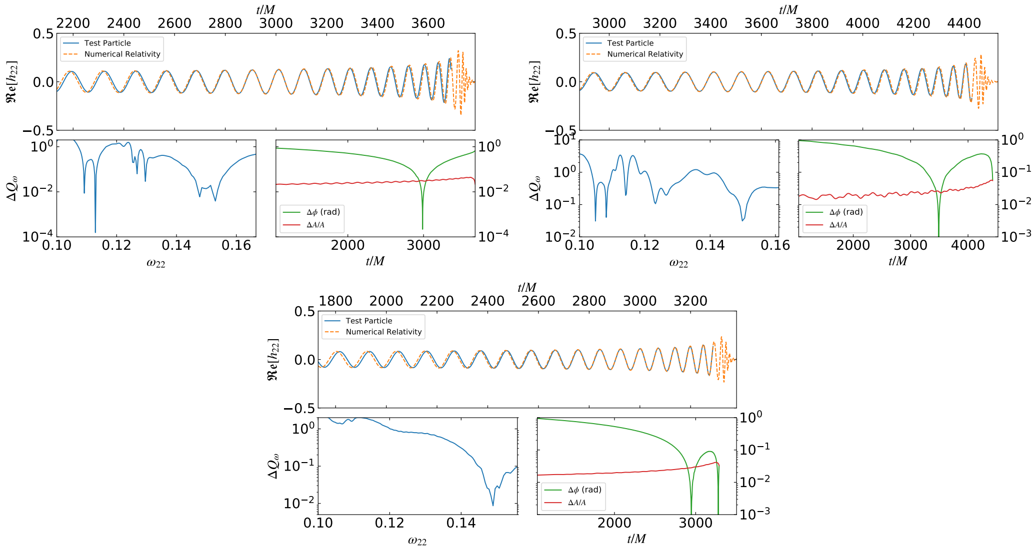

Figure 4.4 Comparison of three numerical-relativity simulations of spinless merging binary BHs with the current HDS approach. Top left panel: `BBH:0169` numerical-relativity waveform of mass ratio $q = 1/2$ SXS Catalog (2018); Buchman et al. (2012). The effective spin for this case is $a_{\text{eff}}/M_f = 0.33$ and the fitting factor between the two waveforms is $F = 0.95$. Top right panel: `BBH:0030` numerical-relativity waveform of mass ratio $q = 1/3$ SXS Catalog (2018); Mroue et al. (2013). The effective spin is $a_{\text{eff}}/M_f = 0.29$ and the fitting factor $F = 0.965$. Bottom panel: `BBH:0182` numerical-relativity simulation of mass ratio $q = 1/4$ SXS Catalog (2018); Blackman et al. (2015). The effective spin is $a_{\text{eff}}/M_f = 0.25$ and the fitting factor $F = 0.963$.

4.4 Mass of the Newly Formed Black Hole

In the previous chapter was argued that no significant gravitational radiation is expected after the passage of the test particle over the last circular orbit. Thus, the mass of the newly-formed BH is expected to be

$$M_{\text{BH}} = M - \Delta E_{\text{rad}}, \tag{4.5}$$

$$\Delta E_{\text{rad}} = m - H_{\text{plunge}}, \tag{4.6}$$

where $H_{\text{plunge}} \equiv H(t = t_{\text{plunge}})$ is the value of the Hamiltonian (energy) of the particle (3.18) during the final smoothly merging into the BH. Due to the radial drift and the radiation-reaction, when the particle passes over the location of the last circular orbit, H_{plunge} is smaller than the energy of that circular orbit in the Kerr geometry. This facilitates the smooth merging of the particle to the Kerr BH and constitutes the extra radiation of the transition to the plunge. It is expected that before the passing of the ISCO the background spin parameter changes toward the value of the newly formed BH. Figure 4.5 shows that the energy radiated is a monotonically increasing function of a/M, therefore if the spin of the final BH is used to calculate Δ_{rmrad}, this constitutes an upper limit on the energy radiated and a lower limit on the final mass, within the present formalism.

Figure compares the (lower limit) mass of the newly-formed BH predicted by the test par-

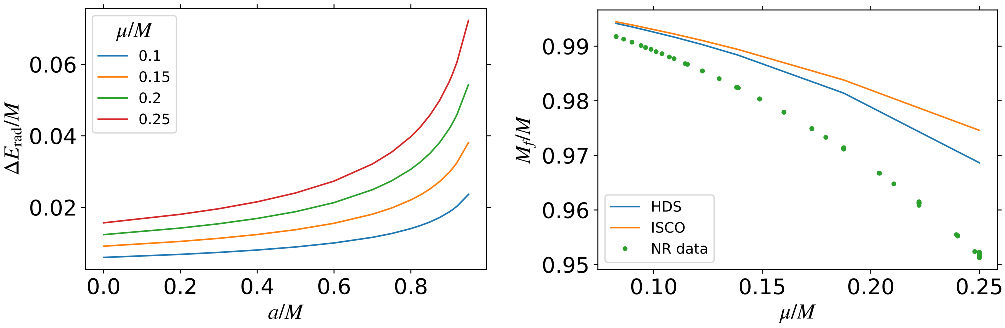

Figure 4.5 Left: Energy radiated in HDS up to the ISCO as a function of the spin parameter of background BH. Curves for different symmetric mass ratio are shown. All the curves increase monotonically with a/M. Right: comparison of the mass of the newly-formed BH predicted by the HDS and numerical-relativity simulations of binary BH mergers. Blue curve: test particle prediction by eq. (4.5) with $\Delta E_{\rm rad} = m - E_{\rm ISCO}$. Orange curve: test particle prediction by eqs. (4.5) and (4.6). The mass of the particle, m, is equal to the binary reduced-mass, μ, and the spin of the Kerr BH is equal to spin of the newly-formed BH in the merger. Green dots: data from the SXS Catalog (2018) of numerical-relativity simulations with spinless initial BHs.

ticle treatment (4.5) and by the numerical-relativity simulations SXS Catalog (2018). The numerical-relativity data in this plot refer to all the available simulations of the waveform catalog of coalescences of binary BHs with non-spinning components. These simulations correspond to different values of the mass-ratio $q = m_2/m_1$ (we adopt $m_1 \geq m_2$), thus different values of the ratio $\mu/M = q/(1+q)^2$. In the case of the above simulations of non-spinning components, the spin parameter of the newly-formed Kerr BH ranges from ≈ 0.3 (for $\mu/M \approx 0.1$) to ≈ 0.7 (for $\mu/M = 1/4$). Recall that in the comparison the spin of the HDS Kerr BH is equal to spin of the newly-formed BH in the numerical-relativity merger. Despite the agreement in the waveforms, the mass of the newly-formed BH in numerical-relativity simulations is smaller than the one from the HDS of the test particle. It implies the existence in the numerical-relativity simulations of an additional gravitational radiation after the passage of the particle over the last circular orbit, in contrast with the expectations. *From the point of view adopted here*, there is no physical reason that explains such an extra loss of gravitational energy at expenses of the BH mass. Numerical calculations of the GW emission from the solution of the Teukolsky partial differential equation adopting the actual plunge trajectory into the Kerr BH are needed to understand and to possibly answer this questioning. This task epresent a important future work, some very early advance is shown in D.

4.5 Discussion

The numerical-relativity simulations of the coalescence of two BHs can gain physical insight with the use of the current approach. In the author's opinion, if developed further, this formalism can be used to construct complete GW templates with a very low computational cost. Furthermore, it is based on a strong-field exact solution of the EFE, the Kerr solution

(Kerr, 1963), which captures the frame-dragging due to the rotation of the source. The agreement between the two treatments, with and without considering the intrinsic spins of the merging BHs, appears to be due to the dominating value of the binary angular momentum over the one of the individual spins of the merging BHs. What clearly stands from this work is a call for attention to the non-applicability of relativistic orbits in the Schwarzschild metric and the neglect of the total binary angular momentum which needs to be taken to the general attention.

Chapter 5

Gravitational Wave Events

Since GWs have been proposed to exist, they seemed very hard to be detected. The classic textbook of Landau & Lifshitz (1951) stated: "…radiation of gravitational waves is a fifth order effect in 1/c. Together with the smallness of the gravitational constant k, makes the usual effects extremely small." In fact, for a 4 km length interferometer and a typical GW strain $h_0 \sim 10^{-21}$, the displacement of the mirrors is $\delta L \sim 10^{-18}$ m, a thousandth of the radius of the atomic nucleus. This establish a challenge to experimentalists. Some early claims of the detection of GWs (Weber, 1969) were later shown not to be true, in the sense that they could be reproduced with similar detectors, see e.g Amaldi & Pizzella (1979). On the other hand, theoretical implications of the result lead to inconsistencies, e.g. such a frequent radiation implies a very small life time of the universe. Fortunately, indirect detection of GW by its effect on the orbits of a binary system was announced in (Taylor et al., 1979), and the existence of GWs was experimentally shown. Long effort took until the announcement of the first direct detection of GWs consistent with the merger of two BHs (Abbott et al., 2016a). Other 5 GW events have been announced (Abbott et al., 2016c, 2017b,c,d,a). Five of them are consistent with the merger of binary black hole, and the last with the merger of a binary neutron star. This chapter will analyze some features of first binary black event and of the binary neutron star.

5.1 Matched-Filter

The GW wave signal can be inside the noise, but this does not imply that it can not be detected. In order to extract the signal, similar to the case of radio signals, the matched-filter technique is used (see e.g. Maggiore, 2008, for a review). A brief review will be presented. The Fourier transform, $\tilde{h}(f) = \mathcal{F}\{h(t)\}$, is defined by,

$$\tilde{h}(f) = \int_{-\infty}^{\infty} h(t) e^{-i2\pi f t} dt \tag{5.1}$$

$$h(t) = \int_{-\infty}^{\infty} \tilde{h}(f) e^{i2\pi f t} df \tag{5.2}$$

Within this work it is supposed that the detector noise $n(t)$ is *gaussian* and *stationary*. The expected value of the correlation of the noise at two different times only depends on the time difference:

$$\langle n(t+\tau)n(t)\rangle = R(\tau), \tag{5.3}$$

and therefore the Fourier components obey the following relation:

$$\langle \tilde{n}(f)\tilde{n}^*(f')\rangle = \frac{1}{2}\delta(f-f')S_n(f). \tag{5.4}$$

The function $S_n(f)$ is the power spectrum density of the noise which gives the energy content of the noise as a function of the frequency. When the signal is smaller than the noise, it can be "extracted" by using a (linear) filter. The output of a linear filter $M(t)$ acting on the data $s(t) = n(t) + h(t)$, which may have the (gravitational wave) signal $h(t)$ is:

$$\hat{s} = \int_{-\infty}^{\infty} s(t)M(t)dt = \int_{-\infty}^{\infty} \tilde{s}(f)\tilde{M}(f)df. \tag{5.5}$$

The matched filter $K(t)$ is defined as the filter which gives the maximum signal-to-noise ratio (SNR) ρ, defined as the ratio between the expected output when the signal is present and the standard deviation data output when there is no signal:

$$\langle\rho\rangle^2 = \frac{\langle\hat{s}\rangle^2|_{h\neq 0}}{\langle\langle\hat{s}^2\rangle - \langle\hat{s}\rangle^2\rangle|_{h=0}} \tag{5.6}$$

It is convenient to define the inner product of two real functions f and g:

$$(g|h) = \Re\int_{-\infty}^{\infty} \frac{\tilde{h}(f)\tilde{g}^*(f)}{(1/2)S_n(f)}df = 4\Re\int_{0}^{\infty} \frac{\tilde{h}(f)\tilde{g}^*(f)}{S_n(f)}df. \tag{5.7}$$

The matched-filter is

$$\tilde{K}(f) = \text{const.} \times \tilde{h}(f)/S_n(f), \tag{5.8}$$

and the expected SNR can be written in terms of the inner product defined in eq. (5.7),

$$\langle\rho\rangle = (h|h)^{1/2} \tag{5.9}$$

5.2 Projection onto the detector frame

The gravitational radiation in the TT frame is usually decomposed into spin-weighted spherical harmonics of spin $s = -2$ (see appendix B),

$$h_+ - ih_\times = \sum_{l=2}^{\infty}\sum_{m=-l}^{m=l} h_{lm}(T,R)\,{}_{-2}Y_{lm}(\Theta,\Phi) = A_{\mathrm{GW}}e^{-i\Phi_{\mathrm{GW}}} \tag{5.10}$$

where R is the distance from the source to the observer. The angles Θ and Φ are polar and azimuthal angles of the unit vector from the source to observer, with respect to the source frame. For a binary it is customary to choose the z axis of the source frame parallel to the orbital momentum of the binary. The detector frame is chosen so that the arms are along the x and the y axes. The response of the interferometer to the GW is denoted by $h(t)$. The GW passing changes the length of the arms and induces a interference pattern. The behaviour of the length of the arms L, in the limit $L \ll \lambda_{\mathrm{GW}}$, is given by the geodesic deviation (2.21). Therefore the detector response is $h(t) = (h_{xx}^{\mathrm{TT}} - h_{yy}^{\mathrm{TT}})/2$. Recall that the polarizations h_+ and $h_\times$ are defined in the plane perpendicular to the propagation direction, which does not coincide in general with the detector frame z axis. Consequently, a rotation has to be done in order to find $h_{xx}^{\mathrm{TT}}, h_{yy}^{\mathrm{TT}}$ in the detector frame (Maggiore, 2008). After the rotation is done it is found that,

$$h(t) = F_+(\theta, \phi, \psi)h_+ + F_\times(\theta, \phi, \psi)h_\times, \tag{5.11}$$

where (Forward, 1978),

$$F_+ = \frac{1}{2}\left(1 + \cos^2\theta\right)\cos 2\phi \cos 2\psi - \cos\theta \sin 2\phi \sin 2\psi, \tag{5.12}$$

$$F_\times = \frac{1}{2}\left(1 + \cos^2\theta\right)\cos 2\phi \sin 2\psi + \cos\theta \sin 2\phi \cos 2\psi, \tag{5.13}$$

are called the antenna patterns. The angles θ and ϕ are the polar and azimuthal angles of the unit vector from the source to the detector, respect to the detector frame, and ψ is the polarization angle which represents a rotation around the direction of propagation, see fig. 5.1. Usually the position of the source is given in celestial coordinates. The correct expression for the antenna patterns in terms of the right ascension and declination of the source, and the earth localization of the detector can be found in the Ref. (Schutz, 2011).

From the Eqs. (5.10) and (5.11), the detector response $h(t)$ can be written as

$$h(t) = A\cos[\Phi_{\mathrm{GW}} - \alpha], \tag{5.14}$$

where $A = A_{\mathrm{GW}}(F_+^2 + F_\times^2)^{1/2}$ and $\tan\alpha = F_\times/F_+$. If there are two or more detectors the amplitude ratio A_1/A_2 can be used to infer the position. The angles Θ, Φ are given by the direction from the source to a fixed frame on the earth (the celestial coordinate frame) relative to the frame system. Therefore on both detectors A_{GW} and Φ_{GW} are the same. The antenna patterns depend on the celestial coordinates of the source; on the longitude, latitude, and arms orientation of the detector; and on the GPS time. Thus the amplitude ratio depends only on the antenna patterns,

$$\frac{A_1}{A_2} = \left[\frac{F_{+,1}^2 + F_{\times,1}^2}{F_{+,2}^2 + F_{\times,2}^2}\right]^{\frac{1}{2}} \tag{5.15}$$

The GW spectrum can be used to estimate the SNR of astrophysical sources. For a general source it is given by,

$$\rho^2 = 4\int_0^\infty \frac{|F_+\tilde{h}_+ + F_\times\tilde{h}_\times|^2}{S_n(f)}df. \tag{5.16}$$

The orientation and localization of the source is not known a priori, thus the SNR is averaged in order to assess the detectability. The averages of the detector pattern functions satisfy $\langle F_+^2\rangle = \langle F_\times^2\rangle$ and $\langle F_+F_\times\rangle = 0$. Consequently, the averaged ρ^2 is,

$$\begin{aligned}\langle\rho^2\rangle &= 4\langle F_+^2\rangle\int_0^\infty \frac{\langle|\tilde{h}_+(f)|^2 + |\tilde{h}_\times(f)|^2\rangle}{S_n(f)}df \\ &= 4\frac{G}{c^3}\frac{\langle F_+^2\rangle}{2\pi^2 d^2}\int_0^\infty \frac{1}{f^2 S_n(f)}\frac{dE}{df}df. \end{aligned}\tag{5.17}$$

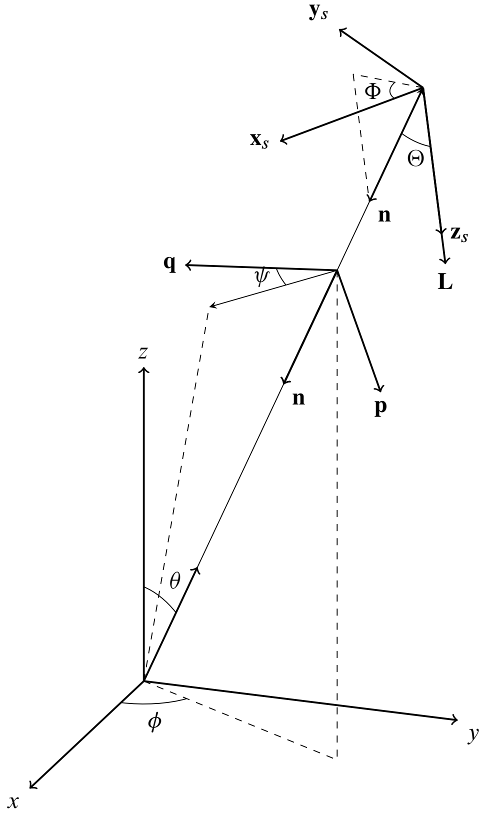

Figure 5.1 Illustration of the angles involved in the projection of the GW onto the detector frame. The angles θ, ϕ are the spherical polar and azimuthal angles of the source, with respect to the detector frame. The unit vector from the source to the detector is $\mathbf{n}$. The intersection of the plane perpendicular to the propagation direction (TT plane) and the plane xy is called the TT-detector line of nodes. A triad is constructed to describe the GW in the TT frame, $\mathbf{n} = \mathbf{p} \times \mathbf{q}$. The arbitrariness in the choice of $\mathbf{p}, \mathbf{q}$ is given by the polarization angle ψ, defined as the angle between the TT-detector line of nodes and $\mathbf{q}$, $\tan\psi = \mathbf{z} \cdot \mathbf{q} / \mathbf{z} \cdot \mathbf{p}$. This last angle corresponds to a rotation around the propagation direction (see eq. (2.18)). Another coordinate frame is constructed in the source. The z_s axis is in the same of the total angular momentum of the system. The intersection of the plane perpendicular to $\mathbf{z}_s$ and the TT plane is called the TT-source line of nodes. The corresponding triad $\mathbf{z}_s = \mathbf{x}_s \times \mathbf{y}_s$ is constructed so that $\mathbf{y}_s$ lies in the TT-source line of nodes. The spherical polar and azimuthal angles of the propagation direction $\mathbf{n}$ with respect the source frame are Θ and Φ, respectively.

This last equation allows to define the characteristic strain $h_c(f)$ as,

$$h_c(f) \equiv \frac{1}{\pi d} \sqrt{\frac{\langle F_+^2 \rangle}{2} \frac{G}{c^3} \frac{dE}{df}} = \sqrt{\langle F_+^2 \rangle \langle |\tilde{h}_+|^2 + |\tilde{h}_\times|^2 \rangle} f. \tag{5.18}$$

When the detector is an interferometer, $\langle F_+^2 \rangle = 1/5$ and this last expression reduces to the definition given in (Kobayashi & Mészáros, 2003).

As stated before, the averaged $\langle \rho^2 \rangle$ is useful to estimate the signal-to-noise ratio when the exact localization of the source is not known, but is not useful for calculating rates of detection. For this task it is introduced the range of the detector. The range $\mathcal{R}$ is related (not equal) to the maximum possible distance $d_{\rm GW}$ (horizon distance) at which some GW source will produce $\rho = \rho_0 = 8$. Since not all the sources are optimally located and oriented, there is some probability that inside a sphere of radius $d_{\rm GW}$ there will be a source inducing $\rho = 8$. For an arbitrary located and oriented binary, the signal-to-noise ratio is given by (Maggiore, 2008):

$$\rho^2 = 4A^2 \frac{\Theta^2}{d^2} \int_0^\infty \frac{f^{-7/3}}{S_n(f)} df, \tag{5.19}$$

where

$$\Theta^2 = \frac{F_+^2(1+\cos^2\iota)^2 + 4F_\times^2\cos^2\iota}{4}, \tag{5.20}$$

and the pattern functions are given by eqs. (5.12) and (5.13). The binary is optimally oriented when $\theta = \phi = \iota = 0$, i.e., $\Theta^2_{\rm opt} = 1$. Hence, the distance to a binary optimally oriented, that will induce a signal-to-noise ratio equal to the threshold is,

$$d_{\rm GW} = \frac{2A}{\rho_0}\left(\int_0^\infty \frac{f^{-7/3}}{S_n(f)} df\right)^{1/2}, \tag{5.21}$$

where $A = 5/(24\pi^{4/3})^{1/2}(GM_c/c^3)^{5/6}c$ (Allen et al., 2012). On the other hand, if some source has $(d^2/\Theta^2) < d^2_{\rm GW}$, it will be detected given the threshold ρ_0. Thus, the probability of detection depends on probability that $\Theta^2 > d^2/d^2_{\rm GW}$ Finn & Chernoff (1993). This latter is related to ratio of the number of detected sources $N_{\rm det}$ to the total number of sources $N_{\rm tot}$ within a sphere of radius $d_{\rm GW}$:

$$\mathcal{F}^3 = \frac{N_{\rm det}}{N_{\rm tot}} = \frac{3 \times 1.84}{4^3}, \tag{5.22}$$

which defines the detector's range, $\mathcal{R} = \mathcal{F} d_{\rm GW}$.

5.3 GW150914 phenomenological analysis

This section will show how the Newtonian center of mass view can be used to make a phenomenological analysis of GW150914 Rodriguez et al. (2016). It is worthwhile saying that this procedure does not intend to make an strict map between the real problem (two comparable mass objects) with the problem of a test particle. In the same spirit of EOB (Buonanno & Damour, 1999), this analysis is an effective method which gives physical insight of the problem. Indeed, this work was done before the other more elaborated approaches presented in the two previous chapters. This analysis hinted (as well as other works in the literature e.g. (Anninos et al., 1995)) the possibility that a test particle properly analyzed can be used to "understand" the merger of two BHs.

5.3.1 Binary evolution

Following the same framework previously presented in chapter 3, the black hole binary (BHB) evolution is divided into four phases. The first one is the adiabatic inspiral phase in which the binary follows quasi-circular orbits. The GW energy spectrum in this phase can be estimated from the traditional formula of the quadrupole emission within the classic point-like approximation *a la* Landau-Lifshitz given by eq. (2.84). When the quasi-circular dynamics breaks down, the final plunge begins and its corresponding frequency is denoted by $f_{\rm plunge}$. The above adiabatic dynamics breaks down when:

1. The velocity of the radial separation, $\dot{r} = v_r$, becomes of the order of the tangential velocity $v_\varphi = \omega_{\rm orb} r$. The condition for the validity of quasi-circular motion $v_r \ll v_\varphi$ can be translated into $\dot{\omega}_{\rm orb} \ll \omega^2_{\rm orb}$, from the fact that $\omega^2_{\rm orb} = GM/r^3$. In terms of the GW frequency,

$$f_{\rm plunge} \approx \frac{c^3}{G}\frac{(5/96)^{3/5}}{\pi^{8/5} M_{\rm chirp}} \approx \frac{c^3}{G}\frac{0.027}{M_{\rm chirp}}. \tag{5.23}$$

   For a symmetric binary ($m_1 = m_2 = M/2$, $M_{\rm chirp} = M/4^{3/5}$), the above frequency becomes

$$f_{\rm plunge} \approx \frac{c^3}{G}\frac{0.062}{M} \approx 12.6\frac{M_\odot}{M}\ \text{kHz}. \tag{5.24}$$

2. Finite-size effects become important. Since the above plunge frequency was computed within a point-like approximation, it does not incorporate the fact that at a very short separation the two objects could have already merged. For BHB, such a separation is approximately given by the sum of the two Schwarzschild radii, i.e $r \approx 2GM/c^2$, then

$$f_{\rm plunge} \approx \frac{c^3}{G}\frac{1}{4^{3/2}\pi M} \approx 8.1\frac{M_\odot}{M}\ \text{kHz}, \tag{5.25}$$

   This frequency is lower than the one given by eq. (5.24). This implies that the merging process naturally introduces a cutoff in the increasing frequency.

3. The strong-field region is reached, i.e. the flat-background approximation is no longer valid. In Newtonian gravity there is no restriction to the existence of stable circular orbits. When relativistic and strong-field effects are taken into account, there is limit, an inner-most stable circular orbit, the ISCO. For the gravitational field of a Schwarzschild BH the ISCO is at $r = 6Gm_{\rm BH}/c^2$. Moreover, after this point there are no circular orbits, a small perturbation will induce the particle's infall, i.e, the plunge is a strong-field effect. The extrapolation to the case of comparable masses ($m \to \mu$ and $m_{\rm BH} \to M$) leads to $r = 6GM/c^2$, and thus to a GW frequency,

$$f_{\rm plunge} \approx f_{\rm ISCO} = \frac{c^3}{G}\frac{1}{6^{3/2}\pi M} \approx 4.4\frac{M_\odot}{M}\ \text{kHz}. \tag{5.26}$$

This latter frequency value is still lower than the one given by eq. (5.25). Most of the scientific literature on binaries uses the above expression (5.26) to estimate the frequency at which the final merger process starts. There are other corrections coming from the finite-mass and post-Newtonian effects, but for the present analysis $f_{\rm ISCO}$ is frequency of the plunge.

An upper limit of the total energy emitted during the inspiral phase can be computed by integrating eq. (2.84) from the frequency at infinite separation, i.e. $f = 0$, up to the plunge frequency,

$$\Delta E_{\rm inspiral} = \frac{(\pi G)^{2/3}}{2}\left(\frac{\mu}{M}\right) M_{\rm chirp}^{5/3} f_{\rm plunge}^{2/3}. \tag{5.27}$$

If plunge frequency for the all cases presented before is expressed as $f_{\rm plunge} = c^3\eta/(GM)$, where η is a numerical value, the above energy output becomes,

$$\Delta E_{\rm inspiral} = \frac{(\pi\eta)^{2/3}}{32} Mc^2 \approx 0.067\eta^{2/3} Mc^2, \tag{5.28}$$

which for the frequency (5.25) gives $\Delta E_{\rm inspiral} = 0.008Mc^2$ and using the more accurate frequency (5.26), $\Delta E_{\rm inspiral} = 0.005Mc^2$. Moreover, the total energy radiated can be better estimated by noticing that the binding energy of the ISCO of the test-particle m around a Schwarzschild BH is $E_b \approx 0.057mc^2$ (Landau & Lifshitz, 1951; Rees et al., 1974). The center of mass extrapolation for comparable masses gives,

$$\Delta E_{\rm inspiral} = 0.057\mu c^2, \tag{5.29}$$

which for a symmetric binary is $\Delta E_{\rm inspiral} = 0.014Mc^2$.

Plunge, merger and ringdown

At the end of the adiabatic evolution the final phase composed by the plunge, merger and ringdown phases. As already mentioned, it was shown by Davis et al. (1971, 1972a) that the spectrum in this phase is dominated by the $l = 2$ multipole (quadrupole). There was also shown that the peak of the GW spectrum occurs when the test-particle falls below the maximum of the effective potential (3.2) and is located at,

$$f_{\rm peak} = \frac{0.32}{2\pi}\frac{c^3}{GM}. \tag{5.30}$$

The above energy peak was shown to be associated with the 2^l-pole normal-mode vibrations of the BH excited by the GW train produced by the in-falling body (Press, 1971). The GW spectrum in this phase has a peaked form (see sec. 3.1 for details), first raising with a power-law behavior. This can be understood in the context of perturbation theory on a flat background, i.e. by using Newtonian equations of motion, the low-frequency spectrum is (Rees et al., 1974; Maggiore, 2008),

$$\left(\frac{dE}{df}\right)_{\rm plunge} \approx 2\pi \times 0.18\frac{G\mu^2}{c}\left(\frac{4\pi GMf}{c^3}\right)^{4/3}. \tag{5.31}$$

The spectrum raises following approximately (5.31) until it reaches a maximum at the peak frequency (5.30), then falls off following an approximate (phenomenological) form

$$\left(\frac{dE}{df}\right)_{\rm ringdown} \approx 2\pi\frac{G\mu^2}{c}\exp(-9.9 \times 2\pi GMf/c^3). \tag{5.32}$$

The spectrum of the $l = 2$ multipole radiation obtained numerically is shown in figure 3.2. It is clear that an approximate analytic formula of the spectrum can be obtained from the interpolation function,

$$\frac{dE}{df} \approx \left[\frac{1}{(dE/df)_{\rm plunge}} + \frac{1}{(dE/df)_{\rm ringdown}} \right]^{-1}. \tag{5.33}$$

The total energy radiated to infinity in GWs during this plunge-merger-ringdown phase is (Davis et al., 1971),

$$\Delta E_{\rm merger} = \sum_{l \geq 2} \int df \left(\frac{dE}{df} \right)_{2^l-{\rm pole}} \approx 0.01 \frac{\mu^2}{M} c^2. \tag{5.34}$$

The above analysis implies that for BHB: i) the final GW frequency of the inspiral phase, $f_{\rm ISCO}$, is lower than the peak frequency, $f_{\rm peak}$; ii) the energy emitted in GWs during the total inspiral phase is larger than the energy emitted in the final plunge-merger-ringdown phase; iii) the merger point can be set as the point where the GW spectrum reaches the maximum value,

$$f_{\rm merger} \equiv f_{\rm peak}, \tag{5.35}$$

where $f_{\rm peak}$ is given by equation (5.30).

5.3.2 Effect of the angular momentum in the merger phase

The energy emitted during the plunging of a test particle into a BH was shown to be affected by the initial angular momentum of the particle in (Detweiler & Szedenits, 1979). The total energy output in form of GWR was there computed for selected initial angular momenta of the particle (which correspond to start the plunge of the particle from different orbits). The results of the numerical integration by Detweiler & Szedenits (1979) are approximately fitted (with a maximum error of $\sim 10\%$) by the phenomenological function,

$$\Delta E_{\rm merger} \approx \Delta E^{J=0}_{\rm merger} [1 + 0.11 \exp(1.53 j)], \tag{5.36}$$

where $j \equiv cJ/(G\mu M)$ and $\Delta E^{J=0}_{\rm merger}$ is the energy radiated by a particle falling radially given by equation (5.34). Thus, from the knowledge of the orbital angular momentum of the last orbit of the adiabatic quasi-circular phase, the amount of energy emitted during the final merger phase (upper limit) can be inferred.

5.3.3 Mass and spin of the merged object

Energy and angular momentum conservation laws are used to estimate the parameter of the BH formed in the merger. Namely, the angular momentum of the final BH will be given by,

$$J_{\rm BH} = J_{\rm ISCO} - \Delta J_{\rm merger}, \tag{5.37}$$

where $J_{\rm ISCO}$ is the angular momentum of the system at start of the plunge (ISCO), and ΔJ is the angular momentum lost by GW emission in the final plunge. The amount of energy emitted in the plunge was used to estimate ΔJ,

$$\Delta J_{\rm merger} = \frac{\Delta E_{\rm merger}}{\pi f_{\rm ISCO}}. \tag{5.38}$$

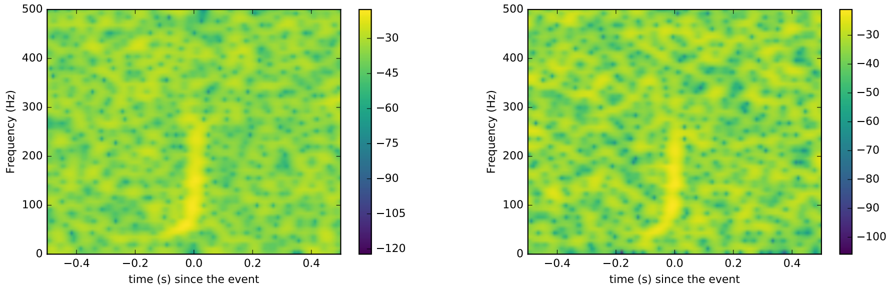

Figure 5.2 Left panel: spectrogram of the gravitational-wave event GW 150914 obtained from the signal observed at the H1. Right panel: spectrogram of the gravitational-wave event GW 150914 obtained from the signal observed at the L1. Both spectrograms are found bu using a window of 1/8 of a second and an overlap of 93.8%.

The energy loss during the total merger phase, according to eqs. (5.34), (5.36) is approximately,

$$\Delta E_{\text{merger}} \approx 0.24\frac{\mu^2}{M}c^2. \tag{5.39}$$

Since the frequency at the ISCO is $f_{\text{ISCO}} \approx 0.02c^3/(GM)$, the angular momentum lost during the merger is,

$$\Delta J_{\text{merger}} \approx 3.81\frac{G\mu^2}{c}. \tag{5.40}$$

The above implies that the dimensionless angular momentum of the newly formed BH is,

$$\alpha \equiv \frac{cJ_{\text{BH}}}{Gm_{\text{BH}}^2} \approx 2\sqrt{3}\frac{\mu M}{m_{\text{BH}}^2} - 3.81\left(\frac{\mu}{m_{\text{BH}}}\right)^2, \tag{5.41}$$

and from conservation of energy the mass is $m_{\text{BH}} \approx M\beta(\nu)$, where the expression (5.39) was used and the function β is,

$$\beta(\nu) \equiv \left[1 - \left(1 - 2\sqrt{2}/3\right)\nu M - 0.24\nu^2\right]. \tag{5.42}$$

Consequently, the dimensionless BH spin parameter is

$$\alpha \approx \frac{1}{\beta(\nu)^2}\left[2\sqrt{3}\nu - 3.81\nu^2\right]. \tag{5.43}$$

5.3.4 Parameters Estimation

In order to extract more information from the signal it is necessary to make an analysis on the frequency-time domain, i.e., find the spectrogram of the signals. Following the procedure shown on The Gravitational Wave Open Science Center (2018) (the author is not a data analyst expert), the spectrograms of the event are shown on figure 5.2. It is not

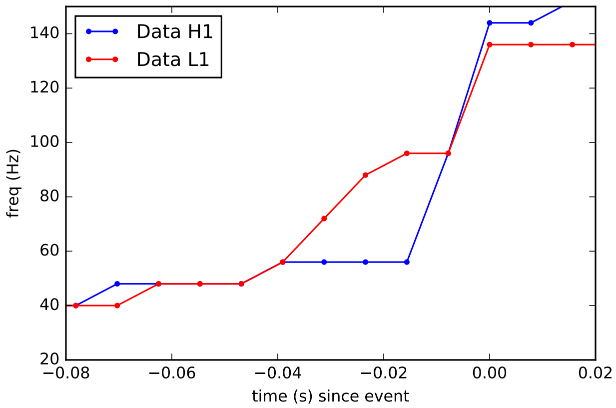

Figure 5.3 The maximum frequency on each bin is ploted as a function of time

intended to perform a complete data analysis, but only a qualitative analysis. The chirp mass of the binary can be extracted from the adiabatic part of the spectrogram,

$$M_{\text{chirp}} = \frac{c^3}{G}\left(\frac{5}{96\pi^{8/3}}\frac{\dot{f}}{f^{11/3}}\right)^{3/5}. \tag{5.44}$$

The evolution is shown in figure 5.3 and an empirical fit was done to obtain the chirp mass, $M_{\text{chirp}}^{\text{H1}} \approx 30.5\ M_\odot$ and $M_{\text{chirp}}^{\text{L1}} \approx 43\ M_\odot$. The chirp mass obtained from the data of the detector H1 is in agreement with the reported value. The total mass of the system can be inferred from eq. (5.30), i.e. the quasinormal frequency of the 22 mode. However, the newly formed black is expected to the be rotating, so the following fitting formula for the quasinormal modes of a Kerr BH must be used (Echeverria, 1989),

$$f_{\text{peak}} = \frac{1 - 0.63(1-a)^{3/10}}{2\pi m_{\text{BH}}}. \tag{5.45}$$

On the other hand, the observed least damped mode of the ringdown is $f_{\text{peak}} = 251 \pm 8$ Hz (Abbott et al., 2016e). Hence, eqs. (5.43) and (5.45), together with $M_c = 30.5 = \nu^{3/5} M$, fix the symmetric mass ration ν, the mass of the final BH and its spin parameter α,

$$\nu = 0.24, \quad m_{\text{BH}} = 71.5\ M_\odot, \quad \alpha = 0.65. \tag{5.46}$$

From the last value the mass-ratio was obtained,

$$q = \frac{m_2}{m_1} = \frac{4\nu}{\left(1+\sqrt{1-4\nu}\right)^2} \approx 0.69, \tag{5.47}$$

the LIGO-Virgo analysis value is $q = 0.79^{+0.18}_{-0-19}$ (Abbott et al., 2016d), therefore the estimate is accurate within an error of 12.7%. The individual masses are,

$$m_{\text{BH},1}^{\text{obs}} = \frac{M_{\text{obs}}}{(1+q)} \approx 42.4\ M_\odot, \tag{5.48}$$

$$m_{\text{BH},2}^{\text{obs}} = \frac{q}{1+q} M_{\text{obs}} \approx 29.2\ M_\odot, \tag{5.49}$$

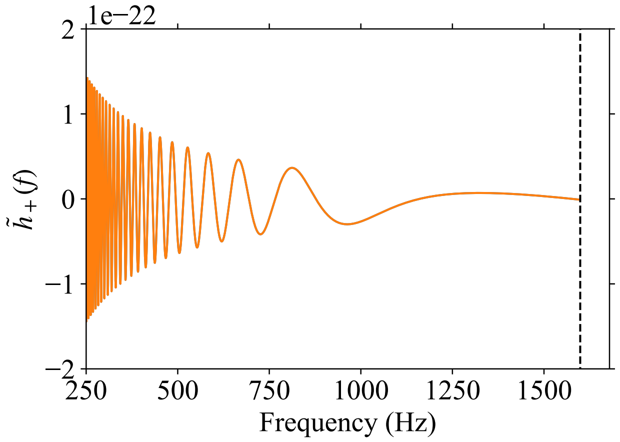

Figure 5.4 Waveform in the frequency domain (right) generated by a Spin-TaylorT4 approximant.

to be compared with the values $m_{\mathrm{BH},1} = 39.4^{+5.5}_{-4.9}\ M_\odot$, $m_{\mathrm{BH},2} = 30.9^{+4.8}_{-4.4}\ M_\odot$ (Abbott et al., 2016d). The above estimates indicate that the newly born BH, not only conserves almost the total mass of the binary, but also that it is rotating fast. Due to the closeness of the results, it can be said that this BHB merger can be easily *modeled* via the Newtonian center of mass view. In other words, the merger can be viewed as a test particle first inspiraling up to ISCO, then plunges into a rotating BH, which is perturbed and emits GWs to reach a stationary state. Of course, this does not replace coherent Bayesian analysis to extract the parameters, and constitutes one example of its applicability.

5.4 GW170817 analysis

The gravitational wave event called GW 170817 was reported to be consistent with the merger of binary neutron star (Abbott et al., 2017a). It is interesting that the GRB 170817, first reported at the GCN524666471 (Fermi GBM, 2017), was latter associated with GW 170817. The bright optical transient SSS17a/AT 2017gfo (Abbott et al., 2017e) was worldwide observed. A brief time line of the first Gamma-Ray Coordinates Network (GCN) related with GRB 170817 or GW179817 is:

1. The Fermi Gamma-ray Burst Monitor (GBM) trigger of a GRB at **12:41:20 GMT**, **GCN524666471**, Fermi GBM telescope (Fermi GBM, 2017).
2. “The online CBC pipeline (gstlal) has made a preliminary identification of a GW candidate associated with the time of Fermi GBM trigger 524666471/170817529 at gps time 1187008884.47”. **GCN21505**, LIGO-Virgo telescope (LIGO Scientific Collaboration et al., 2017a).
3. “ The on-board trigger time of Fermi GBM trigger 170817.529 524666471 at 12:41:06.47 UT is approximately 2 seconds after the single interferometer LIGO trigger reported in GCN 21505”. **GCN21506**, Fermi GBM telescope, (Connaughton et al., 2017).

4. The effective distance of the source inferred from only the date of H1 LIGO detector is $\approx$ 58 Mpc, **GCN21509**, LIGO-Virgo telescope (LIGO Scientific Collaboration et al., 2017b).
5. Updated localization, data from the three detectors, **GCN21513**, LIGO-Virgo telescope (LIGO Scientific Collaboration et al., 2017c).
6. Triangulation between Fermi GBM and Integral, **GCN21515**, IPN (Svinkin & Hurley, 2017).

The complete time line can be found in tab. 6 of (Abbott et al., 2017e). During the GW event there was a glitch at LIGO-Livingston detector (Abbott et al., 2017a).

5.4.1 Matched-Filter

The complete bayesian analysis will not be done here, only a preliminary analysis in order to infer the localization of the source and to compare it with the EM localization. LIGO-Virgo Collaboration used in the analysis the frequency domain post-Newtonian waveform which includes tidal interactions and spin effects (Abbott et al., 2017a). The SNR of this event is 18.8 and 26.4 for LIGO-Hanford (H1) and LIGO-Livingston (L1), respectively. The exact parameters corresponding to this SNR were not reported there.

The value of chirp mass in the detector frame to $M_c = 1.197 M_\odot$ was fixed, and the mass ratio was varied, $q = m_1/m_2$ with $m_1 > m_2$. The frequency domain template was generated by the approximant `SpinTaylorF2` using the `pycbc` package (Nitz et al., 2018). The spin was chosen, $\chi_1 = \chi_2 = 0$ and the tidal parameters are $\Lambda_1 = 300$ and $\Lambda_2 = 15$. These parameters are related to the quadrupole moment induced on the stars by an external tidal potential:

$$\Lambda = \frac{2}{3} k_2 \left(\frac{R}{m_*} \right)^5 , \tag{5.50}$$

where k_2 is the second love number, R and m_* are the radius and the mass of the star, respectively. Thus, this number depends on the equation of state. *The numbers chosen for this template do not come from a physical integration of the structure of the stars.* The total lambda parameter for this template is 249.61, consistent with reported tidal parameter $\tilde{\Lambda} \leq 800$ (low spin priors).

The procedure to calculate the SNR amplitude follows the technique presented on the LOSC website (The Gravitational Wave Open Science Center, 2018) and on the Ref. (Allen et al., 2012). The complex template, $\tilde{h}_{\text{template}}(f) = \tilde{h}_+(f) + i\tilde{h}_\times(f)$, is used to find the complex SNR $z_m(t)$ defined by (Allen et al., 2012):

$$z_m(t) = 4 \int_0^\infty \frac{\tilde{s}(f) \tilde{h}^*_{\text{template}}(f) e^{i2\pi f t}}{S_n(f)} df, \tag{5.51}$$

where $\tilde{s}(f)$ is the fourier transform of the LIGO data. In order to find the Fourier transform of the data 64 s around 1187008882 GPS time were taken with a tukey window and then FFT was performed. The SNR amplitude $\rho_m(t)$ is given by:

$$\rho_m(t) = \frac{|z_m(t)|}{\sigma_m} \tag{5.52}$$

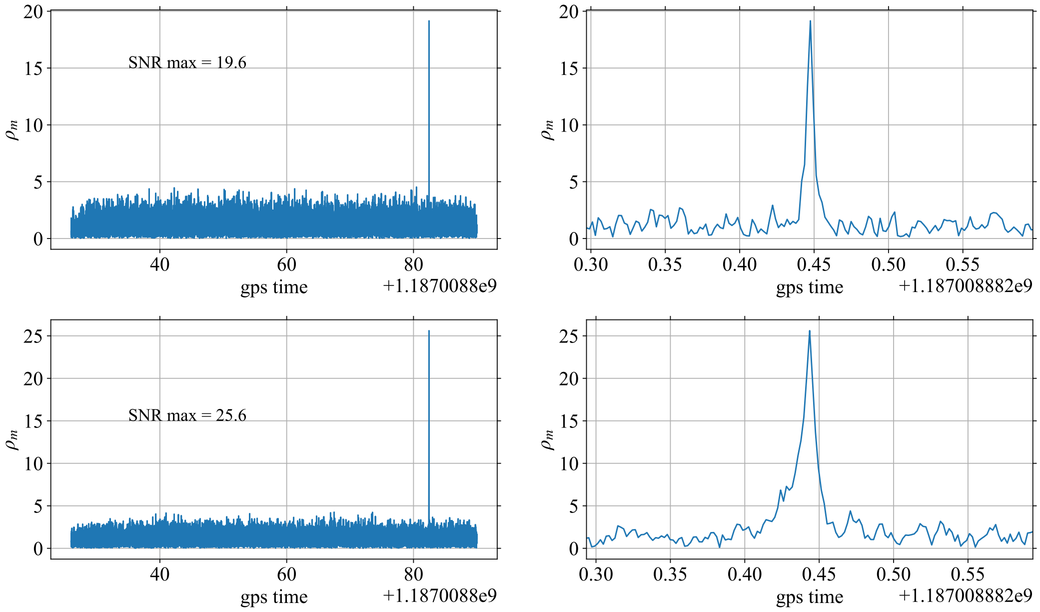

Figure 5.5 SNR amplitude on both LIGO detectors.

where

$$\sigma^2 = 4\int_0^\infty \frac{|\tilde{h}_{\text{template}}(f)|^2}{S_n(f)} df \tag{5.53}$$

The quantity $\rho_m(t)$ correspond to the SNR value once it is maximized over A and α (see Eq. (5.14)). The maximum $\rho_m(t)$ is 19.460 and 25.083, at GPS time (see fig. 5.5),

$$t_{\text{max,H1}} = 1187008882.447021 \quad t_{\text{max,L1}} = 1187008882.443604. \tag{5.54}$$

The time delay $\delta t = t^H_{\text{event}} - t^L_{\text{event}} = 0.003418$ s. On the other hand, if the position of the source is taken to be given by the EM counterpart (LIGO-Virgo Collaboration, 2017; Haggard et al., 2017), RA = $13^h09^m48^s$ and declination = $23°22'53''$, the time delay is $\delta t = 0.003293$ s. Therefore, the localization is consistent with the EM data.

5.4.2 Localization

The maximum SNR and time delay obtained in the last section were used to calculate to estimate the position of the source. The methodology used is similar to BAYESTAR and is described in ref. (Chen & Holz, 2017). Basically, the distribution of the declination and RA, δ, α is constructed from three observables (data): the SNR, the time delay and the phase difference. Bayes theorem states,

$$P(\delta, \alpha|y) = \frac{P(y|\alpha,\delta)P(\alpha,\beta)}{P(y)}, \tag{5.55}$$

i.e., the probability of the template with parameters [1] δ, α (hypothesis), given the data (observables) y, is proportional to the probability (the likelihood) of the data given the

---

[1] All the other parameters of the template such as the masses are held fixed

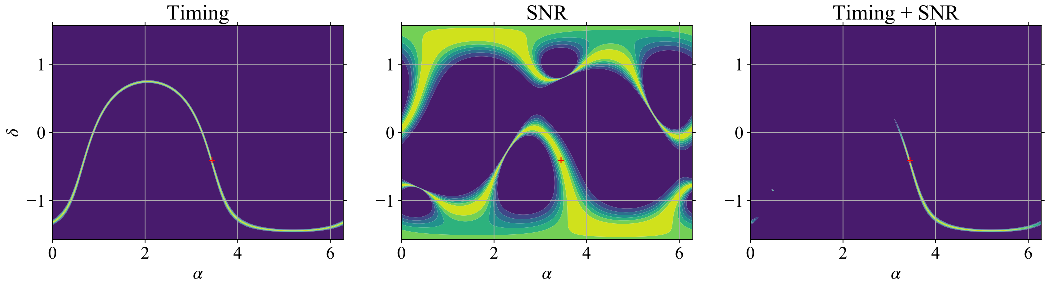

Figure 5.6 Probability distribution of the localization of the source of GW170817 by using only GW data. Left: timing contribution; center: SNR contribution, i.e. the localization was found from the relative amplitude projection weighted by the corresponding detector noise at the time of the event; right: contribution from timing and SNR (see eq. (5.56) and below). The red cross marks the position obtained from the EM data, which is consistent with localization from GW data.

template with δ, α. The output of the detector $s(t)$ contains the signal plus the noise, if the template is subtracted, only the "noise" is left $n(t) = s(t) - h(t)$. Each template leaves a different "noise", i.e. is a different realization of the noise. The probability of observing such a noise provides a probability of the parameters characterizing the template. When the noise is Gaussian, it is proportional to $\exp[-(\tilde{n}_f|\tilde{n}_f)]$. For this particular case,

$$P(y|\alpha, \delta) \propto \exp(\Delta\chi^2(\alpha, \delta)/2), \tag{5.56}$$

where $\Delta\chi^2 = \chi^2(\alpha, \delta) - \chi^2_{\min}(\alpha, \delta)$ can be found in (Chen & Holz, 2017). The chi-squared function is split into two contributions $\chi^2_{t,\delta\phi}(\alpha, \beta) + \chi^2_{\rho}(\alpha, \delta)$, where the first come from the time delay and phase difference, and the latter from the SNR. Figure 5.6 shows the result using data from H1 and L1, with different observable contribution: time delay, SNR (amplitude) and SNR + time delay. The EM localization given by (Haggard et al., 2017) is shown with a red cross. It can be seen that the GW localization is consistent with the EM data.

5.4.3 Electromagnetic Counterpart

On the other hand, GRB 170817A is sub-luminous compared to other observed S-GRB, for example, in the (1-10000) keV band GRB 170817A is 2-3 orders of magnitude less energetic than GRB 15101B (previously the weakest GRB). Four possible explanations were given in ref. (Abbott & et al., 2017). The first explanation proposes off-axis observation of the jet and, the second the existence of a structured jet. The third explanation proposes a different mechanism of emission in which the tail of emission is originated from the interaction of the jet with the surrounding material, i.e. "cocoon" emission. The last one asserts that the luminosity of the system is intrinsically low.

An independent analysis based on a comparison of GRB 170817A with other observed GRBs was done by Rueda et al. (2018b). The lack of any similarities with any known GRB source has led there to a new explanation: the EM emission GRB 170817A has been originated in the merger of two white dwarfs (WDs). The comparison and contrast was

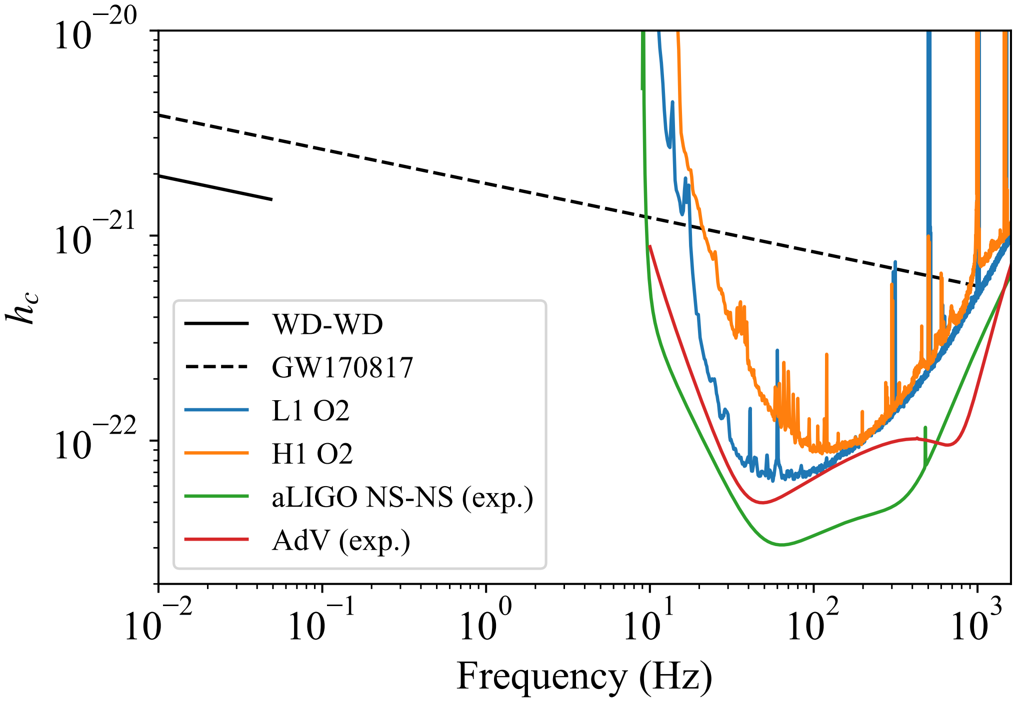

Figure 5.7 Characteristic strain (5.18) for a symmetric BWD with $m_{\rm WD} = 0.6\ M_\odot$ (continuous) and for a symmetric BNS with $m_{\rm NS} = 1.36\ M_\odot$ (dashed) during the inspiral phase at 40 Mpc (similar to GW170817). The ASD for the aLIGO O2 detectors L1, H1 is also shown (blue and orange curves), and the expected sensitivities of AdV and aLIGO (green and red). It can be seen that the BWD is outside the detectors sensitivity band.

done with GRBs 060614, 090510A, 130603 which are the prototypes of three of the families according to the classification given in (Ruffini et al., 2016b). Before continuing with the comparison, it is important to mention that from the analysis of the observational data obtained by the satellites Swift (Gehrels et al., 2004), Fermi and Fermi-LAT (Atwood et al., 2009), it was shown in (Ruffini et al., 2018c) that the GeV emission is a necessary and sufficient condition to indicate the formation of a BH in S-GRBs. The GRB 061614 progenitor is a BNS, and the observational absence of GeV emission implies that the remnant is a newly formed NS; GRB 090510A progenitor is also a BNS but GeV emission indicates that the remnant is a BH; GRB 060614 progenitor is a NS-WD binary. Regardless the different isotropic energy released in the (10 - 1000) keV band, the latter three GRBs converge to the same luminosity in the X-ray band, but GRB170817 does not. GRB 170817 is not consistent with any progenitor subclass of (Ruffini et al., 2016b). This led to the idea that it may have been originated in a different system. It is worthwhile saying that this analysis is based only on the EM data requiring consistency with previous observations.

The optical and infrared band of all the four GRBs converge to a common kilonova behaviour (see fig. 4 in (Rueda et al., 2018b)). The X-ray, optical and infrared emission can be explained with the remnant of a binary WD (BWD) merger. Since no supernova was observed the post-merger object must be a WD. The emission of the kilonova in the BWD scenario is not explained by r-process after the merger (Metzger et al., 2010), but by the fallback of the ejecta (Rueda et al., 2018b,a). The GRB prompt emission can be generated by magnetic stresses during the merger (this emission will be further investigated). Finally, the GW signal is not consistent (detectable) with the merger of two WD given its low frequency cut off, see fig. 5.7. For example, for symmetric BWD with $m = 0.6$, the end of the merger is approximately at the contact point whose frequency is $f_{\rm merger} \approx 0.04$ Hz , The radius of the WD components is $\approx 1 \times 10^9$ cm assuming a Feynman-Metropolis-Teller equation of state (Rotondo et al., 2011). It is hope that more join GW-EM detections will provide additional information on the progenitor of S-GRBs and answer the issue on the low luminosity of GRB 170817A.

Chapter 6

γ-ray Bursts and Gravitational Waves Rates

The observations by γ-ray telescopes, such as BATSE, *Fermi*, *INTEGRAL*, and *Swift*, has improved the understanding of the progenitor of long and short gamma-ray burst (GRB), which according to some models is a binary system. This has led also to a vast literature on their relative occurrence rates, all in general agreement. For long bursts see, e.g., (Soderberg et al., 2006; Guetta & Della Valle, 2007; Wanderman & Piran, 2010; Guetta et al., 2011; Kovacevic et al., 2014); for short bursts see, e.g., (Virgili et al., 2011; Wanderman & Piran, 2015); and for both long and short bursts see, e.g., (Sun et al., 2015; Ruffini et al., 2016b). This gives an extraordinary scenario to test models with data coming from different channels, namely the electromagnetic (GRBs, X-ray, optical, infrared) and gravitatinal (GWs) channel.

This chapter is dedicated to establish the relation between GRBs and GWs within the paradigm that *both long and short GRB progenitors are binaries*. More exactly, the GRB occurrence will be used to assess the detectability of GW emission by the ground-based and space-based interferometers Advanced LIGO, Advanced Virgo, eLISA, as well as by the resonant bars. In order to do this it is needed to identify the different kinds of GRB progenitors. Recently, a new classification of both long and short GRBs has been introduced, in which all the GRBs progenitors are merging and/or accreting binary systems (Ruffini et al., 2016b). For each system the initial state and the final state are respectively referred to as "*in-state*" and "*out-state*". For long GRBs, the induced gravitational collapse (IGC) paradigm (Ruffini et al., 2006, 2007, 2008; Izzo et al., 2012; Rueda & Ruffini, 2012; Fryer et al., 2014) proposes as *in-state* a tight binary system composed of a carbon-oxygen core ($\mathrm{CO}_{\mathrm{core}}$) undergoing a supernova (SN) explosion and a companion compact object, e.g. a neutron star (NS) or a black hole (BH). The SN explosion triggers hypercritical accretion onto the companion. On the other hand, the associated GW detection rate inferred from GRBs has been already calculated but at a time when binaries were considered the progenitors of only short GRBs, see e.g. (Wanderman & Piran, 2015). The electromagnetic data can be used to constraint GW emission models and vice versa. This chapter is based on the publication (Ruffini et al., 2018b).

	Sub-class	In-state	Out-state	$E_{\rm p,i}$ (MeV)	$E_{\rm iso}$ (erg)	$E_{\rm iso,X}$ (erg)	$E_{\rm iso,Gev}$ (erg)	$z_{\rm max}$	$\rho_{\rm GRB}$ (Gpc^{-3}yr^{-1})
I	XRFs	CO$_{\rm core}$-NS	νNS-NS	$\lesssim 0.2$	$\sim 10^{48}$–10^{52}	$\sim 10^{48}$–10^{51}	–	1.096	100^{+45}_{-34}
II	BdHNe	CO$_{\rm core}$-NS	νNS-BH	~ 0.2–2	$\sim 10^{52}$–10^{54}	$\sim 10^{51}$–10^{52}	$\lesssim 10^{53}$	9.3	$0.77^{+0.09}_{-0.08}$
III	BH-SN	CO$_{\rm core}$-BH	νNS-BH	$\gtrsim 2$	$> 10^{54}$	$\sim 10^{51}$–10^{52}	$\gtrsim 10^{53}$	9.3	$\lesssim 0.77^{+0.09}_{-0.08}$
IV	S-GRFs	NS-NS	MNS	$\lesssim 2$	$\sim 10^{49}$–10^{52}	$\sim 10^{49}$–10^{51}	–	2.609	$3.6^{+1.4}_{-1.0}$
V	S-GRBs	NS-NS	BH	$\gtrsim 2$	$\sim 10^{52}$–10^{53}	$\lesssim 10^{51}$	$\sim 10^{52}$–10^{53}	5.52	$\left(1.9^{+1.8}_{-1.1}\right) \times 10^{-3}$
VI	U-GRBs	νNS-BH	BH	$\gtrsim 2$	$> 10^{52}$	–	–	–	$\gtrsim 0.77^{+0.09}_{-0.08}$
VII	GRFs	NS-WD	MNS	~ 0.2–2	$\sim 10^{51}$–10^{52}	$\sim 10^{49}$–10^{50}	–	2.31	$1.02^{+0.71}_{-0.46}$

Table 6.1 Summary of the astrophysical aspects of the different GRB sub-classes and of their observational properties. In the first four columns we indicate the GRB sub-classes and their corresponding *in-states* and the *out-states*. In columns 5–8 we list the ranges of $E_{\rm p,i}$ and $E_{\rm iso}$ (rest-frame 1–10^4 keV), $E_{\rm iso,X}$ (rest-frame 0.3–10 keV), and $E_{\rm iso,GeV}$ (rest-frame 0.1–100 GeV). Columns 9 and 10 list, for each GRB sub-class, the maximum observed redshift and the local observed rate $\rho_{\rm GRB}$ obtained in (Ruffini et al., 2016c).

6.1 Gamma Ray Burst Classification

Long GRBs, according to the IGC paradigm (Ruffini et al., 2015a), are classified into three sub-classes (Ruffini et al., 2016b):

I. X-ray flashes (XRFs) with isotropic energy $E_{\rm iso} \lesssim 10^{52}$ erg and rest-frame spectral peak energy $E_{p,i} \lesssim 200$ keV. This class occurs in $\rm CO_{core}$–NS binaries when the hypercritical accretion onto the NS companion is not enough to induce gravitational collapse into a BH (Becerra et al., 2016, 2015). Thus, the *out-states* of XRFs are binaries composed of a newly-formed $\sim$ 1.4–1.5 $M_\odot$ NS (hereafter νNS) born in the SN explosion, and a massive NS (MNS) which accreted matter from the SN ejecta. Their occurrence rate is $\rho_{\rm XRF} = 100^{+45}_{-34}$ Gpc^{-3} yr^{-1} (Ruffini et al., 2016c), which is in agreement with those for low-luminous long GRBs (Liang et al., 2007; Virgili et al., 2009; Sun et al., 2015).

II. Binary-driven hypernovae (BdHNe) with $E_{\rm iso} \gtrsim 10^{52}$ erg and $E_{p,i} \gtrsim 200$ keV. BdHNe occur in more compact $\rm CO_{core}$–NS binaries which leads to a more massive hypercritical accretion onto the NS, hence leading to BH formation. Therefore, the *out-states* of BdHNe are νNS-BH binaries (Becerra et al., 2016; Fryer et al., 2015; Becerra et al., 2015). Their occurrence rate is $\rho_{\rm BdHN} = 0.77^{+0.09}_{-0.08}$ Gpc^{-3} yr^{-1} (Ruffini et al., 2016c), which is in agreement with those for high-luminous long GRBs (Wanderman & Piran, 2010; Sun et al., 2015).

III. BH-SN with $E_{\rm iso} \gtrsim 10^{54}$ erg and $E_{p,i} \gtrsim 2$ MeV. BH-SN occur in close $\rm CO_{core}$-BH binaries (Ruffini et al., 2001) in which the hypercritical accretion produces, as *out-states*, a more massive BH and a νNS. Such BH-SN systems correspond to the late evolutionary stages of X-ray binaries, as Cyg X-1 and Cyg X-3 (Giacconi & Ruffini, 1978), or microquasars (Mirabel & Rodríguez, 1998). These systems are here considered a sub-set of the BdHNe. Therefore, in the following we assume the rate of BdHNe as an upper limit to the rate of BH-SNe, i.e. $\rho_{\rm BH-SN} \lesssim 0.77^{+0.09}_{-0.08}$ Gpc^{-3} yr^{-1} (Ruffini et al., 2016c).

Short GRBs, which also within the traditional models (see, e.g., Goodman, 1986; Paczynski, 1986; Eichler et al., 1989b; Narayan et al., 1991; Meszaros & Rees, 1997; Rosswog et al., 2003b; Lee et al., 2004b; Berger, 2014) originate from NS-NS or NS-BH binaries, are divided into three sub-classes (Fryer et al., 2015; Ruffini et al., 2015b, 2016c):

IV. Short gamma-ray flashes (S-GRFs), with $E_{\rm iso} \lesssim 10^{52}$ erg and $E_{p,i} \lesssim 2$ MeV, occur when no BH is formed in the NS-NS merger, i.e. they lead to a MNS. Their occurrence rate is $\rho_{\rm S-GRF} = 3.6^{+1.4}_{-1.0}$ Gpc^{-3} yr^{-1} (Ruffini et al., 2016c), which is in agreement with the estimates obtained from the whole short burst population reported in the literature (Wanderman & Piran, 2015; Sun et al., 2015).

V. Authentic short GRBs (S-GRBs), with $E_{\rm iso} \gtrsim 10^{52}$ erg and $E_{p,i} \gtrsim 2$ MeV, occur when a BH is formed in the NS-NS merger. Their occurrence rate is $\rho_{\rm S-GRB} = \left(1.9^{+1.8}_{-1.1}\right) \times 10^{-3}$ Gpc^{-3} yr^{-1} (Ruffini et al., 2016c).

VI. Ultra-short GRBs (U-GRBs), a new sub-class of short bursts originating from νNS-BH merging binaries. Such systems are yet unobserved and present a great challenge not only in the present case of high-energy but also possibly in the radio band where they would manifest themselves as pulsar-BH binaries (see, e.g., Tauris et al., 2015, and references therein). They can originate from BdHNe (see II above) or from BH-SN events (see III above). We recall that in (Fryer et al., 2015) it is shown that the majority of BdHN *out-states* remain bound. We thus assume as an ansatz that $\rho_{\rm U-GRB} \approx \rho_{\rm BdHN} = 0.77^{+0.09}_{-0.08}$ Gpc^{-3} yr^{-1} (Ruffini et al., 2016c).

VII. Gamma-ray flashes (GRFs) have $10^{51} \lesssim E_{\rm iso} \lesssim 10^{52}$ erg and $0.2 \lesssim E_{p,i} \lesssim 2$ MeV. This sub-class of sources originates in NS-WD mergers (Ruffini et al., 2016c). These binaries are notoriously very common astrophysical systems (Cadelano et al., 2015) and possible evolutionary scenarios leading to such mergers have been envisaged (see, e.g., Lazarus et al., 2014; Tauris et al., 2000). GRFs form a MNS and not a BH (see Ruffini et al., 2016c, for details). Their rate of occurrence is $\rho_{\rm GRF} = 1.02^{+0.71}_{-0.46}$ Gpc^{-3} yr^{-1} (Ruffini et al., 2016c).

Interestingly, it has been shown in (Ruffini et al., 2016c; Fryer et al., 2015; Becerra et al., 2015) that the *out-states* of long GRBs can become the *in-states* of short GRBs. Since $\rho_{\rm XRF} > \rho_{\rm S-GRF}$ and $\rho_{\rm XRF} > \rho_{\rm S-GRB}$, the *out-states* of XRFs (νNS-NS) could be the *in-states* of S-GRFs (NS-NS mergers leading to a MNS) and S-GRBs (NS-NS mergers leading to a BH).

There is also an additional evolutionary scenario concerning the NS-WD merger, namely that they are produced from an S-GRF (Ruffini et al., 2016c). The merger of a mass-asymmetric NS-NS binary with total mass $m_1 + m_2$ smaller than $M_{\rm crit}$ can produce a MNS with a low-mass WD companion (see Bildsten & Cutler, 1992, and references therein), a type of binary of great current interest (see, e.g., Lazarus et al., 2014; Tauris et al., 2000).

The rate of occurrence of the above GRB sub-classes has been recently estimated in (Ruffini et al., 2016b) assuming the absence of beaming. Table 6.1 shows a summary of the astrophysical aspects related to the GRB sub-classes and their observational properties.

6.2 Gravitational Wave Emission and Detectability

In order to assess the detectability, it is assumed that the binary evolution is only driven by GW emission, despite the gravitational energy of the system in the merger phase is dominated by the X, gamma-ray and GeV emission (see Table 6.1). This assumption is made with the only aim of establishing an absolute upper limit to the GW emission and its detectability under the most optimistic conditions according to the model.

The minimum GW frequency detectable by the broadband aLIGO interferometer is $f_{\rm min}^{\rm aLIGO} \approx 10$ Hz (LIGO Scientific Collaboration et al., 2015). Since during the binary inspiral the GW frequency is twice the orbital one (see below Sec. 6.2.2), the above implies a binary is inside the aLIGO band for orbital periods $P_{\rm orb} \lesssim 0.2$ s. Thus, CO$_{\rm core}$-NS binaries, *in-states* of XRFs and BdHNe, and CO$_{\rm core}$-BH binaries, *in-states* of BH-SN, are not detectable by aLIGO since they have orbital periods $P_{\rm orb} \gtrsim 5$ min $\gg 0.2$ s. Concerning their *out-states* after the corresponding hypercritical accretion processes, namely νNS-NS, *out-states* of

XRFs, and νNS-BH, *out-states* of BdHNe and BH-SNe, they are not detectable by aLIGO at their birth but only when approaching the merger. In the case of NS-WD binaries, the WD large radius and its very likely tidal disruption by the NS make their GW emission hard to be detected (see, e.g., Paschalidis et al., 2009). Thus, we do not consider NS-WD binaries in the following discussion. The analysis of GW emission during the final coalescence and merger of the νNS-NS binaries produced by XRFs is included in the analysis of the S-GRF and S-GRB sub-classes, and the merger of νNS-BH binaries produced in BdHNe and BH-SNe is included in the one of U-GRBs.

The NS structure is needed in order to define the possible masses of the components of the binary systems. In particular, the maximum stable NS mass is required, i.e., the critical mass for gravitational collapse to a BH. The critical mass lies within the range 2.2–3.4 $M_\odot$ depending on the equation of state (EOS) and on the NS angular momentum (see Cipolletta et al., 2015; Becerra et al., 2015; Belvedere et al., 2014 for details). These values correspond to EOS based on relativistic nuclear mean-field models (in this case the NL3, TM1 and GM1 models) and to a NS angular momentum from $J = 0$ up to $J_{\rm max} \approx 0.7 GM^2/c$ (Cipolletta et al., 2015). Hereafter, the stiffest model is used, namely the NL3 EOS, which leads to the largest NS critical mass: from $M_{\rm crit} \approx 2.7\ M_\odot$ at $J = 0$, that, as expected, is lower than the non-rotating critical mass upper limit of 3.2 $M_\odot$ established by (Rhoades & Ruffini, 1974), to $M_{\rm crit} \approx 3.4\ M_\odot$ at $J_{\rm max}$ (Cipolletta et al., 2015). For S-GRFs, the simple case of symmetric binary (NS-NS) mergers, $m_1 = m_2 = m$, is considered. The precise value of the merging NS masses leading to a BH is still poorly known, thus roughly half the maximum NS critical mass is chosen for the NSs. For the sake of completeness, mass values from $m \approx 1\ M_\odot$ to $m \approx 1.7\ M_\odot$ are also explored. For S-GRBs, non-spinning symmetric binary components are considered with values starting from the upper edge of the S-GRF progenitors, i.e. $m \approx 1.7\ M_\odot$, up to the maximum non-rotating stable mass, i.e. $m \approx 2.8\ M_\odot$. For the U-GRBs which are *out-states* of BdHN, $m_1 = 1.5\ M_\odot$ is chosen for the νNS mass and $m_{\rm BH} = 2.7$–$3.4\ M_\odot$ for the BH mass. For the U-GRBs which are *out-states* of BH-SN , $m_1 = 1.5\ M_\odot$ is adopted for the νNS mass and $m_{\rm BH} = 3.4$–$10\ M_\odot$ for the BH mass.

6.2.1 Signal-to-noise Ratio

Since the GW signal might be deep inside the noise, the signal-to-noise ratio, ρ, is usually computed using the matched filter technique (Flanagan & Hughes, 1998) (see previous chapter). In the detector's frame the GW frequency is redshifted by a factor $1 + z$ with respect to the one in the source's frame, f_s, i.e. $f = f_s/(1 + z)$. The exact position of the binary relative to the detector and the orientation of its rotation plane are usually unknown, thus it is a common practice to estimate the signal-to-noise ratio averaging over all the possible locations and orientations. The average is given by eqs. (5.17) and (5.18), but this time characteristic amplitude receives corrections from the propagation over cosmological distances (Flanagan & Hughes, 1998),

$$h_c = \frac{(1+z)}{\pi d_l}\sqrt{\frac{\langle F_+^2\rangle}{2}\frac{G}{c^3}\frac{dE}{df_s}[(1+z)f]}, \tag{6.1}$$

where,

$$d_l = \frac{(1+z)c}{H_0}\int_0^z [\Omega_M(1+x)^3 + \Omega_\Lambda]^{-1/2}dx, \tag{6.2}$$

is the source luminosity distance. The cosmological model used in the calculation of d_l is ΛCDM, with paramaters $H_0 = 71$ km s^{-1} Mpc^{-1}, $\Omega_M = 0.27$ and $\Omega_\Lambda = 0.73$ (Rigault et al., 2015).

6.2.2 Gravitational Wave Energy Spectrum

A binary system which emits GWs, evolves in time through two different regimes: the first is the *inspiral regime* and the second, here referred as the *merger regime*, is composed in the most general case of the final plunge, the merger, and the ringdown (oscillations) of the newly formed object. During the inspiral regime the system trajectory is a series of quasi-circular orbits and it is well described by the point-like Newtonian quadrupole approximation (Peters & Mathews, 1963; Peters, 1964; Landau & Lifshitz, 1951). The GW frequency is twice the orbital frequency ($f_s = 2f_{\rm orb}$) and grows monotonically. Recall from section 2.3.1 that the energy spectrum during the inspiral regime is,

$$\frac{dE}{df_s} = \frac{1}{3}(\pi G)^{2/3}M_c^{5/3}f_s^{-1/3}. \tag{6.3}$$

The total energy emitted during this regime can be estimated as the binding energy of the binary at the ISCO. For a test-particle in the Schwarzschild background, the ISCO is located at $r_{\rm LSO} = 6GM/c^2$ and the binding energy is,

$$\Delta E_{\rm insp} = \big(1 - 2\sqrt{2}/3\big)\mu c^2. \tag{6.4}$$

The GW spectrum of the merger regime is characterized by a GW burst (see, e.g., Davis et al., 1971; Shibata & Taniguchi, 2011; Bernuzzi et al., 2015a). Thus, to estimate whether this part of the signal contributes to the signal-to-noise ratio, it is sufficient to estimate the location of the GW burst in the frequency domain and its energy content. The frequency range spanned by the GW burst is $\Delta f = f_{\rm qnm} - f_{\rm merger}$, where $f_{\rm merger}$ is the frequency at which the merger starts and $f_{\rm qnm}$ is the frequency of the ringdown. The typical value of the merger regime spectrum can be estimated as,

$$\left(\frac{dE}{df_s}\right)_{\rm merger} \sim \frac{\Delta E_{\rm merger}}{\Delta f}, \tag{6.5}$$

where $\Delta E_{\rm merger}$ is the energy emitted during the merger regime.

6.2.3 Binary Neutron Star Merger

Numerical relativity simulations (e.g. Shibata & Taniguchi, 2011; Bernuzzi et al., 2015a) show that finite size effects might end the inspiral regime before the ISCO. After this point, the GW spectrum damps exponentially. For the case of binary neutron star the merger starts at an orbit larger than the ISCO, and for the case of a NS-BH, the merger can occur below the ISCO making the spectrum similar to a BH-BH merger. When the merger occurs long before the ISCO, there is no plunge. Therefore, the emitted energy will be less than the case when the plunge is present. Therefore, if the energy emitted in the merger is adopted as the one of a binary BH merger, $\Delta E_{\rm merger}$ constitutes an upper limit (Detweiler & Szedenits, 1979; Nagar et al., 2007),

$$\Delta E_{\rm merger} \approx 0.5\nu^2 Mc^2. \tag{6.6}$$

In order to complete the estimate of the merger spectrum, the actual value of Δf is needed.

Table 6.2 Properties of the GW emission of S-GRFs, S-GRBs and U-GRBs. Column 1: GRB sub-class. Column 2: energy emitted in GWs during the inspiral regime $\Delta E_{\rm insp}$ given by Eq. (6.4). Column 3: energy emitted in GWs during the merger regime (plunge+merger+ringdown) $\Delta E_{\rm merger}$ given by Eq. (6.6). Columns 4: GW frequency at merger. Column 5: GW frequency of the ringdown regime. Column 6: lowest cosmological redshift value $z^{\rm obs}_{\rm min}$ at which each sub-class has been observed. Column 7: luminosity distance corresponding to $z^{\rm obs}_{\rm min}$, $d_{l_{\rm min}}$, estimated from Eq. (6.2). Columns 8 and 9: GW horizon calculated with the sensitivity of the first run of aLIGO (O1) and the expected final sensitivity (2022+), respectively. We have used for S-GRFs (1.4+1.4) $M_\odot$, for S-GRBs (2.0+2.0) $M_\odot$ and, for U-GRBs (1.5+3.0) $M_\odot$ and (1.5+10.0) $M_\odot$ respectively for the *out-states* of BdHNe and of BH-SN. Even if no U-GRB has yet been identified, we use here the values of $z^{\rm obs}_{\rm min}$ and $d_{l_{\rm min}}$ corresponding to the closest BdHN observed.

	$\Delta E_{\rm insp}$ (erg)	$\Delta E_{\rm merger}$ (erg)	$f_{\rm merger}$ (kHz)	$f_{\rm qnm}$ (kHz)	$z^{\rm obs}_{\rm min}$	$d_{l_{\rm min}}$ (Mpc)	$d_{\rm GW}$ (Mpc) O1	2022+
S-GRF	7.17×10^{52}	1.60×10^{53}	1.20	3.84	0.111	508.70	168.38	475.61
S-GRB	1.02×10^{53}	2.28×10^{53}	1.43	2.59	0.903	5841.80	226.71	640.29
U-GRB	1.02×10^{53}	2.03×10^{52}	0.98	2.30	0.169	804.57	235.62	665.72
BH-SN	1.34×10^{53}	1.35×10^{53}	0.38	0.90	0.169	804.57	362.27	1023.43

The approach to the merger point, $r = r_{\rm merger}$, depends on the nature of the binary neutron star. Typically, the merger is assumed to start at the point of maximum GW strain (see, e.g., Bernuzzi et al., 2015a, and references therein). However, since the transition from a binary system to a single merged object is not sharp, different definitions of the merger point can be found in the literature (see, e.g., Kawaguchi et al., 2015). For the present calculation it is sufficient to estimate the frequency at "contact", i.e. the frequency at a binary separation $r_{\rm contact} \approx r_1 + r_2$ where r_i is the radius of the i-component. This certainly sets a lower limit to the frequency at maximum strain at merger, i.e. $r_{\rm contact} \gtrsim r_{\rm merger}$. The frequency of merger for a NS-NS system is taken as,

$$f^{\rm NS-NS}_{\rm merger} \approx f^{\rm NS-NS}_{\rm contact} = \frac{1}{\pi}\frac{c^3}{GM}\left[\frac{\mathcal{C}_1\mathcal{C}_2(1+q)}{\mathcal{C}_1 + q\mathcal{C}_2}\right]^{3/2}, \tag{6.7}$$

where $q = m_2/m_1$ is the mass-ratio which is related to the symmetric mass-ratio parameter by $\nu = q/(1+q)^2$, and $\mathcal{C}_i \equiv Gm_i/c^2 r_i$ is the compactness of the i-component. For a symmetric binary neutron star, $f^{\rm NS-NS}_{\rm contact} \approx (1/\pi)(c^3/G)\mathcal{C}^{3/2}_{\rm NS}/M$, where $\mathcal{C}_{\rm NS} \equiv \mathcal{C}_1 = \mathcal{C}_2$ is the compactness parameter of the initial NS. For example, a NS described by NL3 EOS has compactness which lies in the range $\mathcal{C}_{\rm NS} \approx 0.14$–$0.3$ with mass range 1.4–2.8 $M_\odot$ (see, e.g., Cipolletta et al., 2015). Thus, a binary with $M = (1.4 + 1.4)\ M_\odot = 2.8\ M_\odot$, with the same EOS, has $f^{\rm NS-NS}_{\rm contact} \approx 1.34$ kHz, and for $M = (2.0 + 2.0)\ M_\odot = 4.0\ M_\odot$, $f^{\rm NS-NS}_{\rm contact} \approx 1.43$ kHz.

In the merger regime either a BH or a MNS can be formed. If a BH is formed, the $l = 2$ multipole (quadrupole) quasi-normal oscillations lead to a spectrum that peaks at a frequency (Davis et al., 1971, 1972a)

$$f_{\rm qnm}^{\rm BH} \approx \frac{0.32}{2\pi}\frac{c^3}{GM}, \tag{6.8}$$

i.e. $f_{\rm qnm} \approx 3.4$ kHz for a Schwarzschild BH of 3 $M_\odot$. In the case of a rotating BH, namely a Kerr BH, the peak frequency shifts to higher values (Detweiler, 1980). Thus, the value of $f_{\rm qnm}^{\rm BH}$ for a non-rotating BH can be considered as a lower bound to the peak frequency.

When the merger does not lead to a BH, the merger frequency is dominated by the oscillations of a MNS. This last frequency is of the order of

$$f_{\rm qnm}^{\rm MNS} \approx \frac{1}{\pi}\left(\frac{GM}{R^3}\right)^{1/2} = \frac{1}{\pi}\left(\frac{c^3}{G}\right)\frac{\mathcal{C}_{\rm MNS}^{3/2}}{M}, \tag{6.9}$$

where R is the radius of the MNS and $\mathcal{C}_{\rm MNS} \equiv GM/(c^2 R)$ its compactness. In both cases of BH or MNS formation, it is satisfied $f_{\rm qnm} > f_{\rm contact}$. The above frequency estimates are consistent with values obtained from full numerical relativity simulations (see, e.g., (Anninos et al., 1995; Bernuzzi et al., 2015a)).

6.2.4 Neutron-Black Hole Merger

For a NS-BH merger, the approach to the merger is different since general relativistic effects induce the end of inspiral before the "contact". As as example, a NS-BH system with $m_1 = m_{\rm BH} \approx 3\ M_\odot$ and $m_2 = M_{\rm NS} \approx 1.5\ M_\odot$, $M = 1.5 + 3.0\ M_\odot = 4.5\ M_\odot$ will be analyzed below. In this case $r_1 = 2Gm_{\rm BH}/c^2$ (for a Schwarzschild BH) and $r_2 = Gm_2/(c^2\mathcal{C}_2)$, so $r_{\rm contact} \approx 3.3GM/c^2$. Within the test-particle limit, the ISCO around a Schwarzschild BH occurs at $r_{\rm ISCO} = 6Gm_{\rm BH}/c^2 \approx 6GM/c^2 > r_{\rm contact}$. Thus, $r_{\rm contact} < r_{\rm ISCO}$ which suggests that a NS-BH binary, similar to a binary BH, can pass from the inspiral regime to the plunge at $r_{\rm plunge} = r_{\rm ISCO}$, then to the merge at $r_{\rm merger} \approx r_{\rm contact}$, to final formation of the BH which settles down during the ringdown. At $r_{\rm plunge}$, the GW frequency is,

$$f_{\rm plunge}^{\rm NS-BH} \approx \frac{1}{\pi}\left(\frac{GM}{r_{\rm ISCO}^3}\right)^{1/2} = \frac{1}{\pi 6^{3/2}}\left(\frac{c^3}{GM}\right). \tag{6.10}$$

As in the previous case of BH formation from a binary neutron star merger, the NS-BH post-merger GW spectrum will be dominated by frequencies given by eq. (6.8). Namely, for the present example $f_{\rm plunge}^{\rm NS-BH} \approx 980$ Hz and $f_{\rm qnm}^{\rm BH} \approx 2.3$ kHz. Hence, in the class of U-GRBs $\Delta f_{\rm U-GRB}$ is,

$$\Delta f_{\rm U-GRB} = f_{\rm qnm}^{\rm BH} - f_{\rm plunge}^{\rm NS-BH} \approx 0.092\frac{c^3}{\pi GM}. \tag{6.11}$$

The above analysis neglected the possibility that the NS can be tidally disrupted by the BH before it reaches the ISCO. The NS is disrupted by the BH if $r_{\rm ISCO} < r_{\rm td}$, where $r_{\rm td}$ is the tidal disruption radius. Numerical simulations of NS-BH binary mergers suggest

$r_{\rm td} \approx 2.4q^{-1/3}R_{\rm NS}$ and $r_{\rm ISCO} \approx 6GM/c^2[1-0.44q^{1/4}(1-3.54\mathcal{C}_{\rm NS})]^{-2/3}$ (see Shibata & Taniguchi, 2011 and references therein), where $q \equiv m_2/m_1 \leq 1$ is the binary mass-ratio $R_{\rm NS}$ the NS radius, and $C_{\rm NS}$ its compactness. It can be seen that the ratio of the tidal to the ISCO radius is a decreasing function of the BH mass keeping constant the NS mass, but it is always close to unity. In the range $m_{\rm BH} = 3 - 10\ M_\odot$ and $m_{\rm NS} = 1.5\ M_\odot$, with NL3 EOS, the NS is tidally disrupted when $m_{\rm BH} \lesssim 6\ M_\odot$. It remains to investigate the dependence of tidal disruption on the EOS through $C_{\rm NS}$, which can only be answer by a vast range of simulations. However, for the mass range of the system in consideration, it turns out that $r_{\rm td} \approx r_{\rm ISCO}$, so in order to avoid uncertainties, the end of inspiral is chosen to be at the frequency given by (6.10).

6.2.5 Characteristic Strain and Detectors Sensitivity

The characteristic strain (6.1) is now estimated from the information given above. This is used to assess the detectability by comparing and contrast with the strain noise of the different detectors. Figure 6.1 shows characteristic strain (6.1) corresponding to S-GRFs, S-GRBs and U-GRBs. In this figure the following masses are chosen: $(1.4+1.4)\ M_\odot$ νNS-NS merger for S-GRFs, a $(2.0 + 2.0)\ M_\odot$ νNS-NS merger for S-GRBs, a $(1.5 + 3.0)\ M_\odot$ νNS-BH merger for U-GRBs produced by *out-states* of BdHNe, and a $(1.5 + 10.0)\ M_\odot$ νNS-BH merger for U-GRBs produced by *out-states* of BH-SNe. This plot assumes that these sources are located at the closest luminosity distance d_l at which each sub-class has been observed (see Table 6.2 for details). It is also shown the strain noise of aLIGO (for the O1 and expected 2022+ runs), of Advanced Virgo (expected), of NAUTILUS bar detector, and the expected strain noise curve of the space-based interferometer eLISA (see, e.g., Klein et al., 2016). Narrow-band resonant bar detectors such as ALLEGRO, AURIGA, EXPLORER, NAUTILUS and NIOBE are sensitive within a bandwidth of $\sim$ 1–10 Hz around the resonant frequency which is typically $f_0 \sim 1$ kHz (see, e.g., Table 2 in Camp & Cornish, 2004, for a summary of the properties of the bar detectors). The bar detector with the wider bandwidth is NAUTILUS with a minimum strain spectral noise $\sqrt{S_n} = 10^{-21}\ {\rm Hz}^{-1/2}$ at $f_0 = 935$ Hz and $\sqrt{S_n} \leq 10^{-20}\ {\rm Hz}^{-1/2}$ in a bandwidth ~ 30 Hz around f_0 (Astone et al., 2008). This implies that a 1 ms GW burst would be detected by this instrument if it has a strain amplitude $h \gtrsim 3 \times 10^{-19}$ (Astone et al., 2006, 2008).

From this figure it can be concluded: i) before the merge all the systems transit, during their inspiral regime which spans the frequency range $f < f_{\rm merger}/(1 + z)$, first in the eLISA frequency band to then enter the aLIGO one in the final circular orbits (when $P_{\rm orb} < 0.2$ s). The narrow bandwidth of the bar detectors does not cover these frequencies. For the adopted distances the characteristic strain generated by all these sources is below the sensitivity of eLISA. S-GRBs are also below the aLIGO sensitivity. S-GRFs and U-GRBs are marginally inside aLIGO and AdV noise curve. ii) The merger regime, which expands frequencies from $f_{\rm contact}/(1 + z)$ to $f_{\rm qnm}/(1 + z)$ (see in Table 6.2 the frequencies and redshift), is outside the eLISA frequency band but inside the aLIGO and bar detectors ones. The characteristic strain in this final merger phase $h \sim 10^{-24}$–10^{-23} is unfortunately well below the sensitivity of both aLIGO (see also Kobayashi & Mészáros, 2003 for similar conclusions) and bar detectors.

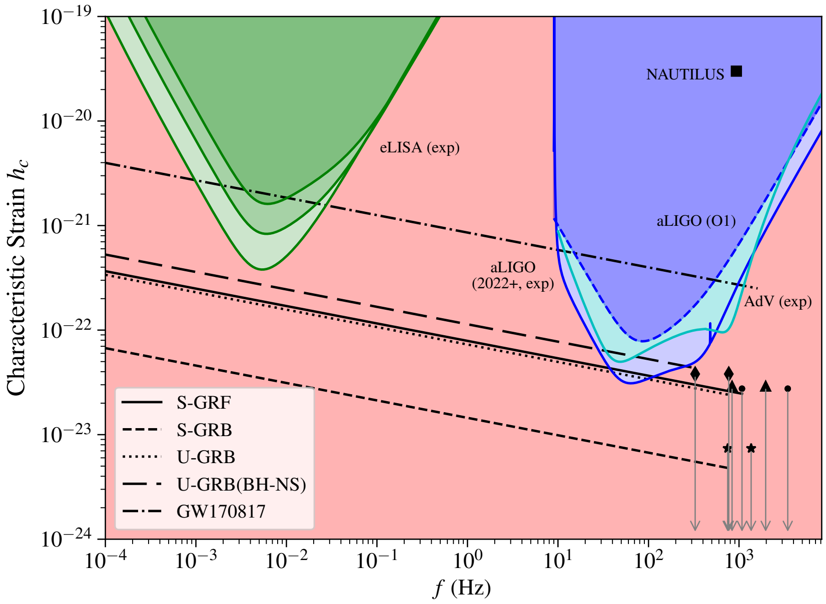

Figure 6.1 Comparison of the characteristic strain h_c of S-GRFs, S-GRBs and U-GRBs with the strain noise (i.e. $\sqrt{f S_n(f)}$. The cosmological redshift and corresponding luminosity distance of the closest observed source of each sub-class was used (see Table 6.2). The following three curves correspond to the inspiral regime of the coalescence: S-GRFs with $(1.4 + 1.4)\ M_\odot$ (solid curve), S-GRBs with $(2.0 + 2.0)\ M_\odot$ (short-dashed curve), U-GRB with $(1.5 + 3.0)\ M_\odot$, (dotted curve) and U-GRB (BH-SN) with $(1.5 + 10.0)\ M_\odot$ (long dashed curve). The dot, star, triangle and diamond correspond to the typical h_c after the merger, for S-GRF, S-GRB, U-GRB and U-GRB (BHSN), respectively. The first point is located at $f_{\rm merger}/(1 + z)$ and the second at $f_{\rm qnm}/(1 + z)$ for the configuration. The green lines, from top to bottom, are the sensitivity curves of the N2A1, N2A2 and N2A5 configurations of eLISA (Klein et al., 2016). The dashed and continuous blue lines correspond to the sensitivity curves of aLIGO O1 (2015/2016) and aLIGO 2022+ runs (Abbott et al., 2016b), respectively. The filled square indicates the sensitivity of the NAUTILUS resonant bar. The green and blue filled areas correspond to the regions of detectability of eLISA and aLIGO, respectively. The red filled area indicates the region of undetectability by any of the above instruments.

6.3 Gravitational Wave Detection Rate

As usual, the threshold $\rho_0 = 8$ (Abbott et al., 2016b) for single detector was used to calculate the detection rate. This minimum ρ_0 defines a maximum detection distance or GW horizon distance, denoted by $d_{\rm GW}$ and given by (5.21). Gravitational wave horizons for S-GRFs, S-GRBs and U-GRBs are shown in table 6.1. Since not all the sources are optimally aligned with the detector, the number of detected sources inside a sphere of radius $d_{\rm GW}$ will be a fraction $\mathcal{F}^3$ of the total. This fraction determines the range of the detector $\mathcal{R} = \mathcal{F} d_{\rm GW}$, with $\mathcal{F}^{-1} = 2.2627$ (Finn & Chernoff, 1993). In order to give an estimate of the annual number of detectable binaries associated with GRBs, the *search volume* was computed as described in ref. (Abbott et al., 2016b), $\mathcal{V}_s = V_{\rm max}^{\rm GW} \mathcal{T}$, where $V_{\rm max}^{\rm GW} = (4\pi/3)\mathcal{R}^3$ and $\mathcal{T}$ is the observing time. The lower and upper values of $\mathcal{V}_s$ for

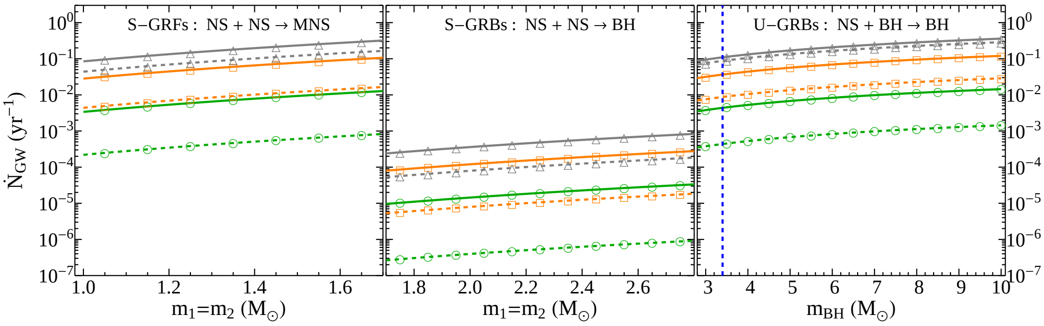

Figure 6.2 Expected annual GW upper and lower bounds (the solid and the dashed lines, respectively) for the detections expected from S-GRFs (left panel), S-GRBs (middle panel), and U-GRBs (right panel), for three selected observational campaigns: 2015/2016 (O1: green curves with circles), 2017/2018 (O3: orange curve with squares), and 2022+ (gray curve with triangles). The vertical blue dashed line in the plot of U-GRBs separates νNS-BH binaries produced by BdHN (BH masses equal to the NS critical mass) and BH-SN (BH masses larger than the NS critical mass).

a (1.4+1.4) $M_\odot$ NS binary for the different observational campaigns reported in (Abbott et al., 2016b) are: 2015/2016 (O1) with $\mathcal{T} = 4$ months, $\mathcal{V}_S = (0.5\text{–}4) \times 10^5$ Mpc^3 yr, and the one by the entire network including LIGO-India at design sensitivity (2022+) with $\mathcal{T} = 1$ yr, $\mathcal{V}_S = 2 \times 10^7$ Mpc^3 yr. The maximum possible sensitivity reachable in 2022+ leads to $d_{\rm GW} \approx 0.2$ Gpc, hence $V^{\rm GW}_{\rm max} \approx 0.033$ Gpc^3, for such a binary. The information for a (1.4+1.4) $M_\odot$ binary was used to extrapolate it to other binaries with different masses since the $d_{\rm GW}$ scales with the chirp mass as $M_c^{5/6}$ (see Fig. 6.2). From the inferred occurrence rates $\rho_{\rm GRB}$ (not to be confused with signal-to-noise ratio ρ) summarized in tab 6.1, fig. 6.2 shows the expected number of GW detections by aLIGO,

$$\dot{N}_{\rm GW} = \rho_{\rm GRB} V^{\rm GW}_{\rm max}, \tag{6.12}$$

The expected GW detection rate by aLIGO given by above equation, $\dot{N}_{\rm GW}$; the inferred occurrence rate of GRBs, $\dot{N}_{\rm GRB}$; and the observed GRB rate from γ-ray telescopes (AGILE, BATSE, BeppoSAX, *Fermi*, *HETE-II*, *INTEGRAL*, Konus/WIND and *Swift*) are compared and contrasted in tab. 6.3. This last rate was simply estimated as $\dot{N}^{\rm obs}_{\rm GRB} = N^{\rm obs}_{\rm GRB}/T_{\rm obs}$ where $N^{\rm obs}_{\rm GRB}$ is the number of GRBs detected in the observing time $T_{\rm obs}$. The rate $\dot{N}_{\rm GRB}$ is obtained from the GRB specific rate through the reconstruction of the GRB luminosity function and the study of its evolution with the redshift (Ruffini et al., 2016b). This estimate, therefore, is larger than $\dot{N}^{\rm obs}_{\rm GRB}$ which is limited to those events beyond the detector sensitivity threshold, falling inside its field of view and within its operational time.

6.4 GW170817 event

Meanwhile the present work was submitted to publication, the GW170817 (Abbott et al., 2017a) was announced by the LIGO-Virgo Collaboration, which is consistent with a binary neutron star merger. This might be seen in tension with the above rates corresponding to

Table 6.3 Column 1: GRB sub-class. Column 2: inferred number of GRBs per year in the entire Universe, $\dot{N}_{\rm GRB}$, for each GRB sub-class (see also Fig. 6 in Ruffini et al., 2016c). Column 3: number of GRBs observed per year, $\dot{N}_{\rm GRB}^{\rm obs}$, obtained from the observations of γ-ray telescopes such as AGILE, BATSE, BeppoSAX, *Fermi*, *HETE-II*, *INTEGRAL*, Konus/WIND and *Swift*, in the indicated years of observations (see also Tables 2–6 in Ruffini et al., 2016c). Column 4: expected rate of GW detections by aLIGO of all the GRB sub-classes, computed for three selected observational campaigns: 2015/2016 (O1), 2017/2018 (O3) and the one by the entire network including LIGO-India at design sensitivity, 2022+. The typical masses used here are the same of Table 6.2.

GRB sub-class	$\dot{N}_{\rm GRB}$ (yr^{-1})	$\dot{N}_{\rm GRB}^{\rm obs}$ (yr^{-1})	$\dot{N}_{\rm GW}$ (yr^{-1})
XRFs	144–733	1 (1997–2014)	undetectable
BdHNe	662–1120	14 (1997–2014)	undetectable
BH-SN	$\lesssim$ 662–1120	$\lesssim$ 14 (1997–2014)	undetectable
S-GRFs	58–248	3 (2005–2014)	O1: $(0.1–2)\times10^{-3}$ O2: $0.2–1\times10^{-2}$ O3: $0.8–5\times10^{-2}$ 2022+: 0.1–0.2
S-GRBs	2–8	1 (2006–2014)	O1: $(0.1–3.1)\times10^{-6}$ O2: $(0.1–1.6)\times10^{-5}$ O3: $(0.6–7.8)\times10^{-5}$ 2022+: $(0.78–3.12)\times10^{-4}$
U-GRBs	662–1120	–	O1: $(0.36–3.6)\times 10^{-3}$ O3: 0.008–0.032 2022+: 0.076–0.095
U-GRBs (BH-SN)	$\lesssim$ 662–1120	–	O1: 0.0016–0.016 O3: $\lesssim$ 0.029–0.12 2022+: $\lesssim$ 0.3–0.36
GRFs	29-153	1 (2005–2014)	undetectable

O2. First, the energetics of this event must be analyzed in order to deduce its implications. The associated GRB called GRB 170817A, has an isotropic energy emitted in gamma rays, $E_{\rm iso} \approx 5 \times 10^{46}$ erg (Goldstein et al., 2017) and a peak luminosity $(1.7 \pm 0.1) \times 10^{47}$ erg s^{-1} (Zhang et al., 2018), thus it belongs to the S-GRF subclass. On the other hand, the local density rate from ref. (Ruffini et al., 2016b) is valid for GRBs with higher luminosity than the lowest one in each subclass. More exactly, the lowest luminosity GRB of the S-GRF subclass was GRB 050509B with $E_{\rm iso} \approx 8.5 \times 10^{48}$ erg and peak luminosity $(1.1 \pm 0.5) \times 10^{51}$ erg s^{-1}. Therefore, the aforementioned rate is not applicable to GW170817. This new event will increase the local density rate and consequently the GW detection rate. The new local density rate for S-GRF including GW170817 was calculated by Zhang et al. (2018) is increased to 30–630 Gpc^{-3} yr^{-1}. This implies a GW detection rate of 0.1–1 yr^{-1} for the O2 run, in agreement with the observation. This is also consistent with the characteristic strain shown in fig. 6.1.

6.5 Discussion

According to ref. (Ruffini et al., 2016b) short and long GRBs are divided into 7 sub-classes, all with binary progenitors. The main physical properties characterizing the outcome of X-rays, gamma-rays, high-energy and ultra high-energy detectors, as well as their occurrence rate, are shown in tab. 6.1. The key point is the specification of the *in-states* and *out-states* of the GRB progenitors, in order to associate GRBs with GW emission.

This allowed to infer for each GRB sub-class the general properties of the GW emission during the inspiral and merger regimes of the evolution. It was shown that S-GRFs, S-GRBs and U-GRBs are the GRB sub-classes relevant for the GW analysis, due to their nature. It is manifest that according to the classification, the release of the gravitational energy of the system in the merger phase is dominated by the X-rays, gamma-rays and GeV emission (see Table 6.1). However, here the GW emission was calculated with the assumption that the binary evolution is only driven by GW emission. This assumption gives an absolute upper limit and to the GW emission. The GW characteristic strain amplitude produced by the inspiral and merger regimes, was compared with the strain noise of the detectors eLISA and aLIGO, as well as of the narrow-band resonant bar NAUTILUS. This was done by using the cosmological redshift and corresponding luminosity distance of the closest observed source of each sub-class (see Table 6.2). It was shown that the inspiral regime is possibly detectable only by aLIGO (see Table 6.2 and Fig. 6.1) and the merger regime is undetectable by any of these instruments.

For each GRB sub-class it can be concluded that:

I. **XRFs:** their νNS-NS *out-states* transit, during the inspiral, first the eLISA frequency band to then enter the aLIGO one in the final orbits prior to the merging process (i.e. when $P_{\rm orb} < 0.2$ s). Resonant bar detectors are not sensitive in this inspiral regime frequency range. The characteristic strain generated by these sources in the inspiral regime is below the sensitivity of eLISA. The merger regime, (see Table 6.2), is outside the eLISA frequency band but inside the frequency band of aLIGO and bar detectors. These νNS-NS mergers can lead either to S-GRFs or S-GRBs (see in IV and V below the conclusion about their GW detectability).

II. **BdHNe:** their νNS-BH *out-states* transit, during the inspiral, first the eLISA frequency band to then enter the aLIGO one in the final orbits prior to the merging process (i.e. when $P_{\rm orb} < 0.2$ s). Resonant bar detectors are not sensitive in this inspiral regime frequency range. The characteristic strain generated by these sources in the inspiral regime is below the sensitivity of eLISA. The merger regime is outside the eLISA frequency band but inside the frequency band of aLIGO and bar detectors. See Fig. 6.1 for details. These νNS-BH mergers lead to U-GRBs (see in VI below the conclusion about their GW detectability).

III. **BH-SN:** their νNS-BH *out-states* transit, during the inspiral first the eLISA frequency band to then enter the aLIGO one in the final orbits prior to the merging process (i.e. when $P_{\rm orb} < 0.2$ s). Resonant bar detectors are not sensitive in this inspiral regime frequency range. The characteristic strain generated by these sources in the inspiral regime is below the sensitivity of eLISA. The merger regime, which expands frequencies from $f_{\rm contact}/(1+z)$ to $f_{\rm qnm}/(1+z)$ (see Table 6.2), is outside the eLISA frequency band but inside the frequency band of aLIGO and bar detectors. See Fig. 6.1 for details. These νNS-BH mergers lead to U-GRBs (see in VI below the conclusion about their GW detectability).

IV. **S-GRFs:** the final orbits of the inspiral regime (when $P_{\rm orb} < 0.2$ s) fall inside the frequency band of aLIGO and bar detectors. However, the GW energy output in the merger regime and distance leads to a characteristic strain which is not sufficient to be detectable either by aLIGO or bar detectors. See Fig. 6.1 for details. The inspiral regime is detectable for sources located at distances smaller than 168 Mpc for the O1 aLIGO run and smaller than 476 Mpc for the 2022+ run (see Table 6.2). The closest S-GRF observed up to now is, however, located at 509 Mpc. See Table 6.3 for the GW detection rate.

V. **S-GRBs:** the final orbits of the inspiral regime (when $P_{\rm orb} < 0.2$ s) fall inside the frequency band of aLIGO and bar detectors. Again, its characteristic strain is not sufficient to be detectable either by aLIGO or bar detectors. See Fig. 6.1 for details. The inspiral regime is detectable for sources located at distances smaller than 227 Mpc for the O1 aLIGO run and smaller than 640 Mpc for the 2022+ run (see Table 6.2). The closest S-GRB observed up to now is, however, located at 5842 Mpc. See Table 6.3 for the GW detection rate.

VI. **U-GRBs:** the final orbits of the inspiral regime (when $P_{\rm orb} < 0.2$ s) fall inside the frequency band of aLIGO and bar detectors. However, they are detectable by aLIGO or bar detectors. See Fig. 6.1 for details. In the case of U-GRBs originating from the BdHN *out-states*, the inspiral regime is detectable for sources located at distances smaller than 235 Mpc for the O1 aLIGO run and smaller than 666 Mpc for the 2022+ run (see Table 6.2). In the case of U-GRBs originating from the BH-SN *out-states*, the inspiral regime is detectable for sources at distances smaller than 362 Mpc for the O1 aLIGO run and smaller than 1023 Mpc for the 2022+ run (see Table 6.2). No U-GRB has yet been electromagnetically identified. The closest distance at which is located its possible progenitor, namely a BdHN, is 805 Mpc.

VII. **GRFs:** The tidal disruption of the WD by the NS produces a not detectable GW emission (see, e.g., Paschalidis et al., 2009).

The most favorable case for GW detection, with a rate of $\dot{N}_{\rm GW} = 0.1$–0.2 yr^{-1}, is that of S-GRFs (see Table 6.3). In such systems however no BH is formed. The merger of the two NSs will instead lead to a MNS. Among those producing a BH, the most favorable cases are that of U-GRBs from BdHNe with a rate $\dot{N}_{\rm GW} = 0.076$–0.095 yr^{-1} and those from BH-SN with $\dot{N}_{\rm GW} = 0.3$–0.36 yr^{-1} (see Table 6.3). Realistic $\dot{N}_{\rm GW}$ values will need the assessment of the GW to electromagnetic energy ratio which is necessarily smaller than unity from energy conservation.

Chapter 7

Gravitational Waves from Ellipsoidal Figures of Equilibrium

Nowadays, the post-merger remnant of a BNS coalescence is not certainly known both theoretically and experimentally. The search of remnant GW signal of GW170817 (Abbott et al., 2017f) could give only upper limits on the emission of the post-merger object. The possible outcomes of a NS-NS merger are the prompt formation of a BH, a unstable NS or a stable NS. Regarding WDs mergers the remnant can be a NS or a WD. In either cases, when there is no prompt formation of a BH, the post-merger object is a highly deformed object which here will be modeled as a compressible ellipsoidal figure of equilibrium. This object can be a NS or a WD. The scenario of a MNS will be studied in the next chapter together with the necessary conditions for disk formation.

In addition, it will be shown that a highly deformed WD-like objects can exhibit a chirping behaviour (similar to binaries), hereafter chirping ellipsoids (CELs) Rodriguez et al. (2018), and they will be studied in the context of space-based interferometers. Space-based, gravitational wave (GW) interferometers, such as *LISA*, *TianQin, Taiji* open the window to the GW low-frequency region and thus to a different set of astrophysical objects with respect to the ones detectable by Earth-based interferometers (eg. LIGO/Virgo). Specifically, *LISA* is sensitive to the frequency range 10^{-5}–1 Hz Barack & Cutler (2004); Amaro-Seoane et al. (2012).

7.1 Equilibrium Sequences

The deformed, rotating star is modeled as a compressible ellipsoidal star with polytropic EOS, following the work of Lai et al. (1993). A NS star is modeled with polytropic index $n = (0.5-1)$ whereas a WD with $n = (1.5-3)$. The equations derived there have basically the same form of those derived by Chandrasekhar (1963). The unit length used in this section is the radius R_0 of the non-rotating polytropic spherical star with same mass M of the ellipsoid. When the ellipsoid whose principal axes are (a_1, a_2, a_3) is *incompressible*, R_0 is equal to the mean radius $\bar{R} = (a_1 a_2 a_3)^{1/3}$. For a compressible star, $\bar{R}$ is not constant and it should not be used for defining units (Lai et al., 1993). The unit of time is $(G\pi\bar{\rho}_0)^{-1/2}$,

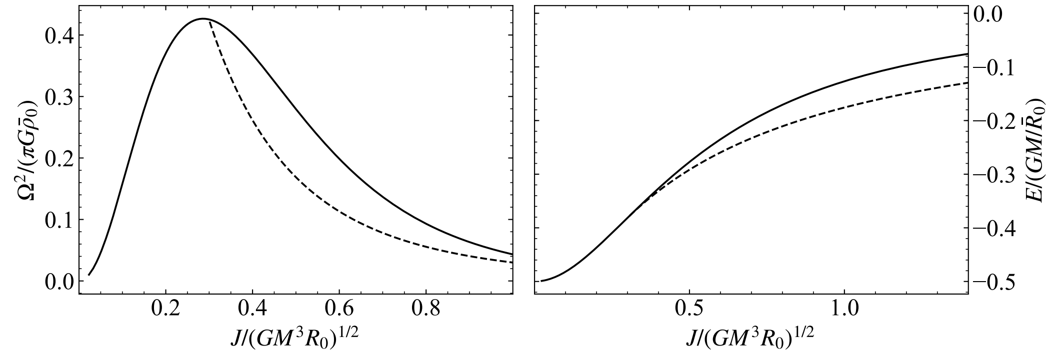

Figure 7.1 Maclaurin and Jacobi sequences for a compressible star with polytropic index $n = 1$. It can be the bifurcation point.

where $\bar{\rho}_0$ is the mean density of the non-rotating star, for example, the normalized angular velocity and vorticity are $\bar{\Omega} = \Omega/\sqrt{\pi G\bar{\rho}_0}$, $\bar{\zeta} = \zeta/\sqrt{\pi G\bar{\rho}_0}$, respectively. The EOS of the ellipsoidal star is also polytropic. The parameters characterising a polytropic star are shown in the table 7.1. The evolution of an ellipsoidal star driven by GWR follows a sequence of Riemann ellipsoids.

7.1.1 Maclaurin spheroids

A Maclaurin spheroid is a self-gravitating Newtonian star that rotates about one of its principle axes. The axis of rotation is chosen to be the axis a_3. The other axes are equal $a_1 = a_2$ and greater than a_3, $a_1 \geq a_3$. The equilibrium configurations can be labeled by the angular velocity of rotation Ω, and the ratio of a_3 with a_1, $\lambda_3 = a_3/a_1$. It was shown that the relation between Ω and the eccentricity $e^2 = 1 - \lambda_3^2$ for an incompressible and for a compressible ellipsoid have the same form (Lai et al., 1993), if the following transformation is done $\bar{\Omega} \mapsto \hat{\Omega} = \sqrt{q_n}\tilde{\Omega} = \sqrt{q_n}\Omega/\sqrt{G\pi\bar{\rho}}$

$$\hat{\Omega}^2 = 2\left[\frac{(1-e^2)^{1/2}}{e^3}(3-2e^2)\sin^{-1}e - 3\frac{(1-e^2)}{e^2}\right] \tag{7.1}$$

It should be noted that when the stars is incompressible ($n = 0$), $q_0 = 1$ and $\bar{\Omega} = \tilde{\Omega} = \hat{\Omega}$.

The Maclaurin spheroids become (dynamical) unstable against perturbations at $\lambda_3 = 0.2838$, where there is a maximum in the angular velocity $\tilde{\Omega}$. If some dissipation mechanism is present, e.g. gravitational radiation, the Maclaurin spheroids become (secular) unstable at $\lambda_3 = 0.5827$. It is interesting that at the onset of secular instability, the fundamental modes (f-modes) are neutralized, i.e. there is a nontrivial perturbation independent of time. Therefore the spheroid can be deformed into a new equilibrium figure with $a_1 \neq a_2$. This point constitutes a bifurcation point, and in fact from this point bifurcates two equilibrium sequences called the Jacobi and Dedekind ellipsoids. The criteria for stability for differently rotating star is strongly related with $\beta = T/|W|$, where T is the kinetic energy and W the gravitational potential energy.

7.1.2 Jacobi and Dedekind ellipsoids

The equilibrium sequence for the Jacobi ellipsoids is determined by the equation:

$$a_1^2 a_2^2 A_{12} = a_3^2 A_3, \tag{7.2}$$

$$\hat{\Omega}^2 = 2B_{12}, \tag{7.3}$$

where the functions A_{12}, B_{12} are defined in terms of the potential integrals A_1, A_2, A_3 found on (Chandrasekhar, 1963). The Dedekind ellipsoids are "adjoint" configurations to the Jacobi ellipsoids. They are non-rotating ellipsoids that maintain its shape due to internal motions with vorticity ζ. The Dedekind sequence is obtained by changing $\hat{\Omega} \mapsto a_1 a_2 \hat{\zeta}/(a_1^2 + a_2^2)$, according to Dedekind's theorem (Chandrasekhar, 1963).

7.1.3 Riemann-S type ellipsoids

The f-mode of a Maclaurin spheroid can be neutralized we viewed from a rotating coordinate system. Therefore, every point of the Maclaurin sequence can be seen as a bifurcation point of a new type of ellipsoids called Riemann ellipsoids (see fig 7.3). These ellipsoids constitute a solution of the Dirichlet's problem. There is a subset of Riemann ellipsoids called of S-type, whose vorticity ζ is parallel to the angular velocity Ω, which is chosen to lie along the a_3 axis. The configuration of a Riemann S-type ellipsoid, satisfy the equations (Chandrasekhar, 1963; Lai et al., 1993):

$$\hat{\Omega}^2 - \frac{a_1^2 a_2^2}{(a_1^2 + a_2^2)^2}\hat{\zeta}^2 - 2B_{12} = 0, \tag{7.4}$$

$$\frac{a_1^2 a_2^2}{(a_1^2 + a_2^2)}\hat{\zeta}\hat{\Omega} - a_1^2 a_2^2 A_{12} + a_3^2 A_3 = 0, \tag{7.5}$$

where $\hat{\zeta} = \sqrt{q_n}\zeta/\sqrt{\pi G \bar{\rho}}$. When the ellipsoid evolves in time driven by GWR (see next sec.), the circulation around the equator of the star C is conserved and is given by

$$\frac{C}{2\pi} = a_1 a_2 (\zeta + 2\Omega). \tag{7.6}$$

The equilibrium sequence with constant circulation parametrized by λ_2 is constructed by selecting some circulation and solving the system of equations for $(\hat{\Omega}, \hat{\zeta}, \lambda_3)$, shown in fig. 7.2.

7.1.4 Quasi-static Evolution driven by Gravitational Radiation

The evolution of an ellipsoid driven by gravitational radiation moves towards a lower energy and lower angular momentum state. Here it is considered, as in the case of a binary system, the adiabatic evolution of equilibrium states with decreasing energy. It was found by Miller (1974) that the circulation is conserved along the evolution (GW driven) of a self-gravitating rotating object, thus one possible evolution path is the Riemann S-type equilibrium sequence. This quasi-static evolution is shown in the figures 7.3 and. The

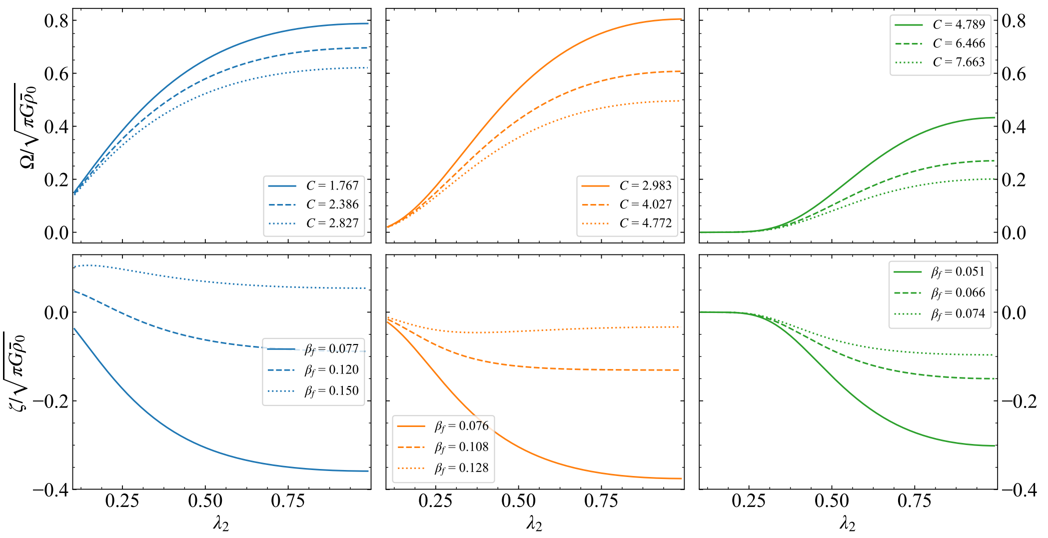

Figure 7.2 Riemann-S type sequences with constant circulation. The blue, orange and green curves correspond to an ellipsoid with polytropic index $n = 1.0, 2.0, 2.7$, respectively. The continuous, dashed and dotted lines show different values of circulation for each polytropic index. It is also shown the parameter $\beta(\lambda_2 = 1) = \beta_f$.

Dedekind theorem implies that there are two types of sequences, with the same circulation, that branch off the Maclaurin sequence. One sequence with $|\zeta| < 2|\Omega|$ which is called Jacobi-like and the other with $|\zeta| > 2|\Omega|$ called Dedekind-like. The Jacobi-like evolution is characterized by $dJ/d\Omega < 0$, so along this sequence the angular velocity increases (spin-up). In contrast, along the Dedekind-like sequence the angular velocity decreases (spin-down). A chirping-like evolution can be found only on the Jacobi-like sequences, where the ellipsoid moves towards a Maclaurin (axis-symmetric) state with the same circulation. The final point of the evolution depends on value of β at the Maclaurin state. If $\beta < 0.1375$ at the Maclaurin point, the spheroid is stable and the evolution driven by gravitational radiation ends. Otherwise, the Maclaurin spheroid may leave its equilibrium state along the decreasing-energy Dedekind-like sequence ending at a Dedekind ellipsoid with $\Omega = 0$.

The quasi-static sequence is confirmed by the numerical integration of the dynamical equations governing a compressible ellipsoid (Lai et al., 1994). The numerical solution shows evolving perturbations oscillating around the constant circulation sequence. These perturbations correspond to f-modes (bar-modes). The dynamical equations are,

$$\bar{\Omega}' = 2\left(\frac{\alpha_1\alpha_2}{\alpha_1^2-\alpha_2^2}\right)\left[\left(\frac{\bar{\Omega}}{\alpha_2}+\frac{\bar{\Lambda}}{\alpha_1}\right)\alpha_1' - \left(\frac{\bar{\Omega}}{\alpha_1}+\frac{\bar{\Lambda}}{\alpha_2}\right)\alpha_2' + \frac{G}{5c^5}\frac{I\!\!\!-^{(5)}_{12}}{\pi G\bar{\rho}_0}\left(\frac{\alpha_1^2+\alpha_2^2}{\alpha_1\alpha_2}\right)\right], \tag{7.7}$$

$$\bar{\Lambda}' = 2\left(\frac{\alpha_1\alpha_2}{\alpha_1^2-\alpha_2^2}\right)\left[\left(\frac{\bar{\Omega}}{\alpha_1}+\frac{\bar{\Lambda}}{\alpha_2}\right)\alpha_1' - \left(\frac{\bar{\Omega}}{\alpha_2}+\frac{\bar{\Lambda}}{\alpha_1}\right)\alpha_2' + \frac{2G}{5c^5}\frac{I\!\!\!-^{(5)}_{12}}{\pi G\bar{\rho}_0}\right], \tag{7.8}$$

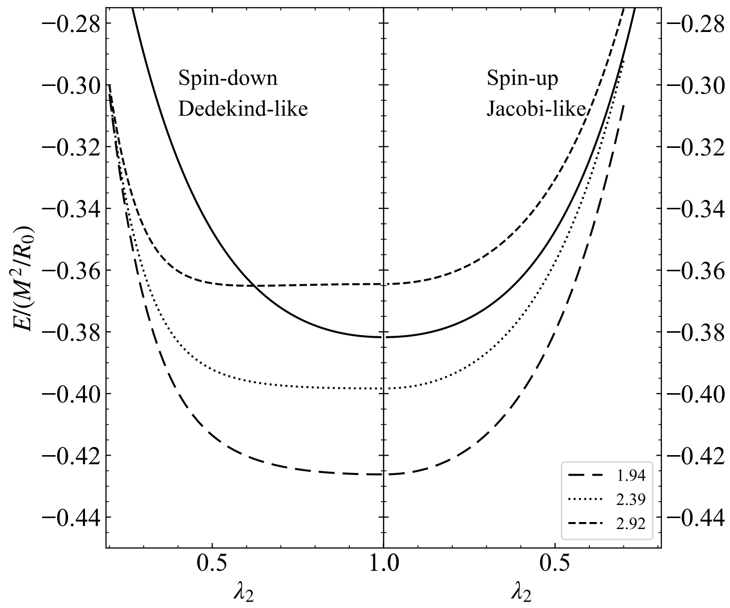

Figure 7.3 Secular quasi-static evolution of a compressible Riemann-S ellipsoid with polytropic index $n = 1$, driven by GR, calculated *a la* Landau-Lifshitz. The vertical line at $\lambda_2 = 0$ corresponds to the Maclaurin sequence from which other equilibrium sequences branch off. The black continuous curve on the left is the Dedekind sequence and on the right the Jacobi sequence. The long-dashed, dotted and dashed curves are the Riemann-S type sequences with constant circulation $C/(2\pi) = 1.94, 2.39, 2.92$, respectively.

$$\alpha_1'' = (\bar{\Omega}^2 - \bar{\Lambda}^2)\alpha_1 - 2\alpha_2\bar{\Omega}\bar{\Lambda} - \frac{2}{q_n}\frac{A_1}{\alpha_2\alpha_3}r_0^3 + \frac{GM}{q_n c^2 R_0 \alpha_1}\left(\frac{r_0^3}{\mathcal{V}}\right)^{1/n} - \frac{2G}{5c^5}\frac{\mathcal{I}_{11}^{(5)}\alpha_1}{\pi G\bar{\rho}_0}, \tag{7.9}$$

$$\alpha_2'' = (\bar{\Omega}^2 - \bar{\Lambda}^2)\alpha_2 - 2\alpha_1\bar{\Omega}\bar{\Lambda} - \frac{2}{q_n}\frac{A_2}{\alpha_1\alpha_3}r_0^3 + \frac{GM}{q_n c^2 R_0 \alpha_2}\left(\frac{r_0^3}{\mathcal{V}}\right)^{1/n} - \frac{2G}{5c^5}\frac{\mathcal{I}_{11}^{(5)}\alpha_2}{\pi G\bar{\rho}_0}, \tag{7.10}$$

$$\alpha_3'' = -\frac{2}{q_n}\frac{A_3}{\alpha_1\alpha_2}r_0^3 + \frac{GM}{q_n c^2 R_0 \alpha_3}\left(\frac{r_0^3}{\mathcal{V}}\right)^{1/n}, \tag{7.11}$$

where the natural unit length is $l_u = c(G\pi\bar{\rho}_0)^{-1/2}$, and $\alpha_n = a_n/l_u$, $r_0 = R_0/l_u$, $\mathcal{V} = \alpha_1\alpha_2\alpha_3$. Prime denotes differentiation with respect to $\bar{t} = [(G\pi\bar{\rho}_0)^{1/2}t]$. The GWR reaction terms $\mathcal{I}_{ij}^{(5)}$ are the fifth time derivative of $\mathcal{I}_{ij}$ (2.60) to lowest order in $\dot{a}_n$. The evolution is shown in fig. 7.4 together with the quasi-static sequence with constant circulation. It can be seen that the evolution follows the corresponding Riemann-S type sequence shown as a dashed line.

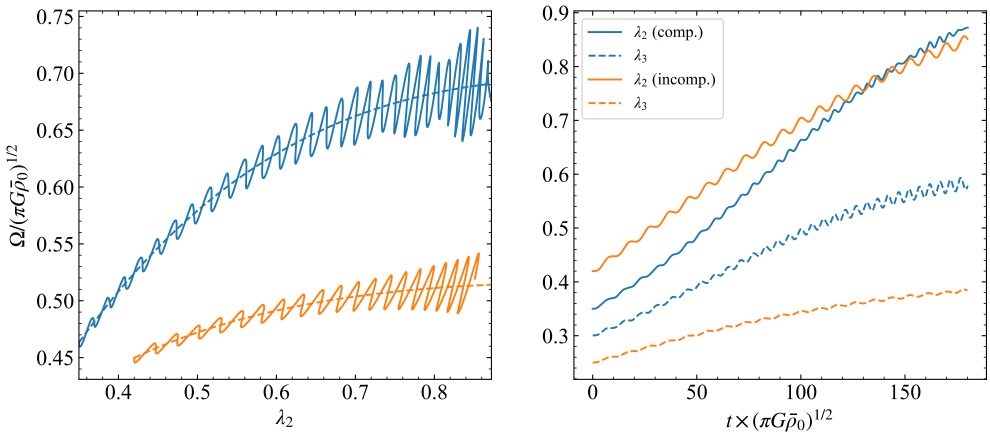

Figure 7.4 Dynamical evolution of a compressible (blue) and incompressible (orange) ellipsoid with polytropic index $n = 1$, $M = 2.54$ and $R_0 = 14.5$ km. Left: Angular frequency of rotation as a function of time. It can be seen that the dynamical evolution follows this sequence which is shown as a dashed line. Right: dynamical evolution of the axis ratios λ_2 and λ_3.

7.2 Gravitational Waves

Following the same approach of binary systems, the leading-order of the gravitational waveform evolution is obtained by substituting the quasi-static evolution in the expression for a rotating deformed star. In the weak-field and low-velocity approximation the GW polarizations are given by eqs. (2.100) and (2.101) (also see sec. 2.3.2). From the GW luminosity (2.102) the typical time scale can be obtained,

$$\tau_{\mathrm{GW}} = \frac{f}{\dot{f}} = f\left|\frac{dE}{df}\left(\frac{dt}{dE}\right)\right|. \tag{7.12}$$

The GW amplitude h_0,

$$h_0 = \frac{4G}{c^4 D}\Omega^2(I_{11} - I_{22}), \tag{7.13}$$

with $I_{ii} = \kappa_n M a_i^2/5$, as a function of the frequency can be easily calculated from the equilibrium sequence (see fig. 7.5). The GW has an early period when both the frequency and the amplitude increase, i.e. a chirping-like period, hence this object is called a chirping ellipsoid (CEL). Different circulations converge during this early period which is characterized by axes ratios $\lambda_2, \lambda_3 \lesssim 0.7$. It was found that the smaller the polytropic index is, the more deformed the star is during the chirping period. In fact, for $n < 1$ the axes ratios $\lambda_2, \lambda_3 \sim 10^{-3}$.

In order to compare and contrast a CEL with a binary , $h_0(f)$ and τ_{GW} were found for the case of a binary system (sec. 2.3.1) whose chirp mass is of the order of the mass of the ellipsoid. It can be seen in Fig. 7.5 that the time-scale and amplitude evolution of the binary system is of the same order of magnitude thana CEL. This suggests that the two signals can have similar waveforms that sweep the same frequency interval at the same time. In order

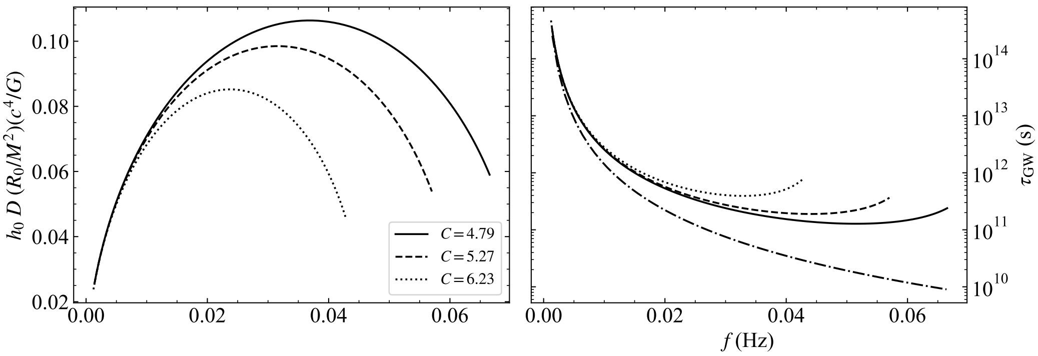

Figure 7.5 The GW amplitude as a function of the frequency for a compressible ellipsoid with polytropic index $n = 2.8$ is shown on the left for different circulations. The typical time scale τ_{GW} is shown in the lower plot. The dot-dashed line corresponds to a binary system whose *chirp mass is half the mass of the ellipsoid.*

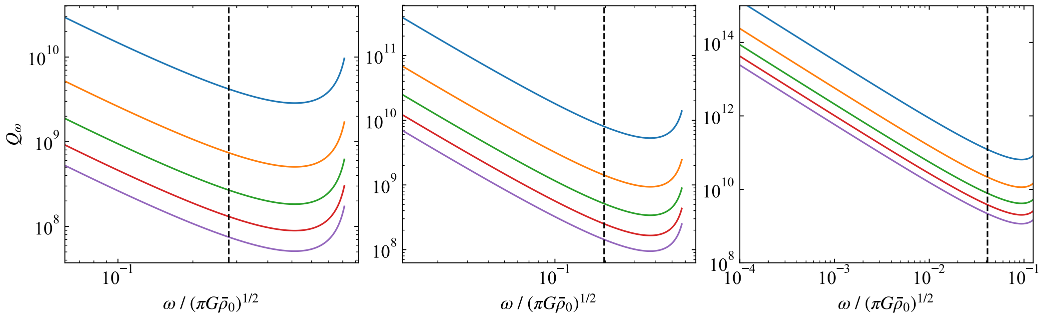

Figure 7.6 Intrinsic phase variation for a Riemann-S type spinning-up ellipsoid for polytropic indices $n = 2.7, 2.8, 2.95$. The different colors represent different compactness parameters for the spherical non-rotating star.

to make a quantitative study of the waveforms, the non-dimensional parameter Q_ω (2.74) was found,

$$Q_\omega = \frac{\omega^2}{\dot{\omega}} = 2\Omega^2 \left| \frac{dE}{d\Omega} \left(\frac{dt}{dE} \right) \right|, \tag{7.14}$$

where $\omega = 2\Omega$ is the angular frequency of the GW. Recall that Q_ω is an intrinsic measure of the phase-time evolution (Damour et al., 2013). An empirical fit is then done to the calculated curves of Q_ω for a CEL with different polytropic indexes n, and assuming different values of the compactness parameter. The general mathematical form of the fitting function is:

$$Q_\omega^{\mathrm{ellip}} \approx \frac{\mathcal{A}_n}{\mathcal{C}^{5/2}} \left[\frac{\omega}{\sqrt{\pi G \bar{\rho}_0}} \right]^\alpha = \frac{\mathcal{A}_n}{\mathcal{C}^m} \left(\frac{2GM\omega}{\sqrt{3}c^3} \right)^\alpha, \tag{7.15}$$

where $m = (5 + 3\alpha)/2$. The values of $\mathcal{A}_n$ and α are shown in table 7.1.

The function Q_ω of both, the CEL and the binary, has a power-law behavior, but with different exponent. The negative exponent implies that both have a monotonically increasing behavior in frequency. The behavior in the CEL can be understood from compressibility,

Table 7.1 Polytropic structure constants $(n, \kappa_n, k_1, k_2, k_3)$ and the Q_ω power-law empirical fitting parameters.

n	κ_n	k_1	k_2	k_3	$\mathcal{A}_n$	α
0.3	0.88562	0.13139	0.90949	2.8656	2.65	−0.926
0.5	0.81482	0.22933	0.87777	2.6594	2.55	−0.973
1.0	0.65345	0.5	0.81289	2.2472	2.68	−1.081
1.5	0.51149	0.79586	0.76077	1.9252	3.753	−1.087
2.0	0.38712	1.1078	0.71618	1.6562	4.003	−1.222
2.5	0.27951	1.4295	0.67623	1.4202	4.060	−1.447
2.7	0.24109	1.55971	0.66110	1.33194	5.926	−1.365
2.8	0.22286	1.62502	0.65367	1.28882	5.632	−1.464
2.9	0.20530	1.69038	0.64630	1.24621	4.940	−1.571
2.95	0.19676	1.72309	0.64265	1.22511	4.369	−1.614
2.97	0.19340	1.73617	0.64119	1.21669	3.760	−1.640
2.99	0.19005	1.74925	0.63973	1.20829	3.817	−1.652

vorticity and conservation of circulation. Riemann S-type ellipsoids have internal motions with uniform vorticity that contributes to the total angular momentum. In spin-up configurations, the radiation of angular momentum induces a vorticity loss. But, since the circulation is constant, this loss must be compensated with a change in the angular velocity and in the axes a_1, a_2. Thus, the spin-up of a CEL has two "components": one due to the change in geometry that depends on the compressibility, and the other one due to the decrease of vorticity. The compressibility of the object changes with the polytropic index, inducing the behaviour seen in Table 7.1 (e.g. when $n \to 3$ $\alpha \to -5/3$). The compressibility of the object changes with the polytropic index, reducing the extra spin-up of the ellipsoid by a change in the moment of inertia. This effect can be seen in Table 7.1 (e.g. when $n \to 3$ $\alpha \to -5/3$).

The empirical power-laws can be used to compute the phase-time evolution of the GW. The angular wave frequency as function of time is in this case given by,

$$\omega = \left[\frac{\mathcal{A}_n}{\mathcal{C}^m (1-\alpha)} \left(\frac{4}{3}\right)^{\alpha/2} \left(\frac{GM}{c^3}\right)^{\alpha} \left(\frac{1}{\tau}\right) \right]^{1/(1-\alpha)}, \tag{7.16}$$

where $\tau = t_{\rm end} - t$, $t_{\rm end}$ is the asymptotic end of the chirping epoch. As in the case of an ideal inspiraling binary, the frequency formally diverges at $t_{\rm end}$. In a real CEL this conditions is never achieved since the objects "leaves" the power-law regime at a time t_1 with a finite angular frequency, let's say ω_1, which is shown in Fig. 7.6 as the dashed vertical line. The phase evolution is given by,

$$\phi_{\rm GW} = \left(\alpha^{\alpha-1} \frac{\mathcal{C}^m}{\mathcal{A}_n} \left[\frac{(1-\alpha)c^3 \tau}{\sqrt{4/3}GM} \right]^{\alpha} \right)^{1/(\alpha-1)} + \phi_{\rm end}, \tag{7.17}$$

where $\phi_{\rm end}$ is the phase when $\omega \to \infty$. The Fourier transform of the GW polarizations are obtained with the stationary phase method (see e.g. Maggiore (2008)):

$$\tilde{h}_+(f) = A(f)e^{i\Psi_+(f)}(1 + \cos^2\Theta)/2, \tag{7.18}$$

$$\tilde{h}_\times(f) = A(f)e^{i\Psi_\times(f)}\cos\Theta, \tag{7.19}$$

where

$$A(f) = \frac{h_0}{2}\frac{Q_\omega^{1/2}}{f\sqrt{2\pi}} = \frac{2G}{c^4 D}(\pi f)^2(I_{11} - I_{22})\frac{Q_\omega^{1/2}}{f\sqrt{2\pi}}, \tag{7.20}$$

and

$$\Psi_+(f) = 2\pi f t_{\text{end}} + \frac{Q_\omega}{\alpha(\alpha - 1)} - \phi_{\text{end}} - \pi/4, \tag{7.21}$$

$$\Psi_\times(f) = \Psi_+(f) + \pi/2. \tag{7.22}$$

It should be noticed that the "intrinsic phase evolution" enters explicitly in the Fourier amplitude $A(f)$ and in the Fourier phase $\Psi_{+,\times}$.

7.2.1 Detectability

The frequency of these CELs lies in the range $f \sim 0.1 - 100$ mHz, making them plausible targets of space-borne GW detectors such as LISA or TianQin. The typical timescale of CELs (7.12), was found to be much greater than the observation time, T_{obs}, of detectors, $\tau_{\text{GW}} \gg T_{\text{obs}} \geq (t - t_0)$. Therefore, a CEL is *quasi-monochromatic*, and its phase can be expanded in powers of $\epsilon = (t - t_0)/\tau_{\text{GW}}$,

$$\Phi = \Phi_0 + 2\pi[\epsilon f(t - t_0) + \frac{1}{2}\epsilon^2\dot{f}(t - t_0)^2 + \ldots], \tag{7.23}$$

where as usual ϵ is a dummy parameter to keep track of the relative strength of the terms. To first order in ϵ the GW is regarded as monochromatic.

The analysis will be illustrated with the *LISA* mission, which consist of three spacecrafts in a equilateral triangle array of length $L = 5 \times 10^6$ km, orbiting around the sun. Each spacecraft can be regarded as a test mass. The passing of a GW will change the distance between the spacecrafts $(\delta L_1, \delta L_2, \delta L_3)$. The array is equipped with laser beams along the sides of the triangle array in order to construct a two-arm interferometer. A pair of two-arm interferometers will be constructed with 6 laser beams. Two time series of data $s_{\text{I,II}}(t)$ will be obtained from the interferometers, which may contain the GW signals $h_{\text{I,II}}(t)$,

$$h_{\text{I,II}}(t) = \frac{\sqrt{3}}{2}\left[F^+_{\text{I,II}}(t)h_+(t) + F^\times_{\text{I,II}}(t)h_\times(t)\right], \tag{7.24}$$

where $F^{+,\times}_{\text{I,II}}$ are the antenna patterns of an interferometer which depend on the source angular position and polarization angle (5.12) (5.13). The GW polarizations, including the Doppler phase-shift $\Phi_D(t)$ due to the proper detector motion, can be obtained from eqs. (2.100) and (2.101), the quasi-monochromatic approximation (7.23),

$$h_+(t) = h_0\cos\left[\Phi_0 + 2\pi f(t - t_0) + \pi\dot{f}(t - t_0)^2 + \Phi_D(t)\right]\left[1 + (\hat{\mathbf{L}}\cdot\hat{\mathbf{n}})^2\right]/2, \tag{7.25}$$

$$h_\times(t) = h_0\sin\left[\Phi_0 + 2\pi f(t - t_0) + \pi\dot{f}(t - t_0)^2 + \Phi_D(t)\right]\hat{\mathbf{L}}\cdot\hat{\mathbf{n}}, \tag{7.26}$$

where $\hat{\mathbf{L}}$ is the unit vector in the same direction of the total angular momentum of the CEL and $\hat{\mathbf{n}}$ the unit vector from the source to the detector (see fig. 5.1). Note that the form of these pattern functions depend on the source position with respect a coordinate system in the detector. Owing to the detector motion, it is convenient to express all the angles with respect to a coordinate system tied with the ecliptic, denoted with an overbar following the notation of Cutler (1998) (see also the aforementioned ref. for the explicit expressions). The polar and azimuthal angles of the source are $(\bar{\theta}_s, \bar{\phi}_s)$ and the same angles of the unit vector $\hat{\mathbf{L}}$ are $(\bar{\theta}_L, \bar{\phi}_L)$, with respect the ecliptic coordinate system.

As a result, the parameters characterizing the template (observables) of a CEL[1] are 8 in total: f, $\dot{f}$, ϕ_0, h_0, $\bar{\theta}_s$, $\bar{\phi}_s$, $\bar{\theta}_L$, $\bar{\phi}_L$. The phase ϕ_0 constitutes a time shift and is not an intrinsic parameter. The intrinsic parameters of the source are f, $\dot{f}$, h_0, this last is quasi-intrinsic because of the fact that it involves the distance to the source. The subsequent analysis will concentrate on these latter parameters. As usual, the characteristic amplitude for a CEL is,

$$h_c \equiv f\sqrt{2\big(|\tilde{h}_+|^2 + |\tilde{h}_\times|^2\big)}\bigg|_{\rm opt} = h_0\sqrt{\frac{dN}{d\ln f}}, \tag{7.27}$$

where the second identity is true when the CEL is optimally oriented. The expected (angle averaged) SNR is related to the latter characteristic amplitude,

$$\langle\rho^2\rangle = \frac{6}{25}\int_{f_0}^{f_1}\frac{h_c^2}{f^2 S_n(f)}df. \tag{7.28}$$

Since these CELs are quasi-monochromatic, the expected SNR can be readily estimated with the "reduced" characteristic amplitude $\tilde{h}_c$,

$$\tilde{h}_c(f) = h_0(f)\sqrt{N} = h_0(f)\sqrt{f T_{\rm obs}},$$

$$\left(\frac{S}{N}\right)^2 \propto \frac{\tilde{h}_c^2(f_0)}{f^2 S_n(f_0)} \tag{7.29}$$

which is shown in fig 7.7 for a CEL with $n = 2.95$ and $M_{\rm CEL} = 1.0\,M_\odot$. Furthermore, in order to illustrate the frequency-time evolution of this latter CEL, it is shown in the same figure, a chart of the time to reach the of the chirp, $\tau_{\rm end} = t_{\rm end} - t$, i.e at $\tau_{\rm end} = 0$ this CEL reaches the GW frequency of ≈ 9.20 mHz and after this point the amplitude decreases.

For the used Galactic distance, $\tilde{h}_c$ is well above the *LISA* noise curve, at least near the end of the chirping regime, and is in principle detectable. The typical value of $\omega/(\pi G\bar{\rho}_0)^{1/2}$ during the chirping phase is $\sim 10^{-5}$–10^{-1}. For typical densities of a white dwarf $\sim 10^6$–10^9 g cm^{-3}, the frequency is $\sim 10^{-6}$–10 Hz, well inside the *LISA* sensitivity band. Detectability CEL properties obtained from eqs. (7.27) and (7.28) are tabulated in the last column of tab. 7.2.

In addition, these CELs can be regarded as monochromatic in some part of their existence. Figure 7.6, shows that the evolution is rather slow at low frequencies, and becomes slower when $n \to 3$, thus CELs are expected to be monochromatic at those regions.

---

[1] The observables are the same for any quasi-monochromatic GW

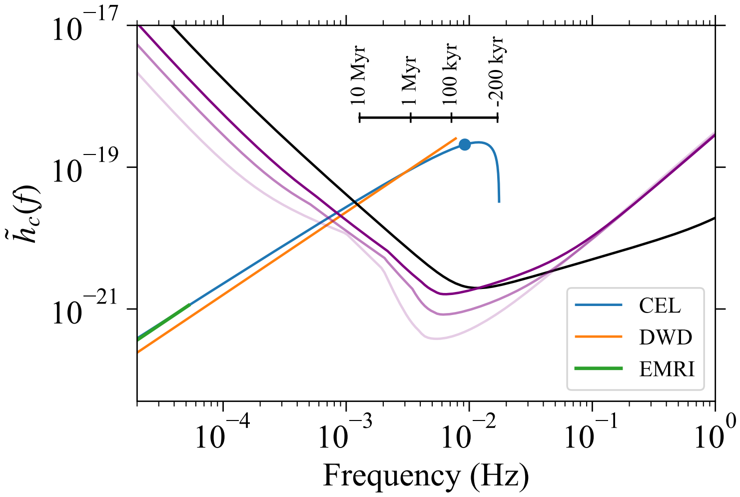

Figure 7.7 Reduced characteristic amplitude, $\tilde{h}_c$, of a CEL with $M_{\rm CEL} = 1.0\ M_\odot$ and $\mathcal{C} \approx 2.5\times10^{-4}$ (blue), according to the relativistic Feynman-Metropolis-Teller equation of state Rotondo et al. (2011). The polytropic index is $n = 2.95$, and the distance is $D = 1$ kpc. The observation time is $T_{\rm obs} = 2$ yr. The blue dot at $f_{\rm end} \approx 9.20$ mHz marks the end of the chirp. A chart showing the time to reach the end of the chirp, $\tau_{\rm end}$, is shown in the middle. In addition, the characteristic amplitude of an EMRI composed of $m_1 = 1940.62\ M_\odot$, $m_2 = 0.0001\ M_\odot$, $D = 1.29$ kpc, up to tidal-disruption frequency (green), and compact star binary composed of $m_1 = 0.45\ M_\odot$, $m_2 = 0.18\ M_\odot$ $D = 1.20$ kpc, up to RLOF frequency (orange). For more details see tab. 7.2. Fits of the amplitude spectral density (ASD) of *LISA* including galactic WD binaries, are shown as purple continuous lines with decreasing intensity for configurations N2A1L4, N2A2L4 and N2A5L4, top to bottom respectively (see (Klein et al., 2016) for the explicit form of the fits and conventions meaning). In addition is shown the ASD of TianQin project as a black continuous line (Luo et al., 2016)

.

More exactly, whether a GW is monochromatic or not depends on the frequency resolution or frequency bin of the detector, $T_{\rm obs}^{-1}$, SNR, and on the frequency evolution of the CEL. The errors in the estimation of the frequency and its rate of change by using matched-filtering are (Takahashi & Seto, 2002),

$$\Delta f = 0.22\left(\frac{S/N}{10}\right)^{-1} T_{\rm obs}^{-1}, \tag{7.30}$$

$$\Delta \dot{f} = 0.43\left(\frac{S/N}{10}\right)^{-1} T_{\rm obs}^{-2}, \tag{7.31}$$

which are frequency independent for $T_{\rm obs} \gtrsim 2$ yr. The ratio of the error in $\dot{f}$, to the rate of change of the frequency of a CEL can be used to determine its monochromaticity Takahashi & Seto (2002),

$$F \equiv \frac{\Delta \dot{f}}{\dot{f}} \tag{7.32}$$

i.e, a source is monochromatic for the detector if $F > 1$. We show this criteria for different polytropic indices in fig. 7.8, and confirm that in some part of the sensitivity band CELs are monochromatic.

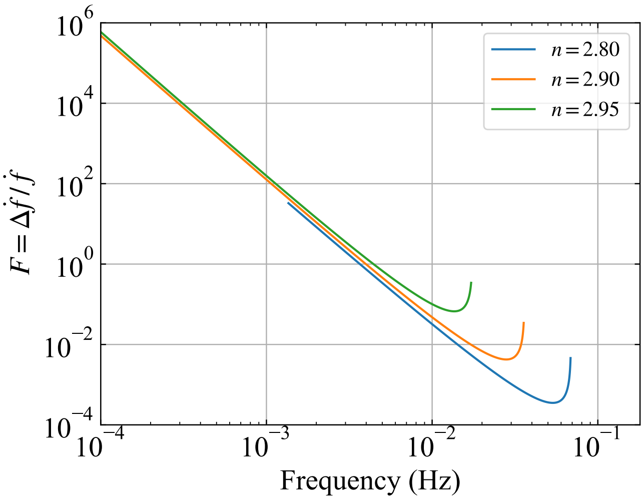

Figure 7.8 Ratio of $\Delta\dot{f}$, error in estimating the time derivative of the frequency, to the value $\dot{f}$ of CELs with different polytropic indices, $F = \Delta\dot{f}/\dot{f}$. The ratio was obtained assuming $S/N = 10$ and $T_{\rm obs} = 2$ yr. When $R > 1$ the error in the estimation of the frequency is greater than the theoretical value of the CEL, i.e., the time derivative of f is inside the error and the system can be regarded as monochromatic (Takahashi & Seto, 2002). For $f \lesssim 3$ mHz CELs are monochromatic for the assumed detection values.

Given the estimations, CELs are detectable for 1 yr of observation, in the frequency band where they are monochromatic, as well in the band where they are not. At very low frequencies, $f < 1$ mHz, the system is monochromatic, but unfortunately its GW amplitude (at $D = 1$ kpc) is not high enough to accumulate the sufficient signal-to-noise ratio during 1 yr in order to be detected.

7.2.2 Degeneracy between CELs and binaries

Next, the above results were compared with the ones of a binary. In the quasi-circular orbits approximation, the intrinsic phase-time parameter of a binary has a power-law exponent equal to $-5/3$. For a CEL whose EOS is modeled as an ultra-relativistic degenerate electron gas ($n = 3$), the intrinsic-phase has the same exponent than the binary. Therefore, there exist a binary system, with the some chirp mass, that matches the phase-time evolution of the CEL. When $\alpha = -5/3$ the dependence on the compactness in Eq. (7.15) disappears. It is interesting that in a compact star like a white dwarf this behavior finds a physical explanation: the ultra-relativistic limit for a Newtonian self-gravitating star made of fermions is approached when $\rho \to \infty$, namely when $R \to 0$. In this limit, when the critical mass is reached, the star properties become radius-independent.

More exactly, for each CEL at a given frequency there exist a binary system with the same intrinsic phase-time evolution parameter Q_ω. Hereafter, the analysis is illustrated with a CEL whose polytropic index is $n = 2.95$. The chirp mass of the equivalent binary system

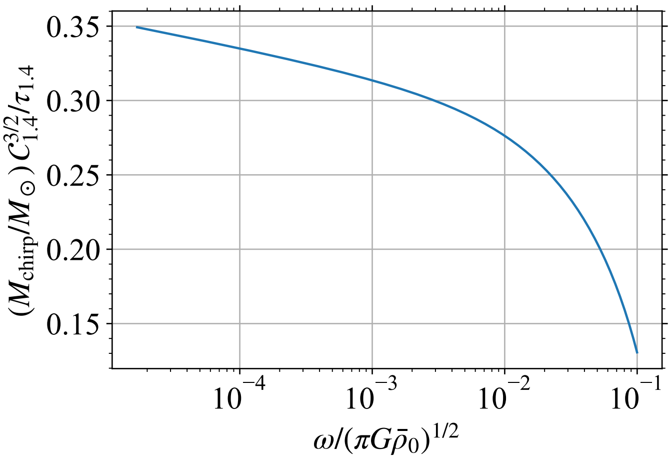

Figure 7.9 Chirp mass of the binary system which has the same intrinsic phase-time evolution Q_ω of a CEL, $n = 2.95$, at a GW angular frequency ω. The value has been normalized by $\mathcal{C}_{1.4} \equiv \mathcal{C}/20\times 10^{-4}$ and $\tau_{1.4} \equiv (\pi G\bar{\rho}_0/\bar{\rho}_{1.4})^{-1/2}$, where $\bar{\rho}_{1.4}$ is the mean density of a non-rotating WD with mass $1.4\,M_\odot$ and radius $R_{\rm WD} \approx 1000$ km, according to the mass-radius relation obtained from the relativistic Feynman-Metropolis-Teller equation of state (Rotondo et al., 2011). Therefore, the values shown in this plot correspond to CEL with $M_{\rm CEL} = 1.4\,M_\odot$, $\mathcal{C} = 20 \times 10^{-4}$ and values for other compactness parameters can be easily inferred.

to this CEL is shown in fig. 7.9. It can be seen that at $\omega/\sqrt{\pi G\bar{\rho}_0} \sim 10^{-3}$ the chirp mass is $\sim 0.4\ M_\odot$ and scales with the compactness, $\mathcal{C}_{1.4}^{3/2}$, where $\mathcal{C}_{1.4} \equiv \mathcal{C}/20 \times 10^{-4}$.

In addition, in order to give a more complete vision of the degeneracy, we plot in fig. 7.10 the chirp mass of the equivalent binary as a function of the observed frequency and the mass of the CEL ($n = 2.95$). This mass can be interpreted as a “CEL chirp mass”, but in contrast to the pure GW-driven binary chirp mass, it changes (very slowly) during the CEL evolution. The mass-radius relation of the non-rotating white dwarf-like object was obtained from the uniform distribution approximation, fully degenerate, free electron gas described by Fermi-Dirac statistics (Rotondo et al., 2011).

As a result of the intrinsic known degeneracy in the chirp mass, many combinations of m_1 and m_2 are equivalent to a CEL, this feature is illustrated in fig. 7.11. The Two types of equivalent binary systems studied here are: detached DWDs and EMRIs composed of an IMBH and an exoplanet. It is worthwhile to mention that the chirp mass of detached DWD, with currently known parameters, ranges from 0.23 to 0.61 $M_\odot$ (Rebassa-Mansergas et al., 2017). For the sake of example, some equivalent binary systems to a CEL, $n = 2.95$, were calculated and the results are tabulated in tab. 7.2.

When n is close to 3 and the chirp mass has been matched, the two systems have nearly equal phase-time evolution and are practically indistinguishable in their phases. This feature can be appreciated in fig. 7.12, where the intrinsic phase-time evolution of a CEL and binary systems were compared and contrasted, with matching and non-matching (but

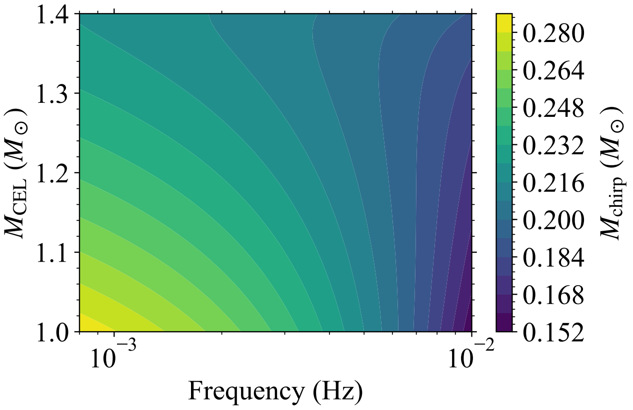

Figure 7.10 Contour plot of the chirp mass of the equivalent binary system as function of the mass of the CEL and the observed frequency. More exactly, the chirp mass of the equivalent binary depends on the compactness, mass of the CEL, and on the observed frequency, but once the equation of state is selected, the mass-radius relation is fixed implying that $M_{\rm chirp}$ depends only on $M_{\rm CEL}$ and f. For the present case we used the "Chandrasekhar" equation of state. However, as shown in (Rotondo et al., 2011), differences between EOSs are neglegible.

close) chirp mass. Some typical LISA targets: EMRI with a supermassive black hole, e.g. $m_1 = 10^5\ M_\odot$ and $m_2 = 1\ M_\odot$, or a binary neutron star, e.g. $m_1 = m_2 = 1.3 M_\odot$, have chirp masses which do not match the phase-time evolution of a CEL. However, a binary white dwarf (also a LISA target) like J0651, the second shortest orbital period, GW emitter, has a chirp mass close to the matching one, thus its phase-time evolution around 1 mHz is nearly equal to the CEL under consideration (see fig. 7.12).

It can be argued that the match does not stay constantly perfect. However, it must be noted that differences between the evolution parameters appear when the systems change appreciably their frequency. Since $Q_\omega \sim 10^{13}$, the evolution is rather slow and they become out phase only when the observation is performed over very long periods of time.

In a pure theoretical context, the amount the systems get out of phase was found by integrating $\Delta Q_\omega = |Q_\omega^{\rm CEL} - Q_{!}^{\rm bin}|$, during 1 yr,

$$\Delta\phi_{\rm 1y} = \int_{\omega_0}^{\omega_{\rm 1y}} \Delta Q_\omega d \ln \omega, \tag{7.33}$$

where ω_0 is the initial observed GW angular frequency and $\omega_{\rm 1y}$ is the GW angular frequency after 1 y. Phase differences, tabulated in tab. 7.2, are extremely small. At very low frequency the systems (CEL and binary) are monochromatic and completely degenerated.

Regarding the GW amplitude it was found that $h_c \propto f^{-1/5}$ and this holds almost for any n, thus $h_0 \propto f^{-1/5-\alpha/2}$. Despite that in the limit $n \to 3$ the intrinsic phase-time evolution of the CEL and the binary tend to follow the same power-law exponent, the CEL amplitude $h_0 \propto f^{0.63}$ grows with a different (but nearly equal) exponent. Once the phase has been matched by some chirp mass, for example, the distance to the source can be

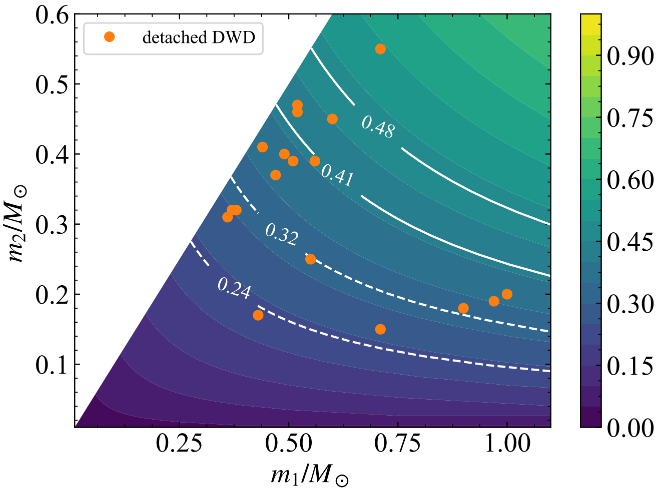

Figure 7.11 Contour plot of the chirp mass of binary systems in the mass range of DWDs. Detached DWD with currently known parameters (Rebassa-Mansergas et al., 2017) are shown as orange circles. The continuous white contour lines correspond a binary with $M_{\rm chirp} = (0.41, 0.48)\ M_\odot$, which matches the Q_ω of the CEL, $\mathcal{C} = 20.0 \times 10^{-4}$, at $f = (9.00, 0.05)$ mHz, respectively. The dashed white contour lines correspond to a binary with $M_{\rm chirp} = (0.24, 0.32)\ M_\odot$, which matches the Q_ω of the a CEL, $\mathcal{C} = 2.5 \times 10^{-4}$, at $f = (3.00, 0.05)$ mHz, respectively.

chosen to match the GW amplitudes. It was found that the distances must have the same order and not highly tuned distances differing by many orders of magnitude. Again, since the exponents are nearly equal and the evolution during observing times is slow, the GW amplitudes remain nearly equal, as shown in the examples of tab. 7.2 and fig. 7.12.

On the other hand, a crucial attribute of these sources is their quasi-monochromaticity. As already mentioned, the intrinsic observables are the f, $\dot{f}$, h_0. Suppose that a quasi-monochromatic GW has been detected, so its "generalized chirp mass" was measured through,

$$M_{\rm chirp}^{\rm gen} \equiv \frac{c^3}{G}\left(\frac{5}{96}\right)^{3/5}\frac{\dot{f}^{3/5}}{\pi^{8/5} f^{11/5}}. \tag{7.34}$$

If the value lies in the range shown in the fig. 7.10, at first this system can be equally identified as a CEL or a binary.

In order to distinguish between these two systems it is important to discuss their intrinsic physical properties, such as the end of the chirp. For the case of a DWD, this is generally given by the Roche-lobe overflow (RLOF) (Postnov & Yungelson, 2014). The frequency at this point was obtained from the approximate formula for the effective Robe-lobe radius, given in ref. (Eggleton, 1983), and the radii of the components were found from a polytropic equation of state with $n = 1.5$ (Chandrasekhar, 1967), due to the fact that this matching binary has low-mass components. RLOF frequencies for selected DWDs are tabulated in tab. 7.2. For the case of an EMRI, the limit is due to the tidal disruption of the less massive component. The GW frequency at tidal disruption is $f_{\rm td} \approx (Gm_2/R_2^3)^{1/2}/(2.4^{3/2}\pi)$, where R_2 is the radius of the (less massive) component m_2, and the tidal radius is $r_{\rm td} \approx 2.4q^{-1/3}R_2$ (Chandrasekhar, 1963) (see also tab. 7.2).

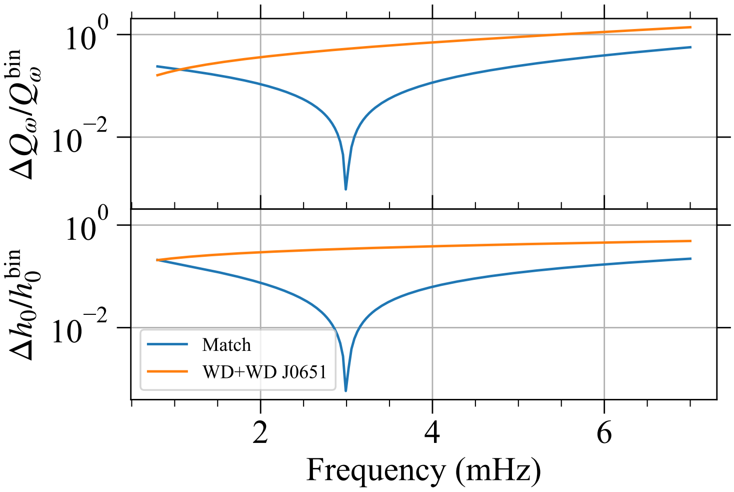

Figure 7.12 Comparison and contrast of the GW evolution, phase (top) and amplitude (bottom), of a CEL, $n = 2.95$, $M_{\rm CEL} = 1.0\ M_\odot$, $\mathcal{C} = 2.5 \times 10^{-4}$ with a binary system, $M_{\rm chirp} = 0.24\ M_\odot$, which exactly matches the Q_ω of the latter CEL at $f = 3$ mHz (blue), and with the non-interacting DWD system J0651, $M_{\rm chirp} = 0.31\ M_\odot$ (orange). Both binaries are located at the same distance from the detector, and the ratio of the distances is $D_{\rm bin}/D_{\rm CEL} = 1.2$.

The above detection degeneracy might be broken since the chirping phase of the CEL and of the binary, owing to RLOF or tidal disruption, end at different frequencies. It would be then possible to discriminate between systems by observing above some frequency. For instance, if a quasi-monochromatic GW is detected at a higher frequency than the RLOF one, this will rule out a detached DWD as the source. In addition, degeneracy between an EMRI and a CEL is broken, owing to the fact the former can not be *individually* detected by currently planned space-borne detectors.

Finally, recall that in the low-velocity, weak-field limit, any monochromatic GW can be *regarded* as being radiated from a deformed (not axially symmetric) rotating star. Equivalently, any monochromatic GW can be thought as a GW from a circular binary. The correspondence between monochromatic GWs and sources is not one-to-one. The proper identification of the source (if possible) relies on the astrophysical implications of the characterizing parameters, and/or on other data.

The previous results showed that given a CEL *in the limit* $n \to 3$, a binary system can be found whose *GW chirping evolution during observational times* matches the one of the CEL, and vice versa. When this evolution is not observable, on account of slow intrinsic evolution, short periods of observation or both, the true nature of the system is highly uncertain.

As already stated, CELs can be monochromatic, thus detection degeneracy extents to even more systems. Namely, in the monochromatic regime there exist degeneracy between CELs, or between CELs and binaries with parameters different from those found previously. This kind of degeneracy will be addressed elsewhere.

7.3 Chirping Ellipsoids and Inspiral Rates

In view of the aforementioned degeneracy between CELs and EMRIs-DWD, it is mandatory to estimate rates for each system in order to evaluate the real impact of the degeneracy. Since this work is interested in DWDs which can enter the interferometer frequency band, only DWDs which can merge within a Hubble time are considered. The DWD merger rate in a typical galaxy is estimated to be (1–80) $\times\, 10^{-13}$ yr^{-1} $M_\odot^{-1}$ (at 2σ) Maoz & Hallakoun (2017); Maoz et al. (2018). Thus, using $M = 6.4 \times 10^{10}\ M_\odot$ for the Milky Way Kalogera et al. (2001),

$$R_{\rm DWD} = 0.0064 - 0.512\ {\rm yr}^{-1}. \tag{7.35}$$

Regarding CELs, can be the result of mass transfer from a companion. The rate at which these events occur could be close to that of novae, i.e. $R_{\rm CEL} \sim 10 - 80\ {\rm yr}^{-1}$. But excitation of a white dwarf during a nova could be of one of many types. If we assume that a fraction β of all white dwarfs potentially becoming novae undergone a spin-up transition, then the rate of chirping ellipsoids may be as high as:

$$R_{\rm CEL} = (10 - 80)\beta\ {\rm yr}^{-1} \tag{7.36}$$

Another mechanism is the merging of white dwarfs in compact binaries. Numerical simulations show that, in the case of mergers not leading to a type Ia supernovae, the merged configuration possesses three regions (Benz et al., 1990; Guerrero et al., 2004; Lorén-Aguilar et al., 2009; Longland et al., 2012; Raskin et al., 2012; Zhu et al., 2013; Dan et al., 2014): a rigidly rotating, central white dwarf, on top of which there is a hot, differentially-rotating, convective corona, finally surrounded by a rapidly rotating Keplerian disk. The corona comprises about half of the mass of the totally disrupted secondary star, while the rest of the secondary mass belongs to the disk, since a small mass ($\sim 10^{-3}\ M_\odot$) is ejected. The rigid core+corona configuration may have the appropriate structure that resemble our CEL. Depending on the merging components masses, the central remnant can be a massive (1.0–1.5 $M_\odot$), fast rotating (P = 1–10 s) white dwarf (see e.g. Rueda et al. (2013); Becerra et al. (2018)).

The white dwarf binary merger rate in a typical galaxy is estimated to be (1–80) $\times\ 10^{-13}$ yr^{-1} $M_\odot^{-1}$ (at 2σ) and (5–9) $\times\ 10^{-13}$ yr^{-1} $M_\odot^{-1}$ (at 1σ) Maoz & Hallakoun (2017); Maoz et al. (2018). On the other hand, the type Ia supernova rate is about (12–22)% of the above rate (see e.g. Ruiter et al. (2009)). Therefore, even requiring the white dwarf binary merger channel to cover the entire supernovae Ia population, a lower limit to the population of deformed white dwarfs from these mergers, potentially observable as a CEL only within the Milky Way, $M = 6.4 \times 10^{10}\ M_\odot$ Kalogera et al. (2001), at a 2σ level, will be:

$$R_{\rm CEL} = 0.005 - 0.5\ {\rm yr}^{-1}, \tag{7.37}$$

The equivalent EMRIs found for the CEL considered in table 7.2 are formed by an IMBH with a mass in the range m_1 = 500–3000 $M_\odot$ and a substellar, planet-like object $m_2 \approx \nu m_1$ = (0.7–4)$\times 10^{-3} M_\odot$. The latter mass range corresponds approximately to masses between the one of Saturn ($M_{\rm Sat} = 3 \times 10^{-4}\ M_\odot$) and the one of Jupiter ($M_{\rm Jup} \sim 10^{-3}\ M_\odot$). The inferred rate turns out to be,

$$R_{\rm EMRI} = 0.02 - 0.5\ {\rm yr}^{-1}, \tag{7.38}$$

which is similar to R_{CEL}.

7.4 Discussion

Compressible, Riemann S-type ellipsoids with a polytropic index $n \gtrsim 2.7$, emit quasi-monochromatic GWs with a frequency that fall in the sensitivity band of planned space-borne detectors (eg. LISA and TianQin; see Fig. 7.5). Inside the sensitivity band, CELs slowly evolve so they hold quasi-monochromatic during the planned observation times. These sources exhibit a chirp behaviour like the one of binary systems. In the limit $n \to 3$, as inferred from empirical fits shown in Table 7.1, both systems have the same intrinsic phase-time evolution Q_ω. This behaviour is due to the change in the compressibility of the CEL with n.

CELs located at galactic distances are detectable by planned space-borne detectors during one year of observation (see last column of tab. 7.2). It was found that within the detectors sensitivity band, CEL ($3 > n \gtrsim 2.9$) intrinsic, quasi-monochromatic parameters, h_0, f, $\dot{f}$, or equivalently h_0, Q_ω can have the same values of those of a binary system, see fig. 7.9 and tab. 7.2. More exactly, given a quasi-monochromatic binary characterized by its frequency, chirp mass and distance, it can be found a CEL mass and distance, whose waveform at the same frequency has the same $\dot{f}$ (or Q_ω) and amplitude of the binary. Hence, CEL and quasi-monochromatic binaries are degenerated. Two kinds of quasi-monochromatic binary families degenerated with CELs were found and studied here: DWD and EMRI composed of a IMBH and a planet-like object.

On the other hand, the physical nature of CELs and binaries is completely different and it principle is possible to distinguish between them. Namely, the final frequency of the quasi-monochromatic, GW-driven chirp of a binary is given by the tidal disruption, in the case of EMRIs (IMBH-exoplanet), or by RLOF in the case of a DWD. The tidal disruption frequency of the IMBH-exoplanet system is $\sim 10^{-5}$ Hz. This system cannot be detected individually by space-borne detectors (see tab. 7.2) and the degeneracy is broken. For the systems considered here, the following relation is in general satisfied, $f_{\mathrm{td}} < f_{\mathrm{RLOF}} < f_{\mathrm{end}}^{\mathrm{CEL}}$. Consequently, the observation of a quasi-monochromatic GW (with “chirp mass” $\sim 0.5\ M_\odot$) above the RLOF will point towards a CEL. Below frequencies $\sim 10^{-2}$ Hz, CELs and binaries are degenerated and cannot be distinguished by using GW data alone. Electromagnetic data, if any, can be used to infer the real nature of the GW source.

In view of the great relevance of this result for space-borne detectors estimates of the occurrence rate of these kind of systems were addressed. For deformed white dwarfs this work adopted the view that they can be formed either by accretion from a companion or by binary white dwarf mergers. Surprisingly, rates of EMRIs, DWD and CELs, appear to be comparable. Despite EMRIs cannot be individually resolved, their occurrence rate make them a plausible stochastic source and will be addressed in a future work. In conclusion, there will be great GW source confusion, for individually resolved events, in the frequency range $f \lesssim 10$ mHz, between DWDs and CELs.

Despite this issue the author thinks it is possible to do science with these sources. Indeed it is presented here some possible solutions for the detection-degeneracy problem. One of the main goals of this work is to encourage the scientific community to explore additional solutions.

Table 7.2 Parameters of a CEL with $n = 2.95$ and equivalent binaries. The CEL is characterized by the mass and the compactness $\mathcal{C}$ obtained from the relativistic Feynman-Metropolis-Teller equation of state Rotondo et al. (2011). The frequency at the end of the chirping phase of the CEL is denoted by $f_{\rm end}^{\rm CEL}$, i.e. when the CEL reaches its maximum GW amplitude. For each CEL, the "matching" binary chirp mass and the mass components are shown in fourth, fifth and sixth columns, respectively. The frequency at the end of the binary chirping regime, $f_{\rm end}^{\rm bin}$, is tabulated in the seventh column. This value is given by the point when one of the stars fills its Roche-lobe, for the case of a DWD, and by point of tidal disruption, where we have assumed $R_2 \approx 70,000$ km for the radius of the less massive component m_2, for the case of an EMRI. The type of binary is shown in the eighth column. When the system is a DWD, the name of the most similar observed system is shown. For more details on the DWD systems see e.g. Rebassa-Mansergas et al. (2017) and references therein. The initial observing frequency f_0, is shown in the ninth column. The phase difference and the relative amplitude difference between the two system after 1 yr are shown in the next two columns. The ratio of the distance of both systems, assuming optimal orientations is shown in the twelfth column. The corresponding signal-to-noise ratio of the CEL located at $D = 1$ kpc, for 1 yr of observation from f_0 is shown in the last column.

$M_{\rm CEL}$ ($M_\odot$)	$\mathcal{C}$ (10^{-4})	$f_{\rm end}^{\rm CEL}$ (mHz)	$M_{\rm chirp}$ ($M_\odot$)	m_1 ($M_\odot$)	m_2 ($M_\odot$)	$f_{\rm end}^{\rm bin}$ (mHz)	Type-like	f_0 (mHz)	$\Delta\phi_{\rm 1y}$	$\frac{\Delta h_0}{h_0}\Big\|_{\rm 1y}$	$\frac{D_{\rm CEL}}{D_{\rm bin}}$	SNR
1.0	2.5	9.20	0.32	1940.62	0.0001	0.053	EMRI	0.05	3.631×10^{-10}	5.937×10^{-13}	0.778	und.
			0.28	0.35	0.30	13.38	PG1101+364	1.0	5.004×10^{-5}	2.515×10^{-9}	0.773	0.687
			0.2 4	0.45	0.18	7.76	J0106-1003	3.0	5.018×10^{-3}	6.455×10^{-8}	0.835	9.079
1.4	20.0	148.70	0.48	2916.81	0.0015	0.064	EMRI	0.05	5.521×10^{-10}	9.322×10^{-13}	0.808	und.
			0.45	0.59	0.45	19.92	WD0028-474	1.0	3.868×10^{-5}	3.106×10^{-9}	0.776	1.511
			0.43	0.52	0.47	21.30	WD0135-052	3.0	2.660×10^{-3}	6.344×10^{-8}	0.766	23.88
			0.42	0.51	0.45	20.25	WD1204-450	6.0	4.148×10^{-2}	4.377×10^{-7}	0.763	119.89
			0.41	0.47	0.47	21.48	WD1704-481[2]	9.0	2.135×10^{-1}	1.375×10^{-6}	0.764	145.73

Chapter 8

Central Remnant of a Binary Neutron Star Merger and Disk Formation

An accretion disk around the central remnant of a BNS merger, i.e. a newborn NS or a BH, is an important ingredient in models of short-duration gamma-ray bursts (GRBs; see e.g. Berger, 2014 and references therein). The classification mentioned in chapter 6 introduced two subclasses of short GRBs from BNS: short gamma-ray flashes (S-GRFs) and authentic short GRBs (S-GRBs), depending on whether the central remnant is a NS or a BH, respectively (see Ruffini et al., 2016b, and sec. 6.1 for details). This chapter analyzes the case of S-GRFs produced in BNS mergers, using conservation laws and quasi-universal laws for fast uniformly rotating NSs. In particular the necessary conditions on the binary mass in order to form a disk will be studied: the specific angular momentum must be larger than the one of the ISCO of the newborn NS, in order to form a disk. Three physically representative EOSs are used in this chapter. Further analysis with more EOSs will be performed in the future.

In U-GRFs the gamma-ray emission is expected to occur in a prompt short radiation phase. The post-merger radiation is drastically reduced in view of the absence of baryonic matter to power an extended emission. A kilonova can still be observed days after the merger, in the infrared, optical and ultraviolet wavelengths, produced in the radioactive decay of r-process material (Li & Paczyński, 1998; Metzger et al., 2010; Tanvir et al., 2013; Berger et al., 2013). In general, theoretical models of kilonovae discriminate between a “dynamical ejecta” composed of matter expelled by tides prior or during the merger, and a “disk-wind ejecta” composed of matter expelled from post-merger outflows in accretion disks (see e.g. Metzger, 2017, and references therein). It is clear that kilonova ejecta from U-GRFs are characterized by having only dynamical and no disk-wind component.

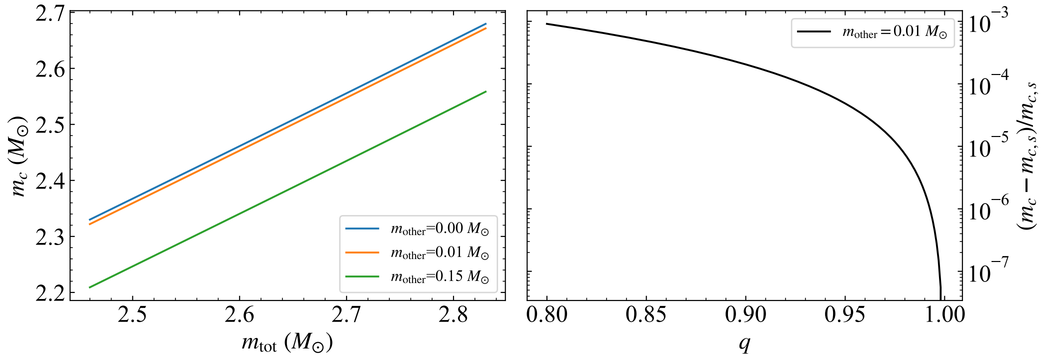

Figure 8.1 Left: inferred mass of the remnant NS as a function of the mass of the BNS components for selected values of $m_{\rm other}$. All the remnant NS masses are smaller than the critical for the maximally rotating configurations. Right: relative variation of the remnant NS mass with respect to the symmetric case $m_c(q = 1) = m_{c,s}$, $[m_c(q) - m_{c,s}]/m_{c,s}$, for constant total binary mass $m_{\rm tot} = 2.66\ M_\odot$.

8.1 Inferences from conservation laws

Conservation laws of baryon number, energy and angular momentum are used in order to analyze the properties of the central remnant NS. For uniformly rotating NSs, the relation among the baryonic mass, m_b, the gravitational mass, m_*, and the angular momentum J is well represented by the following simple equation (Cipolletta et al., 2015):

$$\frac{m_b}{M_\odot} = \frac{m_*}{M_\odot} + \frac{13}{200}\left(\frac{m_*}{M_\odot}\right)^2\left(1 - \frac{1}{137}j^{1.7}\right), \tag{8.1}$$

where $j \equiv cJ/(GM_\odot^2)$. This formula fits, with a maximum error of 2%, the results of the numerical integration of the axially-symmetric Einstein equations for a variety of nuclear EOS. Thus, Eq. (8.1) is a nearly universal, EOS-independent formula. Another EOS-independent property of rotating NSs is the angular momentum of the maximally rotating configurations, i.e. the one of the NS rotating at the maximum rate given by the Keplerian/mass-shedding limit. Along this sequence the gravitational and centrifugal forces are equal, so for faster rotation rates the star sheds mass from its equator (Stergioulas, 2003). The full numerical integration of the Einstein equations show that the angular momentum along the Keplerian sequence satisfies the approximate relation (see, e.g., Cipolletta et al., 2015)

$$J \approx 0.7\frac{Gm_*^2}{c}, \tag{8.2}$$

For simplicity, the BNS components are assumed to have equal gravitational mass, $m_1 = m_2 = m$, and no spin, $J_1 = J_2 = 0$. The analysis can be extended to different mass ratios $q \equiv m_2/m_1 < 1$. The total mass of the binary will denoted by $m_{\rm tot} = m_1 + m_2$. The corresponding baryonic masses, $m_{b1} = m_{b2} = m_b$, are given by Eq. (8.1). The orbital angular momentum at the merger exceeds the maximum angular momentum a NS can support given by eq. (8.2) (see below in sec. 8.3). This implies that the newly-formed, stable fast rotating NS starts at the Keplerian sequence, characterized by the dimensionless

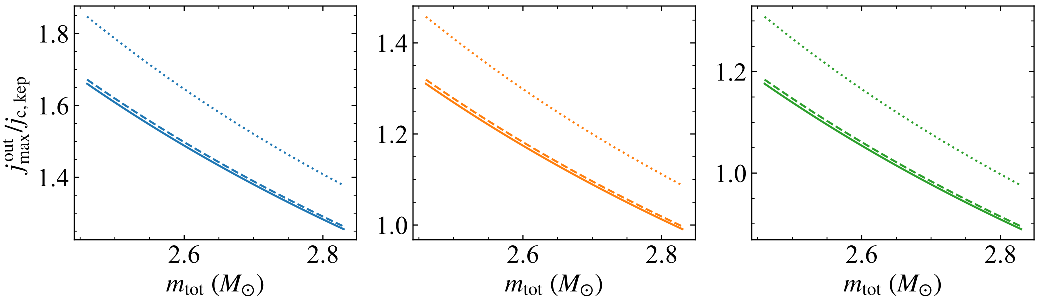

Figure 8.2 Ratio of the discriminant angular momentum $j_{\rm max}^{\rm out}$, to angular momentum of the remnant NS at the Keplerian sequence, $j_{\rm c,kep}$ as a function of the binary total mass. The continuous, dashed and dotted curves denote $m_{\rm other} = 0, 0.01, 0.15\ M_\odot$, respectively in all panels. The left panel shows the results for NL3 (blue), center GM1 (orange) and right TM1 (green). It can be seen that is not possible to form a detached disk for NL3 and GM1.

angular momentum,

$$j_{c,\rm kep} = \frac{cJ_{c,\rm kep}}{GM_\odot^2} \approx 0.7\left(\frac{m_c}{M_\odot}\right)^2 . \tag{8.3}$$

The baryonic mass of the central remnant NS $m_{b,c}$ is found by inserting eq. (8.3) into Eq. (8.1),

$$\frac{m_{b,c}}{M_\odot} = \frac{m_c}{M_\odot} + \frac{13}{200}\left(\frac{m_c}{M_\odot}\right)^2\left[1 - \frac{0.54}{137}\left(\frac{m_c}{M_\odot}\right)^{3.4}\right]. \tag{8.4}$$

The total number of baryons of the binary are redistributed among the central remnant NS, the ejected matter (of mass $m_{\rm ej}$), and the matter kept bound to the system (e.g. in form of a disk of mass m_d), i.e.,

$$M_b = m_{b,c} + m_{\rm ej} + m_d . \tag{8.5}$$

It is clear that by replacing the corresponding expressions for M_b and $m_{b,c}$ in eq. (8.5), this last becomes an algebraic (but non-linear) equation for m_c as a function of $m_{\rm ej}$ and m_d, once the BNS masses are specified. Figure 8.1 (left) shows the remnant NS mass, m_c, for symmetric BNS and for some selected values of disk and ejecta, $m_{\rm other} = m_{\rm d} + m_{\rm ej} = 0.0, 0.01, 0.15\ M_\odot$. The value of the mass components is chosen in the range (1.24–1.42) $M_\odot$, that corresponds to one–σ interval of the galactic observed BNSs. All the expressions used to this moment are EOS-independent. When the binary is not symmetric the effect of q is negligible, as it can seen on the right of fig. 8.1

8.1.1 Absence of surrounding disk

This study will focus on the formation of *supramassive* NSs. By disk it is meant bounded matter and detached from the star, i.e. the radius of the ISCO must be larger than the radius of the star. Since the presence of a disk would necessarily lead to an observable emission, e.g. via an accretion process onto the central remnant, the concept of U-GRF requires that such structure is absent. The first thing to check is whether the ISCO outside the star. The mass of a rotating NS at the Keplerian sequence, for which the equatorial radius is equal to the radius of the ISCO was found in (Cipolletta et al., 2017). Corresponding to this mass there is a discriminant angular momentum $j_{\rm max}^{\rm out}$, i.e. if the angular momentum of the NS is greater than this value, the ISCO is bigger than the equatorial radius. Figure 8.2 shows the ratio of $j_{\rm max}^{\rm out}$ to the angular momentum of the remnant NS at the Keplerian sequence, $j_{\rm c,kep}$ as function of $m_{\rm tot}$, selected values of $m_{\rm other}$ and three different EOSs. It can be seen a monotonically increase of the ratio $j_{\rm max}^{\rm out}/j_{\rm c,Kep}$ with $m_{\rm total}$. Therefore, the larger the disk mass, the less possible is the ISCO outside the star. As a matter of fact, it can be seen that is only possible for the TM1 EOS to form a detached disk (among the studied EOSs). This result can be understood as follows. The mass contribution from the disk and ejecta decreases the mass available for the remnant NS core. Since at the Keplerian sequence the angular momentum follows the quasi-universal law (8.2), when the remnant is less massive, the angular momentum $j_{\rm c,kep}$ is smaller, which in turn makes the equatorial radius closer to the ISCO (the remnant is less compact). This analysis can be used to discriminate between EOSs which form a supramassive NS with a detached disk.

Once it is guaranteed that the equatorial radius less or at most equal to the ISCO, and by assuming conservation of the specific (i.e. per-unit-mass) angular momentum, a *sufficient* condition for the absence of matter circulating around the newly-formed NS is that the largest specific angular momentum at the merger, $l_{\rm mrg}^{\rm max}$, must be less than the specific angular momentum of the ISCO around remnant NS,

$$l_{\rm mrg}^{\rm max} < l_{c,\rm ISCO}. \tag{8.6}$$

The material with $l = l_{\rm mrg}^{\rm max}$ is located at interception of the equatorial/orbital plane with the stellar surfaces. The extreme case when $l_{\rm mrg}^{\rm max} = l_{c,\rm ISCO}$ corresponds to the case of bound matter in form of a shell of a disk. Thus, by assuming the point of contact as the merger, i.e. $r_{\rm mrg} = R_1 + R_2 = 2R$ where $R_1 = R_2 = R$ are the NS radii, the following expression was obtained,

$$l_{\rm mrg}^{\rm max} = r_{\rm mrg}^2 \Omega_{\rm mrg} = 2m\mathcal{C}^{-1/2}, \tag{8.7}$$

where $\mathcal{C} \equiv Gm/(c^2 R)$ is the compactness of the BNS components, and $\Omega_{\rm mrg} = (GM/r_{\rm mrg}^3)^{1/2}$ is the orbital angular velocity at the merger. The formula derived in (Cipolletta et al., 2017) was used to calculate the value of the specific angular momentum of the ISCO (in corotation),

$$l_{c,\rm ISCO} = m_c \left[2\sqrt{3} - 0.37 \left(\frac{j_c}{m_c/M_\odot} \right)^{0.85} \right], \tag{8.8}$$

which fits the numerical results for any NS rotation rate with a maximum error of 0.3%. The expression for $l_{c,\rm ISCO}$ as a function of m_c was obtained by replacing j_c from eq. (8.3) into eq. (8.8). As previously shown, the remnant NS mass m_c depends on the mass of the BNS components, m, and on the disk+ejecta mass, $m_{\rm other}$. NL3 and GM1 have configurations without an ISCO, so it will be analyzed only TM1. The ratio of $l_{\rm mrg}^{\rm max}$ to $l_{c,\rm ISCO}$, as a function of m for selected values of $m_{\rm other}$ is shown in fig 8.3. There are two main opposing effects controlling the formation of a disk: the existence of an ISCO is favored by massive NS, but high massive rotating NS at the keplerian sequence implies higher $l_{\rm ISCO}$. Hence, if the mass of the NS is reduced by assigning some mass to the disk, the angular momentum of the ISCO is reduced reinforcing the its formation, but if the disk is very massive, the NS expands and “absorbs” the disk. From some value of disk and binary mass, the formation of the disk is no longer possible. In addition, fig. 8.3 shows the curve for which tthe final

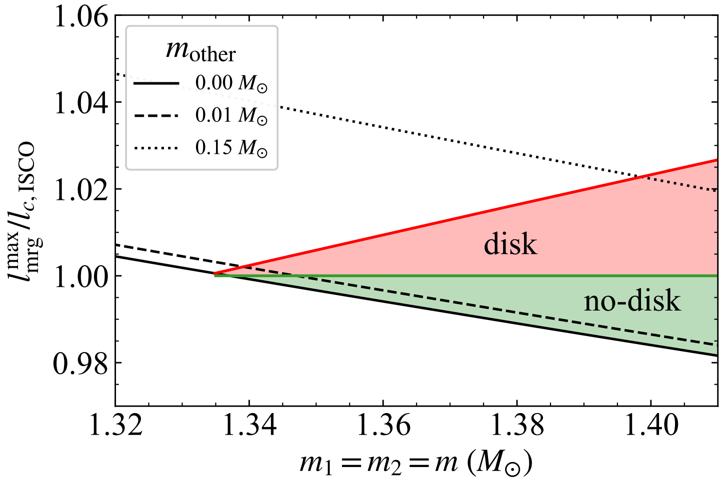

Figure 8.3 Ratio of the angular momentum per-unit-mass at the merger point, $l^{\mathrm{max}}_{\mathrm{mrg}}$ to the angular momentum per-unit-mas of the ISCO, $l_{c,\mathrm{ISCO}}$ of a NS rotating at the Keplerian rate (8.3) with interior matter described by the EOS TM1. Different values of m_{other} are shown. The region below the red curve corresponds to the zone where the remnant NS has an ISCO larger than the equatorial radius. The region above the green curve $l^{\mathrm{max}}_{\mathrm{mrg}}/l_{c,\mathrm{ISCO}} = 1$ correspond to the zone where there is enough angular momentum to form a disk, the region in green correspond to the zone where there is not enough angular momentum. The zone inside the continous black, red and green curves correspond to the detached-disk zone (red zone). When $m \lesssim 1.33\ M_\odot$ is not possible to form a detached-disk.

NS was an ISCO (red). The discriminant mass of the binary, $m_{\mathrm{discr}} = 1.33\ M_\odot$, is located at the intersection of this last curve with the curve $l^{\mathrm{max}}_{\mathrm{mrg}}/l_{c,\mathrm{ISCO}}$ for $m_{\mathrm{other}} = 0$ (continuous black), and with the horizontal line at 1 (green). For larger binary masses it is possible to form a detached disk, which corresponds to the zone between the red and greeen curves. In the above analysis only general conservation laws were used, but m_{discr} depends on the EOS. The analysis for a wider set of EOSs will be done in the future. From this partial analysis some general features can be inferred. For example, when the m is much larger than m_{discr} (and if there is and ISCO) the mass assigned to disk must be also large in order to form it.

The zone $m < m_{\mathrm{discr}}$ represents configurations where the disk is not detached from the star. In these cases, the final configuration is more similar to that of a hypermassive NS (see e.g. Shibata & Taniguchi, 2006, fig. 10), which is short-lived and could rapidly collapse to a BH in $\lesssim 1$ s (Hotokezaka et al., 2013). Therefore, here it is considered that when these last configurations lead to a long-lived supramassive NS, it could only exist without a surrounding disk.

8.2 Constraining the NS EOS with U-GRFs

The NS critical mass is defined by the secular axis-symmetric limit in which the star becomes unstable respect to axially-symmetric perturbations. This instability sequence can

Table 8.1 Critical mass in the non-rotating case, $M_{\rm crit}^{J=0}$, and in the rotating case, $M_{\rm max}^{J\neq 0}$, obtained in Cipolletta et al. (2015) for the NL3, GM1 and TM1 nuclear EOS. We recall that $M_{\rm max}^{J\neq 0}$ is the maximum critical mass value, namely the value of $M_{\rm crit}$ (see Eq. 8.9) for the highest possible angular momentum. This corresponds to the configuration at the intersection between the secular instability sequence and the Keplerian sequence, so with an angular momentum value (8.2).

EOS	$M_{\rm crit}^{J=0}/M_\odot$	$M_{\rm max}^{J\neq 0}/M_\odot$	k	p
NL3	2.81	3.38	0.006	1.68
GM1	2.39	2.84	0.011	1.69
TM1	2.20	2.62	0.017	1.61

be constructed following the turning-point method by Friedman et al. (1988). Namely, they showed that in a constant angular-momentum sequence with increasing central density, ρ_c, the turning point, i.e. where $\partial M/\partial \rho_c = 0$, separates secularly stable from secularly unstable configurations. For example, a fitting formula with a maximum error of 0.45%, was obtained by Cipolletta et al. (2015) from numerical simulations of rotating NSs with NL3, GM1 and TM1 EOS,

$$M_{\rm crit} = M_{\rm crit}^{J=0}(1 + kj^p), \tag{8.9}$$

where k and p are parameters that depend on the EOS, and $M_{\rm crit}^{J=0}$ is the critical mass of the non-rotating (spinless) case. See Table 8.1 for additional details.

The value of the critical mass in both the non-rotating case, $M_{\rm crit}^{J=0}$, and in the maximally rotating case, $M_{\rm crit}^{J_{\rm max}}$, depends on the EOS. Interestingly, the ratio of these two quantities is nearly EOS-independent (see, e.g., Cipolletta et al., 2015; Breu & Rezzolla, 2016),

$$M_{\rm crit}^{J_{\rm max}} \approx 1.2 M_{\rm crit}^{J=0}. \tag{8.10}$$

More exactly, the maximum increase in the mass by rotation is of 20% and is independent of the EOS (see also Table 8.1). This result can be used to constrain the $M_{\rm crit}^{J=0}$ from the observation of an U-GRB produced by a BNS merger.

It was argued before that if the central remnant in a BNS merger is a NS, then it must be initially at the Keplerian limit. Consequently, given that the Keplerian sequence is nearly flat (as a function of the central density) in the high mass region, the mass of the central remnant NS, m_c, must be very close to the maximum value of the NS critical mass, $M_{\rm crit}^{J_{\rm max}}$. This value is located at the crossing between the secular axis-symmetric instability sequence and the Keplerian sequence. Since $m_c \leq M_{\rm crit}^{J_{\rm max}}$, otherwise the merger would have formed a BH, we use Eq. (8.10) to set a lower limit in the critical mass of a *non-rotating* NS,

$$M_{\rm crit}^{J=0} \gtrsim \frac{m_c}{1.2}. \tag{8.11}$$

The above reasoning is general and, in principle can be applied for a central remnant NS with or without an accretion disk. However, in the case with a disk, the uncertainty in the estimate of the disk mass, which is not expected to be negligible with respect to the NS mass, introduces an uncertainty in the determination of m_c, as it can be seen from the conservation equation (8.5). Only if the remnant NS is bare, namely in the case of an U-GRF, the estimate of m_c can be estimated under the above considerations.

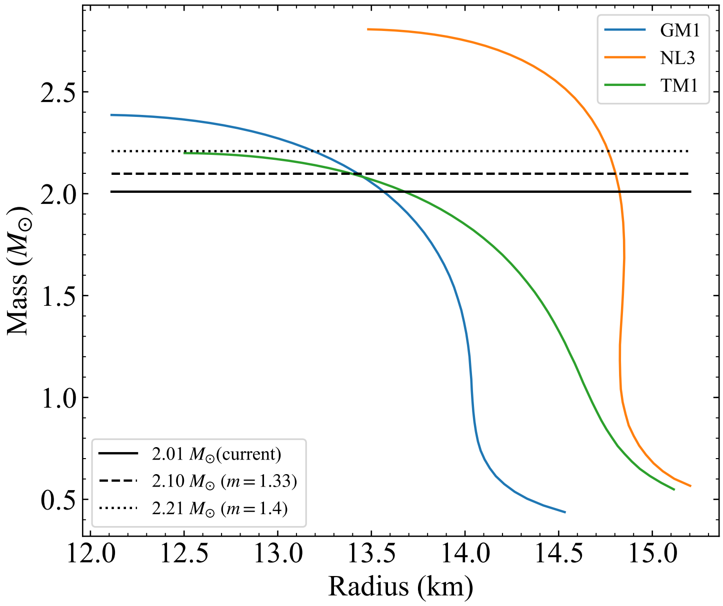

Figure 8.4 Constraints on the NS mass-radius relation imposed by the observation of an U-GRF. It is shown the lower limit to the critical mass of non-rotating NS given by Eq. (8.12) for selected BNS component masses $m = 1.38\ M_\odot$ and $m = 1.4\ M_\odot$.

If it is assumed that an U-GRF have been observed, then by definition $m_d = 0$. Since the expelled/unbound matter in BNS mergers is only 1% (or less) of the remnant NS mass, we can neglect its contribution to the total baryonic mass with $\sim$ 99% of accuracy. With these two assumptions, the conservation of baryon number, Eq. (8.5), leads to $M_b \approx m_{b,c}$, where the baryon mass of the central remnant NS, $m_{b,c}$, is related to its gravitational mass, m_c, by Eq. (8.4). The mass m_c is obtained as described before, and is shown in Fig. 8.1 (see blue curve). This relation is well fitted in the relevant range of merging masses by the linear law, $m_c \approx 1.9m$ which, combined with Eq. (8.11), imply the lower limit to the critical mass,

$$M_{\rm crit}^{J=0} \gtrsim \frac{1.9}{1.2} m \approx 1.58m\,. \tag{8.12}$$

For example, assuming $m \approx 1.33\ M_\odot$ (see e.g. Özel & Freire, 2016), the request that this BNS produces an U-GRF implies via Eq. (8.12) that $M_{\rm crit}^{J=0} \gtrsim 2.10\ M_\odot$. This is more stringent than the current critical mass value set by the mass of PSR J0348+0432, 2.01 $M_\odot$, the heaviest NS observed (Antoniadis et al., 2013). U-GRFs from BNS mergers with higher components could potentially constrain even more tightly the EOS: a BNS with $m = 1.4\ M_\odot$ would lead to a U-GRF if the NS critical mass is $M_{\rm crit}^{J=0} \gtrsim 2.21\ M_\odot$, this would rule out for example TM1. Conversely, an unambiguous determination of the existence of post-merger accretion without collapse to a BH from a binary with $m \approx 1.33\ M_\odot$, would rule out GM1 and NL3.

8.3 Limits on the gravitational wave emission

The conservation of mass-energy applied to the systems prior and after the merger can be written as,

$$\Delta E = \Delta E_{\rm GW} + \Delta E_{\rm other} = \left[m_{\rm tot} - (m_c + m_{\rm ej} + m_d)\right]c^2, \tag{8.13}$$

where $m_{\rm tot} = m_1 + m_2$ is the total mass of the binary, which in the symmetric case is $m_{\rm tot} = 2m$. Namely, the energy emitted should be equal to the mass defect of the system. The energy radiated in GWs, $\Delta E_{\rm GW} = \Delta E^{\rm insp}_{\rm GW} + \Delta E^{\rm pm}_{\rm GW}$, includes the inspiral regime, $E^{\rm insp}_{\rm GW}$, and the merger/post-merger regime, $E^{\rm pm}_{\rm GW}$. The quantity $\Delta E_{\rm other}$ is the energy radiated in channels different to GW emission, e.g. electromagnetic (photon) and neutrino emission.

For the sake of example we adopt here the above $1.33 + 1.33\ M_\odot$ BNS and the NS structure obtained for the NL3 EOS. The inspiral phase emits $E^{\rm insp}_{\rm GW} \approx G m_1 m_2/(2 r_{\rm mrg}) = \mathcal{C} M c^2/8 \approx 0.0165 M c^2 \approx 0.033 m c^2 \approx 7.86 \times 10^{52}$ erg in gravitational waves. The mass defect in the case of an U-GRF is $M - m_c - m_{\rm ej} \approx M - m_c \approx 0.1m$. The upper limit to the gravitational waves energy emitted in the post-merger phase can be obtained by switching off the additional losses, i.e. assuming $E_{\rm other} = 0$. Under this assumption, one obtains $E^{\rm pm}_{\rm GW} \approx (M - m_c)c^2 - E^{\rm insp}_{\rm GW} \approx 0.067 m c^2 \approx 2 E^{\rm insp}_{\rm GW}$.

On the other hand, the angular momentum of the binary can be estimated by adopting a rigid rotation with the Keplerian angular velocity, Ω,

$$J = 2\left(m r^2 + \frac{2}{5}\kappa m R^2\right)\Omega. \tag{8.14}$$

where κ is the ratio between the moment of inertia of the components and that of a homogeneous sphere, $(2/5) m R^2$. The angular momentum at the merger is

$$J_{\rm mrg} = J_{\rm cont} = \frac{G}{c}\left(1 + \frac{2}{5}\kappa\right) m^2 \mathcal{C}^{-1/2}. \tag{8.15}$$

From Eqs. (8.3) and (8.15) we estimate the excess between the angular momentum of the central remnant NS, J_c, and the one at the merger. This last depends on the EOS via the compactness $\mathcal{C}$ and the moment of inertia parameter κ. For the present example parameters we have $J_{\rm mrg} \approx 6.58 G M_\odot^2/c$ and $J_c \approx 4.52 G M_\odot^2/c$. Therefore, an amount of angular momentum, $\Delta J \approx 2.1 G M_\odot^2/c \approx 0.28 G M^2/c$, must be removed from the system by gravitational waves, the ejecta, the surrounding matter and/or by any other channel of angular momentum losses (e.g. neutrino emission). Since the ejecta expansion is nearly radial and for an U-GRF there is no surrounding disk, the above amount of angular momentum should be remove mostly via gravitational radiation.

These gravitational waves are mainly generated by the transitional non-axisymmetric object (e.g. triaxial ellipsoid), formed immediately after the merger, and their emission ends when the stable remnant NS is finally formed. Such a rotating object can be modeled as a compressible ellipsoidal figure of equilibrium, whose internal matter can be approximately described by a polytropic EOS of index $n = 0.5$–1 (Lai & Shapiro, 1995). This object exhibits a spin-up behavior with typical high frequency values of 1.4–2.0 kHz. It is interesting that the above estimates of energy and angular momentum radiated leads to an estimate of the gravitational wave radiation in the post-merger phase, $f^{\rm pm}_{\rm GW} \sim E^{\rm pm}_{\rm GW}/(2\pi\Delta J) \approx 1.48$ kHz.

As usual, in order to estimate the detection efficiency we find the root-sum-squared strain of the signal,

$$h_{\rm rss} = \sqrt{\int 2\big[|\tilde{h}_{+}|^{2} + |\tilde{h}_{\times}|^{2}\big]df}, \tag{8.16}$$

where $\tilde{h}_{+}$ and $\tilde{h}_{\times}$ are the Fourier transform of the gravitational wave polarizations. These signals are expected to be detected with a 50% of efficiency by the LIGO/Virgo pipelines (Abbott et al., 2018a) when $h_{\rm rss} \sim 10^{-22}$ Hz$^{-1/2}$ (Abbott et al., 2017f). The $h_{\rm rss}$ depends on the mean frequency, on the emitted energy and on the distance to the source. Thus, for the aforementioned energy release in the post-merger phase, Advanced LIGO/Virgo could detect these gravitational waves for binaries located up to $\approx$ 10 Mpc. If the matched-filtering technique is used to detect this type of signals, the gravitational-wave horizon is of the order of 19 Mpc, at design sensitivity.

8.4 Discussion and Future Work

The conservation laws of baryon number, energy and angular momentum were used to study disk formation in BNS mergers. The mass of the BNS components for which the central remnant can have a surrounding accretion disk was found. This value was computed when the component masses are equal, $m_1 = m_2 = m$, and when the remnant is a NS (not a BH), namely for the S-GRF subclass of short GRBs (Ruffini et al., 2016b). When the BNS is not symmetric, $0.8 < q < 1$, the results are basically the same. For mass ratios $q < 0.8$, the tidal disruption of the less massive component is highly probable, favoring disk formation. This scenario will be studied in a future work. The range of masses chosen lie between 1σ interval of the observed galactic BNS (Özel & Freire, 2016). Within this interval the EOS TM1 and NL3 do not exhibit an ISCO, therefore do not lead to a supramassive remnant NS with a surrounding disk. Regarding the EOS GM1 it was found that it is possible to form a disk if the mass of the BNS is larger than $m_{\rm crit} = 1.33\ M_{\odot}$. The role of the unbound ejected and disk mass is to favor the disk formation if the binary components satisfy this last condition.

BNS mergers with $m > m_{\rm discr}$ produce a final merged configuration of mass m_c, composed of a fast rotating, massive NS, which can have surrounding matter. However, when the binary mass is much larger than $m_{\rm crit}$, the condition of disk formation requires a large amount of mass. This implies that is highly unlikely to form a disk in very massive BNS mergers. It is advanced here that such BNS mergers lead to a new subclass of bursts, the U-GRFs, where the only high-energy electromagnetic radiation occurs in a prompt emission with a short timescale dominated by the dynamical merger timescale. The X and gamma-rays post-merger emission is expected to be drastically reduced in view of the absence of baryonic matter to power it, e.g., through an accretion process around the newborn NS. Optical, infrared and ultraviolet emission can still be observed from an r-process powered kilonova (Li & Paczyński, 1998; Metzger et al., 2010). Such an emission should emerge on the timescale of a day after the merger (Li & Paczyński, 1998; Metzger et al., 2010; Tanvir et al., 2013; Berger et al., 2013). The imprint of the kilonova associated with an U-GRF is that it contains only dynamical ejecta from matter expelled by tidal interactions prior and/or during the merger. In BNS mergers with a central remnant surrounded e.g. by an accretion disk, the accretion outflows (wind-ejecta) add to the dynamical ejecta.

The limits to the energy and angular momentum that can be carried out by gravitational radiation in the post-merger phase of U-GRFs were obtained in this chapter. This information was used to infer that current detectors, e.g. LIGO, could detect these radiation only up to a maximum distance 10–20 Mpc at design sensitivity. Assuming as an upper limit to the occurrence rate of U-GRFs the one of S-GRF, 2.6–5.0 Gpc^{-3} yr^{-1} (Ruffini et al., 2018b), the above implies an approximate upper limit of gravitational wave detection rate of 0.1–1.0 per century.

The method outlined in this work for the analysis of the properties of the central remnant of mass-symmetric BNS mergers can be extended to a variety of mass-ratios and EOS. This analysis can be also extended to S-GRBs, namely to BNS mergers leading to a BH. S-GRBs show a 0.1–100 GeV emission (Ruffini et al., 2018c) in agreement with the presence of baryonic matter interacting with the newly-formed BH e.g. via accretion (Aimuratov et al., 2017; Ruffini et al., 2016a). Therefore, this kind of analysis can be used to infer the mass of the merging components needed to have 1) BH formation and 2) surrounding matter bound to the BH. This result can be compared with the independent result of the GeV emission analysis to constrain the NS nuclear EOS. This is an ongoing work whose results are going to be presented in a forthcoming publication.

Appendixes

Appendix A

Metric Perturbation

This appendix shows the derivation of the formulas involving the perturbations of the metric. It is supposed that the spacetime metric $g_{\mu\nu}$ can be expressed as follows:

$$g_{\mu\nu} = g^{(\mathrm{B})}_{\mu\nu} + h_{\mu\nu}, \tag{A.1}$$

with $|h_{\mu\nu}| \ll 1$. The inverse of the metric defined by $g_{\mu\lambda} g^{\lambda\nu} = \delta_\mu{}^\nu$, can be expanded as a power series in $h^\mu{}_\nu = g^{(\mathrm{B})\mu\alpha} h_{\alpha\nu}$:

$$[g^{(\mathrm{B})}_{\mu\lambda} + h_{\mu\lambda}][g^{(\mathrm{B})\lambda\nu} - h^{\lambda\nu} + h^\lambda{}_\alpha h^{\alpha\nu} - h^\lambda{}_\beta h^\beta{}_\alpha h^{\alpha\nu} + \mathcal{O}(h^4)] = \delta_\mu{}^\nu \tag{A.2}$$

The difference of the Christoffel symbols derived from the metric $g_{\mu\nu}$ and the background metric $g^{(\mathrm{B})}_{\mu\nu}$ is a tensor denoted by $S^\lambda{}_{\mu\nu}$. This can be shown by first computing the difference of the covariant derivative of a vector A^μ:

$$C^\mu{}_\nu = A^\lambda (\Gamma^\nu_{\lambda\mu} - \Gamma^{\nu(\mathrm{B})}_{\lambda\mu}). \tag{A.3}$$

Since the left hand side is a tensor, $S^\nu{}_{\lambda\mu} = \Gamma^\nu_{\lambda\mu} - \Gamma^{\nu(\mathrm{B})}_{\lambda\mu}$ must be a tensor. In order to calculate $S^\mu{}_{\nu\beta}$ we choose a LIF in the background metric, $\Gamma^{\nu(\mathrm{B})}_{\lambda\mu}|_{\mathrm{LIF}} = 0$:

$$S^\mu{}_{\nu\beta}|_{\mathrm{LIF}} = \frac{1}{2} g^{\mu\lambda}|_{\mathrm{LIF}} \big(h_{\lambda\beta,\mu} + h_{\lambda\nu,\beta} - h_{\nu\beta,\lambda}\big), \tag{A.4}$$

and transform to a general frame by means of the covariance principle, $\eta_{\mu\nu} \mapsto g^{(\mathrm{B})}_{\mu\nu}$, $\partial_\mu \mapsto \nabla_\mu$:

$$S^\mu{}_{\nu\beta} = \frac{1}{2} g^{\mu\lambda} \big(h_{\lambda\nu|\beta} + h_{\lambda\beta|\nu} - h_{\nu\beta|\lambda}\big), \tag{A.5}$$

where the subindex “|” denotes covariant differentiation with respect to the background metric. This last expression is valid to all orders in $h_{\mu\nu}$. The difference of the connections to linear order in $h_{\mu\nu}$ is denoted by $W^\nu{}_{\mu\beta}$, and it is obtained from (A.5) by replacing $g^{\mu\nu} \mapsto g^{(\mathrm{B})\mu\nu}$:

$$W_{\alpha\mu\nu} = \frac{1}{2}\Big(h_{\alpha\mu|\nu} + h_{\alpha\nu|\mu} - h_{\mu\nu|\alpha}\Big). \tag{A.6}$$

A.1 Ricci and Riemann Tensor Perturbations

The difference of the Riemann tensor it is obtained similarly by performing the calculation in a LIF of the background metric:

$$R^{\mu}{}_{\alpha\nu\beta} - R^{(\mathrm{B})\mu}{}_{\alpha\nu\beta} = S^{\mu}{}_{\alpha\beta,\nu} - S^{\mu}{}_{\alpha\nu,\beta} + \Gamma^{\mu}_{\lambda\nu}\Gamma^{\lambda}_{\alpha\beta} - \Gamma^{\mu}_{\lambda\beta}\Gamma^{\lambda}_{\alpha\nu}. \tag{A.7}$$

In the LIF the tensor $S^{\mu}{}_{\alpha\beta}|_{\mathrm{LIF}} = \Gamma^{\mu}_{\alpha\beta}$. Therefore, after transforming to a general frame, the Riemann and the Ricci tensors are given by

$$R^{\mu}{}_{\alpha\nu\beta} - R^{(\mathrm{B})\mu}{}_{\alpha\nu\beta} = S^{\mu}{}_{\alpha\beta|\nu} - S^{\mu}{}_{\alpha\nu|\beta} + S^{\mu}{}_{\lambda\nu} S^{\lambda}{}_{\alpha\beta} - S^{\mu}{}_{\lambda\beta} S^{\lambda}{}_{\alpha\nu}, \tag{A.8}$$

$$R_{\alpha\beta} - R^{(\mathrm{B})}_{\alpha\beta} = S^{\mu}{}_{\alpha\beta|\mu} - S^{\mu}{}_{\alpha\mu|\beta} + S^{\mu}{}_{\lambda\mu} S^{\lambda}{}_{\alpha\beta} - S^{\mu}{}_{\lambda\beta} S^{\lambda}{}_{\alpha\mu}. \tag{A.9}$$

The Ricci tensor can be expanded according to the order of $h_{\mu\nu}$:

$$R_{\alpha\beta} = R^{(\mathrm{B})}_{\alpha\beta} + R^{(1)}_{\alpha\beta}(h) + R^{(2)}_{\alpha\beta}(h) + \mathcal{O}(h^3), \tag{A.10}$$

where the linear part in $h_{\alpha\beta}$ is

$$\begin{aligned} R^{(1)}_{\alpha\beta}(h) &= W^{\lambda}{}_{\alpha\beta|\lambda} - W^{\lambda}{}_{\alpha\lambda|\beta}, \\ &= -\frac{1}{2}\Big(h_{\alpha\beta|\lambda}{}^{\lambda} + g^{(\mathrm{B})}_{\mu\nu} h^{\mu\nu}{}_{|\alpha\beta} - h_{\lambda\alpha|\beta}{}^{\lambda} - h_{\lambda\beta|\alpha}{}^{\lambda}\Big), \end{aligned} \tag{A.11}$$

and the quadratic part is

$$\begin{aligned} R^{(2)}_{\alpha\beta}(h) &= (-h^{\lambda\theta} W_{\theta\alpha\beta})_{|\lambda} + (h^{\lambda\theta} W_{\theta\alpha\lambda})_{|\beta} + W^{\lambda}{}_{\lambda\theta} W^{\theta}{}_{\alpha\beta} - W^{\lambda}{}_{\beta\theta} W^{\theta}{}_{\alpha\lambda}, \\ &= h^{\lambda\theta}(W_{\theta\alpha\lambda|\beta} - W_{\theta\alpha\beta|\lambda}) - \Big(h^{\lambda\theta}{}_{|\lambda} - \frac{1}{2}h^{|\theta}\Big) W_{\theta\alpha\beta} \\ &+ \frac{1}{4}h^{\lambda\theta}{}_{|\beta} h_{\theta\lambda|\alpha} + \frac{1}{2}h_{\beta}{}^{\theta|\lambda}\big(h_{\alpha\theta|\lambda} - h_{\alpha\lambda|\theta}\big). \end{aligned} \tag{A.12}$$

The Ricci scalar to linear order is $R^{(1)}(h) = h_{\alpha\beta}{}^{|\alpha\beta} - h_{|\lambda}{}^{\lambda}$ and the Einstein tensor to linear order is

$$G^{(1)}_{\mu\nu}(h) = h_{\lambda(\mu|\nu)}{}^{\lambda} - \frac{1}{2}\Big(h_{\mu\nu|\lambda}{}^{\lambda} + h_{|\lambda}{}^{\lambda} g^{(\mathrm{B})}_{\mu\nu} - h_{|\mu\nu} - h_{\alpha\beta}{}^{|\alpha\beta} g^{(\mathrm{B})}_{\mu\nu}\Big). \tag{A.13}$$

By substituting $h_{\mu\nu} = \overline{h}_{\mu\nu} - \overline{h} g^{(\mathrm{B})}_{\mu\nu}/2$, and changing to a flat background, the left hand side of eq. (2.3) is obtained.

Appendix B

Multipole expansions

This appendix although can be regarded as mathematical, gives a small review on the tools to systematically compute the multipoles of GR. Moreover, it is an adequate formalism to express the GW field in the local wave zone independent of the technique used to compute the radiation. This appendix is mostly based on the work of Thorne (1980b). The symmetries of the equations play a major role in the laws of physics. The fact that the Laplace, the Poisson and the wave equation are invariant under rotations implies that the most general solution of these equation is expressed in terms of the spherical harmonics, $Y^{lm}(\theta,\phi)$. These last provide a complete set of representations of the rotation group $SO(3)$,

$$Y^{lm}(\theta',\phi') = \sum_{m'=-l}^{l} A_{mm'} Y^{lm'}(\theta,\phi). \tag{B.1}$$

The set of spherical harmonics is an orthogonal basis and any function defined on the sphere can be expanded in terms of them. Since both the spherical harmonics and the STF tensors, which will be denoted by calligraphic capital letters, provide irreducible representations of the rotation group, there is a map between the two sets. The cartesian components of the unit vector can be expressed as $n_x + i n_y = e^{i\phi}\sin\theta,\ n_z = \cos\theta$. This allows to express the spherical harmonics as,

$$Y^{lm}(\theta,\phi) = \mathcal{Y}_L N_L, \tag{B.2}$$

where $N_L = n_{i_1} n_{i_2} \dots n_{i_l}$. For example, the STF tensor corresponding to the spherical harmonic Y^{2m} is given by,

$$Y^{2m}(\theta,\phi) = \mathcal{Y}^{2m}_{ij} n_i n_j. \tag{B.3}$$

Since $m = -l, -l+1, \dots, l$, there are 5 symmetric trace-free constant matrices $\mathcal{Y}^{2m}_{ij}$ (see Maggiore (2008) for explicit expressions), which are linearly independent and thus form a base for STF tensors of rank 2 . These matrices satisfy,

$$\mathcal{Y}^{2m}_{ij} \left(\mathcal{Y}^{2m'}_{ij}\right)^* = \frac{15}{8\pi}\delta_{mm'}, \tag{B.4}$$

thus any STF rank 2 tensor $\mathcal{B}_{ij}$ can be expanded as,

$$\mathcal{B}_{ij} = \sum_{m=-2}^{2} B_m \mathcal{Y}^{2m}_{ij}, \tag{B.5}$$

where B_m are the spherical components of the tensor $\mathcal{B}_{ij}$. The reduced quadrupole moment can be expressed in terms of spherical harmonics with $l = 2$ through the following relation,

$$r^2\left(n_i n_j - \frac{1}{3}\delta_{ij}\right) = r^2 \sum_{m=-2}^{2} \frac{8\pi}{15}(\mathcal{Y}^{2m}_{ij})^* Y^{2m}(\theta,\phi). \tag{B.6}$$

Hence, if the source is spherically symmetric the reduced quadrupole moment is zero, provided that $\int d\Omega Y^{2m} = 0$. Moreover, for an axially symmetric rotating source, the quadrupole moment is constant and there is no GW emission. The relation between the spherical harmonics and STF tensors is summarized as,

$$\mathcal{T}_L N_L = \sum_{m=-l}^{l} T_{lm} Y^{lm}(\theta,\phi). \tag{B.7}$$

Recall that $Y^{lm}(\theta,\phi)$ are the eigenfunctions of the following operators constructed from the orbital angular momentum operator $\mathbf{L} = -i\mathbf{r}\times\mathbf{\nabla}$,

$$L_z Y^{lm}(\theta,\phi) = m Y^{lm}(\theta,\phi), \tag{B.8}$$

$$\mathbf{L}^2 Y^{lm}(\theta,\phi) = l(l+1) Y^{lm}(\theta,\phi). \tag{B.9}$$

B.1 Vector and Tensor Spherical Harmonics

Just as any scalar function defined on the sphere can be decomposed into spherical harmonics, a vector or a tensor function can be decomposed in terms of vector and spherical tensors, which will be constructed from the (scalar) spherical harmonics. Vector spherical harmonics are constructed by combining scalar spherical harmonics with the basis vectors,

$$\boldsymbol{\xi}^{\pm 1} = \mp(\hat{\mathbf{x}} \pm i\hat{\mathbf{y}}), \quad \boldsymbol{\xi}^0 = \hat{\mathbf{z}}, \tag{B.10}$$

which represent the spin wavefunction of a vector particle with spin (helicity) $s = 1$, and its projection along the z axis is given by the superindex. The procedure is done by following the quantum mechanics formalism for expressing states of total angular momentum, $\mathbf{J} = \mathbf{L} + \mathbf{S}$, with quantum numbers, $|j, j_z\rangle$, in terms of states with spin $|s, s_z\rangle$ and orbital angular momentum $|l, m\rangle$,

$$\mathbf{Y}^{l,jj_z} = \sum_{s_z=-1}^{1} \sum_{m=-l}^{l} \langle 1 l s_z m | j j_z\rangle \boldsymbol{\xi}^{s_z} Y^{lm}(\theta,\phi), \tag{B.11}$$

with $l = j-1, j, j+1$ and where $\langle 1 l s_z m | j j_z\rangle$ are the Clebsch-Gordan coefficients. These vector spherical harmonics are eigenfunctions of the orbital angular momentum operator $\mathbf{L}^2$, and are called "pure orbital" vector spherical harmonics. However, they are neither purely transverse nor purely radial, and therefore are not convenient for describing vector radiation. Instead, the following combinations called "pure spin" vector harmonics, are introduced (see Thorne (1980b) for the value of the coefficients),

$$\mathbf{Y}^{E,lm} = a_{11}\mathbf{Y}^{l-1,lm} + a_{12}\mathbf{Y}^{l+1,lm} = \sqrt{l(l+1)}\,r\mathbf{\nabla} Y^{lm}(\theta,\phi) \tag{B.12}$$

$$\mathbf{Y}^{R,lm} = a_{21}\mathbf{Y}^{l-1,lm} + a_{22}\mathbf{Y}^{l+1,lm} = Y^{lm}(\theta,\phi)\mathbf{n}, \tag{B.13}$$

$$\mathbf{Y}^{B,lm} = i\mathbf{Y}^{l,lm}_i = i\mathbf{L} Y^{lm}(\theta,\phi). \tag{B.14}$$

Note that the "electric" and "magnetic" vector spherical harmonics $\mathbf{Y}^{E,lm}$ and $\mathbf{Y}^{B,lm}$ are orthogonal to $\mathbf{n}$. Both the pure orbital and pure spin vector spherical harmonics are orthonormal,

$$\int Y_i^{F,lm} Y_i^{F',l'm'} d\Omega = \delta_{FF'}\delta_{ll'}\delta_{mm'}, \tag{B.15}$$

where $F = l-1, l, l+1$ for pure orbital and $F = E, B, R$ for pure spin, therefore both sets can be used to expand a vector function on the sphere.

Now, the wavefunction of total spin 2 is formed with the tensor product of the spin 1 wavefunctions[1],

$$\mathbf{t}^m = \sum_{m_1,m2} \langle 11 m_1 m_2 | 2m \rangle \boldsymbol{\xi}^{m_1} \otimes \boldsymbol{\xi}^{m_2}, \tag{B.16}$$

Then, tensor spherical harmonics are constructed in the same way,

$$\mathbf{T}^{l',lm} = \sum_{m''=-2}^{2} \sum_{m'=-l'}^{l'} \langle 2l'm'm'' | lm \rangle \mathbf{t}^{m''} Y^{l'm'}(\theta,\phi), \tag{B.17}$$

with $l' = l-2, l-1, \dots l+2$. These tensors are pure orbital and are eigenfunctions of $\mathbf{L}^2$ and L_z, again they are neither transverse nor radial. The following pure spin tensor harmonics are defined,

$$T_{ij}^{S0,lm} = (n_i n_j - \delta_{ij}/3) Y^{lm}(\theta,\phi), \tag{B.18}$$

$$T_{ij}^{E1,lm} = \frac{2}{r}\left[\frac{2}{l(l+1)}\right]^{1/2} (n_i \partial_j + n_j \partial_i) Y^{lm}(\theta,\phi), \tag{B.19}$$

$$T_{ij}^{B1,lm} = \frac{2}{r}\left[\frac{2}{l(l+1)}\right]^{1/2} (n_i L_j + n_j L_i) Y^{lm}(\theta,\phi), \tag{B.20}$$

$$T_{ij}^{E2,lm} = \left[\frac{2(l-2)!}{(l+2)!}\right]^{1/2} r^2 \Lambda_{ij,mn} \partial_m \partial_n Y^{lm}(\theta,\phi), \tag{B.21}$$

$$T_{ij}^{B2,lm} = \frac{ir}{2}\left[\frac{2(l-2)!}{(l+2)!}\right]^{1/2} \Lambda_{ij,lm}(\partial_m L_n + \partial_n L_m) Y^{lm}(\theta,\phi), \tag{B.22}$$

note that $\mathbf{T}^{E2,lm}$ and $\mathbf{T}^{B2,lm}$ are TT symmetric tensors. The pure orbital and pure spin tensor spherical harmonics are orthonormal

$$\int T_{ij}^{F,lm} T_{ij}^{F',l'm'} d\Omega = \delta_{FF'}\delta_{ll'}\delta_{mm'}, \tag{B.23}$$

but the pure spin are more convenient to expand the gravitational field in the local wave zone (to leading term in r),

$$h_{ij}^{\mathrm{TT}}(t,r,\theta,\phi) = \frac{G}{rc^4} \sum_{l=2}^{\infty} \sum_{m=-l}^{l} \left[u_{lm}(u) T_{ij}^{E2,lm}(\theta,\phi) + v_{lm}(u) T_{ij}^{B2,lm}(\theta,\phi)\right]. \tag{B.24}$$

---

[1] Tensor wavefunction with total spin 1 or 0 can be constructed but they are not symmetric nor trace-free.

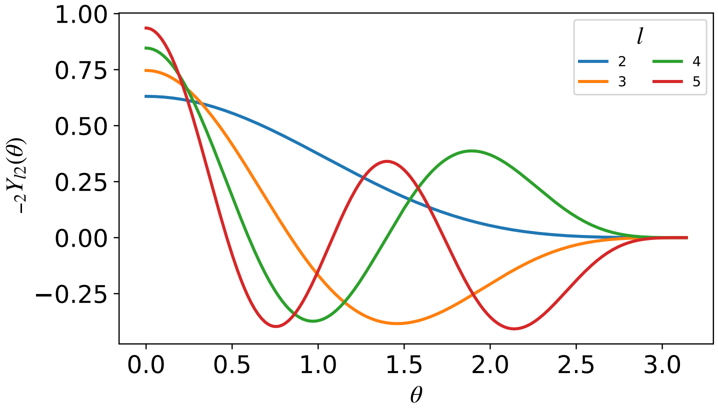

Figure B.1 Spin-weighted Spherical Harmonic with $s = -2$, $m = 2$ for selected values of l. It is shown only the part that depends on polar the angle, ${}_sY_{lm}(\theta,\phi) = e^{im\phi}\,{}_sY_{lm}(\theta)$.

In the weak-field and low-velocity approximation, the coefficients $u_{lm} = d^l I_{lm}/dt^l$ and $v_{lm} = d^l S_{lm}/dt^l$ are related to source mass and moment by (Maggiore, 2008),

$$I_{lm} = \frac{1}{c^l}\frac{16\pi}{(2l+1)!!}\sqrt{\frac{(l+1)(l+2)}{2l(l-1)}}\int r^l T^{00}(Y^{lm})^* d^3x, \tag{B.25}$$

$$S_{lm} = \frac{1}{c^l}\frac{32\pi}{(2l+1)!!}\sqrt{\frac{(l+2)}{2(l-1)}}\int r^l T^{i0}(Y_i^{B,lm})^* d^3x. \tag{B.26}$$

These three last expression are the ultimate relations to calculate the all the multipoles of GR in the weak-field and low-velocity approximation.

B.2 Spin-weighted Spherical Harmonics

The behaviour of GW polarizations h_+ and $h_\times$ under a rotation ψ around the propagation direction can be summarized as,

$$\eta = h_+ \mp i h_\times \mapsto \eta' = e^{\mp i2\psi}(h_+ \mp i h_\times). \tag{B.27}$$

The function η is said to have spin-weight ± 2. A scalar function defined on the sphere has spin-weight 0, because it is invariant under rotations around the radial direction. In contrast, the polarizations of spherical GWs change under rotation around the radial direction. A mathematical formalism to study spin-weighted quantities was developed by Newman & Penrose (1966). They found a base for spin-weighted functions called spin-weighted spherical harmonics ${}_sY_{lm}(\theta,\phi)$. These latter are the eigenfunctions of the operator $\eth$, put operator, and can be constructed iteratively from the spherical harmonics (spin weight 0) (see e.g. Hughes, 2000, appendix 2). For example, spin-weighted spherical harmonics with $s = -2$ are shown in fig. B.1, for more details see (Goldberg et al., 1967). Since the GWs polarization have spin-weight ∓ 2, (B.27) can be decomposed into spin-weighted spherical harmonics components. For GR propagating radially, following the convention of Kidder (2008), a TT coordinate frame is chosen with triad $(\mathbf{n}, \mathbf{p}, \mathbf{q})$,

$$\mathbf{n} = \mathbf{p} \times \mathbf{q}, \quad \mathbf{n} = \hat{\mathbf{e}}_r, \quad \mathbf{p} = \hat{\mathbf{e}}_\theta, \quad \mathbf{q} = \hat{\mathbf{e}}_r, \tag{B.28}$$

so the GW polarizations are given by,

$$h_+ = \frac{1}{2}(p_i p_j - q_i q_j) h_{ij}^{\mathrm{TT}}, \tag{B.29}$$

$$h_\times = \frac{1}{2}(p_i q_j + q_i p_j) h_{ij}^{\mathrm{TT}}. \tag{B.30}$$

The pure spin tensor spherical harmonics are related to the spin-weighted spherical harmonics via (Thorne, 1980b),

$$\mathbf{T}^{E2,lm} = 2^{-1/2}({}_{-2}Y_{lm}\mathbf{m} \otimes \mathbf{m} + {}_{2}Y_{lm}\mathbf{m}^* \otimes \mathbf{m}^*), \tag{B.31}$$

$$\mathbf{T}^{B2,lm} = -i 2^{-1/2}({}_{-2}Y_{lm}\mathbf{m} \otimes \mathbf{m} - {}_{2}Y_{lm}\mathbf{m}^* \otimes \mathbf{m}^*), \tag{B.32}$$

where $\mathbf{m} = 2^{1/2}(\hat{\mathbf{e}}_\theta + i\hat{\mathbf{e}}_\phi)$, which implies that,

$$h_+ - i h_\times = \sum_{l=2}^{\infty} \sum_{m=-l}^{l} h_{lm}(t, r)_{-2}Y_{lm}(\theta, \phi). \tag{B.33}$$

This last eq. expresses the fact that a function of spin-weight -2 is decomposed in terms of ${}_{-2}Y_{lm}$, and shows that the components h_{lm} depend on the moments of the source,

$$h_{lm}(t, r) = \frac{G}{rc^4}[u_{lm}(u) - i v_{lm}(u)]. \tag{B.34}$$

Usually, the GWs from numerical relativity simulations are given in terms of h_{lm}. In addition the post-Newtonian and EOB approaches are more easily developed in terms of these components.

B.3 STF Tensors and the Wave Equation

The most general solution of the scalar wave equation is expressed in terms of STF tensors (Pirani, 1965) ,

$$\psi(t, r, \theta, \phi) = \sum_{l=0}^{\infty} \left[r^{-1}\mathcal{A}_L(u)\right]_{,L}, \tag{B.35}$$

where A_L depends only the retarded time and the angular dependency comes from the repeated application of the partial derivative $\partial_i r = n_i$. Each term of the sum, the 2^l-pole, is a solution of the wave equation. That this is a solution of the wave equation follows from $\Box(A_L(u)/r) = 0$ and from the commutativity between the d'Alembertian and partial differentiation. For a compact source $S(t, \mathbf{x})$, each multipole is obtained by integration,

$$\mathcal{A}_L = \int d^3y \hat{y}_L \int_{-1}^{1} d\alpha \delta_l(\alpha) S(u + \alpha|\mathbf{y}|/c, \mathbf{y}), \tag{B.36}$$

where $\delta_l(\alpha) \equiv (2l+1)!!(1-\alpha^2)^l/(2^{l+1}l)$, and $\hat{y}_L$ denotes the symmetric and trace-free part of the tensor x_L. The same procedure can be applied to the vector or tensor wave equation. At linearized level, in principle, the solution depends on the tensor $H_L^{\mu\nu}$ (see (2.40)), which has 10 free indices. After performing a gauge transformation which preserves the Lorentz gauge condition, the solution can be expressed in terms of *two* families of STF tensors $\mathcal{M}_L, \mathcal{S}_L$. This is related to the fact that GWs have only two degrees of freedom and its physical components are given by (Damour & Iyer, 1991),

$$
\begin{aligned}
\bar{h}^{00} &= \frac{4G}{c^2}\sum_{l=0}^{\infty}\frac{(-1)^l}{l!}\partial_L\left[\frac{\mathcal{M}_L(u)}{r}\right], \\
\bar{h}^{0i} &= -\frac{4G}{c^3}\sum_{l=1}^{\infty}\frac{(-1)^l}{l!}\partial_{L-1}\left[\frac{\mathcal{M}^{(1)}_{iL-1}(u)}{r} + \frac{l}{l+1}\epsilon_{imn}\partial_m\left(\frac{\mathcal{S}_{nL-1}(u)}{r}\right)\right], \\
\bar{h}^{ij} &= \frac{4G}{c^2}\sum_{l=2}^{\infty}\frac{(-1)^l}{l!}\partial_{L-2}\left[\frac{1}{r}\mathcal{M}^{(2)}_{ijL-2}(u)\frac{2l}{l+1}\partial_m\left(\frac{1}{r}\epsilon_{mn(i}\mathcal{S}^{(1)}_{j)nL-2}(u)\right)\right],
\end{aligned}
\tag{B.37}
$$

where the explicit expressions for $\mathcal{M}_L$ and $\mathcal{S}_L$ can be found in Maggiore (2008) sec. 3.5.1. The components of the GWs in the TT frame are found by projecting the purely spatial part of (2.40) with $\Lambda_{ij,mn}$. It is important to mention that this latter projection still depends on the above mentioned tensors (the degrees of freedom cannot be further reduced). This formalism can be promoted to the non-linear level in the local wave zone, and it is called the multipolar post-Minkowskian expansion (see e.g. Blanchet, 2006).

Appendix C

Relaxed Einstein Equations

The relaxed Einstein field equations were presented for the first time by Landau & Lifshitz (1951). This derivation was motivated by the search of an energy-momentum tensor for the gravitational field. A brief outline will be shown here. This particular form of the EFE constitutes the starting point for post-Minkowskian formalism and helps to understand the applicability of the quadrupole formula to weak-field, self-gravitating systems.

C.1 Energy-Momentum Pseudotensor

The *local* conservation of energy and momentum in flat spacetime can elegantly be written as ${T^{\mu\nu}}_{,\nu} = 0$. By means of the covariance principle this law can be extended to the case when gravitational fields are present, ${T^{\mu\nu}}_{;\nu} = 0$. However, this expression does not represent a conservation law (Landau & Lifshitz, 1951), in the sense that Gauss theorem cannot be applied. The first aim is to rewrite the local conservation of energy-momentum in curved spacetime in such a way that Gauss theorem can be applied. The Equivalence Principle forbids the definition of *local* gravitational energy or momentum: the gravitational interaction can be eliminated locally by a change of coordinates. Thus, the "local conservation" law expresses how the energy and momentum of matter change when gravity is present (Hartle, 2003). The covariant four-divergence of $T^{\mu\nu}$ can be written as,

$$\frac{1}{\sqrt{-g}}\frac{\partial({T_\mu}^\nu\sqrt{-g})}{\partial x^\nu} - \frac{1}{2}T^{\alpha\beta}\frac{\partial g_{\alpha\beta}}{\partial x^\mu} = 0. \tag{C.1}$$

In a LIF, i.e. $g_{\mu\nu,\alpha} = 0$, this last expression becomes $({T_\mu}^\nu\sqrt{-g})_{,\nu} = {T_\mu}^\nu{}_{,\nu} = 0$. Now, if by definition $T^{\mu\nu} = {h^{\mu\nu\lambda}}_{,\lambda}$, and if this last tensor is antisymmetric in the last two indices $h^{\mu\nu\lambda} = -h^{\mu\lambda\nu}$, then trivially ${T^{\mu\nu}}_{,\nu} = 0$. On the other hand, from the EFE, $T^{\mu\nu} = (c^4/8\pi G)(R^{\mu\nu} - g^{\mu\nu}R/2)$, and from the expression of $R^{\mu\nu}$ in the LIF,

$$R^{\mu\nu} = \frac{1}{2}g^{\mu\lambda}g^{\nu\sigma}g^{\alpha\beta}\big[g_{\alpha\lambda,\sigma\beta} + g_{\alpha\sigma,\lambda\beta} - g_{\alpha\beta,\lambda\sigma} - g_{\lambda\sigma,\alpha\beta}\big], \tag{C.2}$$

it can be obtained that,

$$T^{\mu\nu} = \frac{\partial}{\partial x^\lambda}\left\{\frac{c^4}{16\pi G}\frac{1}{(-g)}\frac{\partial}{\partial x^\rho}\big[(-g)(g^{\mu\nu}g^{\rho\lambda} - g^{\mu\lambda}g^{\nu\rho})\big]\right\} = \frac{1}{(-g)}\frac{\partial}{\partial x^\lambda}h^{\mu\nu\lambda}, \tag{C.3}$$

where

$$h^{\mu\nu\lambda} = \frac{\partial}{\partial x^\rho}\left[\frac{c^4}{16\pi G}(-g)(g^{\mu\nu}g^{\rho\lambda} - g^{\mu\lambda}g^{\nu\rho})\right] = \frac{\partial}{\partial x^\rho}H^{\mu\nu\lambda\rho}, \tag{C.4}$$

which is antisymmetric in ν and λ and consequently $h^{\mu\nu\lambda}{}_{,\lambda} = 0$, satisfying the desired conservation equation. Hence, the expression of the $T^{\mu\nu}$ in the LIF, in terms of $g^{\mu\nu}$ was obtained. However this expression is valid only in the LIF. In a general coordinate system corrections, represented by the tensor $t^{\mu\nu}_{\mathrm{LL}}$, arrive from the first derivatives of $g^{\mu\nu}$. This last tensor can be obtained from the EFE through,

$$(-g)(T^{\mu\nu} + t^{\mu\nu}) = H^{\mu\nu\lambda\rho}{}_{,\lambda\rho}, \tag{C.5}$$

with,

$$H^{\mu\nu\lambda\rho} = \frac{c^4}{16\pi G}(\mathfrak{g}^{\mu\nu}\mathfrak{g}^{\lambda\rho} - \mathfrak{g}^{\mu\lambda}\mathfrak{g}^{\nu\rho}), \tag{C.6}$$

where $\mathfrak{g}^{\mu\nu} \equiv (-g)^{1/2}g^{\mu\nu}$, which implies that (Landau & Lifshitz, 1951),

$$\begin{aligned} t^{\alpha\beta}_{\mathrm{LL}} = \frac{c^4}{16\pi G}\big[&\mathfrak{g}^{\alpha\beta}{}_{,\lambda}\mathfrak{g}^{\lambda\mu}{}_{,\mu} - \mathfrak{g}^{\alpha\lambda}{}_{,\lambda}\mathfrak{g}^{\beta\mu}{}_{\mu} + (1/2)(g^{\alpha\beta}g_{\lambda\mu}\mathfrak{g}^{\lambda\nu}{}_{,\rho}\mathfrak{g}^{\rho\mu}{}_{,\nu}) \\ &- g^{\alpha\lambda}g_{\mu\nu}\mathfrak{g}^{\beta\nu}{}_{,\rho}\mathfrak{g}^{\mu\rho}{}_{,\lambda} - g^{\beta\lambda}g_{\mu\nu}\mathfrak{g}^{\alpha\nu}{}_{,\rho}\mathfrak{g}^{\mu\rho}{}_{,\lambda} + g_{\lambda\mu}g^{\nu\rho}\mathfrak{g}^{\alpha\lambda}{}_{,\nu}\mathfrak{g}^{\beta\mu}{}_{,\rho} \\ &+ (1/8)(2g^{\alpha\lambda}g^{\beta\mu} - g^{\alpha\beta}g^{\lambda\mu})(2g_{\nu\rho}g_{\sigma\tau} - g_{\rho\sigma}g_{\nu\tau})\mathfrak{g}^{\nu\tau}{}_{,\lambda}\mathfrak{g}^{\rho\sigma}{}_{,\mu}\big]. \end{aligned} \tag{C.7}$$

The equation (C.5) is not more than a recast of the EFE. The right hand side of eq. (C.5) by construction (C.4) satisfy $H^{\mu\nu\lambda\rho}{}_{,\lambda\rho\nu} = 0$, consequently $[(-g)(T^{\mu\nu} + t^{\mu\nu}_{\mathrm{LL}})]_{,\nu} = 0$. This last tensor can be regarded as the energy-momentum tensor of gravity. It is worthwhile saying that $t^{\mu\nu}_{\mathrm{LL}}$, called the Landau-Lifshitz pseudo tensor, is not a general tensor, because it is expressed in terms of the first derivatives of the metric (Christoffel symbols), but it is a tensor under linear transformations of coordinates, e.g. Lorentz transformations (Landau & Lifshitz, 1951). It vanishes in a LIF in accordance with the Equivalence Principle.

C.2 Relaxed Equations

This particular form of the EFE can be used to study post-Minkowskian expansion of the gravitational field. The field quantity $\mathrm{h}^{\mu\nu}$ defined as,

$$\mathrm{h}^{\mu\nu} \equiv \mathfrak{g}^{\mu\nu} - \eta^{\mu\nu}, \tag{C.8}$$

is replaced in the right hand side of the EFE (C.5), and terms of second order in $\mathrm{h}^{\mu\nu}$ are brought to the left. Afterwards, the De Donder or harmonic gauge is imposed,

$$\mathrm{h}^{\mu\nu}{}_{,\nu} = 0, \tag{C.9}$$

which implies that the EFE take the form (Blanchet, 2006; Maggiore, 2008),

$$\Box\mathrm{h}^{\mu\nu} = \frac{16\pi G}{c^4}\tau^{\mu\nu}, \tag{C.10}$$

where,

$$\tau^{\mu\nu} = (-g)(T^{\mu\nu} + t^{\mu\nu}_{\mathrm{LL}}) - \frac{c^4}{16\pi G}\left(\mathrm{h}^{\mu\nu}\mathrm{h}^{\lambda\rho} - \mathrm{h}^{\mu\lambda}\mathrm{h}^{\nu\rho}\right)_{,\lambda\rho}, \tag{C.11}$$

the last term comes from the non-linear part in $\mathrm{h}^{\mu\nu}$ of eq. (C.6). This form of the EFE has conveniently been expressed as an inhomogeneous wave equation in flat space, whose general solution in vacuum is given by (2.40). The EFE are equivalent to the pair of eqs. (C.9) and (C.10), this last one is called the *relaxed* EFE. The de Donder gauge is equivalent to ${\tau^{\mu\nu}}_{,\nu} = 0$, which is equivalent to ${T^{\mu\nu}}_{;\nu} = 0$. Both equations must be satisfied in order to be equivalent EFE (2.1).

Now, when perturbation theory is performed, i.e. $g^{\mu\nu} = \eta^{\mu\nu} - h^{\mu\nu}$, with $|h^{\mu\nu}| \ll 1$, (C.8) takes the form, $\mathrm{h}^{\mu\nu} = (1/2)\eta^{\mu\nu}h - h^{\mu\nu} = -\bar{h}^{\mu\nu}$, which is the same field presented in chapter 2. From here it is clear that to first order in $\mathrm{h}^{\mu\nu}$, the EFE are reduced to eq. (2.3). The non-linear part represents the contribution of the internal gravity of the source, which at first order for a weak-field, self-gravitating system can be neglected. In addition, when a post-Minkowskian expansion in $\mathrm{h}^{\mu\nu}$ is done,

$$\mathrm{h}^{\mu\nu} = \sum_{n=1}^{\infty} G^n \mathrm{h}^{\mu\nu}_n, \tag{C.12}$$

and replaced in (C.10), the EFE can be solved iteratively in vacuum by equating terms of the same order in G (see e.g. Blanchet, 2006, for details).

Appendix D

Teukolsky Equation

The study of perturbation theory by means of curvature invariants brought the great opportunity to compute the GWR from a test particle in the field of a Kerr BH. This appendix will briefly discuss general aspect of this formalism and some details on the computation of the GWR presented in chapters 3 and 4. Hereafter geometrized units, $G = c = 1$, will be used and over-bar denotes complex conjugation.

D.1 Newman-Penrose Formalism

The line element of the Kerr spacetime in the Boyer-Linquist coordinates is given by,

$$ds^2 = -dt^2 + \Sigma\left(\frac{dr^2}{\Delta} + d\theta^2\right) + \left(r^2 + a^2\right)\sin^2\theta d\phi^2 + \frac{2Mr}{\Sigma}\left(dt - a\sin^2\theta d\phi\right)^2, \quad \text{(D.1)}$$

where $\Delta = r^2 - 2Mr + a^2$ and $\Sigma = r^2 + a^2\cos^2\phi$. The Newman-Penrose (NP) formalism (Newman & Penrose, 1962) is based on the choice of a *null-tetrad*, i.e., $\ell_\mu\ell^\mu = n_\mu n^\mu = m_\mu m^\mu = \bar{m}_\mu\bar{m}^\mu = 0$ and $\ell_\mu n^\mu = 1, m_\mu\bar{m}^\mu = -1$. In the case of Kerr, the following set (among others) is selected,

$$\ell^\mu = \left[(r^2 + a^2)\Delta^{-1}, 1, 0, a\Delta^{-1}\right], \quad \text{(D.2)}$$

$$n^\mu = \left[r^2 + a^2, -\Delta, 0, a\right](2\Sigma)^{-1} \quad \text{(D.3)}$$

$$m^\mu = \left[ia\sin\theta, 0, 1, i(\sin\theta)^{-1}\right]\left[\sqrt{2}(r + ia\cos\theta)\right]^{-1}, \quad \text{(D.4)}$$

$$\bar{m}^\mu = \left[-ia\sin\theta, 0, 1, -i(\sin\theta)^{-1}\right]\left[\sqrt{2}(r - ia\cos\theta)\right]^{-1}, \quad \text{(D.5)}$$

and the metric (D.1) can be expressed as,

$$g_{\mu\nu} = 2\ell_{(\mu}n_{\nu)} - 2m_{(\mu}\bar{m}_{\nu)}. \quad \text{(D.6)}$$

The following *covariant derivative operators* along the null-tetrad are defined,

$$\hat{D} \equiv \ell^\mu\nabla_\mu, \quad \hat{\Delta} \equiv n^\mu\nabla_\mu, \quad \hat{\delta} \equiv m^\mu\nabla_\mu. \quad \text{(D.7)}$$

and the 12 Ricci rotation coefficients are found. In addition, the Weyl and Ricci tensors are projected onto the null-tetrad. The full set of quantities are called the Newman-Penrose quantities. The field equations are obtained from the Ricci and second Bianchi identities, together with the EFE, $R_{\mu\nu} = 8\pi[T_{\mu\nu} - (1/2)g_{\mu\nu}T]$. The explicit form of the NP quantities and the full set of equations can be found in (Pirani, 1965). The NP quantities of the Kerr spacetime that will be used in the computations are given by,

$$\rho = -(r - ia\cos\theta)^{-1}, \qquad \beta = -\bar{\rho}\cot\theta/(2\sqrt{2}), \tag{D.8}$$

$$\pi = ia\rho^2\sin\theta/\sqrt{2}, \qquad \tau = ia\rho\bar{\rho}\sin\theta/\sqrt{2}, \tag{D.9}$$

$$\mu = \rho^2\bar{\rho}\Delta/2, \qquad \gamma = \mu + \rho\bar{\rho}(r - \mu)/2, \tag{D.10}$$

$$\alpha = \pi - \bar{\beta}, \qquad \psi_2^A = M\rho^3, \tag{D.11}$$

The most important thing to mention is that GR is encoded in NP quantities ψ_0 and ψ_4,

$$\psi_0 = -C_{\alpha\beta\mu\nu}l^\alpha m^\beta l^\mu m^\nu, \quad \psi_4 = -C_{\alpha\beta\mu\nu}n^\alpha \bar{m}^\beta n^\mu \bar{m}^\nu. \tag{D.12}$$

For example, in the weak-field limit, radially out-going GWs imply $\psi_4 = -(\ddot{h}_+ - i\ddot{h}_\times)/2$.

D.2 Teukolsky Formalism

The NP formalism can be used to describe the behaviour of perturbations in Kerr spacetime. The perturbation is done as follows. Each member of the null-tetrad is perturbed, e.g. $\boldsymbol{\ell} = \boldsymbol{\ell}^A + \boldsymbol{\ell}^B$, where the indices A and B denote the unperturbed and perturbed parts, respectively. In this way, the NP quantities are also perturbed (see Teukolsky, 1973, for details), and terms to linear order in "B" are kept in the field equations. Teukolsky showed that the equation governing the perturbation ψ_4^B is given by,

$$\begin{aligned}\Big[(\hat{\Delta} + 3\gamma - \bar{\gamma} + 4\mu + \bar{\mu})(\hat{D} + 4\epsilon - \rho)& \\ - (\hat{\bar{\delta}} - \bar{\tau} + \bar{\beta} + 3\alpha + 4\pi)(\bar{\delta} - \tau + 4\beta) - 3\psi_2^A\Big]\psi_4^B &= 4\pi T_4,\end{aligned} \tag{D.13}$$

where,

$$\begin{aligned}T_4 = {}&(\hat{\Delta} + 3\gamma - \bar{\gamma} + 4\mu + \bar{\mu})\big[(\hat{\bar{\delta}} - 2\bar{\tau} + 2\alpha)T_{n\bar{m}} - (\hat{\Delta} + 2\gamma - 2\bar{\gamma} + \mu)T_{\bar{m}\bar{m}}\big] \\ &+ (\hat{\bar{\delta}} - \bar{\tau} + \bar{\beta} + 3\alpha + 4\pi)\big[(\hat{\Delta} + 2\gamma + 2\bar{\mu})T_{n\bar{m}} - (\hat{\bar{\delta}} - \bar{\tau} + 2\bar{\beta} + 2\alpha)T_{nn}\big].\end{aligned} \tag{D.14}$$

Since the NP field equation are invariant under $\boldsymbol{l} \leftrightarrow \boldsymbol{n}$, $\boldsymbol{m} \leftrightarrow \bar{\boldsymbol{m}}$, the equation governing ψ_0 can be obtained from (D.13).

This formalism also describes the behaviour of scalar and vector perturbations, Teukolsky derived a single master equation for all of them,

$$\begin{aligned}-\left[\frac{r^2 + a^2}{\Delta} - a^2\sin^2\theta\right]\partial_{tt}\Psi - \frac{4Mar}{\Delta}\partial_{t\varphi}\Psi - 2s\left[r\frac{M(r^2 + a^2)}{\Delta} + ia\cos\theta\right]\partial_t\Psi& \\ + \Delta^s\partial_r(\Delta^{s+1}\partial_r\Psi) + \frac{1}{\sin\theta}\partial_\theta(\sin\theta\,\partial_\theta\Psi) + \left[\frac{1}{\sin^2\theta} - \frac{a^2}{\Delta}\right]\partial_{\varphi\varphi}\Psi& \\ + 2s\left[\frac{a(r - M)}{\Delta} + i\frac{\cos\theta}{\sin^2\theta}\right]\partial_\varphi\Psi - \big(s^2\cot^2\theta - s\big)\Psi &= 4\pi\Sigma T\end{aligned} \tag{D.15}$$

where Ψ is classified according to the spin and T is related to the different projections of the energy-momentum tensor onto the Newman-Penrose null-tetrad (see table 1 of Ref. Teukolsky (1973)).

D.2.1 Frequency Domain Solution

It was demonstrated on (Teukolsky, 1973) that eq. (D.15) can be separated, in particular for $s = -2$ the separation is given by,

$$\Psi = (r - a\cos\theta)^4 \psi_4 = \int d\omega\, e^{-i\omega t} \sum_{lm} {}_sS_{lm\omega}(\theta) e^{im\phi} R_{lm\omega}(r), \tag{D.16}$$

$$4\pi\Sigma T = \int d\omega e^{-i\omega t} \sum_{lm} {}_sS_{lm\omega}(\theta) e^{im\varphi} T_{lm\omega}(r). \tag{D.17}$$

where ψ_4 without B, for notational ease, denotes the Newman-Penrose scalar perturbation. The equation governing the radial part is,

$$\Delta^2 \frac{d}{dr}\Big(\frac{1}{\Delta}\frac{R_{lm\omega}}{dr}\Big) - V(r)R_{lm\omega} = T_{lm\omega}, \tag{D.18}$$

where

$$V = \frac{K^2 + 4i(r-M)K}{\Delta} + 8i\omega r + \mathcal{E}_{lm} - 2am\omega + (a\omega)^2. \tag{D.19}$$

And the polar equation is,

$$\frac{1}{\sin\theta}\partial_\theta\big[\sin\theta\,\partial_\theta({}_sS_{lm\omega})\big] - \left[\frac{m^2}{\sin^2\theta} + \frac{s^2 + 2ms\cos\theta}{\sin^2\theta} - (a\omega)^2\cos^2\theta \right.$$
$$\left. + 2a\omega s\cos\theta - \mathcal{E}_{lm}\right] {}_sS_{lm\omega} = 0. \tag{D.20}$$

The solution of the last equation was found following the procedure described in appendix A of (Hughes, 2000). These solutions ${}_sS_{lm\omega}$, called spin-weighted spheroidal harmonics, are crucial for the subsequent computation given that the radial equation depends on determination of the eigenvalues $\mathcal{E}_{lm\omega}$. The solution for $s = -2$, $a/M = 0.9$, $\omega M = 0.1$ and its comparison with the spin-weighted spherical harmonics is shown in fig. D.1

The NP scalar ψ_0 also describes a tensor perturbation but with spin $s = 2$. The choice of studying ψ_4 comes from the fact that ψ_0 diverges at the horizon, whereas ψ_4 is bounded at the horizon and at ∞ (Krivan et al., 1997). However, the potential of the radial equation does not decay rapidly enough making the numerical integration difficult. A change of variables, found by Sasaki & Nakamura (1982b), introduces a new the short-ranged potentials $F(r)$ and $U(r)$,

$$X''_{lm\omega} - F(r)X'_{lm\omega} - U(r)X_{lm\omega} = 0, \tag{D.21}$$

where prime denotes differentiation with respect to

$$r^* = r + \frac{2Mr_+}{r_+ - r_-}\ln\frac{(r - r_+)}{2M} - \frac{2Mr_-}{r_+ - r_-}\ln\frac{(r - r_-)}{2M}, \tag{D.22}$$

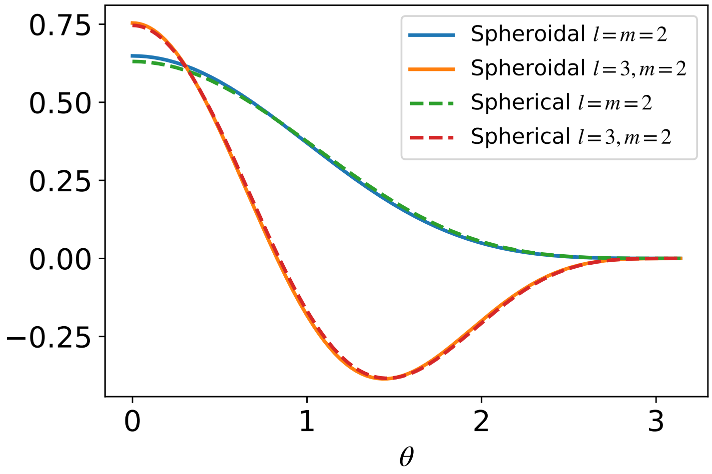

Figure D.1 Spin-weighted spheroidal harmonics with $s = -2$ and for $a/M = 0.9, \omega M = 0.1$ and selected values of l, m. Comparison with spin-weighted spherical harmonics is shown. It can be seen that the correction is small even though the BH is rotating fast.

and $r_\pm = M \pm \sqrt{M^2 - a^2}$ are the outer and inner horizons. The potential F is given by (see e.g. Mino et al., 1997),

$$F = \frac{\eta_{,r}}{\eta} \frac{\Delta}{r^2 + a^2}, \quad \eta = c_0 + c_1/r + c_2/r2 + c_3/r^3 + c_4/r^4, \tag{D.23}$$

where

$$c_0 = -12i\omega M + \lambda(\lambda + 2) - 12a\omega(a\omega - m), \tag{D.24}$$

$$c_1 = 8ia[3a\omega - (a\omega - m)], \tag{D.25}$$

$$c_2 = -24iaM(a\omega - m) + 12a^2[1 - 2(a\omega - m)^2], \tag{D.26}$$

$$c_3 = 24ia^3(a\omega - m) - 24Ma^2, \tag{D.27}$$

$$c_4 = 12a^4, \tag{D.28}$$

with $\lambda = \mathcal{E}_{lm\omega} - 2am\omega + a^2\omega^2$. The potential U,

$$U = \frac{\Delta U_1}{(r^2 + a^2)^2} + G^2 + \frac{\Delta G_{,r}}{r^2 + a^2} - FG, \tag{D.29}$$

where

$$G = -\frac{2(r - M)}{r^2 + a^2} + \frac{r\Delta}{(r^2 + a^2)^2}, \tag{D.30}$$

$$U_1 = V + \frac{\Delta^2}{\beta}\left[(2\alpha + \beta_{,r}/\Delta)_{,r} - (\eta/\eta_{,r})(2\alpha + \beta_{,r}/\Delta)\right], \tag{D.31}$$

$$\alpha = -iK\frac{K\beta}{\Delta^2} + 3iK_{,r} + \lambda\frac{6\Delta}{r^2}, \tag{D.32}$$

$$\beta = 2\Delta(-iK + r - M - 2\Delta/r). \tag{D.33}$$

The solution of the original radial equation (D.18) was found with the same procedure implemented for the Zerilli equation, reviewed in chapter 3.1. However this time the homogeneous solution was not found from the original equation, but from the Sasaki-Nakamura homogeneous equation (D.21). Following the same notation, the change of variables implies that the in-going and out-going solutions are given by Hughes (2001),

$$R^{H,\infty}_{lm\omega} = \frac{1}{\eta}\left[\left(\alpha + \frac{\beta_{,r}}{\Delta}\right)\chi^{H,\infty}_{lm\omega} - \frac{\beta}{\Delta}\chi^{H,\infty}_{lm\omega}\right], \tag{D.34}$$

where $\chi^{H,\infty}_{lm\omega} = X^{H,\infty}\Delta/(r^2 + a^2)^{1/2}$, and $X^H_{lm\omega}, X^{\infty}_{lm\omega}$ are the solutions satisfying the in-going and out-going boundary conditions, respectively. The in-going solution has the following asymptotic form,

$$X^H_{lm\omega} = A^{\text{in}}_{lm\omega}e^{-i\omega r^*} + A^{\text{out}}_{lm\omega}e^{i\omega r^*}, \quad r^* \to \infty, \tag{D.35}$$

$$X^H_{lm\omega} = e^{-ikr^*}, \quad r^* \to -\infty, \tag{D.36}$$

where $k = \omega - ma/(2M_+)$. The function $Z^H_{lm\omega}$ (in the limit $r^* \to \infty$) was found from eqs. (3.10), by changing $S_{l\omega} \mapsto T_{lm\omega}/\Delta^2$ and $\beta_\omega \mapsto A^{\text{in}}_{lm\omega}$. The explicit form of $T_{lm\omega}$ is given by (Mino et al., 1997; Hughes, 2001),

$$\begin{aligned} T_{lm\omega} = \int dt e^{i(\omega t - m\phi_0)}\Delta^2\{[A_{nn0} + A_{n\bar{m}0} + A_{\bar{m}\bar{m}0}]\delta(r - r_0) \\ + [(A_{\bar{m}n1} + A_{\bar{m}\bar{m}1})\delta(r - r_0)]_{,r} + [A_{\bar{m}\bar{m}2}\delta(r - r_0)]_{,rr}\} \end{aligned} \tag{D.37}$$

where ϕ_0, r_0 are the coordinates of the particle trajectory and μ is the mass of test particle. The explicit form of the coefficients can be found in appendix B of (Drasco & Hughes, 2006) and in (Drasco & Hughes, 2014). Finally, in the case of circular orbits, $\omega \rightsquigarrow \omega_m = m\Omega$, the NP scalar at ∞ is given by,

$$\psi_4(t, r, \theta, \phi) = \frac{1}{r}\sum_{lm}\frac{Z^H_{lm\omega_m}}{\sqrt{2\pi}}{}_{-2}S_{lm}(\theta)e^{im\phi}e^{-i\omega_m(t-r^*)} = -\frac{1}{2}(\ddot{h}_+ - i\ddot{h}_\times). \tag{D.38}$$

From this expression, the GW luminosity can be found from eq. (2.31), and from the fact that spheroidal harmonics ${}_{-s}S_{lm\omega}$ are "l-orthonormal", the expression (3.13) was obtained. The numerical solution of eq. (D.21) was implemented in `python` using the packages `Numpy` and `SciPy`.

D.2.2 Time Domain Solution

This subsection will show some progress on the solution of the partial differential equation (D.15), i.e. the time-domain solution. During the plunge phase it is expected that corrections from deviations of circular orbits can arise. The trajectory of the particle in the plunge is given by the HDS and its Fourier transform is not trivial, in contrast, for circular orbits, (D.15) is easily separated in the frequency-domain. This motivated the search of the solution in the time-domain. First, the homogeneous equation was solved following the methodology described in (Krivan et al., 1997) and (Pazos-Ávalos & Lousto, 2005). The field variable used in the calculations is given by (Krivan et al., 1997),

$$\Phi(t, r, \theta, \tilde{\phi}) \equiv e^{mi\tilde{\phi}}r^3\Psi(t, r, \theta), \tag{D.39}$$

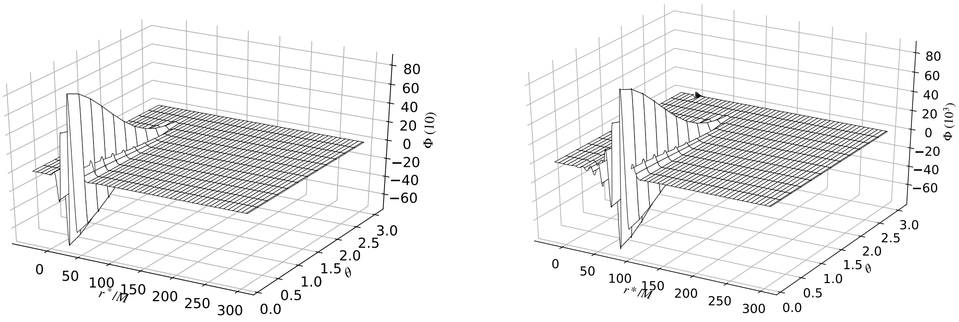

Figure D.2 Three dimensional snapshots of Φ, with $l = m = 2$, at two different times, $t/M = 120, 175$, left and right, respectively. It can be seen the outward propagation of the pulse and the formation of the ringing modes.

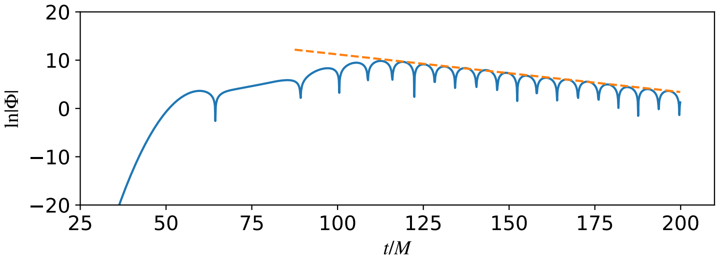

Figure D.3 Slice at $\theta = \pi/2$ of the real part of Φ extracted at $r^*/M = 20$. The damped oscillations are clearly visible with $\Phi \propto e^{-0.078t}$ (orange dashed line).

where $\tilde{\phi}$ is the Kerr coordinate, $d\tilde{\phi} = d\phi + a dr/\Delta$. The Lax-Wendroff method for hyperbolic partial differential equations (see e.g. Press et al., 1992) was used to solve the equation. The solution for $a/M = 0.7$ and $l = m = 2$ for selected times of integration is shown in fig. D.2. The propagation outward is clearly seen and the formation of the ringing tail. The behaviour of the ringing tail is shown in detail in fig. D.3. In order to proceed to the solution of the equation with source, and as test of the method, the standard normal modes of a Kerr BH must be reproduced. Different parameters for a/M have been studied and the results agree with (Kokkotas, 1991). Then next step is currently under development. On the hand, due to the fact that the system after the passage of the ISCO does not suddenly stop satisfying the adiabatic condition $\dot{r} \ll r\Omega$, circularized waveforms (B.4) can describe approximately the radiation during this part. However, in order to confirm this conjecture, effects coming from the radial velocity must be calculated, e.g. by solving the time-domain Teukolsky equation.

Bibliography

Abbott, B. P., Abbott, R., Abbott, T. D., et al. 2016a, Phys. Rev. Lett., 116, 061102

—. 2016b, Living Reviews in Relativity, 19, 1

—. 2017a, Phys. Rev. Lett., 119, 161101

Abbott, B. P., & et al. 2017, ApJ, 848, L13

Abbott, B. P., Abbott, R., Abbott, T. D., et al. 2016c, Phys. Rev. Lett., 116, 241103

—. 2016d, Phys. Rev. Lett., 116, 241102

—. 2016e, Phys. Rev. Lett., 116, 221101

—. 2017b, Phys. Rev. Lett., 118, 221101

—. 2017c, ApJ, 851, L35

—. 2017d, Phys. Rev. Lett., 119, 141101

—. 2017e, ApJ, 848, L12

—. 2017f, ApJ, 851, L16

—. 2018a, Classical and Quantum Gravity, 35, 065009

—. 2018b, arXiv e-prints, arXiv:1811.12907

Accadia, T., Acernese, F., Alshourbagy, M., et al. 2012, Journal of Instrumentation, 7, 3012

Aimuratov, Y., Ruffini, R., Muccino, M., et al. 2017, ApJ, 844, 83

Ajith, P., Babak, S., Chen, Y., et al. 2007, Classical and Quantum Gravity, 24, S689

Ajith, P., Hannam, M., Husa, S., et al. 2011, Phys. Rev. Lett., 106, 241101

Allen, B., Anderson, W. G., Brady, P. R., Brown, D. A., & Creighton, J. D. E. 2012, Phys. Rev. D, 85, 122006

Amaldi, E., & Pizzella, G. 1979, in Relativity, Quanta and Cosmology in the Development of the Scientific Thought of Albert Einstein, 9–139

Amaro-Seoane, P., Audley, H., Babak, S., et al. 2017, arXiv e-prints, arXiv:1702.00786

Amaro-Seoane, P., Aoudia, S., Babak, S., et al. 2012, Classical and Quantum Gravity, 29, 124016

Anninos, P., Hobill, D., Seidel, E., Smarr, L., & Suen, W.-M. 1995, Phys. Rev. D, 52, 2044

Antoniadis, J., Freire, P. C. C., Wex, N., et al. 2013, Science, 340, 448

Apostolatos, T. A. 1995, Phys. Rev. D, 52, 605

Arcavi, I., McCully, C., Hosseinzadeh, G., et al. 2017, ApJ, 848, L33

Arfken, G. B., & Webber, H. J. 2005, Mathematical Methods for Physicist, burlington, USA, Elsevier Academic Press. (2005)

Astone, P., Ballantini, R., Babusci, D., et al. 2006, Classical and Quantum Gravity, 23, S57

—. 2008, Classical and Quantum Gravity, 25, 114048

Atwood, W. B., Abdo, A. A., Ackermann, M., et al. 2009, ApJ, 697, 1071

Barack, L., & Cutler, C. 2004, Phys. Rev. D, 69, 082005

Bardeen, J. M., Press, W. H., & Teukolsky, S. A. 1972, ApJ, 178, 347

Barish, B. C., & Weiss, R. 1999, Physics Today, 52, 44

Becerra, L., Bianco, C. L., Fryer, C. L., Rueda, J. A., & Ruffini, R. 2016, ArXiv e-prints, arXiv:1606.02523

Becerra, L., Cipolletta, F., Fryer, C. L., Rueda, J. A., & Ruffini, R. 2015, ApJ, 812, 100

Becerra, L., Rueda, J. A., Lorén-Aguilar, P., & García-Berro, E. 2018, ApJ, 857, 134

Belvedere, R., Boshkayev, K., Rueda, J. A., & Ruffini, R. 2014, Nuclear Physics A, 921, 33

Benz, W., Cameron, A. G. W., Press, W. H., & Bowers, R. L. 1990, ApJ, 348, 647

Berger, E. 2014, Annual Review of Astronomy and Astrophysics, 52, 43

Berger, E., Fong, W., & Chornock, R. 2013, ApJ, 774, L23

Bernuzzi, S., Dietrich, T., & Nagar, A. 2015a, Phys. Rev. Lett., 115, 091101

Bernuzzi, S., Nagar, A., Dietrich, T., & Damour, T. 2015b, Phys. Rev. Lett., 114, 161103

Bildsten, L., & Cutler, C. 1992, ApJ, 400, 175

Blackman, J., Field, S. E., Galley, C. R., et al. 2015, Phys. Rev. Lett., 115, 121102

Blanchet, L. 2006, Living Reviews in Relativity, 9, 4

Bondi, H. 1960, Nature, 186, 535

Bondi, H., Pirani, F. A. E., & Robinson, I. 1959, Proceedings of the Royal Society of London Series A, 251, 519

Bondi, H., van der Burg, M. G. J., & Metzner, A. W. K. 1962, Proceedings of the Royal Society of London Series A, 269, 21

Breu, C., & Rezzolla, L. 2016, MNRAS, 459, 646

Brill, D. R., & Hartle, J. B. 1964, Physical Review, 135, 271

Buchman, L. T., Pfeiffer, H. P., Scheel, M. A., & Szilagyi, B. 2012, Phys. Rev., D86, 084033

Buonanno, A., & Damour, T. 1999, Phys. Rev. D, 59, 084006

—. 2000, Phys. Rev. D, 62, 064015

Byram, E. T., Chubb, T. A., & Friedman, H. 1966, AJ, 71, 379

Cadelano, M., Pallanca, C., Ferraro, F. R., et al. 2015, ApJ, 812, 63

Camp, J. B., & Cornish, N. J. 2004, Annual Review of Nuclear and Particle Science, 54, 525

Cano, Z., Wang, S.-Q., Dai, Z.-G., & Wu, X.-F. 2017, Advances in Astronomy, 2017, 8929054

Chandrasekhar, S. 1963, Ellipsoidal Figures of Equilibrium (New Haven: Dover Publications)

Chandrasekhar, S. 1967, An introduction to the study of stellar structure

Chen, H.-Y., & Holz, D. E. 2017, ApJ, 840, 88

Chu, T., Fong, H., Kumar, P., et al. 2016, Class. Quant. Grav., 33, 165001

Cipolletta, F., Cherubini, C., Filippi, S., Rueda, J. A., & Ruffini, R. 2015, Phys. Rev. D, 92, 023007

—. 2017, Phys. Rev. D, 96, 024046

Cocke, W. J., Disney, M. J., & Taylor, D. J. 1969, Nature, 221, 525

Connaughton, V., et al. 2017, GCN, 21506

Cutler, C. 1998, Phys. Rev. D, 57, 7089

Cutler, C., Kennefick, D., & Poisson, E. 1994, Phys. Rev. D, 50, 3816

Damour, T. 2001, Phys. Rev. D, 64, 124013

—. 2015, Classical and Quantum Gravity, 32, 124009

Damour, T., & Iyer, B. R. 1991, Phys. Rev. D, 43, 3259

Damour, T., & Nagar, A. 2009, Phys. Rev. D, 79, 081503

—. 2010, Phys. Rev. D, 81, 084016

Damour, T., Nagar, A., & Bernuzzi, S. 2013, Phys. Rev. D, 87, 084035

Dan, M., Rosswog, S., Brüggen, M., & Podsiadlowski, P. 2014, MNRAS, 438, 14

Davis, M., Ruffini, R., Press, W. H., & Price, R. H. 1971, Phys. Rev. Lett., 27, 1466

Davis, M., Ruffini, R., & Tiomno, J. 1972a, Phys. Rev. D, 5, 2932

Davis, M., Ruffini, R., Tiomno, J., & Zerilli, F. 1972b, Physical Review Letters, 28, 1352

Della Valle, M. 2011, International Journal of Modern Physics D, 20, 1745

Detweiler, S. 1980, ApJ, 239, 292

Detweiler, S. L. 1978, ApJ, 225, 687

Detweiler, S. L., & Szedenits, Jr., E. 1979, ApJ, 231, 211

Drasco, S., & Hughes, S. A. 2006, Phys. Rev. D, 73, 024027

—. 2014, Phys. Rev. D, 90, 109905

Drever, R. W. P. 1977, Quarterly Journal of the Royal Astronomical Society, 18, 9

Echeverria, F. 1989, Phys. Rev. D, 40, 3194

Eddington, A. S. 1922, Proceedings of the Royal Society of London Series A, 102, 268

Eggleton, P. P. 1983, ApJ, 268, 368

Eichler, D., Livio, M., Piran, T., & Schramm, D. N. 1989a, Nature, 340, 126

—. 1989b, Nature, 340, 126

Einstein, A. 1915, Sitzungsber. Preuss. Akad. Wiss. Berlin (Math. Phys.), 1915, 844

—. 1916, Sitzungsberichte der Königlich Preußischen Akademie der Wissenschaften (Berlin), 688

—. 1918, Sitzungsberichte der Königlich Preußischen Akademie der Wissenschaften (Berlin), 154

Einstein, A., & Rosen, N. 1937, Journal of The Franklin Institute, 223, 43

Faber, J. A., & Rasio, F. A. 2012, Living Reviews in Relativity, 15, 8

Fermi GBM. 2017, GCN, 524666471

Ferrari, A., & Ruffini, R. 1969, ApJ, 158, L71

Feynman, R. P. 1995, Feynman lectures on gravitation

Finn, L. S., & Chernoff, D. F. 1993, Phys. Rev. D, 47, 2198

Finn, L. S., & Thorne, K. S. 2000, Phys. Rev. D, 62, 124021

Fitchett, M. J., & Detweiler, S. 1984, MNRAS, 211, 933

Flanagan, É. É., & Hughes, S. A. 1998, Phys. Rev. D, 57, 4535

Forward, R. L. 1978, Phys. Rev. D, 17, 379

Friedman, J. L., Ipser, J. R., & Sorkin, R. D. 1988, ApJ, 325, 722

Fryer, C. L., & New, K. C. B. 2011, Living Reviews in Relativity, 14, 1

Fryer, C. L., Oliveira, F. G., Rueda, J. A., & Ruffini, R. 2015, Physical Review Letters, 115, 231102

Fryer, C. L., Rueda, J. A., & Ruffini, R. 2014, ApJ, 793, L36

Gair, J. R., Flanagan, É. É., Drasco, S., Hinderer, T., & Babak, S. 2011, Phys. Rev. D, 83, 044037

Galama, T. J., Vreeswijk, P. M., van Paradijs, J., et al. 1999, A&AS, 138, 465

Galilei, G. 1610, Sidereus Nuncius (Italy: Thomas Baglioni)

Gehrels, N., Chincarini, G., Giommi, P., et al. 2004, ApJ, 611, 1005

Gertsenshteĭn, M. E., & Pustovoĭt, V. I. 1963, Soviet Journal of Experimental and Theoretical Physics, 16, 433

Giacconi, R., Gursky, H., Paolini, F. R., & Rossi, B. B. 1962, Phys. Rev. Lett., 9, 439

Giacconi, R., & Ruffini, R., eds. 1978, Physics and astrophysics of neutron stars and black holes

Goldberg, J. N., Macfarlane, A. J., Newman, E. T., Rohrlich, F., & Sudarshan, E. C. G. 1967, Journal of Mathematical Physics, 8, 2155

Goldstein, A., Veres, P., Burns, E., et al. 2017, ApJ, 848, L14

Goodman, J. 1986, ApJ, 308, L47

Gralla, S. E., Hughes, S. A., & Warburton, N. 2016, Classical and Quantum Gravity, 33, 155002

Guerrero, J., García-Berro, E., & Isern, J. 2004, A&A, 413, 257

Guetta, D., & Della Valle, M. 2007, ApJ, 657, L73

Guetta, D., Pian, E., & Waxman, E. 2011, A&A, 525, A53

Haggard, D., Nynka, M., Ruan, J. J., et al. 2017, ApJ, 848, L25

Han, W.-B., & Cao, Z. 2011, Phys. Rev. D, 84, 044014

Hartle, J. B. 2003, Gravity: An Introduction to Einstein's General Relativity (San Francisco: Addison Wesley)

Hemberger, D. A., Lovelace, G., Loredo, T. J., et al. 2013, Phys. Rev., D88, 064014

Hewish, A., Bell, S. J., Pilkington, J. D. H., Scott, P. F., & Collins, R. A. 1968, Nature, 217, 709

Hotokezaka, K., Kiuchi, K., Kyutoku, K., et al. 2013, Phys. Rev. D, 88, 044026

Hotokezaka, K., & Piran, T. 2017a, arXiv e-prints, arXiv:1707.08978

—. 2017b, ApJ, 842, 111

Hughes, S. A. 2000, Phys. Rev. D, 61, 084004

—. 2001, Phys. Rev. D, 64, 064004

Hulse, R. A., & Taylor, J. H. 1975, ApJ, 195, L51

Husa, S., Khan, S., Hannam, M., et al. 2016, Phys. Rev. D, 93, 044006

Izzo, L., Rueda, J. A., & Ruffini, R. 2012, A&A, 548, L5

Jackson, J. D. 1998, Classical Electrodynamics, 3rd Edition

Jansky, K. G. 1933, Nature, 132, 66

Jantzen, R. T., Carini, P., & Bini, D. 1992, Annals of Physics, 215, 1

Kalogera, V., Narayan, R., Spergel, D. N., & Taylor, J. H. 2001, ApJ, 556, 340

Kawaguchi, K., Kyutoku, K., Nakano, H., et al. 2015, Phys. Rev. D, 92, 024014

Kerr, R. P. 1963, Physical Review Letters, 11, 237

Kidder, L. E. 2008, Phys. Rev. D, 77, 044016

Klebesadel, R. W., Strong, I. B., & Olson, R. A. 1973, ApJ, 182, L85

Klein, A., Barausse, E., Sesana, A., et al. 2016, Phys. Rev. D, 93, 024003

Klimenko, S., Yakushin, I., Mercer, A., & Mitselmakher, G. 2008, Classical and Quantum Gravity, 25, 114029

Kobayashi, S., & Mészáros, P. 2003, ApJ, 589, 861

Kojima, Y., & Nakamura, T. 1984, Progress of Theoretical Physics, 71, 79

Kokkotas, K. D. 1991, Classical and Quantum Gravity, 8, 2217

Kouveliotou, C., Meegan, C. A., Fishman, G. J., et al. 1993, ApJ, 413, L101

Kovacevic, M., Izzo, L., Wang, Y., et al. 2014, A&A, 569, A108

Krivan, W., Laguna, P., Papadopoulos, P., & Andersson, N. 1997, Phys. Rev. D, 56, 3395

Lai, D., Rasio, F. A., & Shapiro, S. L. 1993, ApJS, 88, 205

—. 1994, ApJ, 420, 811

Lai, D., & Shapiro, S. L. 1995, ApJ, 442, 259

Landau, L. D., & Lifshitz, E. M. 1951, The Classical Theory of Fields (Cambridge, Mass.: Adisson-Wesley)

—. 1969, Mechanics (Oxford: Pergamon Press)

—. 1975, The classical theory of fields (4th edition) (Oxford, UK: Butterworth-Heinemann)

Lazarus, P., Tauris, T. M., Knispel, B., et al. 2014, MNRAS, 437, 1485

Lee, W. H., Ramirez-Ruiz, E., & Page, D. 2004a, ApJ, 608, L5

—. 2004b, ApJ, 608, L5

Lehner, L., & Pretorius, F. 2014, Annual Review of Astronomy and Astrophysics, 52, 661

Li, L.-X., & Paczyński, B. 1998, ApJ, 507, L59

Liang, E., Zhang, B., Virgili, F., & Dai, Z. G. 2007, ApJ, 662, 1111

LIGO Scientific Collaboration, Virgo Collaboration et, et al. 2017a, GCN, 21505

—. 2017b, GCN, 21509

—. 2017c, GCN, 21513

LIGO Scientific Collaboration, Aasi, J., Abbott, B. P., et al. 2015, Classical and Quantum Gravity, 32, 074001

LIGO-Virgo Collaboration. 2017, GW170817 Factsheet, `https://dcc.ligo.org/public/0146/G1702000/006/GW170817_Factsheet.pdf`

Liu, H., Creswell, J., von Hausegger, S., Jackson, A. D., & Naselsky, P. 2018, J. Cosmology Astropart. Phys., 2, 013

Longland, R., Lorén-Aguilar, P., José, J., García-Berro, E., & Althaus, L. G. 2012, A&A, 542, A117

Lorén-Aguilar, P., Isern, J., & García-Berro, E. 2009, A&A, 500, 1193

Lovelace, R. B. E., Sutton, J. M., & Craft, H. D. 1968, International Astronomical Union Circular, 2113, 1

Luo, J., Chen, L.-S., Duan, H.-Z., et al. 2016, Classical and Quantum Gravity, 33, 035010

MacFadyen, A. I., & Woosley, S. E. 1999, ApJ, 524, 262

Maggiore, M. 2008, Gravitational Waves: Volume 1: Theory and Experiments, Gravitational Waves (Oxford: Oxford University Press)

Maoz, D., & Hallakoun, N. 2017, MNRAS, 467, 1414

Maoz, D., Hallakoun, N., & Badenes, C. 2018, MNRAS, 476, 2584

Mészáros, P., & Rees, M. J. 1997, ApJ, 482, L29

Meszaros, P., & Rees, M. J. 1997, ApJ, 482, L29

Metzger, B. D. 2017, Living Reviews in Relativity, 20, 3

Metzger, B. D., Martínez-Pinedo, G., Darbha, S., et al. 2010, MNRAS, 406, 2650

Miller, B. D. 1974, ApJ, 187, 609

Mino, Y., Sasaki, M., Shibata, M., Tagoshi, H., & Tanaka, T. 1997, Progress of Theoretical Physics Supplement, 128, 1

Mirabel, I. F., & Rodríguez, L. F. 1998, Nature, 392, 673

Misner, C. W. 1972, Physical Review Letters, 28, 994

Misner, C. W., Thorne, K. S., & Wheeler, J. A. 2017, Gravitation (Princeton, New Jersey: Princeton University Press)

Mitsou, E. 2011, Phys. Rev. D, 83, 044039

Mroue, A. H., et al. 2013, Phys. Rev. Lett., 111, 241104

Nagar, A., Damour, T., & Tartaglia, A. 2007, Classical Quantum Gravity, 24, S109

Nakano, H., Sago, N., Tanaka, T., & Nakamura, T. 2016, Progress of Theoretical and Experimental Physics, 2016, 083E01

Narayan, R., Piran, T., & Shemi, A. 1991, ApJ, 379, L17

Newman, E., & Penrose, R. 1962, Journal of Mathematical Physics, 3, 566

Newman, E. T., & Penrose, R. 1966, Journal of Mathematical Physics, 7, 863

Newman, E. T., & Penrose, R. 1966, Journal of Mathematical Physics, 7, 863

Nitz, A. H., Dal Canton, T., Davis, D., & Reyes, S. 2018, Phys. Rev. D, 98, 024050

Ori, A., & Thorne, K. S. 2000, Phys. Rev. D, 62, 124022

Özel, F., & Freire, P. 2016, ARA&A, 54, 401

Paczynski, B. 1986, ApJ, 308, L43

—. 1991, Acta Astron., 41, 257

Paschalidis, V., Liu, Y. T., Etienne, Z., & Shapiro, S. L. 2011, Phys. Rev. D, 84, 104032

Paschalidis, V., MacLeod, M., Baumgarte, T. W., & Shapiro, S. L. 2009, Phys. Rev. D, 80, 024006

Pazos-Ávalos, E., & Lousto, C. O. 2005, Phys. Rev. D, 72, 084022

Penzias, A. A., & Wilson, R. W. 1965, Astrophys. J., 142, 419

Peters, P. C. 1964, Physical Review, 136, 1224

Peters, P. C., & Mathews, J. 1963, Physical Review, 131, 435

Pirani, F. A. E. 1965, INTRODUCTION TO GRAVITATIONAL RADIATION THEORY (Notes by J. J. J. Marek and the Lecturer), 249

Poisson, E., Pound, A., & Vega, I. 2011, Living Reviews in Relativity, 14, 7

Postnov, K. A., & Yungelson, L. R. 2014, Living Reviews in Relativity, 17, 3

Pound, A., & Poisson, E. 2008, Phys. Rev. D, 77, 044013

Press, W. H. 1971, ApJ, 170, L105

Press, W. H., Teukolsky, S. A., Vetterling, W. T., & Flannery, B. P. 1992, Numerical recipes in C: the art of scientific computing (Cambridge, UK: Cambridge University Press)

Pretorius, F. 2005, Physical Review Letters, 95, 121101

Raskin, C., Scannapieco, E., Fryer, C., Rockefeller, G., & Timmes, F. X. 2012, ApJ, 746, 62

Rebassa-Mansergas, A., Parsons, S. G., García-Berro, E., et al. 2017, MNRAS, 466, 1575

Rees, M., Ruffini, R., & Wheeler, J. A. 1974, Black holes, gravitational waves and cosmology: an introduction to current research

Regge, T., & Wheeler, J. A. 1957, Physical Review, 108, 1063

Rhoades, C. E., & Ruffini, R. 1974, Physical Review Letters, 32, 324

Rigault, M., Aldering, G., Kowalski, M., et al. 2015, ApJ, 802, 20

Rodriguez, J. F., Rueda, J. A., & Ruffini, R. 2016, ArXiv e-prints, arXiv:1605.04767

—. 2017, ArXiv e-prints, arXiv:1706.06440

Rodríguez, J. F., Rueda, J. A., & Ruffini, R. 2018, Journal of Cosmology and Astro-Particle Physics, 2018, 030

Rodriguez, J. F., Rueda, J. A., & Ruffini, R. 2018, Astronomy Reports, 62, 940

Rodríguez, J. F., Rueda, J. A., & Ruffini, R. 2018, in European Physical Journal Web of Conferences, Vol. 168, European Physical Journal Web of Conferences, 02006

Rodriguez, J. F., Rueda, J. A., Ruffini, R., et al. 2018, *Chirping* compact stars: gravitational radiation and detection degeneracy with binary systems *A conceptual pathfinder for space-based gravitational-wave observatories* (submitted to Phys. Rev. D)

Rosswog, S., Ramirez-Ruiz, E., & Davies, M. B. 2003a, MNRAS, 345, 1077

—. 2003b, MNRAS, 345, 1077

Rotondo, M., Rueda, J. A., Ruffini, R., & Xue, S.-S. 2011, Phys. Rev. D, 84, 084007

Rueda, J. A., Boshkayev, K., Izzo, L., et al. 2013, ApJ, 772, L24

Rueda, J. A., & Ruffini, R. 2012, ApJ, 758, L7

Rueda, J. A., Ruffini, R., Wang, Y., et al. 2018a, ArXiv e-prints, arXiv:1807.07905

—. 2018b, Journal of Cosmology and Astro-Particle Physics, 2018, 006

Ruffini, R. 1973a, Phys. Rev. D, 7, 972

Ruffini, R. 1973b, in Black Holes (Les Astres Occlus), ed. C. Dewitt & B. S. Dewitt, 451–546

Ruffini, R., Bernardini, M. G., Bianco, C. L., et al. 2006, in The Tenth Marcel Grossmann Meeting, ed. M. Novello, S. Perez Bergliaffa, & R. Ruffini (Singapore: World Scientific), 369

Ruffini, R., Bernardini, M. G., & Bianco et al., C. L. 2008, in The Eleventh Marcel Grossmann Meeting, ed. H. Kleinert, R. T. Jantzen, & R. Ruffini, 368–505

Ruffini, R., Bianco, C. L., Fraschetti, F., Xue, S.-S., & Chardonnet, P. 2001, ApJ, 555, L117

Ruffini, R., & Wheeler, J. A. 1969, ESRO, SP, No. 52, p. 45 - 174, 52, 45

—. 1971, Physics Today, 24, 30

Ruffini, R., Bernardini, M. G., Bianco, C. L., et al. 2007, in ESA Special Publication, Vol. 622, ESA Special Publication, 561

Ruffini, R., Wang, Y., Enderli, M., et al. 2015a, ApJ, 798, 10

Ruffini, R., Muccino, M., Kovacevic, M., et al. 2015b, ApJ, 808, 190

Ruffini, R., Muccino, M., Aimuratov, Y., et al. 2016a, ApJ, 831, 178

Ruffini, R., Rueda, J. A., Muccino, M., et al. 2016b, ApJ, 832, 136

—. 2016c, ArXiv e-prints, arXiv:1602.02732

Ruffini, R., Wang, Y., Aimuratov, Y., et al. 2018a, ApJ, 852, 53

Ruffini, R., Rodriguez, J., Muccino, M., et al. 2018b, ApJ, 859, 30

Ruffini, R., Muccino, M., Aimuratov, Y., et al. 2018c, arXiv e-prints, arXiv:1802.07552

Ruiter, A. J., Belczynski, K., & Fryer, C. 2009, ApJ, 699, 2026

Sasaki, M., & Nakamura, T. 1982a, Physics Letters A, 89, 68

—. 1982b, Progress of Theoretical Physics, 67, 1788

Sathyaprakash, B. S., & Schutz, B. F. 2009, Living Reviews in Relativity, 12, 2

Schutz, B. F. 2011, Classical and Quantum Gravity, 28, 125023

Shibata, M. 2016, Numerical Relativity (Singapore: World Scientific Publishing Co. Pte. Ltd.)

Shibata, M., & Taniguchi, K. 2006, Phys. Rev. D, 73, 064027

—. 2011, Living Rev. Relat., 14

Smarr, L. L. 1975, PhD thesis, THE UNIVERSITY OF TEXAS AT AUSTIN.

Smartt, S. J., Chen, T. W., Jerkstrand, A., et al. 2017, Nature, 551, 75

Soderberg, A. M., Kulkarni, S. R., Nakar, E., et al. 2006, Nature, 442, 1014

Stergioulas, N. 2003, Living Reviews in Relativity, 6, 3

Sun, H., Zhang, B., & Li, Z. 2015, ApJ, 812, 33

Svinkin, D., & Hurley, K. 2017, GCN, 21515

SXS Catalog. 2018, `http://www.black-holes.org/waveforms`

Takahashi, R., & Seto, N. 2002, ApJ, 575, 1030

Tanvir, N. R., Levan, A. J., Fruchter, A. S., et al. 2013, Nature, 500, 547

Taracchini, A., Buonanno, A., Khanna, G., & Hughes, S. A. 2014, Phys. Rev. D, 90, 084025

Tauris, T. M., van den Heuvel, E. P. J., & Savonije, G. J. 2000, ApJ, 530, L93

Tauris, T. M., Kaspi, V. M., Breton, R. P., et al. 2015, Advancing Astrophysics with the Square Kilometre Array (AASKA14), 39

Taylor, J. H., Fowler, L. A., & McCulloch, P. M. 1979, Nature, 277, 437

Taylor, J. H., & Weisberg, J. M. 1982, ApJ, 253, 908

Teukolsky, S. A. 1972, Physical Review Letters, 29, 1114

—. 1973, ApJ, 185, 635

Teukolsky, S. A., & Press, W. H. 1974, ApJ, 193, 443

The Gravitational Wave Open Science Center. 2018, LOSC GW150914 event tutorial, `https://www.gw-openscience.org/GW150914data/LOSC_Event_tutorial_GW150914.html`

Thorne, K. S. 1977, in NATO Advanced Science Institutes (ASI) Series B, Vol. 27, 1

Thorne, K. S. 1980a, Reviews of Modern Physics, 52, 285

—. 1980b, Reviews of Modern Physics, 52, 299

—. 1989, Gravitational Radiation: A New Window onto the Universe (Unpublished manuscript)

Troja, E., Piro, L., van Eerten, H., et al. 2017, Nature, 551, 71

Usov, V. V. 1992, Nature, 357, 472

—. 1994, MNRAS, 267, 1035

Verrecchia, F., Tavani, M., Donnarumma, I., et al. 2017, ApJ, 850, L27

Virgili, F. J., Liang, E.-W., & Zhang, B. 2009, MNRAS, 392, 91

Virgili, F. J., Zhang, B., O'Brien, P., & Troja, E. 2011, ApJ, 727, 109

Wald, R. 2010, General Relativity (University of Chicago Press)

Wanderman, D., & Piran, T. 2010, MNRAS, 406, 1944

—. 2015, MNRAS, 448, 3026

Weber, J. 1960, Physical Review, 117, 306

—. 1969, Phys. Rev. Lett., 22, 1320

Weber, J., & Wheeler, J. A. 1957, Reviews of Modern Physics, 29, 509

Weinberg, S. 1972, *Gravitation and Cosmology: Principles and Applications of the General Theory of Relativity*, new York, USA: John Wiley & Sons, Inc.

—. 2008, *Cosmology*, oxford, UK: Oxford University Press

Weisberg, J. M., & Taylor, J. H. 2005, in Binary Radio Pulsars, ed. F. A. Rasio & I. H. Stairs, Vol. 328, 25

Weiss, R. 1972, Quarterly Progress Report, Research Laboratory of Electronics, MIT, 105, 54

Wheeler, J. A. 1955, Physical Review, 97, 511

Wiener, N. 1949, The Extrapolation, Interpolation and Smoothing of Stationary Time Series with Engineering Applications (New York, USA: Wiley)

Woosley, S. E., & Bloom, J. S. 2006, ARA&A, 44, 507

Woosley, S. E., & MacFadyen, A. I. 1999, Astronomy and Astrophysics Supplement Series, 138, 499

Zerilli, F. J. 1970, Phys. Rev. D, 2, 2141

Zhang, B. B., Zhang, B., Sun, H., et al. 2018, Nature Communications, 9, 447

Zhu, C., Chang, P., van Kerkwijk, M. H., & Wadsley, J. 2013, ApJ, 767, 164